Infrared Methods Applied to Photonic Crystal Device Development

A Thesis
Presented to
The Academic Faculty

by

Gregory R. Kilby

In Partial Fulfillment
of the Requirements for the Degree
Doctor of Philosophy

School of Electrical and Computer Engineering
Georgia Institute of Technology
August 2005

Copyright © 2005 by Gregory R. Kilby

Infrared Methods Applied to Photonic Crystal Device Development

Approved by:

Professor Thomas K. Gaylord, Advisor
School of Elect. and Comp. Engineering
Georgia Institute of Technology

Professor Ali Adibi
School of Elect. and Comp. Engineering
Georgia Institute of Technology

Professor John A. Buck
School of Elect. and Comp. Engineering
Georgia Institute of Technology

Professor Russell W. Callen
School of Elect. and Comp. Engineering
Georgia Institute of Technology

Professor Phillip N. First
School of Physics
Georgia Institute of Technology

Date Approved: June 27, 2005

To my family

Meredith, Michael and Lorelyn

ACKNOWLEDGEMENTS

The research presented in this thesis could not have been completed without the support and contributions of many people. First, I owe a great debt of gratitude to Prof. Thomas K. Gaylord for his support, encouragement and guidance throughout my studies at Georgia Tech. I have learned a tremendous amount from Dr. Gaylord, both about research and life. His tireless curiosity and quest for knowledge are inspiring. I will strive to live up to the example he has set in scholarly activities. I would also like to thank the members of my thesis defense committee, Prof. Ali Adibi, Prof. John Buck, Prof. Russell Callen, and Prof Philip First for their guidance, comments, insightful questions, and observations.

I also must thank my fellow students for their support throughout this research, the camaraderie during some long days, and for all the experiences we have shared in Atlanta and on our group trips. The quality of my fellow students and their willingness to help one another has made this experience enjoyable.

Brent Bachim has provided constant advice, counsel and assistance on every aspect of my research. I have infringed on his time for many countless problems I encountered. He patiently listened and provided his thoughts on just about every aspect of this work. His careful review of my thesis was tremendous! I learned very quickly to incorporate every comment he made on the work. I am extremely grateful and indebted to him for all of his help.

I must also thank Pejman Monajemi for his willingness to help in etching and optimizing the fabrication of the photonic crystal structures. I must also thank Dr. Carole Montarou for research discussions and assistance in writing my proposal and thesis, as well as for the many interesting conversations and debates initiated within the group. I would also like to thank Dr. Tony Mulé for his assistance in the cleanroom early in this research and Sergio Pieiga for his simulation programming that was used to compute theoretical structure transmittances and reflectances. Many thanks also to our research group members, Dr.

Ricardo Villalaz, Dr. Shun-Der Wu, Oluwafemi Ogunsola, Justin Stay, and John Makaisch for their discussions, encouragement and assistance at many different times.

Finally, I would like to thank my family. I owe an apology to Michael and Lorelyn for the missed events over the past years (particularly the last several months) and I owe them a word of thanks for the acceptance of our transitory lifestyle. I am so proud of you both! Most of all I must thank my wife Meredith, for her love and patience in this and every endeavor. She makes everything worthwhile!

Gregory R. Kilby

Georgia Institute of Technology June 2005

This research is supported by the Army Research Office under grant DAAD19-03-1-0286.

TABLE OF CONTENTS

LIST OF TABLES

LIST OF FIGURES

SUMMARY

Photonic crystal (PC) technology has many important potential applications. The concept of PC structures was introduced almost 20 years ago. The technology potentially offers lossless control of light propagation at a size scale near the order of the wavelength of light. The advantages and benefits of using such a technology in commercial devices are staggering. Yet, the commercial development of PC structures has been slow. Challenges associated with the repeatable fabrication and testing of structures has been identified as one cause of the slow development pace.

In this thesis, a development methodology that utilizes PC structures that operate in the long-wavelength infrared is presented. Scaling the operating wavelength to the infrared spectral region increases the dimensions of the structures that must be fabricated to produce PC devices. The increase in size significantly reduces the difficulty of fabricating PC structures. With fewer resources and less effort committed to small-scale fabrication, the pace of PC technology development can be increased. Although research must continue on structures designed to operate at telecommunications wavelengths, this present approach can accelerate the development of PC technology.

To demonstrate the methodology, 1-dimensional PC structures, consisting of alternating regions of silicon and air were fabricated. With a single layer of silicon and a single layer of air forming one period, structures containing from 5 to 75 periods were characterized by measuring the transmittance or reflectance of the structure over the wavelength range from $\lambda = 5\ \mu m$ to $\lambda = 15\ \mu m$. Realistic simulations were developed to model the fabricated structures and calculate the theoretical transmittances and reflectances.

For this methodology, a model of a focused infrared beam typically used in infrared applications has been developed. The model has been tested in several measurement configurations showing excellent agreement between measurements and theoretical calculations.

A novel characterization method, enabling the calculation of the single-angle plane-wave transmittances and reflectances from composite, multiple-angle transmittance and reflectance measurements, has been formulated. Simulations show that the single-angle transmittances or reflectances of PC structures can be deconvolved from composite, multiple-angle measurements when the measurement error is less than 5%. The characterization method is successfully applied to measurements obtained using new and existing infrared characterization tools. Measured and theoretical plane-wave transmittances and reflectances are shown to be in good agreement. The developed technique's success is dependent upon the acquisition of data with relatively low measurement noise.

A new characterization tool using a discretely tunable carbon-dioxide (CO_2) laser has been designed, constructed, and demonstrated. The system is shown to be capable of measuring the spectral characteristics of PC structures to include the spectral location of photonic band gaps and band passes. Measurement noise, introduced primarily by the existing power detector, limits the application of the apparatus as presented. Spectral variations from wavelength to adjacent wavelength are generally small. Improvements to the apparatus are suggested.

A measurement apparatus employing an FTIR microspectroscopy system has been developed to record measurements for the single-angle plane-wave characterization method. Transmittance measurements are shown to be in excellent agreement with theory. Band edge spectral locations and small variations in the spectra are characterized accurately in the measurements. Calculations of the single-angle plane-wave transmittances of PC structures to light incident over a 30°angular range are demonstrated. The apparatus is also demonstrated in the reflection mode; however, reflectance measurements and single-angle plane-wave calculations from reflectance measurements are currently hindered by low optical power present in the measurement system.

The results of this research are analyzed to identify the advantages and limitations of the long-wavelength infrared method. Short- and long-term directions for future research are presented. The presented long-wavelength design and development methodology, developed characterization tools, and single-angle plane-wave characterization method offer the

promise to accelerate development of PC technology.

CHAPTER 1

INTRODUCTION

Photonic crystal (PC) technology offers unprecedented capabilities to control the propagation of light [3, 4]. Theoretically, devices designed using PC technology offer complete, lossless control of photon propagation and a corresponding unmatched performance capability. The physical size of PC structures is on the order of several wavelengths of light making feature sizes and device periods a fraction of this wavelength. The potential benefits of lossless control of light and the small-size advantage offered in these devices makes this technology attractive for many optoelectronic applications. However, rapid development of PC devices is hindered by challenges in the fabrication and testing of the structures. In this chapter, issues related to PC device development are discussed and a new approach for addressing these development challenges is presented.

1.1 Demonstrated Photonic Crystal Devices and Applications

A PC is a periodic lattice of a dielectric material where the lattice periodicity can extend in one, two, or all three spatial dimensions. Photons traveling through the material experience a periodic potential caused by the contrasting regions of low and high refractive indices. If the index contrast is sufficient, the light will be restricted to propagating within only one of the dielectric materials. Reflection and diffraction from the contrasting dielectric regions will cause constructive and destructive interference giving rise to allowed and forbidden ranges of propagation energies in the structure. The forbidden regions are referred to as photonic band gaps. Photons possessing energies within the band gap cannot propagate through the material [5]. By introducing intentional defects into the lattice, selected modes within the band gap may once again propagate. A PC designed with such a defect can then be used to control the propagation of light at a specific energy level or, equivalently,

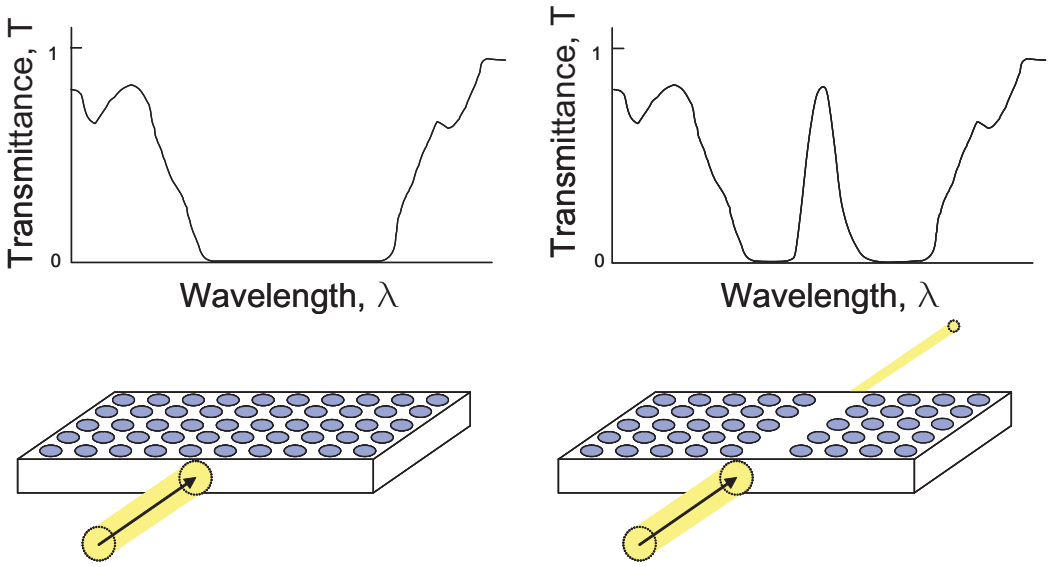

Figure 1.1: A 2-dimensional PC waveguide is constructed by first designing a material with a photonic band gap. Wavelengths within the band gap cannot propagate through the material, as shown in the left diagram. The introduction of a linear defect, as shown in the right diagram, permits certain wavelengths within the band gap to once again propagate.

wavelength.

Various research groups have demonstrated a wide variety of components and capabilities for optoelectronic devices that incorporate PC structures. Many of the proposed or demonstrated devices are considered to be the basic components required for constructing complex all-photonic circuits. Demonstrated or proposed devices include waveguides [6–10], waveguide bends [11–17], resonators [10, 18–22], multiplexers [23–25], filters [26–29], couplers [30, 31], switches [32], and active emission devices [33, 34]. Though the volume of the research prohibits addressing all of these accomplishments, a representative sampling illustrates the advantages PC technology brings to these devices.

PC waveguides are fabricated by introducing a linear defect into a PC structure where modes within the band gap of the crystal lattice can propagate as a result of the defect site as shown in Fig. 1.1. Since the bulk crystal portion is impervious to light, the mode can only propagate along the defect. This enables PC structures to demonstrate characteristics such as the right angle bending of light on a scale of tens of wavelengths. In an early effort, simulation and modeling efforts predicted greater than 95% transmission through a 90° waveguide bend [11]. Later, the sharp, low-loss light-bending capability of these structures

was demonstrated with near 100% transmission through waveguides at microwave frequencies [12]. More recently, efficient guiding through a 120° bend by way of a PC waveguide fabricated on a silicon-on-insulator (SOI) substrate was demonstrated at a wavelength of 1.5 μm [13]. Once commercially viable, the ability to transmit light from component to component along PC waveguides on a size scale of several wavelengths will permit fabrication of dense optical circuits and offer significant reduction in the size of optical interconnect and telecommunication devices.

Cavity resonators can be used to implement a variety of optoelectronic functions. In PC format, these resonators can be fabricated with exceptionally high quality factors (Q-factors) and, once again, on a size scale of several wavelengths. Resonators consist of a PC structure with a point defect introduced into the crystal structure. Modes of a specific frequency resonate at the defect site. Resonator simulations first predicted the existence of cavities at point defect sites in a crystal slab with theoretical Q-factors in the 6,000 to 10,000 range [26]. Experimental results followed with measured Q-factors reported in the first PC resonators as high as 816 [10, 19]. Recent work has stressed the important role that these devices will play in the development of photonic integrated circuits [21, 22].

Since these initial results were reported, cavities have been combined with PC waveguides to demonstrate couplers, multiplexers, filters, and switches [23–25, 27, 28, 34]. PC multiplexers have been demonstrated with the capability of channeling light vertically out of the two-dimensional crystal plane by means of a resonator [23, 27]. The wavelength of emission is selected by varying the defect geometry and the distance of the defect from the source waveguide. Similarly, in-plane filtering and demultiplexing has been demonstrated by coupling light from a waveguide through a resonant cavity to a second waveguide [24,25,28]. High Q-factor and tunable characteristics of the PC devices permit linewidth selection with high resolution. In one demonstration, an optical pulse was demultiplexed into as many as six channels with individual bandwidths of 2 nm [25]. A PC-based Mach-Zehnder interferometer has been proposed which consists of two coupled-resonator optical waveguides with differing lengths [32]. This device was demonstrated at microwave frequencies. At optical wavelengths, such a device is a possible sampling component in the development of

next-generation analog-to-digital (A/D) converters [35].

PC lasers and electroluminescent devices have also been proposed, fabricated and tested. In these devices, PC resonant cavities are created by patterning and etching a multiple quantum well semiconductor material. Room temperature operation has been demonstrated in PC lasers with pump powers as low as 220 μW [34]. These devices offer a potentially viable low-power optical source for all-photonic circuits.

With the impressive advances in PC research and the existence of a technology that could enable all-photonic circuits, the potential impact on the telecommunications field is stunning. In its present state, the telecommunications industry uses both optical and electronic technologies. Transmission, processing, and storage requires frequent signal conversion between electrical and optical formats. The advent of all-optical circuits offers the possibility of eliminating these format conversions. The characteristic of lossless information transfer and transmission could further increase efficiency and decrease component requirements.

PC waveguide components could be used to facilitate chip-scale integration of optical PC elements; light could then be routed from one structure on a chip to another on an extremely small size scale. Demultiplexing, filtering, and even processing tasks could potentially be accomplished with PC components. The theoretical existence of PC-based devices such as optical transistors, logic circuits, and memory elements have been described in the literature [5, 36, 37]. These all-photonic circuits would operate at faster speeds and with greater efficiency than present day electronic components.

As these PC-based components migrate into the telecommunications infrastructure, continual decreases in component size would also be realized. Though unproven at this point, PC technology offers great potential for advances in the efficiency, capacity, and cost of telecommunications systems.

Following its integration into the telecommunications field, PC technology could be expected to migrate to other industries. In the computing industry, data processing and data storage could become optically based functions. Optical computers employing PC technology have been envisioned operating at speeds in the Terrahertz range [5]. From this

point, PC technology could spread to virtually all industries.

1.2 Development Challenges

Despite the significant potential benefits of PC technology and the research efforts to date, relatively few PC devices have made the transition to full-scale commercial use. Table 1.1 lists several PC start-up companies and the published status of PC developments. Despite the fact that many of these companies were chartered to develop PC products, few have succeeded in producing PC-based components for commercial use. This is caused, in part, by challenges associated with PC fabrication, testing, modeling, and integration.

Fabrication and testing challenges originate directly from the physical size of PC devices. At telecommunications wavelengths (1.3 μm to 1.5 μm), the required period for a PC device is less than one micron, with device feature sizes a fraction of the period. Fabrication of devices at these dimensions pushes or exceeds the capabilities of current microelectronics fabrication technology. Though new nano-fabrication technologies are in development, the widespread capability to produce devices does not exist. Similarly, characterization methods and tools for sub-micron device testing must also be developed and implemented. These challenges have created a situation where limited experimental data on fabricated devices is available. While many tools to model PC devices exist, few researchers have the ability to produce and test PC devices.

Modeling and simulation tools must be available that accurately predict the performance of fabricated devices. Variables that include design parameter changes and fabrication variability must be taken into account in the models. Though many impressive modeling and simulation techniques have been developed, fabricated structures have yet to achieve many of the predicted performance benchmarks. Additional experimental data on fabricated devices is required to analyze the models so the models can be improved and used to reconcile the differences between observed and predicted performance. Device characterization techniques capable of showing the effects of minor variations in fabricated structures are needed.

Many of the demonstrated devices, though representing important advances in PC technology development, are not useful structures by themselves. They must be integrated with

Table 1.1: The development of commercial PC products is a stated objective of the following companies [38–45]. Products offered or the current status of development is listed for each company as of 030105. The slow migration of the technology to commercial products is shown by the extremely limited number of products offered. The need for increased participation and additional development tools is evident.

Company Name	Location	Products offered or development status
NanoOpto	Somerset, New Jersey	A polarization beam splitter and a broad-band polarizer are listed on the company web site. A news release states that a bandpass filter will soon be available. The extent that products incorporate PC technology is unclear. Products are described as using proprietary nano-optic technology.
Galian Photonics	Vancouver, British Columbia	Closed due to technical hurdles.
Mesophotonics	Southhampton, United Kingdom	Waveguide "Continuum" chips were offered starting in July 2004. The research community appears to be the primary user of of the devices. Klarite substrates for Raman spectroscopy were introduced in January 2005.
Luxtera	Carlsbad, California	Silicon-based optical modulator. Development efforts are on-going.
Clarendon Photonics	Newton, Massachusetts	A grating-based optical add-drop multiplexer is available. The extent to which PC technology is used in the device is unclear. The technology is described as proprietary.
Crystal Fibre	Birkerød, Denmark	Company produces PC fiber.
Neophotonics	San Jose, California	PC devices are in development for future planar lightwave circuits. Current products rely primarily upon conventional, standard waveguide technology.
Photeon	Bregenz, Austria	PCs are listed as a research activity. The extent to which current products contain PC technology is uncertain.

other optical or PC devices to be useful in practical applications. The risk associated with the commercial development of PC technology is significant, partially due to the lack of demonstrated functional systems containing multiple integrated PC devices. Methods are needed capable of demonstrating multiple-component PC systems to mitigate this risk for commercial PC device development.

The combined effects of fabrication and testing challenges, incomplete model information, and the lack of a method to reduce integration risk have played a role in the relatively slow commercial development of this field. Methods of design and development that address some of these shortcomings will hasten the movement of PC devices to commercial applications.

A long-wavelength approach to the design and development of PC structures addresses many of these needs. Such an approach offers the advantage of conducting device fabrication and testing at micro-scale dimensions. Fabrication and characterization tools are more readily available for devices of this size. The advanced state of microelectronics fabrication equipment and analysis equipment enables rapid design and test cycles. Iterative design will improve the understanding of the impact that design changes and fabrication variations have on devices. The advanced analysis equipment available suits the development of characterization methods that provide needed fundamental device performance data. These data can be incorporated into PC models and provide a valuable tool for reconciling of the differences between theoretical and experimental device performance. Large-scale prototype devices and systems could be produced to verify the technology and reduce the risks associated with multiple-device integration. Insight and conclusions from the long-wavelength testing can be directly applied to PC devices designed at shorter wavelengths via the scaling property of PCs [46]. Though such a method cannot replace needed research at nano-scale dimensions, long-wavelength based investigations can enhance the understanding of how PC devices will operate.

1.3 Research Objectives

PC technology has been shown to be a promising technology for future optoelectronic systems. Theoretically, devices incorporating PC technology can significantly out-perform their existing counterparts. Despite the potential advantages of this technology, development is hampered by research and development challenges. The main objective of this research is to develop a long-wavelength infrared PC design methodology to assist in the development and application of PC structures. The main contributions of this research are listed below:

1. The development of an infrared methodology that exploits the advantages of long-wavelength PC research is presented. The method provides a framework for increased participation in PC research and a corresponding increase in the experimental data available on fabricated structures.

2. A detailed analysis of incident light from a reflecting infrared objective is presented along with a method to quantify the focused beam.

3. For the first time, a method is presented for computing the single-angle plane-wave transmittances and reflectances of a test device from composite, multiple-incident-angle measurements. The method provides a fundamental quantitative approach for the analysis of fabricated device performance.

4. The first transmittance measurements of PC structures using a discretely tunable carbon-dioxide (CO_2) laser-based testing apparatus is demonstrated. A single-angle plane-wave characterization technique is applied to the measurements.

5. The application of the single-angle plane-wave characterization technique to spectral measurements from a Fourier Transform Infrared (FTIR) spectroscopy system is presented.

6. The first analysis of FTIR reflectance measurement geometry is presented and the single-angle plane-wave characterization technique is applied to the composite, multiple-incident-angle reflectance measurements.

1.4 Thesis Overview

The objective of this research is to develop a methodology for the design and development of PC structures using micro-scale structures at infrared wavelengths. Devices are fabricated using standard optical lithography and microelectronics fabrication equipment. A wavelength-tunable, CO_2-laser system and an FTIR microspectroscopy system are used to characterize the fabricated devices. A novel data processing scheme is developed to obtain the single-angle plane-wave transmittances or reflectances of the test device. The design method employs feedback so that results from one design iteration can be used as input into the next cycle, in order to garner a thorough understanding of PC structures.

In the future, this method can be used to provide rapid studies of proposed structures and prototyping prior to fabrication at smaller dimensions. The methodology can be employed concurrently with research on smaller-size devices. The ability to produce large-scale prototype devices rapidly will be an important tool as devices are prepared for commercial use. Insight, procedures, and techniques resulting from long-wavelength infrared device development can be scaled and applied to devices for shorter-wavelength applications.

Additionally, this research serves the infrared community with added characterization tools in the study of components operating at infrared wavelengths. The research will demonstrate the use of a discretely tunable CO_2-laser system as a source for characterization in infrared studies. The single-angle plane-wave characterization tool can be applied to other research efforts employing microscopy and focusing objectives.

The research described above is detailed in the following chapters. Chapter 2 presents the history of long-wavelength research and presents a framework for the application of infrared sources in the development of PC devices. Chapter 3 addresses the analysis and modeling tools that can be applied to the infrared methodology to model accurately theoretical performance. Chapter 4 discusses the fabrication of PC devices at the infrared wavelength scale. Chapter 5 presents a novel approach to compute the single-angle plane-wave transmittances or reflectances of fabricated devices from composite, multiple angle transmittance and reflectance measurements. Chapter 6 contains a discussion of the testing apparatus for the two characterization methods presented in this thesis. Chapters 7 and 8

present the results of measurements and calculations for each characterization tool as well as an analysis of the conditions required for the successful application of the methodology. Finally, Chapter 9 summarizes the research and provides ideas for the extension of the research into the future.

CHAPTER 2

LONG-WAVELENGTH INFRARED RESEARCH

This chapter presents a long-wavelength infrared methodology for the design and development of PCs. Past and present long-wavelength research contributions are discussed followed by the presentation of a method employing infrared tools and techniques for the development of PC devices.

2.1 Background

Photonic bandgap theory is derived from the macroscopic Maxwell equations. The equation typically used to design PC devices is

$$\nabla \times \left(\frac{1}{\epsilon(\mathbf{r})} \nabla \times \mathbf{H}(\mathbf{r}) \right) = \left(\frac{\omega}{c} \right)^2 \mathbf{H}(\mathbf{r}). \tag{2.1}$$

In this equation, $\mathbf{H}(\mathbf{r})$ represents an electromagnetic mode of frequency ω in a dielectric region $\epsilon(r)$ and c is the speed of light in a vacuum. There is no fundamental length scale associated with the constants in this equation. A solution for a specific wavelength can be scaled to another wavelength by a contraction or expansion of all distances. This scaling property of PCs allows research to be conducted over a wide range of wavelengths, with the results shared by users across the wavelength spectrum. This scaling feature can be exploited to develop a long-wavelength design and development methodology.

Some of the first PCs were fabricated with large-scale methods and tested at microwave frequencies. These included structures fabricated by the mechanical drilling of holes into substrate materials [47] and the manual arraying of alumina rods to form a spatial lattice [48]. Research at mid-infrared wavelengths has been conducted on PC samples fabricated by chemical etching to produce macroporous silicon [10, 49]. At the same time, other research groups have used state-of-the-art micro- and nano-technology fabrication techniques to produce devices that operate at telecommunications wavelengths. Important,

significant research contributions have resulted and continue to originate from the research conducted at all wavelength scales [50–52].

2.1.1 Research at Millimeter Wavelengths

At microwave frequencies, PC structures have periodicities on a millimeter-size scale. Fabrication of such structures often consists of the orderly mechanical arraying of dielectric materials into a lattice. Devices at this scale have been tested and significant contributions have been transferred to the PC research community [1, 47, 48, 50, 53–59].

Initial demonstrations of the photonic bandgap were conducted in the microwave region of the electromagnetic spectrum. In the early 1990s, pioneering research at low Gigahertz frequencies confirmed the existence of the band gap and helped establish analogies between a photonic and electronic band gap [47, 48, 53]. The concept of localized sites, where dielectric material was removed or inserted, was developed. These sites are currently termed *defect sites*. Work conducted at millimeter wavelengths demonstrated fabrication techniques and introduced PC geometries that would later be used when devices were scaled to smaller dimensions [54]. An example of the characterization apparatus used for devices fabricated at microwave frequencies is shown in Fig. 2.1 [1].

Research at microwave wavelengths is still an active field with new PC structures are being developed for microwave applications [1, 50]. Research efforts in 1999 demonstrated electrically controllable PCs structures at microwave wavelengths [57, 58]. Recently, negative refraction of microwaves in a metallic PC structure was reported [50].

Results from work at microwave frequencies are also being applied to other spectral regions via the scaling property of PCs. In 2002, Agilent Technologies reported research on the development of stub tuners in the Gigahertz frequency range. The group acknowledges that applications are more likely at optical communications wavelengths. This demonstrates that from the perspective of industry, scaled research is beneficial to the development of PC devices [55]. A more recent example of the application of microwave research results to other wavelength scales is the development of a PC-based directional coupler, with coupling lengths as small as 3.5 wavelengths [59].

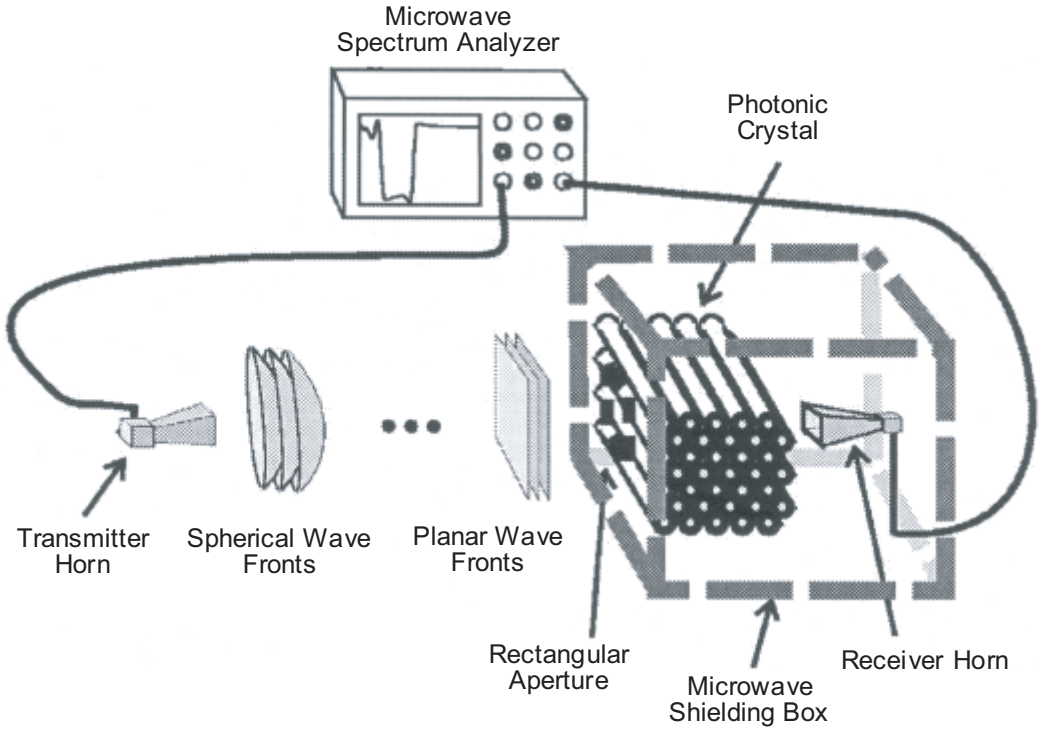

Figure 2.1: A typical testing apparatus for microwave PCs. Microwave-scale PC structures are often constructed by the mechanical assembly of elements into the crystal structure. With the long wavelengths and structure dimensions, the probe beam is not focused in the apparatus [1].

Research conducted at microwave frequencies continues to contribute to the PC knowledge base. The research is conducted both for microwave device applications and for the development of devices at shorter wavelengths through the scaling property of PCs. Though not all characteristics scale, both industry and academia have embraced long-wavelength PC research as a valuable approach for examining PC structures.

2.1.2 Research at Infrared Wavelengths

In parallel with the efforts in the microwave regime, research has also been performed at infrared wavelengths. At these wavelengths, microelectronics tools and techniques are available to fabricate structures with the desired periodicities. Although the devices are large-scale, the testing apparatus for these devices requires focusing of the infrared probe beam. Typically, this is accomplished with a reflecting microscope objective, as shown in Fig 2.2 [2].

Macroporous silicon has proven to be an excellent material to use in producing photonic bandgap structures in this wavelength range. Macroporous silicon is produced by patterning a silicon substrate using optical lithography and etching the substrate with an electrochemical, wet potassium-hydroxide (KOH) etch. Deep, high-aspect-ratio structures can be fabricated with this fabrication technique. Methods employed in testing the resulting infrared PCs include FTIR microscopy and optical parametric oscillator (OPO) microscopy [2, 10, 20, 49, 60–63]. This work has been pursued primarily by Birner *et al.* in a German-Canadian effort with a simultaneous effort from Rowson *et al.* at the University of Paris.

In both of these research programs one major objective of the research was to reduce the operating wavelength of demonstrated devices from mid-infrared to near-infrared wavelengths. Birner *et al.* perfected and developed the macroporous fabrication techniques and first demonstrated photonic band gaps at wavelengths of $\lambda = 10\ \mu m$ to $\lambda = 20\ \mu m$ [64]. With further efforts, the device period was reduced and band gaps were demonstrated at a wavelength of $\lambda = 4.9\ \mu m$. Additionally, the ability to engineer defects into the macroporous silicon was presented. Though most device characterization was completed using FTIR microscopy, OPO microscopy was also used for testing in cases where FTIR microscopy was

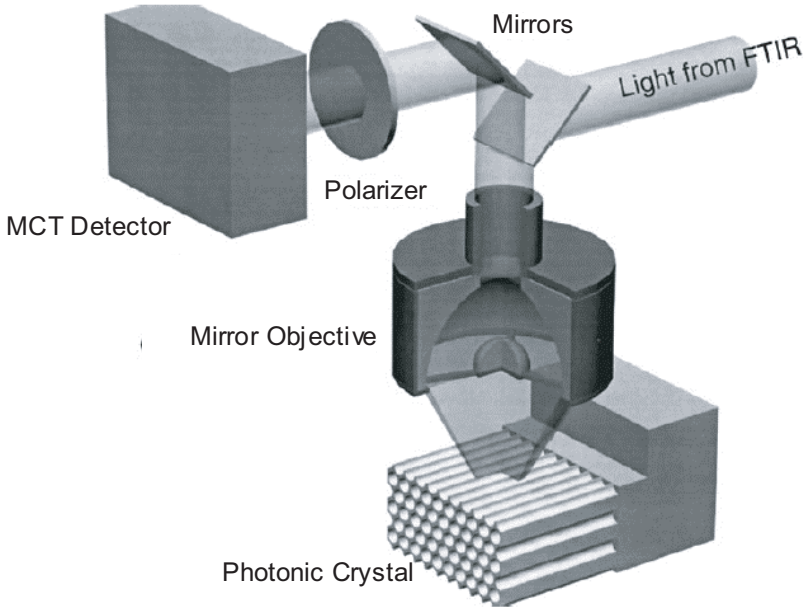

Figure 2.2: Light focused using a reflecting microscope objective. Here, an objective is shown focusing infrared light onto a PC test sample. The focused beam consists of light incident on the sample over a range of incident angles [2].

unable to resolve PC device performance due to limited incident optical power [10, 20]. This group also investigated the transmission of light through macroporous samples as a function of the number of device periods. Their analysis was conducted in parallel with efforts to reduce the device operating wavelength range to the $\lambda = 3\ \mu m$ to $\lambda = 5\ \mu m$ band. Ultimately, the collaboration was able to demonstrate a photonic bandgap at $\lambda = 1.3\ \mu m$ [62].

Rowson *et al.* employed macroporous silicon technology in a similar manner starting with demonstrated band gaps at a wavelength of $\lambda = 5.8\ \mu m$ [49]. The group then tested structures operating at these wavelengths to study the contributions of the various effects that degrade transmission through PC structures. The converging beam used to illuminate the samples was found to introduce band broadening of the photonic band gap, along with shifting the band gap to higher frequencies [60]. Diffraction losses were found to be heavily dependent on the crystal termination plane, with losses from the termination plane measuring as high as 60%. Finally, fabrication inhomogeneities were shown to have a large effect on the reflectivity of the PC structure [60, 61]. In further attempts to reduce the size of the devices, the group demonstrated a complete photonic band gap 200 nm wide centered at a wavelength of $\lambda = 1.55\ \mu m$ as well as a bandgap located at a wavelength of $\lambda = 1.1\ \mu m$ in the macroporous silicon lattice [2].

In addition to these studies with macroporous silicon, research at long infrared wavelengths has also been employed to investigate PCs fabricated in single-crystal silicon wafers. Xu *et al.* fabricated devices in single-crystal silicon material for operation at telecommunications wavelengths [65]. Fabrication capability was proven with sub-micron sized devices followed by the fabrication of scaled devices that could be tested at wavelengths in the $\lambda = 2\ \mu m$ to $\lambda = 3\ \mu m$ range. The long-wavelength spectral data were presented as evidence of the expected performance of the devices fabricated for shorter wavelength operation. Deviations from simulated performance were qualitatively attributed to the effects of a converging beam.

In each case, the measured spectra were compared to computed band diagrams that show the location of the band gaps in the frequency spectrum. Though agreement was demonstrated between the measurements and the computations, the comparison suffers as

band diagrams are computed for infinite-extent, perfect crystals while the measurements reflect finite-extent, imperfect samples.

Though these groups all demonstrated the value of scaled PC research, their work did not propose the use of long-wavelength techniques as a long-term tool in the study of PCs. In all cases, the long-wavelength research was viewed as an intermediate step towards the fabrication and testing of devices designed for operation at shorter wavelengths.

2.2 Advantages and Limitations of Scaled Photonic Crystal Research

There are several significant advantages to conducting PC research at a long-wavelength scale. Several limitations must also be addressed.

2.2.1 Long-Wavelength Infrared Research Advantages

The most significant advantage gained by conducting PC research at long wavelengths is the increased size of the structures that need to be fabricated. Figure 2.3 shows the effect of scaling a device from an operating wavelength of $\lambda = 1.5\ \mu m$ to $\lambda = 10.5\ \mu m$. As the operating wavelength is scaled by a constant multiplier (greater than unity), the period of the device and any features required are scaled to larger dimensions by the same multiplier. This fact significantly eases the issues associated with fabricating these devices.

For structures designed with a bandgap at telecommunications wavelengths, device features are typically in the hundreds of nanometers size range. State-of-the-art micro- and nano- fabrication tools and techniques are required to produce devices with these dimensions. Though the fabrication tools and techniques are often capable of producing the required PC structures, as a whole, they are still at an early stage of development; this introduces challenges in the repeatable production of devices and the obtaining of consistent results with fabricated structures. Additionally, relatively few research groups have the capability to produce devices at this scale. By using a long-wavelength approach and scaling devices so that band gaps are opened in the longer infrared wavelength region, the required fabrication techniques and tools move into the widespread and mature microelectronics domain. Devices can be produced using lithographic tools and techniques that have

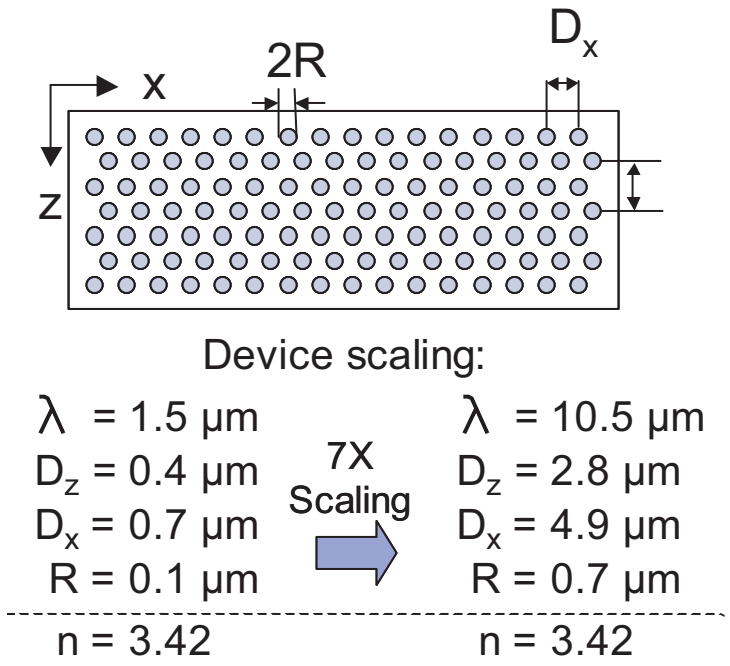

Figure 2.3: Structure dimensions for a 2-dimensional, triangular PC lattice with a band gap positioned at wavelengths of $\lambda = 1.5\ \mu m$ and $\lambda = 10.5\ \mu m$. By scaling the device by a factor of 7, fabrication moves from the nano-scale regime to the micro-scale regime.

been perfected and proven over time and are readily available in many locations.

Similarly, research conducted with devices that operate at long wavelengths also takes advantage of the highly developed systems available for device characterization. Network analyzer systems at microwave frequencies and FTIR spectrometer systems at long infrared wavelengths are readily accessible. Equipment suited to test nanometer-scale devices are less readily available or developed.

The advantages in the fabrication and characterization of long-wavelength PC devices combine to provide an opportunity to employ a rapid design-test-redesign cycle in PC research. A device can be fabricated and tested in a matter of days, allowing results from one design iteration to be used as input to the next iteration. This can lead to an improved understanding of PC structures to include the effects of design changes and fabrication variables on device performance.

2.2.2 Long-Wavelength Infrared Research Limitations

Despite the advantages of conducting research at longer wavelength scales, there are limitations that can only be overcome by conducting research at the actual application wavelength scale. Properties and physical effects related to material absorption, dispersion, and emission cannot be inferred from the design equation and expansion or contraction of device dimensions [46, 65]. Actual scale sized devices must be designed and tested with nanofabrication and nano characterization tools to gain more knowledge of these issues as well as to understand the integration of PC devices into current systems. The greatest synergy can be obtained by coordinated research at both wavelength scales. The rapid, iterative approach enabled through long-wavelength research can provide a volume of data concerning device manufacture and performance in different situations. Actual-scale device research offers insight into actual fabrication issues and material effects at wavelengths more likely to be used in functional devices.

2.3 A Long-Term, Long-Wavelength Infrared Methodology

In this thesis, a long-wavelength infrared method for the design, development and optimization of PC structures is presented. Rather than focusing on the characterization of final-size

PC structures designed to operate at telecommunications wavelengths, the methodology employs the advantages of large-scale fabrication and testing to develop devices at longer infrared wavelengths near $\lambda = 10\ \mu m$. Concepts, designs, and understanding gained at the longer wavelengths, will be scaled to structures that will operate at shorter wavelengths.

The primary role of the methodology is to provide a framework and tools where long-wavelength PC development is used as an integrated component of the larger-scope effort to develop the technology for applications. Investigations suitable to the long-wavelength approach can be completed more rapidly by leveraging the long-wavelength research advantages. Although long-wavelength infrared studies may need to be verified at the shorter wavelengths, the overall speed of PC development can be increased with the long-wavelength approach.

Figure 2.4 provides an overview of the methodology. If research objectives are compatible with a long-wavelength infrared approach, structures designed to operate at wavelengths in the $\lambda = 5\ \mu m$ to $\lambda = 15\ \mu m$ range are fabricated using microelectronics techniques. This wavelength range was selected because materials and fabrication processes for devices that operate at these wavelengths are similar to the materials and processes used in final-sized PC devices. The materials and processes used at microwave and other wavelength ranges can be significantly different. Compatible processing techniques at both wavelength scales will assist in the transition from the one scale to the other.

From this point in this thesis, references to long-wavelength or large-scale devices refers to research conducted at wavelengths between $\lambda = 5\ \mu m$ and $\lambda = 15\ \mu m$. Similarly, references to short-wavelength or small-scale devices refers to research conducted at wavelengths near $\lambda = 1.5\ \mu m$.

The fabricated devices are characterized using a discretely tunable carbon-dioxide (CO_2) laser system over the $\lambda = 9\ \mu m$ to $\lambda = 11\ \mu m$ wavelength range or an FTIR spectrometer system operating with a globar source and an mercury-cadmium-telluride (MCT) detector over the full $\lambda = 5\ \mu m$ to $\lambda = 15\ \mu m$ range. The CO_2-laser system provides a high power characterization and measurement tool over the limited $\lambda = 9\ \mu m$ to $\lambda = 11\ \mu m$ band. The high power available in this system enables direct spectral transmittance measurements of

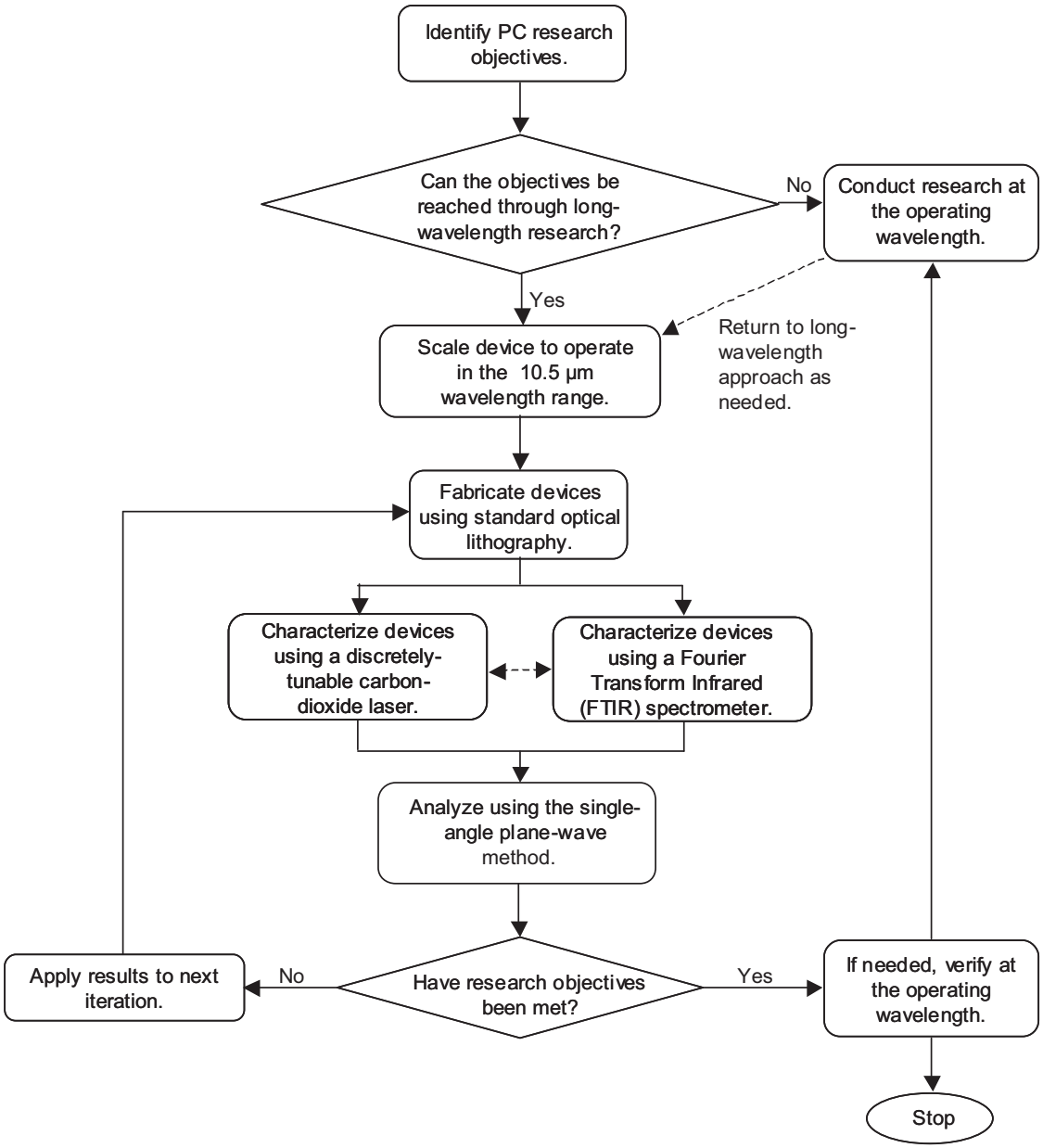

Figure 2.4: A flowchart detailing the steps used in the long-wavelength methodology.

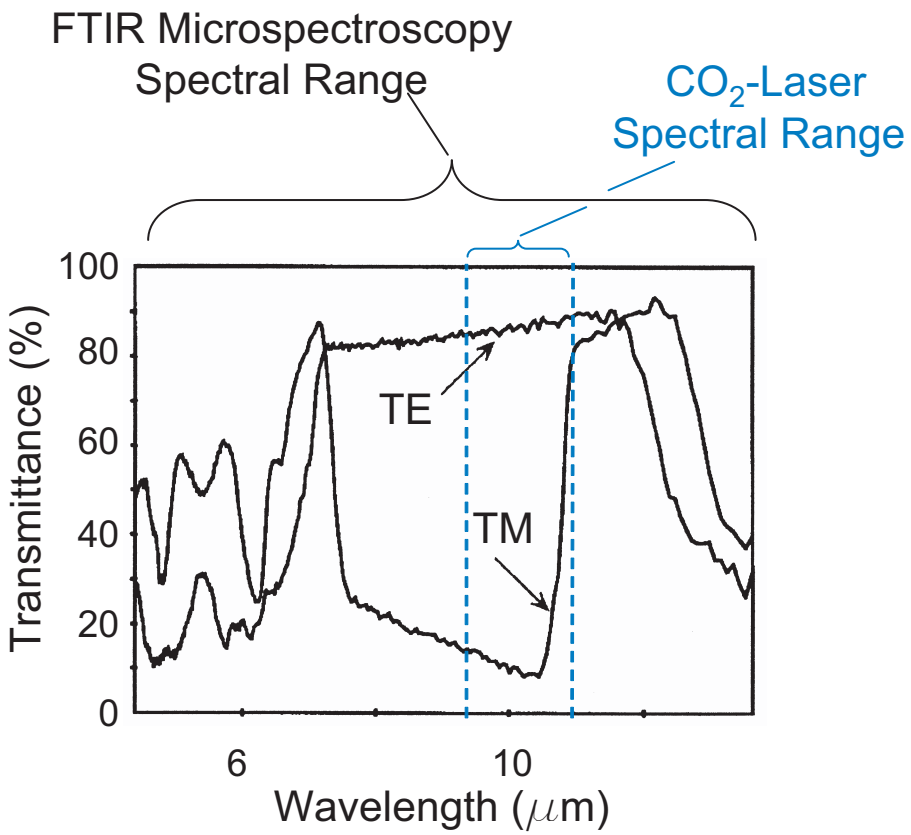

Figure 2.5: A comparison of the spectral ranges of the FTIR microspectroscopy and CO_2-laser systems. The FTIR system provides a rapid, repeated scanning capability producing a complete spectra in one measurement. The CO_2-laser system provides sufficient power to perform a detailed analysis on different design geometries and their effects over a limited tuning range. With the CO_2-laser system, each wavelength and angle must be measured separately.

devices. Existing infrared characterization systems often suffer from low incident power making the detection of subtle transmittance variations difficult. The FTIR spectrometer system provides a method for the rapid characterization of devices using a turn-key system. Figure 2.5 shows how the two characterization systems can be used together to study the spectral characteristics of a PC sample.

For both characterization systems, the beam emerging from a test structure contains information on the transmittance or reflectance of the device to a composite, many-angle incident beam. By analyzing the incident beam, an opportunity exists to derive the individual plane-wave transmittances or reflectances of the test device. This detailed characterization data can be used in the optimization of devices through design iterations. At some point,

when desired performance characteristics are met, the long-wavelength results may be scaled to the appropriate application wavelength.

As depicted in the methodology flowchart by the dashed arrow from the short-wavelength domain to the long-wavelength infrared method, frequent transitions between short- and long-wavelength scales may be needed. As device challenges surface at shorter wavelengths, it may be beneficial to return to the large-scale devices. After solving the issue at the large scale, the solution can then be scaled to the smaller scale for verification.

The secondary role of the long-wavelength methodology is to increase participation in PC research thus increasing the volume of experimental measurements on fabricated devices. Currently, theoretical studies on PCs dominate the literature with predicted performance benchmarks exceeding experimentally demonstrated performance. By applying the tools developed in this thesis, additional research groups will be able to participate in PC research and produce experimental data on the performance of fabricated devices.

Finally, the methodology can be applied to the integration challenges associated with PC devices. Complete PC systems consisting of multiple, cascaded PC devices can be constructed at the large-scale and tested prior to reduction to small-scale wavelengths. This can reduce risk factors associated with device manufacture and integration and potentially encourage development of commercial PC-based devices.

Investigations that employ this methodology must focus on PC topics that can scale between the long and short wavelength scales. Some of the potential topics that may be investigated include device development studies and experiments in fabrication tolerances. More precise control of fabrication processes and the detailed characterization of devices will enable researchers to identify the thresholds for large-scale manufacturing of devices. This method, employed in parallel with research on small-scale devices, can assist in the development of PC technology for commercial applications.

2.4 Summary

In this chapter, a long-term, long-wavelength methodology for the design and development of PC structures was presented. First, past and present scaled-research contributions from

a variety of research groups were reviewed to demonstrate the value of scaled research. The progression of the research within each group showed that efforts are typically focused on reducing the operating wavelength of demonstrated devices. Typical characterization schemes were described and shortcomings identified. The methodology, capitalizing on the advantages of scaled PC research, employs a CO_2 laser and an FTIR microspectroscopy system along with a detailed analysis of incident light to determine the single-angle plane-wave transmittances or reflectances of a device. Application of the methodology was discussed. Detailed analysis of the characterization apparatus and computations is presented in later chapters.

CHAPTER 3

ANALYSIS OF PHOTONIC CRYSTAL STRUCTURES

This chapter begins with a presentation of basic crystal structure and geometry as it applies to PC devices and dielectric regions. The PC design equation is derived from Maxwell's equations and solved for various dielectric profiles. Band diagrams showing the location of photonic band gaps for infinite-extent PCs are discussed and analyzed. Simulation tools appropriate for the long-wavelength PC design methodology are discussed and results from the simulations are compared to the band diagrams. In this thesis, band diagram analysis provides a qualitative evaluation of fabricated structure performance while the simulation methods provide a quantitative, theoretical basis for the evaluation of fabricated structures.

3.1 Photonic Crystal Design

To understand the solutions to the design equation for PCs, a review of PC geometry and crystal structure is required. This background follows the presentation of material as presented in [46] and [66].

3.1.1 Crystal Structures and Geometry

A lattice is a set of discrete points that repeats periodically in 1-, 2-, or 3-dimensions. In a crystalline material, it is easy to visualize molecules as the lattice points in the crystal. The distance and direction from one molecule to one of its neighboring molecules within this lattice specifies a primitive lattice vector $\mathbf{a_1}, \ldots, \mathbf{a_i}$ for this crystal where i is dependent upon the dimension of the system ($i = 1, 2$, or 3). A basis set of primitive lattice vectors consists of i primitive lattice vectors that allows all lattice vectors $\mathbf{R}$ to be represented as combinations of the primitive lattice vectors. That is, $\mathbf{R} = m\mathbf{a_1} + n\mathbf{a_2} + p\mathbf{a_3}$ in 3 dimensions where m, n and p are integers. A basis set of primitive lattice vectors spans a primitive unit cell of the lattice.

In a PC, equivalent quantities and vectors exist. The lattice describes the periodic

permittivity profile $\epsilon(\mathbf{r})$ of the PC where $\mathbf{r}$ is the position vector. Primitive lattice vectors $\mathbf{a_1}, \ldots \mathbf{a_i}$ exist that map the permittivity profile onto itself such that $\epsilon(\mathbf{r}) = \epsilon(\mathbf{r} + \mathbf{R})$. The primitive unit cell is once again defined by a basis set of primitive lattice vectors and contains one complete copy of the permittivity profile.

To analyze this periodic structure, Fourier techniques are employed. The periodic permittivity function of the material can be represented by a Fourier expansion as a sum of harmonic components with various reciprocal lattice vectors $\mathbf{q}$,

$$\epsilon(\mathbf{r}) = \int g(\mathbf{q}) e^{j\mathbf{q}\cdot\mathbf{r}} \, d\mathbf{q}, \tag{3.1}$$

where $g(\mathbf{q})$ is the Fourier coefficient for reciprocal lattice vector $\mathbf{q}$. Likewise, the permittivity function translated by a lattice vector $\epsilon(\mathbf{r} + \mathbf{R})$ can be represented by

$$\epsilon(\mathbf{r} + \mathbf{R}) = \int g(\mathbf{q}) e^{j\mathbf{q}\cdot\mathbf{r}} e^{j\mathbf{q}\cdot\mathbf{R}} \, d\mathbf{q}. \tag{3.2}$$

Since the dielectric function is periodic, $\epsilon(\mathbf{r}) = \epsilon(\mathbf{r} + \mathbf{R})$, setting Eq. 3.1 and Eq. 3.2 equal yields

$$g(\mathbf{q}) = g(\mathbf{q}) e^{j\mathbf{q}\cdot\mathbf{R}}. \tag{3.3}$$

For Eq. (3.3) to be correct, either $g(\mathbf{q}) = 0$ or $e^{j\mathbf{q}\cdot\mathbf{R}} = 1$. This means that the transform of the permittivity function is zero except for reciprocal lattice vectors $\mathbf{q}$ where $e^{j\mathbf{q}\cdot\mathbf{R}} = 1$.

Therefore, to analyze the PC lattice with a periodic dielectric function $\epsilon(\mathbf{r})$ in Fourier space, only the harmonics with reciprocal lattice vectors $\mathbf{q}$ for all lattice vectors $\mathbf{R}$ need to be considered. Similar to the real lattice, primitive reciprocal lattice vectors exist so that all reciprocal lattice vectors can be represented by combinations of the primitive reciprocal lattice vectors. That is, $\mathbf{q} = h\mathbf{b_1} + k\mathbf{b_2} + l\mathbf{b_3}$ in 3 dimensions where h, k and l are integers and $\mathbf{b_1}$,$\mathbf{b_2}$, and $\mathbf{b_3}$ are the primitive reciprocal lattice vectors. The reciprocal lattice vectors span reciprocal space and can be thought of as the Fourier transform of the real lattice. Since the lattice vectors have dimensions of length, the reciprocal lattice vectors have dimensions of inverse length. Optical waves in a PC structure will be described by their optical wavevectors. These optical wavevectors, in turn, will be represented in terms of the reciprocal lattice vectors.

In the reciprocal lattice, a region called the first Brillouin zone is defined as a unit cell in which all points in space are closer to a single reciprocal lattice point than any other reciprocal lattice point. All wavevectors outside the first Brillouin zone can be defined as a wavevector within the first Brillouin zone plus a reciprocal lattice vector. By translational symmetry and Bloch's theorem [67], solutions for these wavevectors outside of the first Brillouin zone are identical to the solution for the wavevectors in the first Brillouin zone. This limits the set of wavevectors that must be considered when determining the response of the PC lattice to only the wavevectors in the first Brillouin zone.

3.1.2 Eigenvalue Problem for Photonic Band Calculations

Electromagnetic modes of photonic structures are solutions to Maxwell's equations. A photonic band gap is formed when there is a range of frequencies over which there are no real values of the wavevector that satisfy Maxwell's equations in the media. These equations can be formulated into an eigenvalue problem where frequencies are viewed as functions of wavevectors. Once frequencies are computed for all available wavevectors, band gaps can be identified and exploited.

The Maxwell curl equations are

$$\nabla \times \tilde{\mathbf{E}}(r,t) = -\frac{\partial \tilde{\mathbf{B}}}{\partial t}, \tag{3.4}$$

$$\nabla \times \tilde{\mathbf{H}}(r,t) = \frac{\partial \tilde{\mathbf{D}}}{\partial t}. \tag{3.5}$$

where $\tilde{\mathbf{E}}$, $\tilde{\mathbf{B}}$, $\tilde{\mathbf{H}}$, and $\tilde{\mathbf{D}}$ are the time-dependent values of the electric field intensity, magnetic flux density, magnetic field intensity and electric displacement fields respectively. For a lossless, nonmagnetic, linear, and isotropic media

$$\tilde{\mathbf{D}} = \epsilon_\circ \epsilon(r) \tilde{\mathbf{E}}, \tag{3.6}$$

$$\tilde{\mathbf{B}} = \mu_\circ \tilde{\mathbf{H}}. \tag{3.7}$$

where $\epsilon(r)$ is the dielectric function of the material, $\epsilon_\circ$ is the permittivity of free space and $\mu_\circ$ is the permeability of free space. These can be substituted into the curl equations to produce a set of equations relating only $\tilde{\mathbf{E}}$ and $\tilde{\mathbf{H}}$.

$$\nabla \times \tilde{\mathbf{E}}(r,t) = -\frac{\mu_\circ \partial \tilde{\mathbf{H}}}{\partial t} \tag{3.8}$$

$$\nabla \times \tilde{\mathbf{H}}(r,t) = \frac{\epsilon_\circ \epsilon(r) \partial \tilde{\mathbf{E}}}{\partial t} \tag{3.9}$$

Time dependence can be separated from the equations by expanding the fields into harmonic modes, with the form of the harmonic modes being

$$\tilde{\mathbf{E}}(\mathbf{r},\mathbf{t}) = Re[\mathbf{E}(\mathbf{r})e^{-j\omega t}], \tag{3.10}$$

$$\tilde{\mathbf{H}}(\mathbf{r},\mathbf{t}) = Re[\mathbf{H}(\mathbf{r})e^{-j\omega t}] \tag{3.11}$$

where $\mathbf{E}$ and $\mathbf{H}$ are the electric and magnetic complex field intensities and ω is the frequency. Substituting these into the modified curl equations (Eqs. 3.8 and 3.9) and simplifying leaves

$$\nabla \times \mathbf{E}(r) = \mu_\circ j\omega \mathbf{H}(\mathbf{r}), \tag{3.12}$$

$$\nabla \times \mathbf{H}(r) = -\epsilon_\circ \epsilon(r) j\omega \mathbf{E}(\mathbf{r}). \tag{3.13}$$

The $\mathbf{E}$ and $\mathbf{H}$ fields can be decoupled by dividing Eq. (3.13) by $\epsilon(r)$ and taking the curl of both sides. The result can be substituted into Eq. (3.12) to eliminate $\mathbf{E}$. Using

$$c = \frac{1}{\sqrt{\mu_\circ \epsilon_\circ}} \tag{3.14}$$

yields the vector Helmholz equation

$$\nabla \times \left(\frac{1}{\epsilon(\mathbf{r})} \nabla \times \mathbf{H}(\mathbf{r}) \right) = \left(\frac{\omega}{c} \right)^2 \mathbf{H}(\mathbf{r}). \tag{3.15}$$

This equation can be viewed as an eigenvalue problem where an operation performed on an eigenvector is equal to the same eigenvector multiplied by a constant. In this case, the operator takes the curl, divides by $\epsilon(\mathbf{r})$ and takes the curl again. The eigenvector is $\mathbf{H}(\mathbf{r})$ and the eigenvalue is $(\frac{\omega}{c})^2$. Electromagnetic modes $\mathbf{H}(\mathbf{r})$ and the frequencies ω that satisfy this relation are the only allowed modes in the PC.

3.1.3 Device Scaling

The long-wavelength PC development methodology is based on the ability to conduct research at one region of the wavelength spectrum and transfer results to other wavelength regions by scaling structure dimensions. This scaling property of PCs can be understood by a closer inspection of the Helmholz equation, Eq. (3.15).

If the index distribution in Eq. (3.15) is replaced with a new index distribution represented by

$$\epsilon_2(r) = \epsilon(r/\sigma), \tag{3.16}$$

$\epsilon_2(r)$ has the same shape as the original distribution but is scaled in r by a factor of $1/\sigma$. With a change of variable substitution, where the position variable is rescaled, the original equation can be recovered by scaling the frequency such that $\omega_2 = \omega/\sigma$. Consequently, scaling the index function in r does not introduce any new solutions to the eigenvalue problem. Solutions are scaled in r by the same amount that the permittivity is scaled.

3.1.4 Photonic Crystal Design

To analyze and design PC structures, the profile for a dielectric region must be defined and Eq. (3.15) must be solved for all supported modes of $\mathbf{H}(\mathbf{r})$. When a dielectric profile possesses a photonic band gap for a given frequency range, real wavevector solutions to this equation do not exist. The computed solutions are typically displayed graphically using band or dispersion diagrams. In these diagrams, values of the wavevector are plotted as the independent variable on the x-axis and corresponding frequency solutions are plotted on the y-axis. The frequency is expressed in terms of the normalized period and the scaling property ensures that this solution can be applied to all scaled dielectric profiles.

In this thesis, band diagrams are generated using the commercial software package BandSOLVE [66]. In the BandSOLVE program, the user defines the index distribution for one period of the structure and the supported field modes are computed for an infinite structure using the plane wave expansion method.

The index distribution for a 1-dimensional PC lattice is specified by the period a and the fill factor F. The fill factor F is defined as the ratio of the length of the dielectric-filled region to the device period. Band diagrams for 1-dimensional PC structures consisting of alternating layers of silicon and air with fill factors $F = 0.5$ and $F = 0.4$ are shown in Figs. 3.1 and 3.2 respectively. The diagrams show the band gap position plotted on a normalized frequency scale based on the device period a. As the fill factor varies, photonic band gap widths and the frequency of the gap edges vary. For structures used in this thesis,

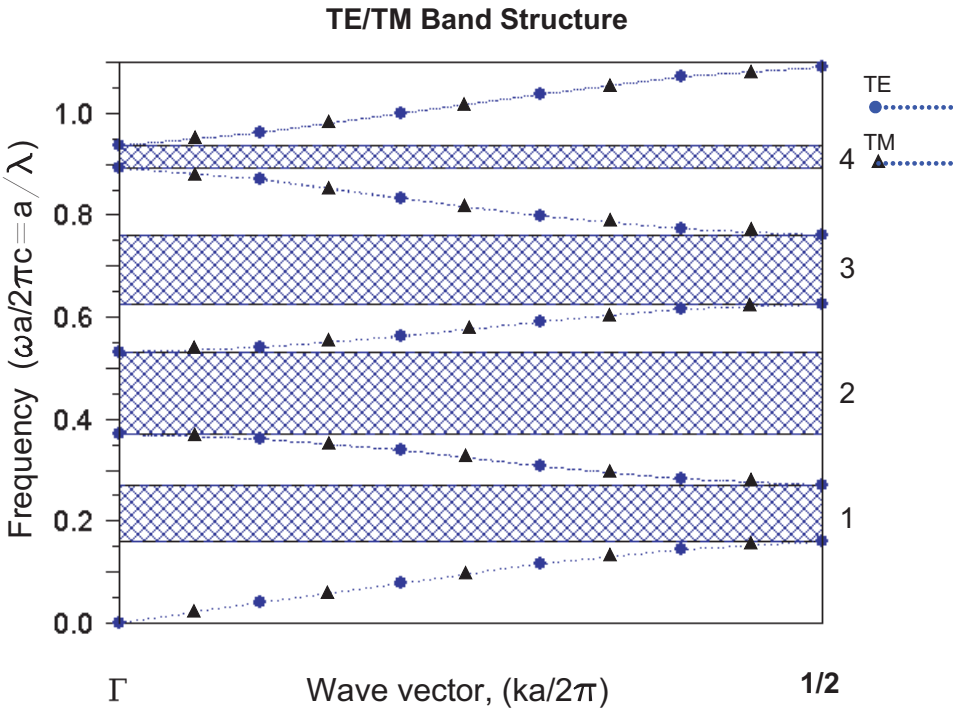

Figure 3.1: A band diagram shows the first four photonic band gaps for a 1-dimensional PC structure consisting of alternating regions of silicon and air. The dielectric fill factor is $F = 0.5$. By selecting a device period $a = 3.9\ \mu m$, the second band edge can be positioned at a wavelength within the tuning range of the CO_2-laser system.

the period must be selected so the photonic band gaps are placed within the wavelength ranges of the characterization tools; this is particularly important for the CO_2-laser system as its tuning range is limited to wavelengths between $\lambda = 9.2\ \mu m$ and $\lambda = 10.8\ \mu m$. In the 1-dimensional case, note that the photonic band gaps are identical for both transverse electric (TE) and transverse magnetic (TM) polarized light for normal incidence.

Figure 3.1 is the photonic band diagram for a structure with a fill factor $F = 0.5$. The band gaps for this dielectric structure are relatively wide and a value for the period cannot be selected so that an entire photonic band gap is within the tuning range of the CO_2 laser. However, by selecting a period of $a = 3.9\ \mu m$, the second photonic band gap edges are positioned at wavelengths of $\lambda = 7.35\ \mu m$ and $\lambda = 10.54\ \mu m$. The band edge at a wavelength of $\lambda = 10.54\ \mu m$ is within the tuning range of the CO_2 laser.

The band diagram shown in Fig. 3.2 corresponds to a structure with a fill factor $F = 0.4$. This structure possesses a narrow third photonic band gap. By selecting a device period of

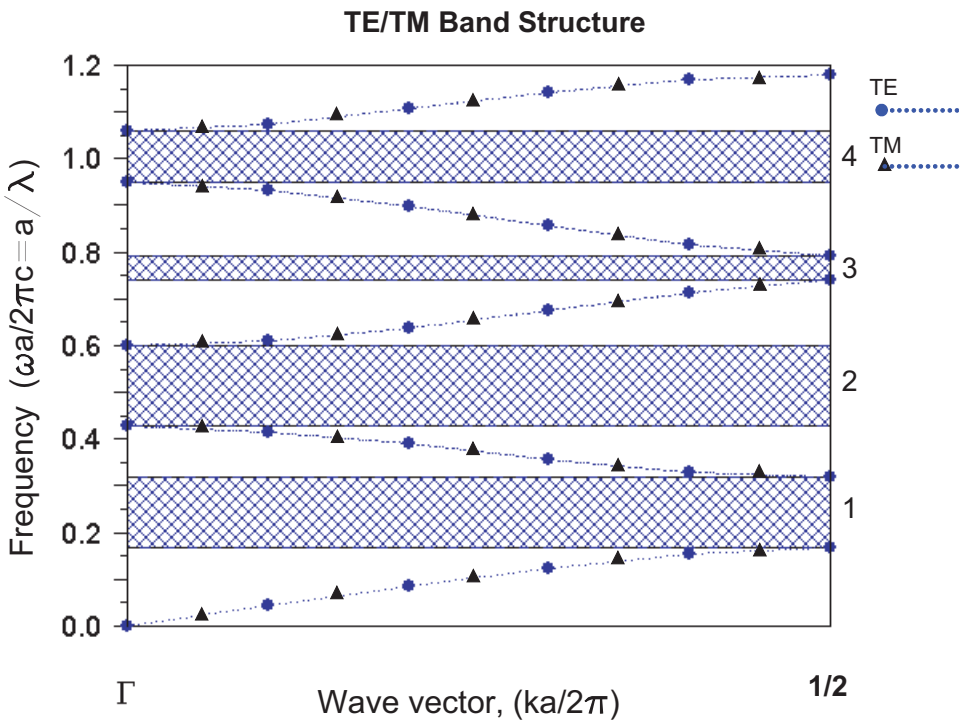

Figure 3.2: A band diagram shows the first four photonic band gaps for a 1-dimensional PC structure consisting of alternating regions of silicon and air. The dielectric fill factor is $F = 0.4$. By selecting a device period $a = 7.8\ \mu m$, the entire third band gap can be positioned at a wavelength within the tuning range of the CO_2-laser system.

$a = 7.8\ \mu m$, the band edges are positioned at wavelengths $\lambda = 9.87\ \mu m$ and $\lambda = 10.54\ \mu m$, both of which are within the tuning range of the CO_2 laser.

A similar analysis can be used for 2- and 3-dimensional structures. The band diagrams are similar, though significant differences may exist for TE and TM polarized light. Figure 3.3 shows the TE and TM band diagrams for a 2-dimensional triangular PC lattice of air holes etched into a silicon substrate. The hole radius for the lattice is $r = 0.4215a$. The differences in the band structure between polarization states are evident. Once again, photonic band gaps can be positioned by selecting an appropriate structure period for the characterization apparatus or application.

In this research, band diagrams for 1-dimensional structures are used to provide a qualitative measure of device performance. Since the computations produce band information for perfect, infinite structures, measurements resulting from imperfect, finite test structures

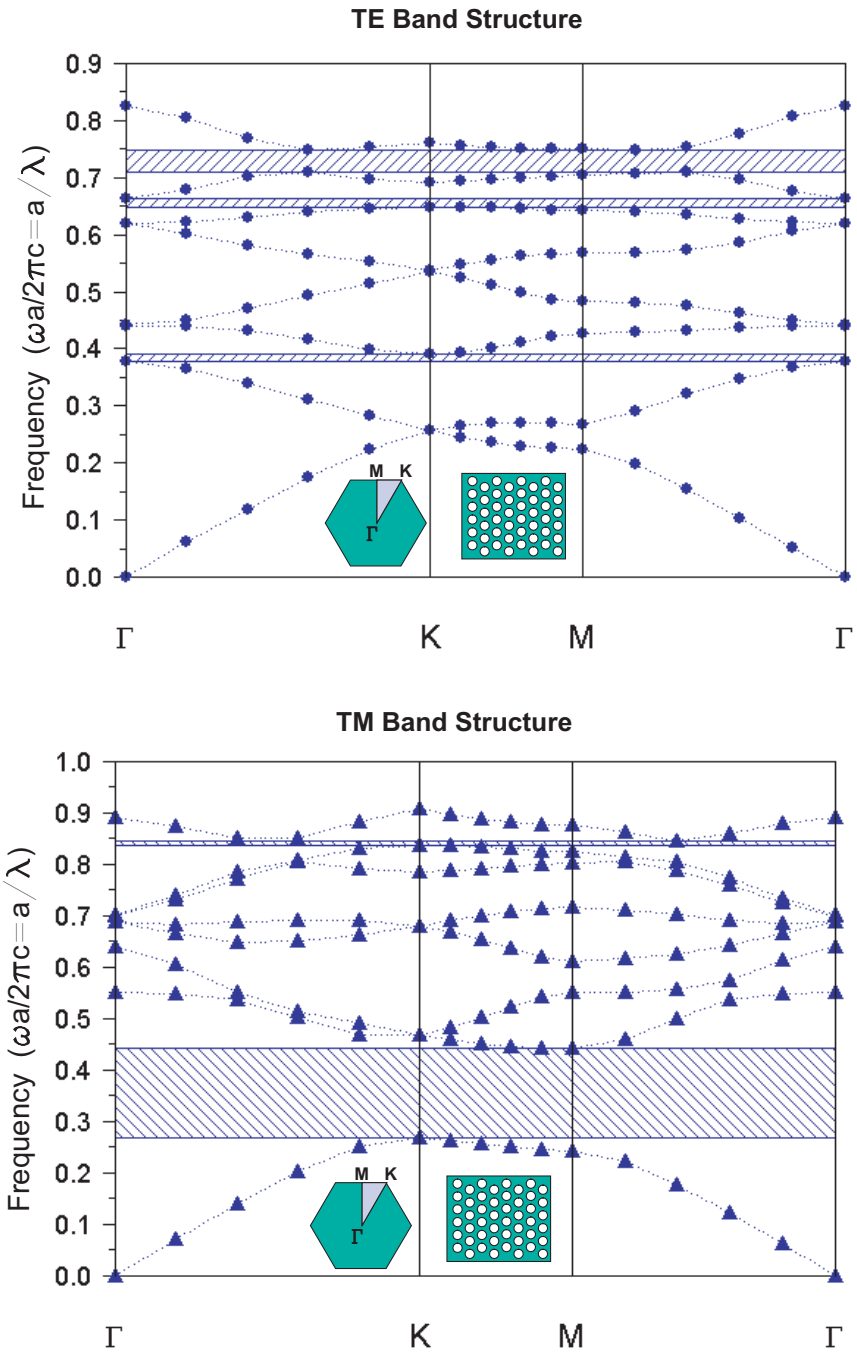

Figure 3.3: The band diagram for TE and TM polarized light for a 2-dimensional, triangular PC lattice with the ratio of the radius to the period $r/a = 0.4215$. In both band diagrams, the left inset shows the complete Brillouin zone along with the k-space symmetry points for this crystal geometry. The right inset shows the triangular crystal lattice of air holes in the silicon substrate.

will not exhibit the complete band gaps shown in the band diagrams. Additional modeling and simulation tools must be developed to provide a basis for quantitative theoretical calculations.

3.2 Structure Modeling and Simulation

Simulation and modeling tools are necessary to facilitate the design of PC structures and to provide a theoretical performance basis to compare with the measured performance of fabricated devices. Many modeling methods and algorithms are available and appropriate to use in the modeling of PC structures [68–70]. In this thesis, two of the suitable methods are discussed. The first method, finite-difference time-domain (FDTD) modeling is applicable for PC structures of all dimensions. Applying the long-wavelength PC design methodology to 2- and 3- dimensional structures will require the use of FDTD or similar modeling methods. The second method discussed, the transfer matrix method, is ideal for the analysis of 1-dimensional PC structures. The transfer matrix method is used almost exclusively in this thesis.

3.2.1 Finite-Difference Time-Domain Modeling

The FDTD algorithm solves for the electric and magnetic fields propagating in a structure as functions of time. In a region of space void of currents or isolated charges, Maxwell's curl equations can be written in Cartesian coordinates as six scalar equations.

$$\frac{\partial H_x}{\partial t} = -\frac{1}{\mu}\left(\frac{\partial E_y}{\partial z} - \frac{\partial E_z}{\partial y}\right) \tag{3.17}$$

$$\frac{\partial E_y}{\partial t} = -\frac{1}{\epsilon}\left(\frac{\partial H_x}{\partial z} - \frac{\partial H_z}{\partial x}\right) \tag{3.18}$$

$$\frac{\partial H_y}{\partial t} = -\frac{1}{\mu}\left(\frac{\partial E_z}{\partial x} - \frac{\partial E_x}{\partial z}\right) \tag{3.19}$$

$$\frac{\partial E_z}{\partial t} = -\frac{1}{\epsilon}\left(\frac{\partial H_y}{\partial x} - \frac{\partial H_x}{\partial y}\right) \tag{3.20}$$

$$\frac{\partial H_z}{\partial t} = -\frac{1}{\mu}\left(\frac{\partial E_x}{\partial y} - \frac{\partial E_y}{\partial x}\right) \tag{3.21}$$

$$\frac{\partial E_x}{\partial t} = -\frac{1}{\epsilon}\left(\frac{\partial H_z}{\partial y} - \frac{\partial H_y}{\partial z}\right) \tag{3.22}$$

The FDTD method solves these equation by discretizing the equations in time and space and numerically solving for the fields. The permittivity distribution and initial electromagnetic field excitation must be defined for the model. The computational space is divided into increments, typically using a Yee's mesh [71], and the E and H field components are computed at points on a grid, with grid points separated by δx, δy, and δz. Time is divided into intervals of δt and the fields are typically computed in time intervals of $\delta t/2$ [72].

The advantage of this modeling tool is its applicability to all permittivity profiles in all dimensions. The major limitations are the complexity of the calculation and the associated computing power required to solve for all fields in the computational space over all time.

3.2.2 Transfer Matrix Method Modeling

The transfer matrix method is well suited to model the theoretical performance of 1-dimensional PC devices. In this method, the 1-dimensional structure is treated as a multilayer dielectric stack where each layer is represented by a transfer matrix. The transfer matrix relates the fields in adjacent layers by applying the electromagnetic boundary conditions at the interface. For cascaded multiple-layer systems, the transfer matrices of all layers are multiplied to calculate the overall system reflected and transmitted field amplitudes. Each computation corresponds to a single plane wave incident on the multilayer stack for a particular wavelength and incident angle. Transmitted and reflected power can be computed from the field amplitudes and physical constants of the input and transmitted regions. The details of the transfer matrix method are presented in Ref. [73].

For this thesis, transfer matrix computations were coded using MATLAB [74] software. The transmitted and reflected power through a multilayer stack are computed for a range of incident angles and a range of wavelengths at specified angle and wavelength increments. Two versions of the code were written to model the 1-dimensional PC structures.

The first version, termed MIP-SI, computes the reflected and transmitted power for a 1-dimensional PC fabricated by etching air layers into a silicon substrate. The incident and transmitted regions are air. The Sellmeier formula [75] is used compute the index of silicon at each wavelength. Since the structure consists of alternating, constant-width layers of

silicon and air, only two transfer matrices are formed in the computation.

A more generic version of the code, termed MIP-GEN, computes the transmitted and reflected power through any user-defined multilayer structure. The layer thickness and index must be specified for each layer and the index of the incident and transmitted regions must be defined. The transfer matrix for each layer is formed and the matrices are multiplied to compute field amplitudes followed by the computation of the transmitted and reflected power. Since each layer is represented by an individual matrix, variations in period and fill factor can be modeled with the MIP-GEN code.

The significance of small deviations from the specified fill factor and period is illustrated by comparing the simulation results from an ideal 1-dimensional PC structure simulated using MIP-SI and the results from a simulation of a non-ideal structure simulated using MIP-GEN. Figure 3.4 shows the calculated normalized transmittance of a 20-period structure consisting of alternating 2 μm layers of silicon and air over the $\lambda = 10$ μm to $\lambda = 14$ μm wavelength range. The structure for the non-ideal case contains a random, uniformly distributed 5% deviation in fill factor and a random, uniformly distributed 1% deviation in period. In the ideal case, the photonic band gap, extending from the start of the x-axis to approximately 10.8 μm, ends at a shorter wavelength and more abruptly than in the non-ideal case. In the transmission band from approximately $\lambda = 11$ μm through $\lambda = 14$ μm, oscillations are apparent in both the ideal and non-ideal cases but higher overall transmittance is present in the ideal structure.

To model composite beams consisting of superimposed combinations of plane waves over a range of incident angles, data from MIP-SI and MIP-GEN simulations are processed by another program, designated MIP-COMP. This code superimposes the weighted computations from the individual plane waves in accordance with the desired weighting scheme. The theoretical composite transmittance or reflectance of a device can be directly compared with the composite measured data.

The effect of the composite beam is illustrated by comparing the normalized transmittance of a single, normally-incident plane wave with the normalized transmittance of a

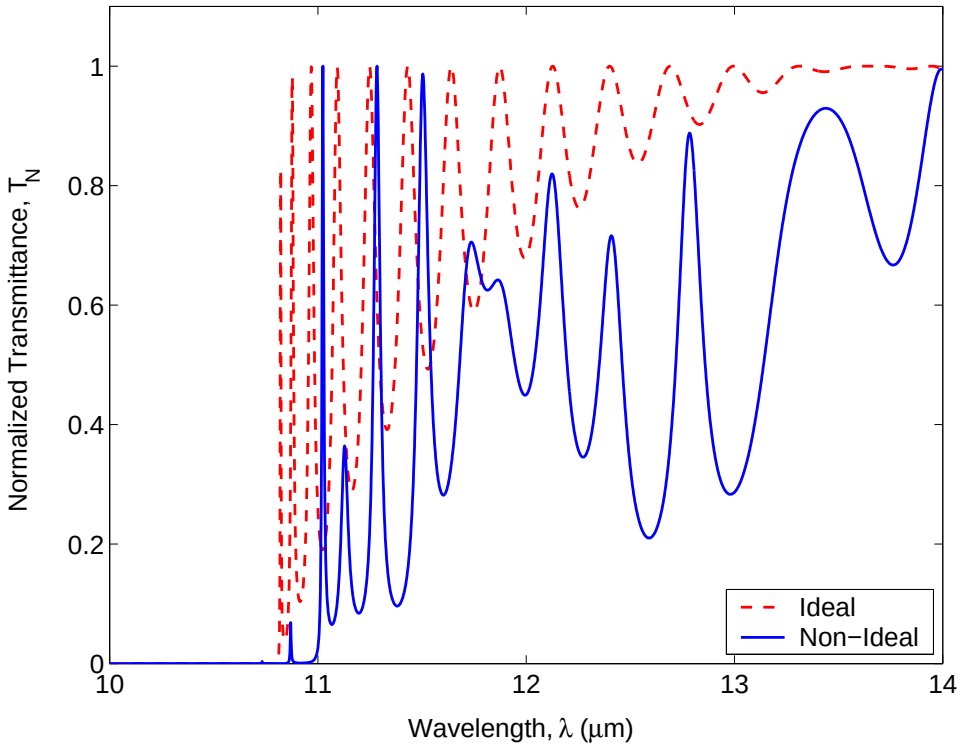

Figure 3.4: Ideal and non-ideal structure normalized transmittance. The significance of fabrication variations in PC structures is shown as the normalized transmittance of an ideal structure is compared to the normalized transmittance of a non-ideal structure with a random, uniformly distributed 5% fill factor variation and random, uniformly distributed 1% period variation. The simulated structure is a 20-period, 1-dimensional PC with alternating 2 μm regions of air and silicon.

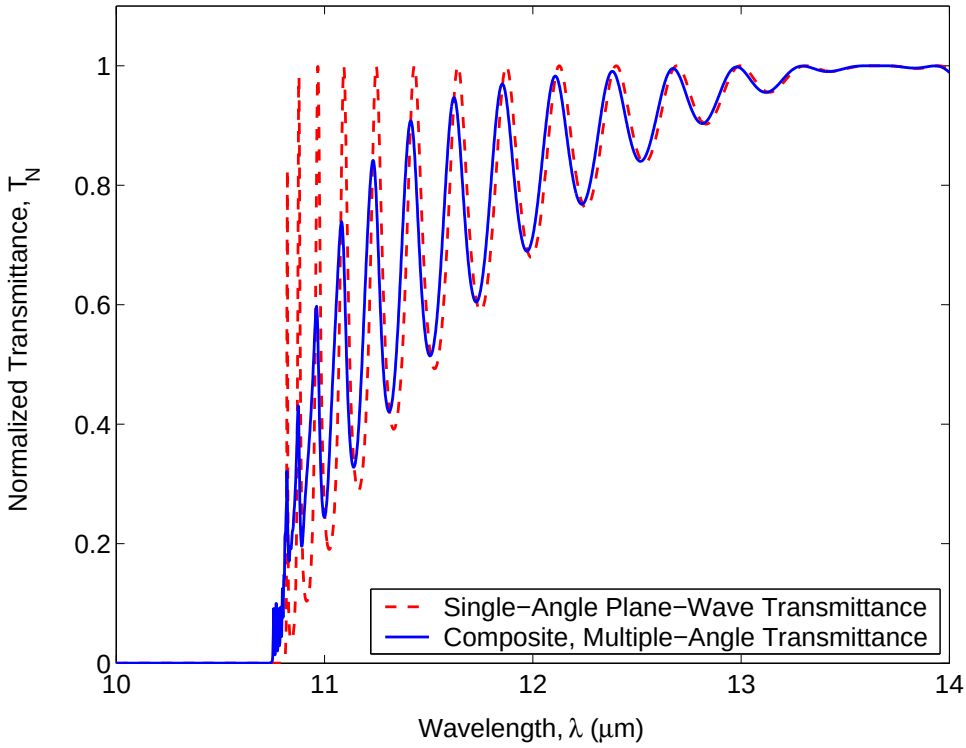

Figure 3.5: Calculated single-angle and multiple-angle plane-wave normalized transmittances, T_N. The normalized transmittance of a 1-dimensional PC structure is shown for a single-angle normally-incident plane wave and for a composite, multiple-angle incident beam. The composite beam consists of superimposed plane waves over the $-10°$ to $+10°$ range at $1°$ increments. The simulated structure is a 20-period, 1-dimensional PC with alternating 2 μm regions of air and silicon.

composite beam consisting of multiple plane waves with a range of incident angles. Figure 3.5 shows the calculated transmittance of a 20-period structure consisting of alternating 2 μm layers of silicon and air over the $\lambda = 10$ μm to $\lambda = 14$ μm wavelength range. The normalized transmittance, T_N for an ideal, normally incident plane wave is compared to the normalized transmittance of the same structure for a composite, multiple-incident-angle beam consisting of 21 plane waves with incident angles ranging from -10° to +10° at 1° increments. All plane waves are weighted equally and the sum of the combined response is normalized. The composite incident normalized transmittance shows a small shift in the transmission band to shorter wavelengths and a broadening of the photonic band gap consistent with the results reported by Rowson *et al.* and Xu *et al.* [2, 60, 65].

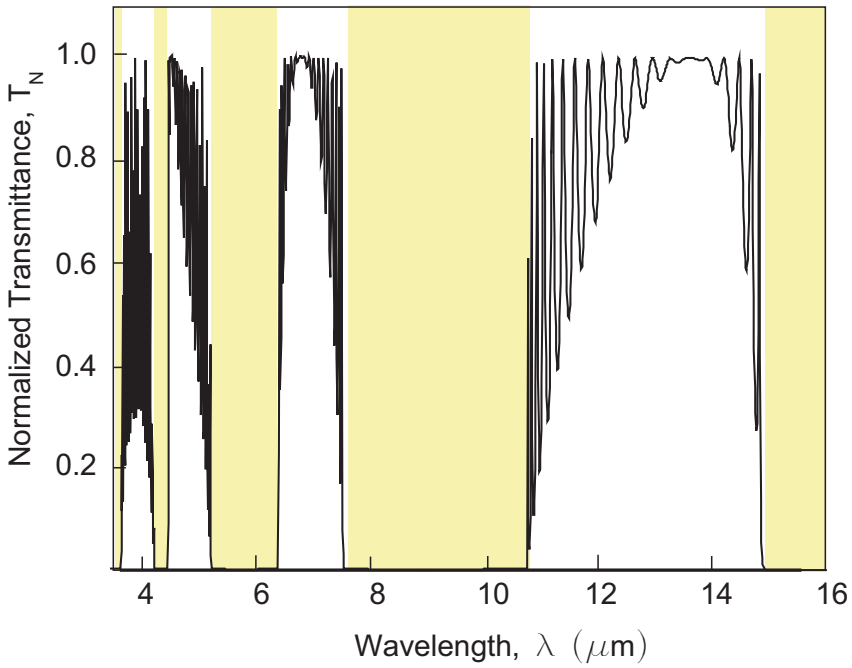

Figure 3.6: The normalized transmittance for a 1-dimensional PC structure consisting of alternating equal-width regions of silicon and air (fill factor $F = 0.5$). The shaded regions correspond to photonic band gaps identified in the band diagram for the PC structure.

3.3 Comparison of Band Diagram Analysis and Simulation Results

In this thesis, band diagrams provide a qualitative indication of device performance while the MIP-GEN, MIP-SI, and MIP-COMP programs provide quantitative theoretical results to compare with measured data from actual PC structures. Figure 3.6 shows the simulation of an ideal, 1-dimensional, 20-period device constructed with alternating 2 μm regions of silicon and air. The shaded regions correspond to the photonic band gaps identified by the band diagram for a silicon and air structure with a fill factor of $F = 0.5$. The associated band diagram is given in Fig. 3.1. The complete photonic band gaps and complete transmission bands shown in the band diagram are the result of computations for infinite-extent PCs. The simulation of finite-extent PCs provides a more realistic theoretical basis to compare with experimental measurements.

3.4 Summary

This chapter discussed the analysis of PC structures. The PC design equation was derived followed by an analysis of design equation solutions in the form of photonic band diagrams. Finally, simulation tools necessary to model device performance were discussed.

Band structures are computed by solving the PC design equation for all supported electromagnetic modes. Frequency ranges over which real wavevector solutions do not exist correspond photonic band gaps in these structures. These computations calculate the band structure for PC structures of infinite extent. To model more realistic, finite-extent structures, other methods are required. Structure modeling using FDTD methods was discussed as a potential method for modeling the performance of multiple-dimension PC structures. The transfer matrix method was discussed as a tool specifically to model 1-dimensional structures.

CHAPTER 4

FABRICATION OF INFRARED PHOTONIC CRYSTAL DEVICES

In this chapter, the fabrication of infrared PC structures designed to operate at wavelengths from $\lambda = 5\ \mu m$ to $\lambda = 15\ \mu m$ is described. The resulting structures are used to demonstrate the long-wavelength, infrared PC design and development methodology. Established microelectronics fabrication tools and techniques can be used to make devices that operate over this wavelength range. Material considerations are presented followed by a description of the fabrication process and fabrication parameters used to produce the PC structures. Scanning electron microscope (SEM) images of the fabricated structures are included.

4.1 Infrared Methodology Demonstration Structures

To demonstrate the infrared PC design methodology, 1-dimensional PC structures fabricated from silicon substrates are needed. The substrate material, silicon, was selected because it is a likely candidate for final-scale commercial PC devices and fabrication equipment is readily available for creating silicon PC structures at both the long- and short-wavelength scales. Additionally, silicon has an index of refraction of approximately $n_{Si} = 3.42$ over the $\lambda = 5\ \mu m$ to $\lambda = 15\ \mu m$ wavelength range while air has an index of refraction near $n_{air} = 1.0$ over the same wavelength range. The refractive index contrast between the two materials, $\Delta n = 2.42$, is sufficient to produce photonic band gaps at both long- and short-wavelength scales.

The profile of a 1-dimensional PC structure consisting of a silicon substrate that has been etched to form alternating regions of silicon and air is shown in Fig. 4.1. Structure variables include the fill factor F, the period a, the groove depth d, the air layer thickness t_{air}, and the silicon layer thickness t_{Si}. The silicon layer thickness and the air layer thickness

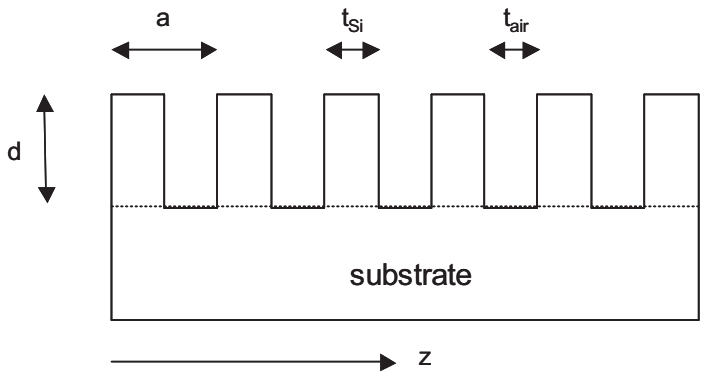

Figure 4.1: The critical parameters for a 1-dimensional PC structure fabricated in silicon are the structure period a, the fill factor F, and the groove depth d. The silicon layer thickness, t_{Si}, and the air layer thickness, t_{air}, can be computed from the period a and fill factor F. Light propagates through the structure along the z-axis. The dotted line shows the boundary between the PC region in the top of the substrate and the unetched substrate region.

are related to F and a by the equations

$$t_{Si} = Fa \tag{4.1}$$

$$t_{air} = a(1-F). \tag{4.2}$$

The PC structure layer is shown formed in the top portion of the substrate. For structures used in this thesis, the period a ranged from 4 $\mu m < a <$ 10 μm, the fill factor F ranged from $0.2 < F < 0.6$, and the device depth d ranged from 38 $\mu m < d <$ 56 μm.

4.2 Fabrication

In this section, silicon substrates suitable for fabrication of devices for the long-wavelength infrared methodology are discussed. A description of the processes used to fabricate 1-dimensional PC structures for this thesis then follows.

4.2.1 Substrate Selection

Single-crystal silicon wafers, ultrathin silicon wafers, and SOI wafers with a silicon device layer thickness in the 40 μm to 50 μm range, are produced using either the Czochralski (CZ) growth method or the float-zone (FZ) growth method. Each growth method produces silicon wafers possessing differing infrared transmission and reflection characteristics. Additionally,

the physical structure of each wafer type significantly affects the transmission and reflection measurements of PC structures. The various growth methods and wafer types must be considered before infrared PC devices can be fabricated.

4.2.1.1 Silicon Growth Methods

In the CZ growth method, a silicon crystal boule is grown from a silicon melt and seed crystal. Polycrystalline silicon is placed into a fused silica crucible and heated to temperatures in excess of $1500°C$ to form the melt. A seed crystal is brought into contact with the melt; the seed crystal induces the formation of crystalline silicon with the same crystal orientation as the seed and becomes the beginning of the boule. The initial crystalline silicon formation is pulled from the liquid to create an elongated boule. One potentially negative aspect of the CZ growth method is contamination of the silicon melt resulting from contact with the crucible. At this high processing temperature, the fused silica crucible holding the melt introduces oxygen impurities into the melt that are incorporated into the resulting silicon boule.

To avoid the oxygen impurities inherent to the CZ growth method, the FZ growth method may be used. FZ silicon is grown by placing a rod of high purity polycrystalline silicon in a chuck. A metal coil, driven by a high-power radio frequency (RF) signal, is then slowly translated over the rod's length. The electro-magnetic field of the RF signal induces eddy currents in the rod. The eddy currents, through resistive heating, melt the silicon. A seed crystal is often used to ensure proper growth orientation. The absence of the crucible in this manufacturing technique eliminates oxygen impurities [76].

Figure 4.2 shows the normalized transmittance of CZ- and FZ-grown silicon. The transmittance minimum at a wavelength of approximately $\lambda = 9\ \mu m$ in the CZ silicon spectrum is attributed to absorption by the oxygen impurity inherent to CZ-grown silicon. Since the transmittance minimum is near the tuning range of the CO_2-laser and almost centered in the $\lambda = 5\ \mu m$ to $\lambda = 15\ \mu m$ wavelength range, CZ-grown silicon cannot be used for long-wavelength structures fabricated for this thesis. Silicon grown using the FZ growth method is the more suitable material for long-wavelength structures.

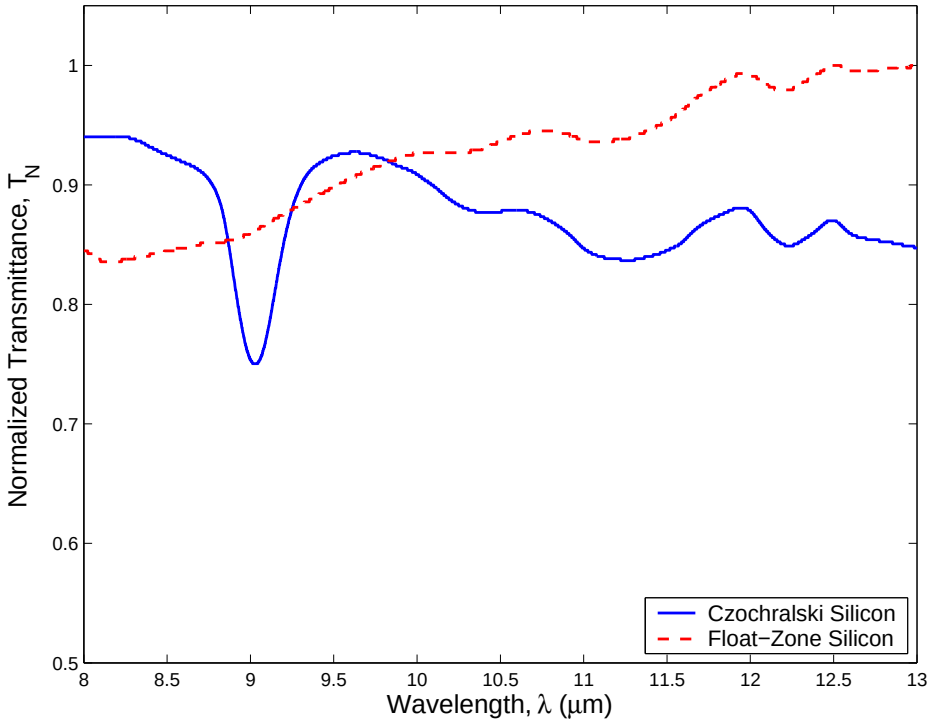

Figure 4.2: Normalized transmittance of CZ- and FZ-grown silicon measured using an FTIR spectrometer. The transmittance minimum at $\lambda = 9\ \mu m$ is attributed to oxygen contaminants resulting from the crucible used in the CZ growth method.

4.2.1.2 Wafer Type

FZ-grown silicon substrates are available as bulk single-crystal wafers, ultrathin single-crystal wafers, and SOI wafers. In the SOI substrates, only the device layer, on top of the buried oxide, must be FZ-grown silicon. In selecting a suitable wafer type for fabricating PC structures, light propagation and material handling issues must be examined.

Bulk single-crystal silicon wafers are approximately 500 μm thick. PC structures can be fabricated into the surface of the substrate thereby creating a PC region of the substrate and an unpatterned, unetched region of the substrate. Since there is no material boundary between the patterned and unpatterned regions, light propagating in the PC structure is not confined to the PC region. As light propagates through the PC structure, light can leave the PC region and propagate through the unpatterned, unetched portion of substrate below the device. Including this errant light in transmittance or reflectance measurements corrupts the measurements with substrate transmittance or reflectance data. Restricting measurements so this light is not included in measurements creates a source of loss. Despite this limitation, Xu *et al.* demonstrated functional PC structures with depths of $d = 8.2\ \mu m$ in bulk silicon wafers [65]. In Xu's work, an aperture was used to restrict measurements to light passing only through the PC region. Measured transmittances were normalized to a reference measurement using a substrate with a similar light path without the patterned PC region.

To provide confinement of light in a single-crystal silicon wafer, the wafer must be thinned so that the PC structure can be etched through the entire wafer. The thinning process can be avoided by using ultrathin single-crystal silicon wafers, which are available with thicknesses ranging from 30 μm to 100 μm. Confinement of light in the vertical direction results from total internal reflection (TIR) at the silicon–air interfaces at the top and bottom of the wafer. However, ultrathin silicon substrates are extremely fragile and fracture easily even under routine handling. Wafer handling and processing equipment used in many fabrication processes cannot be used to process the ultrathin substrates. Alternate fabrication methods are time consuming. Since one of the primary motivations for using the infrared long-wavelength approach is to fabricate and test devices rapidly, ultrathin

substrates are not feasible candidates for this methodology.

SOI substrates with a FZ-grown silicon device layer can be processed without the handling difficulties associated with ultrathin silicon wafers while offering vertical confinement of light. Various research groups have demonstrated the use of this wafer type to create PC structures [9, 77]. In SOI substrates, vertical confinement of light is the result of TIR at the silicon–air interface at the top of the wafer and at the silicon–oxide interface at the buried oxide layer. Once etched, the SOI wafer is difficult to cleave due to possible crystal orientation mismatch between the substrate layer (handle) and the device layer. Despite this difficulty, SOI wafers are suitable for creating PC structures for testing using the long-wavelength infrared development methodology.

In this research, FZ single-crystal silicon substrates and SOI substrates were used to fabricate PC structures. Both substrates permit rapid processing of silicon to create a variety of structures for use with the long-wavelength infrared methodology.

4.2.2 Optical Photolithography

The selected silicon substrates must be etched to form the PCs. Etch region dimensions were computed with PC design and analysis tools. The desired patterns were laid out using AutoCAD software [78]. Photomasks with the desired patterns were produced for the photolithography steps.

Photolithography is used to transfer the pattern from a mask to the photoresist layer coating a silicon substrate. In a typical processing sequence, photoresist is applied to a substrate to a specified uniform thickness using a spin coater. A mask is loaded into an exposure tool and the coated substrate is held tightly against the mask. The exposure tool illuminates the mask. Clear regions on the mask allow the light from the exposure tool to propagate into the photoresist layer beneath the clear areas on the mask. Dark regions on the mask block light from reaching the photoresist layer. Depending on the photoresist type (positive or negative), either the exposed or unexposed regions will dissolve in the chemical developer during development. The silicon surface is exposed in regions where the photoresist dissolves. With the mask pattern transferred to the photoresist layer, the wafer

is ready for the etch process.

The photolithographic steps and parameters used in creating PC structures for investigating the long-wavelength infrared PC design methodology are summarized below:

1. The wafer was rinsed sequentially with acetone, isopropanol, methanol, and deionized water.

2. The wafer was placed on a 115°C hotplate for 15 minutes to evaporate water off of the substrate.

3. The substrate was mounted onto the chuck of a CEE 100 CB Photoresist Spinner. Shipley 1813 positive photoresist was applied to the wafer and the wafer was coated using a spin speed of 4000 revolutions per minute (RPM) for 40 seconds. This process produced a 1.2 μm layer of photoresist on the wafer.

4. To drive off solvent in the resist, the wafer was soft-baked for 30 seconds on a 100°C hotplate.

5. A mask and the wafer were loaded into a Karl Suss MA-6 aligner. Light with a wavelength $\lambda = 405\ nm$ was used to expose the wafer to the optimum exposure intensity dosage of 100 mW/cm^2.

6. The exposed wafer was developed in Shipley MF319 developer for 45 seconds and rinsed in a deionized water bath.

7. The wafer was hard-baked on a 110°C hotplate for 10 minutes to harden the photoresist prior to etching.

With dedicated equipment, all photolithography steps could be completed in approximately 1 hour.

4.2.3 Etching

To fabricate PC structures in silicon, high aspect ratio etching is required. Tools developed primarily for the fabrication of Micro-Electro-Mechanical system (MEMs) components are

well suited for this task [79–81]. Inductively coupled plasma (ICP) technology using a Bosch etch chemistry [79] to etch the wafers is typically used.

The Bosch process consists of alternating cycles of sidewall passivation with octafluorocyclobutane (C_4F_8) and silicon etching with sulphur hexafluoride (SF_6). During the passivation cycle, C_4F_8 is deposited on all surfaces of the sample to create the protective passivation layer. When the etch cycle starts, ions from the SF_6 are accelerated vertically onto the sample. The passivating polymer is quickly removed from the horizontal surfaces, thus exposing the silicon to the reactive fluorine-based ions. As the etch cycle progresses, the polymer on the vertical surfaces continues to erode slowly. The etch cycle is timed to end when a new C_4F_8 deposition is required to protect the sidewalls.

A Surface Technology Systems Advance Silicon Etch (STS-ASE) system was used to etch the silicon using a proprietary modified Bosch process. Etch parameters were adjusted to obtain the best possible etch quality with the highest possible aspect ratios. The optimum parameters are dependent upon the structure geometry and the substrate type. The STS-ASE system has two etch-cycle frequency settings that can be used to etch silicon. The high-frequency etch setting at a frequency of 13.56 MHz is used for etching single-crystal silicon wafers. The low-frequency etch setting at a frequency of 380 KHz is used to etch SOI wafers near the oxide layer. The etch quality was evaluated by visual inspection of scanning electron microscope (SEM) images of the etched PC structures.

Figure 4.3 shows an SEM image of a 1-dimensional PC structure etched in silicon using the STS-ASE high-frequency setting. The structure period is $a = 6.7\ \mu m$ and the structure depth is $d = 38\ \mu m$. Figure 4.4 shows an SEM image of a structure with a device period of $a = 9.8\ \mu m$. This structure contains a defect in the center of the structure. The defect width is $1.7\ \mu m$ and the structure depth is $d = 52\ \mu m$. One-dimensional devices were etched to depths up to $d = 56\ \mu m$.

Close inspection of the etch profile reveals the effects of the cyclical Bosch process. Figure 4.5 shows the etched sidewalls after a high-frequency STS-ASE etch process. The ripple present on the vertical sidewall surfaces is caused by the cycling between passivation and etching.

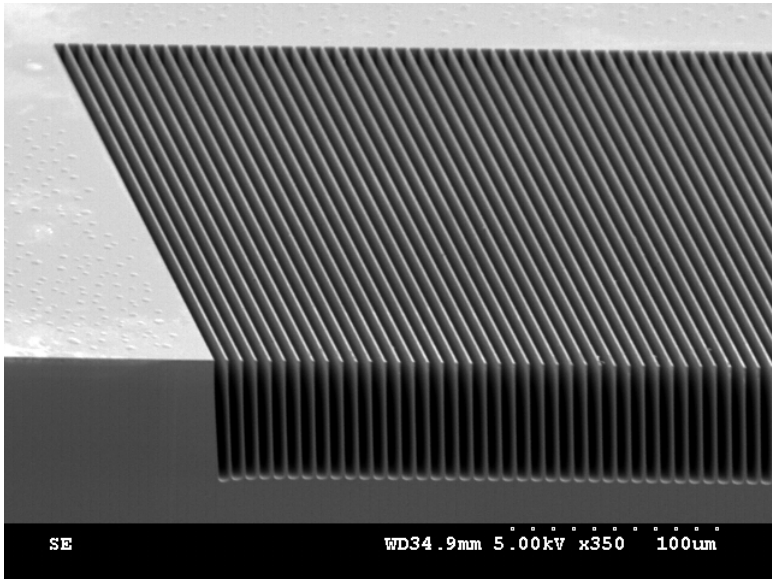

Figure 4.3: A 1-dimensional PC structure etched into a silicon wafer. The device period is $a = 6.7\ \mu m$ and the structure depth is $d = 38\ \mu m$.

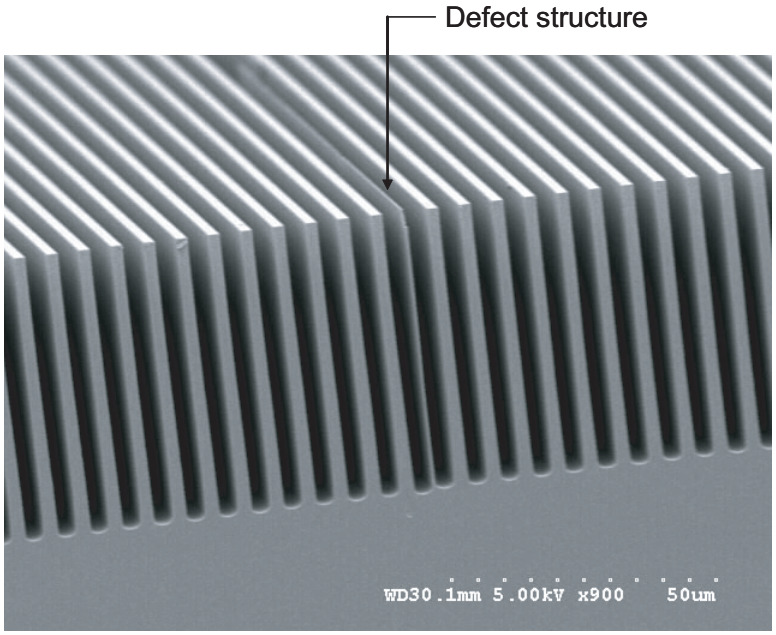

Figure 4.4: A 1-dimensional PC defect structure etched into a silicon wafer. The device period is $a = 9.8\ \mu m$, the defect structure width is $1.7\ \mu m$, and the structure depth is $d = 52\ \mu m$.

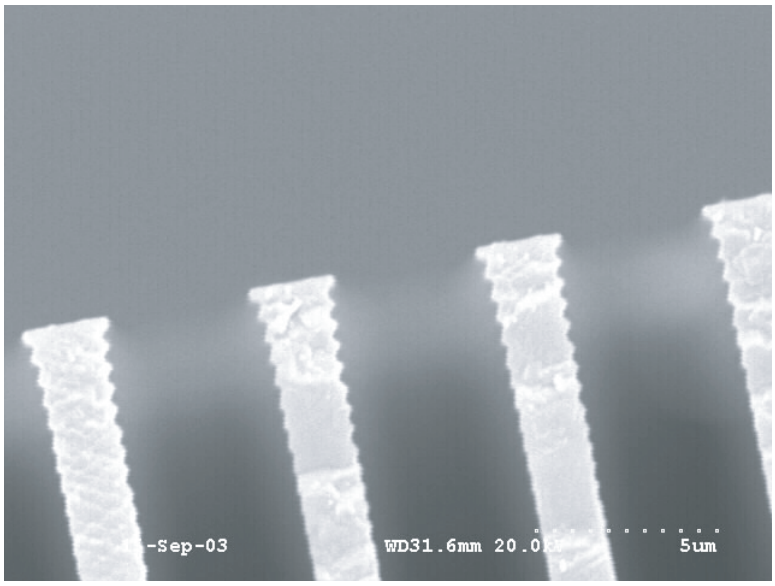

Figure 4.5: The etch/passivation cycling inherent to the Bosch process produces rippled sidewalls. The ripple period is several hundreds of nanometers long for the sidewalls shown in this SEM image.

The structure dimensions have a significant effect on the quality and the etch rate of the etch process. Figure 4.6 shows the etch profile for an STS-ASE high-frequency etch process with trench widths of $t_{air} = 10, 5, 3$ and 2 μm. The 10 μm trench etched to a greater depth than the narrower trenches. Sidewall taper is more evident in the etches as the trench width decreases.

For SOI substrates, the high-frequency etch setting and the low-frequency etch setting are used sequentially to produce desired structures. First, the high-frequency etch setting is used to rapidly etch the silicon until the etch depth approaches to within approximately 2 μm of the buried oxide layer. The oxide layer is almost impervious to the fluorine-based ions. If the high-frequency etch is continued, charge from the etchant ions will accumulate at the oxide layer. Accelerated ions approaching the accumulated charge are deflected into the sidewall, resulting in sidewall etching. By switching to the low-frequency etch setting when the etch depth reaches to within 2 μm of the oxide, charge accumulation is minimized. Even with the low-frequency setting, some sidewall etching occurs. An SEM image of an SOI substrate etched using the two-frequency process is shown in Fig. 4.7. Some sidewall etching is evident at the base of the trench near the oxide layer, as shown in the SEM image

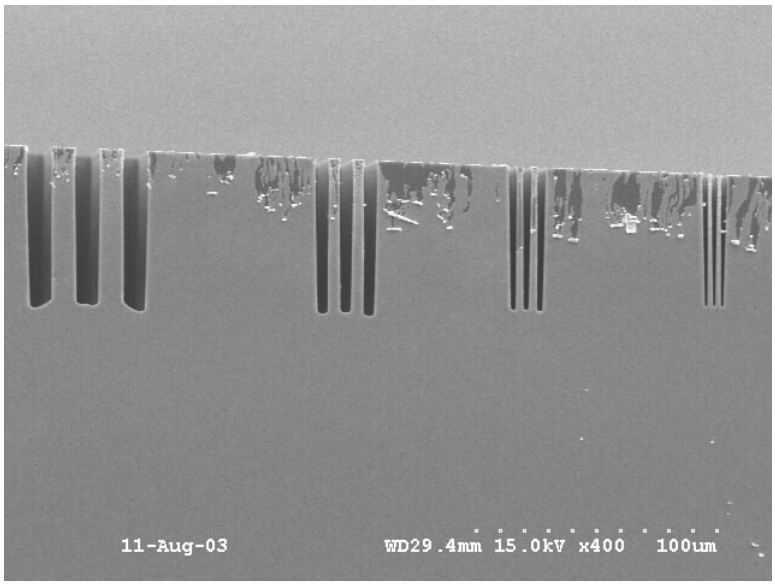

Figure 4.6: Trenches with dimensions of $t_{air} = 10, 5, 3$ and 2 μm after 140 etch cycles in the STS-ASE system. As t_{air} decreases, the etch depth decreases and the sidewall-taper increases.

in Fig. 4.8.

Etch parameters for the STS-ASE systems and gas flow rates are listed in Tables 4.1 and 4.2 respectively. The time required to etch a single wafer with the STS-ASE system is approximately 45 minutes.

4.2.4 Wafer Cleaning

After completing the etch process, wafers were cleaned to remove any remaining photoresist. Relatively thick photoresist residue on the wafer surface was removed using a rinse with acetone, methanol, and isopropanol. Residue adhering to the etched structures was removed using a 1 minute oxygen ashing process in a Gasonics Aura 1000 Plasma Ashing System.

4.2.5 Sample Cleaving

Sample structures for use in testing, were manually cleaved from the substrate. The top surface of the wafer was scribed with a diamond-tipped scribe in the direction of the desired cleave plane. Pressure applied to the back surface of the wafer opposite the scribe mark cleaved the wafer along the desired plane. Cleaved edges that extended across the entire wafer produced desirable mirror-like interfaces along the cleave. Using this approach yielded

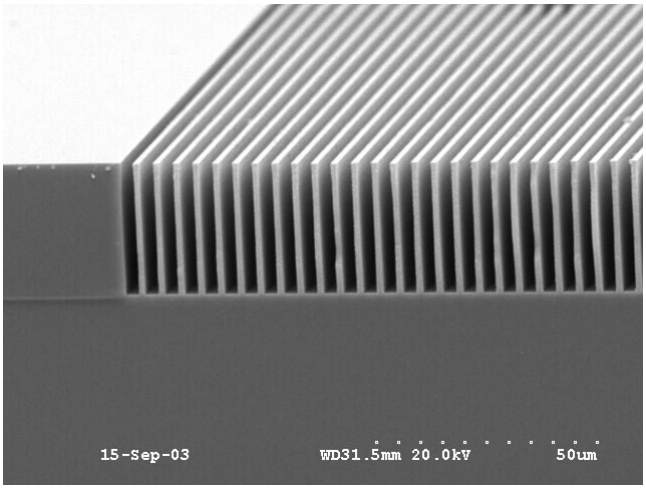

Figure 4.7: SEM image showing etched structures on an SOI substrate. The 1-dimensional PC was etched to a depth of approximately 38 μm using a high-frequency etch cycle for 30 minutes. At this point, a low-frequency etch cycle was used for 4 additional minutes to achieve a structure depth d=40 μm. The line at the base of the structure is the oxide-silicon interface.

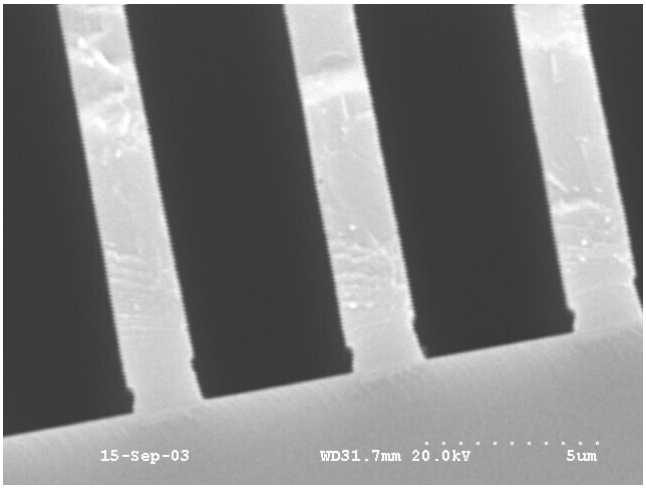

Figure 4.8: Etching of the sidewall base is caused by accumulated charge present on the substrate. The charge deflects the etchant ions into the sidewall resulting in sidewall etching. Even with the combined 2-step etch process, detrimental etching of the sidewall base still occurs.

Table 4.1: Parameters used in etching PC structures with the STS-ASE system.

Etch Cycle Time (sec)	10.0
Passivation Cycle Time (sec)	8.0
RF Power ($watts$)	600
Platen Power ($watts$)	10.0
Etch Frequency-High Frequency for Bulk Silicon (MHz)	13.56
Etch Frequency-Low Frequency Near Buried Oxide (KHz)	380
Etch rate - High Frequency ($\mu m/min$)	1.3
Etch rate - Low Frequency ($\mu m/min$)	0.6
Average Forward Power ($watts$)	604
Average Reflected Power ($watts$)	12
Typical Helium Cooling Rate ($sccm$)	< 7

Table 4.2: Gas flow rates in standard cubic centimeters per minute (sccm) are listed for etching in the STS-ASE system.

	Etch parameters		Passivation parameters	
Gas Type	Flow (sccm)	Ramp rate (sccm/min)	Flow (sccm)	Ramp rate (sccm/min)
C_4F_8	20	-4.0	85	0
SF_6	130	0	0	0
O_2	13.0	0	0	0

rows of structures, with each row having a 3 mm to 4 mm width. The second cleave, required to detach a single structure from a row of structures, was more difficult to perform. The row of structures was placed with the PC structure side down. A line was scribed approximately 200 μm from the previously cleaved edge using a diamond tipped scribe. A metal straight edge was used to guide the scribe. By applying pressure during the scribing motion, the row of samples fractured along the scribe line.

The separated structures were inspected using a microscope. Due to the pressure applied while scribing, many devices were destroyed. Approximately 5% to 10% of the cleaved devices were intact after the scribing process and could be used for characterization. Since an individual wafer contains approximately 600 structures, the low yield was not a concern. Devices were cleaned with compressed air and rinsed with solvent before being reinspected prior to testing.

Figure 4.9 shows an image of a device that has been cleaved from the substrate. The top edge was the result of the first cleave across the entire wafer separating the structures into 3 mm - 4 mm rows. The more jagged bottom cleaved edge resulted from the cleave on the backside of the wafer using pressure on the scribe. The probe beam used in characterization passes directly into the structure and does not pass through either cleaved edge (Chapter 6). In the figure, the PC structure is located on the right. The region on the left is solid silicon region and is used to facilitate background measurements for the FTIR spectrometer system (Chapter 6).

4.3 Summary

The fabrication of PC structures used to demonstrate the long-wavelength infrared methodology has been described. With dedicated equipment, this process, from the initial mask design through final sample cleaning, could be accomplished in less than one day. The fabrication methods used for these structures are similar to the methods used in final-scale PC device fabrication.

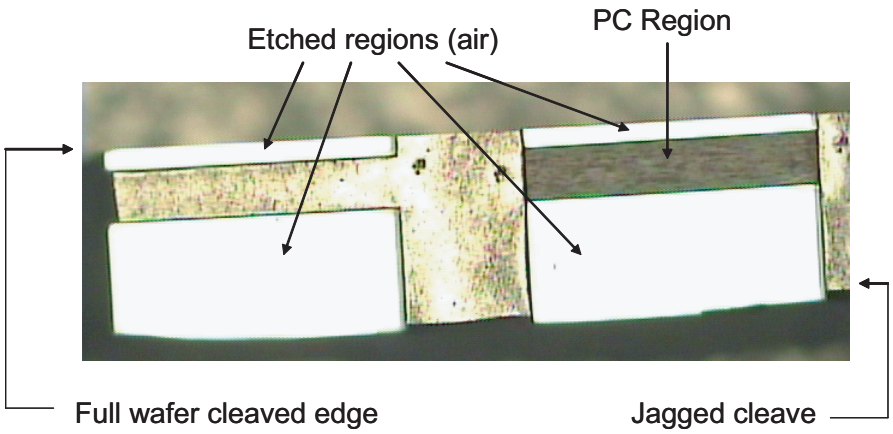

Figure 4.9: A single PC structure after being cleaved from the substrate. The upper edge was initially cleaved across the entire wafer. The more jagged lower edge cleave resulted from the pressure applied to the scribe during scribing process on the backside of the wafer. The probe beam used in characterization passes directly into the structure and does not pass through either cleaved edge.

CHAPTER 5

PHOTONIC CRYSTAL STRUCTURE CHARACTERIZATION

A device characterization scheme has been developed for use with the long-wavelength infrared PC design and development methodology. Typical spectral measurements of fabricated structures that provide the transmittance or reflectance as a function of wavelength represent the structure transmittance or reflectance to a composite beam consisting of superimposed plane waves incident over a range of angles. By processing the spectral transmittances or reflectances from composite measurements, the single-angle plane-wave transmittances or reflectances of fabricated structures can be computed.

This chapter begins with an overview of the structure characterization method. The problem is formulated as a linear matrix algebra problem for both transmittance and reflectance measurements. The resulting algebraic matrix equations suffer from inherent instability and must be regularized to obtain meaningful solutions that accurately portray the single-angle plane-wave transmittances and reflectances of the structures. A regularization scheme that reduces instability is presented and tested using simulated PC transmittance calculations for hypothetical structures. The simulations are used to identify the system noise limits for the application of this characterization method.

5.1 Characterization Method Overview

The single-angle plane-wave transmittance or reflectance of a PC structure is an appropriate characterization parameter. By having the single-angle plane-wave transmittance or reflectance for plane waves incident over a range of angles, any incident beam composed of combinations of these plane waves can be computed.

To measure the transmittance of a structure, the probe beam propagates through the sample and the transmitted power is measured with wavelength as a parameter. Likewise,

to measure the reflectance of a structure, the probe beam reflects from the surface of the sample and the reflected power is measured as a function of wavelength. If the incident beam is decomposed into plane waves, a single transmittance or reflectance measurement can be represented by the equations

$$T_{\theta_S} = \sum_{j=1}^{n} a_j t_j, \tag{5.1}$$

$$R_{\theta_S} = \sum_{j=1}^{n} a_j r_j, \tag{5.2}$$

where T_{θ_S} is the transmittance of the composite beam with the objective axis at an angle of θ_S with respect to the surface normal of the sample, R_{θ_S} is the measured reflectance of the composite beam with the objective axis at an angle of θ_S with respect to the surface normal of the sample, n is the number of plane wave components in the incident beam, j is an index number for each plane wave, a_j is the weighting coefficient associated with the j^{th} plane wave, t_j is the single-angle plane-wave transmittance of the j^{th} plane wave, and r_j is the single-angle plane-wave reflectance of the j^{th} plane-wave. Since the total beam is represented by the coefficients, the sum of all coefficients in a single measurement must equal 1,

$$\sum_{j=1}^{n} a_j = 1. \tag{5.3}$$

If the incident beam is a single-angle plane-wave, $n = 1$, $a_j = 1$, $T = t_j$, and $R = r_j$. If an incident beam consists of 5 plane-wave components, Eqs. (5.1) and (5.2) become

$$T_{\theta_S} = a_1 t_1 + a_2 t_2 + a_3 t_3 + a_4 t_4 + a_5 t_5, \tag{5.4}$$

$$R_{\theta_S} = a_1 r_1 + a_2 r_2 + a_3 r_3 + a_4 r_4 + a_5 r_5, \tag{5.5}$$

which represent a single transmittance measurement and a single reflectance measurement. In both of these equations, the composite measurements, T_{θ_S} and R_{θ_S}, are known quantities while the single-angle plane-wave transmittance and reflectances, t_j and r_j, are unknown and are to be determined. The coefficients for the component plane waves, a_j, are also unknown and to be determined.

Equations (5.4) and (5.5) can be combined with Eq. (5.3) to form 2 systems of equations. Each system consists of 2 equations containing 10 unknown values. To solve for these

unknown values, additional measurements are needed until the number of measurements, and hence equations, is at least equal to the number of unknown values.

The additional measurements are obtained by measuring the composite transmittance or reflectance of a structure multiple times where, in each measurement, the composite beam consists of various subsets of plane waves. By using the data from all measurements, the plane-wave transmittances or reflectances of a PC structure over a wide range of angles can be obtained; the thus determined single-angle plane-wave transmittances or reflectances can then be used to analyze PC structures. As a structure characterization tool, the spectral response of a device to any arbitrary beam consisting of combinations of the computed plane-wave transmittances or reflectances can be used to identify the performance limits of a fabricated PC structure. Working in the opposite direction, as a design tool, the single-angle plane-wave transmittance or reflectance data can be used to identify the required fabrication tolerances required to meet application-specific performance requirements.

The general approach followed in the single-angle plane-wave characterization scheme is described in the following sections. First, the probe beam is analyzed to determine the composition of the incident beam. This process identifies the component plane waves incident on the structure (Section 5.2). The number of component plane waves is restricted so that the incident component plane waves have wavevector components primarily in 2-dimensions rather than 3-dimensions (Section 5.3). The intensity of the probe beam is measured to determine the weighting coefficient values, a_j, for each plane wave (Section 5.4). A scheme is developed for recording a sufficient number of measurements to produce an appropriate number of equations to solve for single-angle plane-wave transmittances or reflectances of the structure (Section 5.5). These problems are formulated for both transmittance and reflectance measurements (Section 5.6). The resulting matrix algebra problem requires stabilization to obtain meaningful solutions for the single-angle plane-wave transmittances and reflectances (Section 5.7).

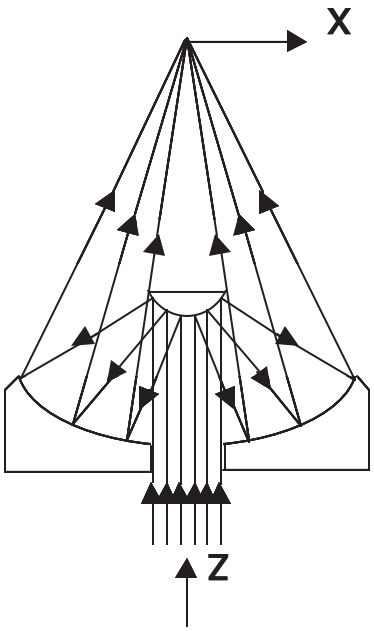

Figure 5.1: Optical configuration of a Schwarzchild reflecting focusing objective. Light passes through a hole in the large outer mirror and is reflected by the smaller mirror back to the large mirror. This mirror reflects the light to the focal point.

5.2 Schwarzchild Objective Design

To calculate the single-angle plane-wave transmittance or reflectance of a device, it is necessary to analyze the incident beam to determine the plane-wave components that constitute the composite beam. For PC structures designed to operate in the $\lambda = 5\ \mu m$ to $\lambda = 15\ \mu m$ wavelength range, the small structure dimensions require that the probe beam be focused to a small spot size. Typical focusing systems for infrared light employ Schwarzchild reflecting microscope objectives. The physical configuration of these objectives significantly influences the measurement and analysis of PC structures.

The Schwarzchild reflecting objective is a two-mirror optical system. Figure 5.1 shows the reflection-based mirror configuration and optical path through the objective. Light, as it enters the objective, passes through an aperture in the center of the large, outer concave mirror. The light strikes the small, central convex mirror that is mounted on arms extending from the objective housing. The incident light is reflected from the convex surface of the small mirror diverging onto the large mirror. The light then reflects from the concave surface of the large mirror to the focal point. Near-normal incident light reflects from the small

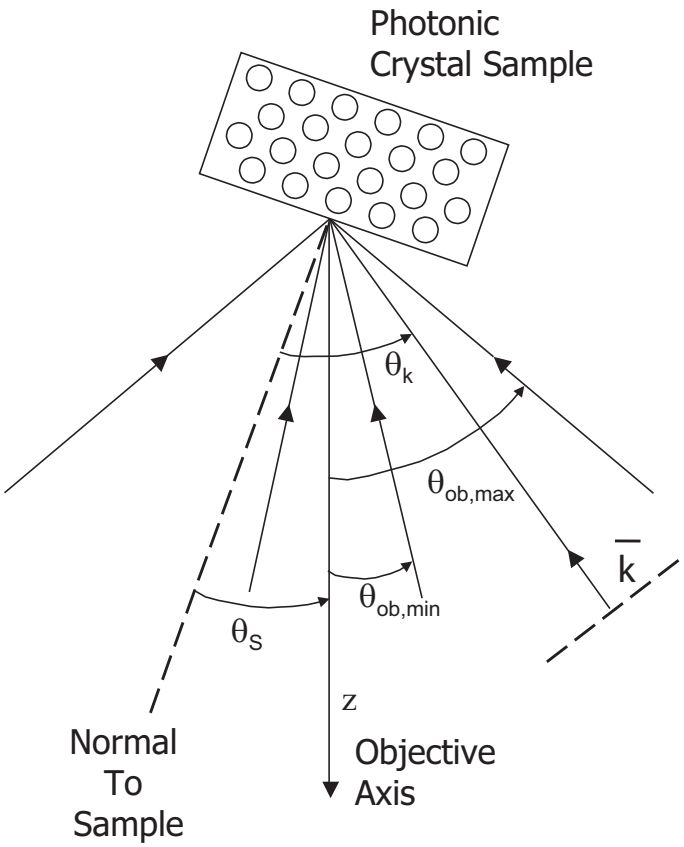

Figure 5.2: Light rays from a Schwarzchild objective are focused onto a photonic crystal sample. The objective axis is at an angle θ_S with respect to the normal of the sample. The minimum and maximum ray angles of the objective are given by $\theta_{ob,min}$ and $\theta_{ob,max}$ respectively. An example single-angle plane-wave angle incident at an angle of θ_k with respect to the sample normal is shown.

mirror's convex surface and travels back through the entrance aperture. The amount of near-normal incident light lost depends on the aperture size and the curvature of the small mirror. The percentage of incident light reflected from the small mirror back through the objective entrance aperture is specified by the objective's central obscuration and is given as an area percentage of the entrance aperture [82].

To analyze and model the incident light being focused on PC structures by the reflecting objective, the parameters shown in Fig. 5.2 are used. The objective angles incident on the sample are determined solely by the objective design and range from $-\theta_{ob,max}$ to $-\theta_{ob,min}$ and from $+\theta_{ob,min}$ to $+\theta_{ob,max}$. The angle θ_S is determined by the objective axis angular orientation with respect to the sample normal. Each ray incident on the sample is within

Table 5.1: Example commercially available Schwarzchild reflecting objectives including their minimum and maximum ray angles.

Manufacturer	Model No.	Magnification	Numerical Aperture	$\theta_{ob,min}$ (deg)	$\theta_{ob,max}$ (deg)
Thermo-Oriel	13595	15X	0.4	9.8	23.6
Thermo-Oriel	13596	36X	0.5	10.3	30
Ealing	25-0514	25X	0.4	9.4	23.5
Ealing	25-0522	36X	0.5	10.0	30.0

the allowed θ_{ob} ranges and is incident at an angle θ_k where k specifies the direction of the wavevector of the incident ray. This wavevector may have wavevector components in the x, y, and z directions. Values for $\theta_{ob,max}$ and $\theta_{ob,min}$ vary depending on the numerical aperture of the objective. Typical values for several commercial objectives available from Ealing [82] and Oriel [83] are listed in Table 5.1.

The angles specified by $\theta_{ob,max}$ and $\theta_{ob,min}$ include all angles with circular symmetry about the z-axis of the objective. Figure 5.3 shows the resulting cone of incident light introduced by the objective. The plane waves that form the composite beam contain rays with wavevectors in all planes that include the z-axis. The absence of rays incident on the sample along the z-axis is a result of the central obscuration of the objective.

To formulate a solution for the single-angle plane-wave transmittances and reflectances of the structure, the composite incident beam must be divided into sectors and the relative weighting of each sector must be determined. To reduce the computational difficulties while still obtaining meaningful response data, the incident beam is restricted to plane waves with wavevector components predominantly in the $x - z$ plane.

5.3 Restricting Light to the Photonic Crystal Region

The light cone emerging from the Schwarzchild reflecting objective consists of plane waves with wavevectors having components in all three coordinate directions, $k = k_x\mathbf{x} + k_y\mathbf{y} + k_z\mathbf{z}$. To simplify the measurement of the beam weights associated with each plane wave, a slit is inserted into the optical path prior to the objective to block incident rays with wavevectors

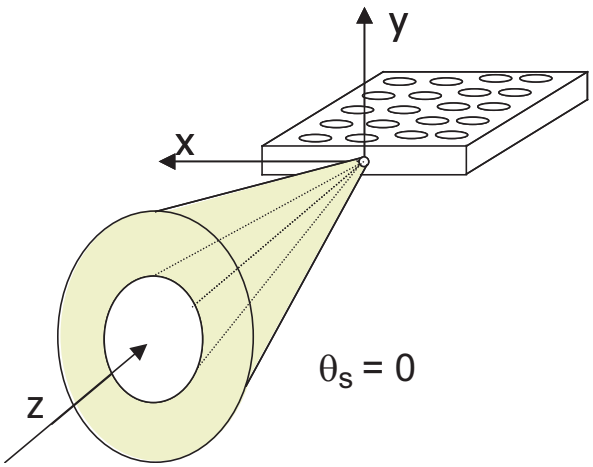

Figure 5.3: Light is focused onto a sample by the objective. Light at normal incidence is blocked by the small mirror. The circularly symmetric focusing light forms a cone illuminating the sample where the incident light wavevectors are in the structure plane as well as outside of the structure plane.

having significant **y** components. Figure 5.4 shows the orientation of the objective slit in reference to the sample. The slit is oriented with the long axis along the x-direction and the short axis along the y-direction. In the limit of allowing the slit width along the short axis to approach zero, light could be restricted to a single plane (the $x - z$ plane) with wavevectors containing only x- and z- components; however, such a severe restriction drastically reduces the throughput even to the point that power levels would fall below the detection threshold. A slit with a slighter greater width significantly reduces the quantity of light with large y-component wavevectors incident on the system. The corresponding effects of these rays on the transmittance and reflectance measurements are also reduced while detectable power levels are maintained.

In this thesis, although incident waves with x-, z-, and small, nonzero y-component wavevectors are incident on the structure, the incident light will be represented by plane waves in 2-dimensions with only x- and z- wavevector components. The objective slit restricts light primarily to the structure plane. The incident beam in the structure plane is divided into sectors and the beam weighting coefficients for each sector are measured.

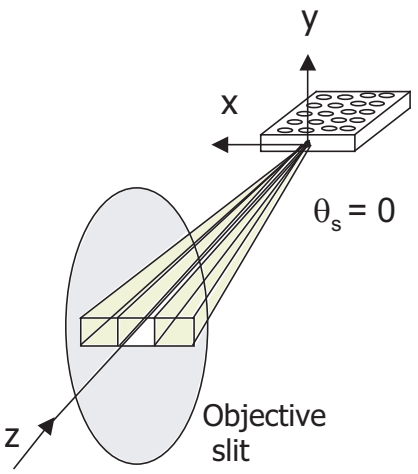

Figure 5.4: A horizontal slit positioned before the objective restricts light primarily to the plane of the structure. Out-of-plane light is blocked by the slit and does not enter the objective. The objective is not shown in the diagram. In this diagram, the slit is shown with the objective axis at normal incidence to the sample ($\theta_S = 0$).

5.4 Two-Dimensional Beam Intensity Weighting

The reflecting microscope objective focuses the incident light into the cone of angles bounded by $\theta_{ob,max}$ and $\theta_{ob,min}$. The objective slit restricts light primarily to the structure plane. The light in this plane is divided into sectors, with the angular range for each sector being $\Delta\theta_{ob}$ given by

$$\Delta\theta_{ob} = \frac{2(\theta_{ob,max} - \theta_{ob,min})}{i} \tag{5.6}$$

where i is the number of sectors. The intensity of light being focused within each sector is represented by a weighting coefficient a_i for the sector.

If the incident beam intensity is uniform across the input aperture of the objective and the objective perfectly focuses the light, the light intensity within each sector would be uniform. In this case, the corresponding weighting coefficients are equal for each sector ($a_i = 1/i$). If, however, the beam is not uniform or the objective does not perfectly focus the light, the intensity within each sector is not equal. In this case, the focused beam for each objective axis position can be described as the summation of the weighted plane waves where the weights for each plane wave, a_j in Eq. (5.1) and Eq. (5.2), are given by the intensity of light in the plane wave's sector a_i. By measuring and then constructing the power profile of the focusing beam, the weighting coefficients can be obtained. Equipment

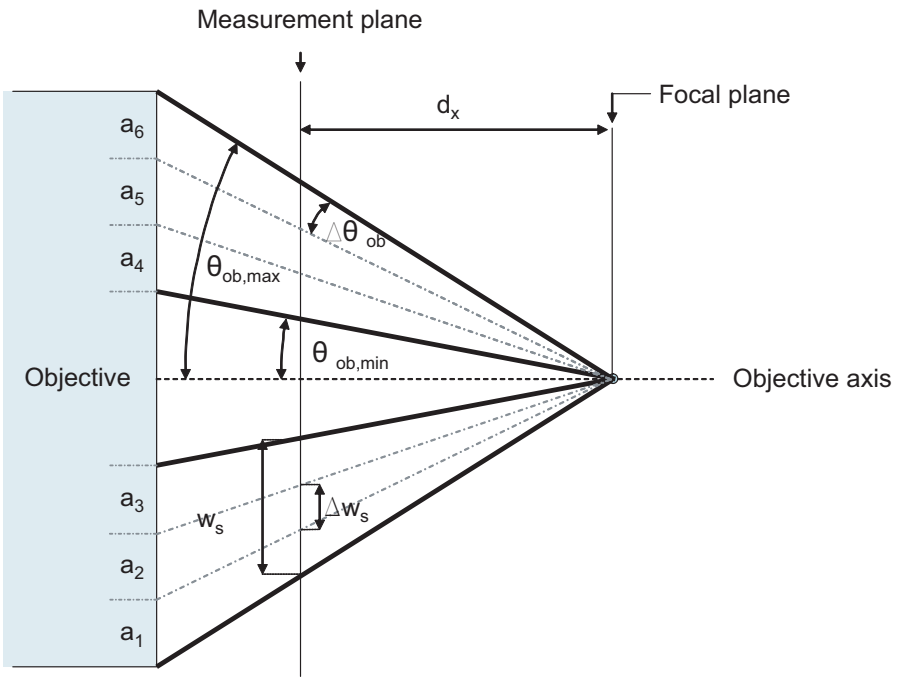

Figure 5.5: The weighting factors $[a_1 \;\; a_2 \ldots a_6]$ account for the intensity variation in the focusing beam. The variations can be caused by nonuniform illumination of the small mirror or by imperfect focusing caused by manufacturing errors in the objective.

used to measure the power profile of the focusing beam are addressed for each measurement apparatus in Chapter 6.

Figure 5.5 shows the method used to determine the coefficients for the constructed profile. In the figure, the focusing light is shown divided into six sectors. The profile is measured a known distance, d_x, from the objective focal point. The width of the beam on each side of the objective axis, w_s, and the width of the individual sectors, Δw_s, are computed using,

$$w_s = d_x(\tan\theta_{ob,max} - \tan\theta_{ob,min}), \tag{5.7}$$

$$\Delta w_s = w_s\left(\frac{\Delta\theta_{ob}}{\theta_{ob,max} - \theta_{ob,min}}\right). \tag{5.8}$$

With these values computed, the measured profile is divided into the sectors Δw_s and the area under the beam power profile in each sector is calculated and normalized to the total area under all sectors to determine the weighting coefficients a_i. Once the beam weighting coefficients are obtained, generating a sufficient number of equations to solve for the single-angle plane-wave transmittances or reflectances of the structures becomes the foremost

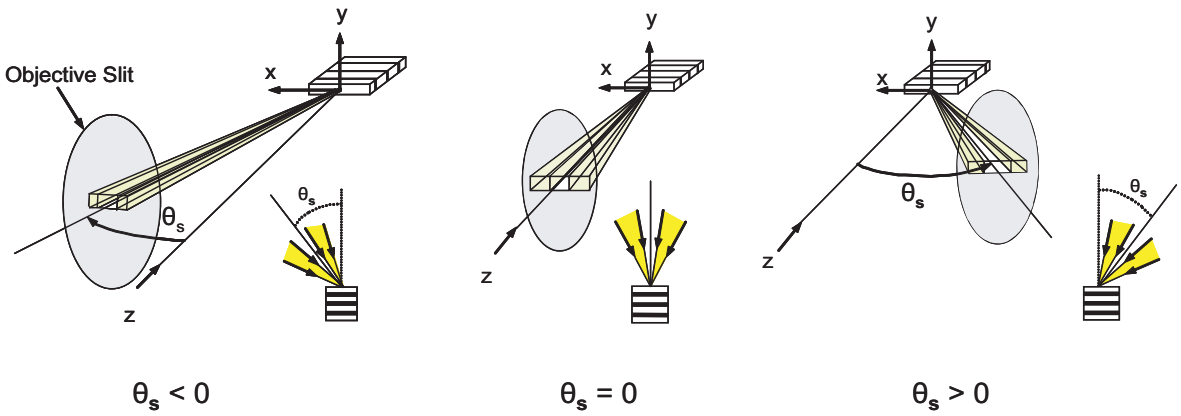

Figure 5.6: As the objective axis is rotated with respect to the sample normal in the half-plane in front of the sample, various sets of incident angle plane waves are selected by the objective. By rotating and measuring the transmittance or reflectance of the composite beam in discrete increments, new angles are added while some are removed in each subsequent measurement. If θ_S is rotated to sufficient limits, all angles in the half-plane before the sample can be selected. The increment from one axis angular orientation to the next is given as $\Delta\theta_S$.

concern.

5.5 Multiple Measurements

For each objective axis angular orientation relative to the sample normal, θ_S, a unique set of plane waves is selected and weighted by the objective. To obtain a sufficient number of equations to solve for all unknown values in Eqs. (5.1) and (5.2), a system of equations must be generated by measuring the transmittance or reflectance of the structure at discrete angular positions of θ_S. Each measurement provides a unique equation that can be used to solve the system. Theoretically, θ_S could range from $-90° + \theta_{ob,max}$ to $90° - \theta_{ob,max}$. At the extreme objective axis positions, the maximum incident ray angles, $\theta_k = \pm 90°$, are at grazing incidence. However, the actual rotation range may be limited to values less than these extreme values by physical constraints of the objective housing and the sample.

Figure 5.6 shows an isometric view of the slit and sample at several objective axis positions in the half-plane in front of the sample. The inset shows the corresponding objective axis position in the plane of incidence. Transmittance or reflectance measurements are conducted at specified angular increments ($\Delta\theta_S$) across the objective-axis rotation range. As

Table 5.2: The number of measurements (composite transmittances), M, and the number of unknowns (single-angle-plane-wave transmittances), N, as a functions of $\theta_{ob,max}$, $\theta_{S,max}$, $\Delta\theta_S$, and $\Delta\theta_k$.

$\theta_{ob,max}$ (deg)	$\theta_{S,max}$ (deg)	$\Delta\theta_S$ (deg)	M (T's)	$\Delta\theta_k$ (Deg)	N (t's)
24	42	2	43	2	34
24	24	2	25	2	25
24	40	2	25	4	17
30	40	5	15	5	17
30	40	10	11	7	11
30	40	5	15	10	8

the objective axis is rotated with respect to the sample normal across the half-plane in front of the device, the transmittance or reflectance of the structure to various subsets of incident light is measured. At adjacent angular orientations of the objective axis with respect to the sample normal, light incident at some angles are added to the measurement and others dropped from the previous measurement. By measuring the response at incremental steps across the entire half-plane in front of the sample, a large volume of information can be obtained about the transmission characteristics of the test structure.

With careful selection of $\Delta\theta_S$, sufficient equations can be added to the system to solve for the single-angle plane-wave transmittances or reflectances. For transmission measurements, the number of measurements M is given by

$$M = 2\frac{\theta_{S,max}}{\Delta\theta_s} + 1, \tag{5.9}$$

while the number of unknown single-angle plane-wave transmittances is given by

$$N = \frac{\theta_{S,max} + \theta_{ob,max}}{\Delta\theta_k} + 1. \tag{5.10}$$

Table 5.2 lists the number of composite transmittances (M) and the number of single-angle plane-wave transmittances (N) computed with Eqs.(5.9)and (5.10) for typical values of the angular measurement increment and the separation between single-angle plane-wave transmittances. The incremental measurement approach can be applied to both transmittance and reflectance measurements, although the problem structure changes for each.

5.6 Transmission and Reflection Problem Formulation

For both transmittance and reflectance measurements, the incremental-step measurement scheme and the weighted incident beam coefficients are formulated as algebraic matrix equations. The resulting sets of equations are manipulated to compute the single-angle plane-wave transmittances or reflectances of the structures. The position of the detector and the method of collecting the transmitted or reflected light results in different formulations for the transmission and reflection problems.

5.6.1 Transmission Problem Formulation

To measure the transmittance of fabricated structures, incident light is focused onto fabricated samples and the transmitted power is measured. The matrix formulation of this method [84] can be interpreted as a source mixing problem where individual weighted plane waves incident over a range of angles are selected and mixed by some operator which, in this case, is the Schwarzchild reflecting objective. Incident angles outside of the collected angular range are effectively weighted with zero-valued coefficients while those incident angles within the objective's angular range are weighted by a measured non-zero coefficient value related to the incident light intensity and the optical focusing characteristics of the objective. For each objective axis angular orientation θ_s, light is incident over the range of angles from $\theta_s + \theta_{ob,min}$ to $\theta_s + \theta_{ob,max}$ and from $\theta_s - \theta_{ob,min}$ to $\theta_s - \theta_{ob,max}$. As θ_S is rotated along an arc located in the half-plane in front of the sample, the included angles shift. If the objective is rotated to sufficient limits, all possible incident angles in the half-plane in front of the sample are included within at least one measurement. If θ_s is rotated in small increments across this plane, composite measurements contain overlapping information about the device transmittance. Determining the individual plane-wave transmittance then becomes a deconvolution problem.

In matrix notation, transmittance measurements are represented by

$$[T] = [A_T][t], \tag{5.11}$$

where $[T]$ is a matrix containing the composite transmittances at each objective axis angular orientation, $[A_T]$ is the coefficient matrix containing the sector weighting coefficients a_i that

weight individual plane waves for the transmission case, and $[t]$ is a matrix containing the single-angle plane-wave transmittances of the structure.

In the measurement scheme, the objective axis orientation is constant with respect to the beam and the objective axis angle with respect to the surface normal, θ_S, is varied by rotating the sample at the focal point of the objective; this is equivalent to rotating the objective axis relative to the sample (as was described in the previous sections of the chapter). Since the objective position is constant relative to the beam, each line of the weighting coefficient matrix will be a shifted version of all other lines. As the sample is rotated, different plane waves fall within each sector of the focusing beam.

For illustrative purposes, the matrices for a set of measurements are constructed using a Schwarzchild objective with $\theta_{ob,min} = 10^\circ$ and $\theta_{ob,max} = 30^\circ$. Additionally, a large angular spacing of 10° is used for both the objective axis position θ_S, and the single plane wave angles j. A maximum objective axis angle of $\pm 30^\circ$ is also used. When the objective axis is at 30°, the maximum plane wave angle selected by the objective is 60°. With these conventions, the measured composite transmittances, T_{θ_S}, in terms of the single-angle plane-wave transmittances, t_j, are given by

$$\begin{bmatrix} T_{30} \\ T_{20} \\ T_{10} \\ T_0 \\ T_{-10} \\ T_{-20} \\ T_{-30} \end{bmatrix} = \begin{bmatrix} a_1 & a_2 & a_3 & 0 & a_4 & a_5 & a_6 & 0 & 0 & 0 & 0 & 0 & 0 \\ 0 & a_1 & a_2 & a_3 & 0 & a_4 & a_5 & a_6 & 0 & 0 & 0 & 0 & 0 \\ 0 & 0 & a_1 & a_2 & a_3 & 0 & a_4 & a_5 & a_6 & 0 & 0 & 0 & 0 \\ 0 & 0 & 0 & a_1 & a_2 & a_3 & 0 & a_4 & a_5 & a_6 & 0 & 0 & 0 \\ 0 & 0 & 0 & 0 & a_1 & a_2 & a_3 & 0 & a_4 & a_5 & a_6 & 0 & 0 \\ 0 & 0 & 0 & 0 & 0 & a_1 & a_2 & a_3 & 0 & a_4 & a_5 & a_6 & 0 \\ 0 & 0 & 0 & 0 & 0 & 0 & a_1 & a_2 & a_3 & 0 & a_4 & a_5 & a_6 \end{bmatrix} \begin{bmatrix} t_{60} \\ t_{50} \\ t_{40} \\ t_{30} \\ t_{20} \\ t_{10} \\ t_0 \\ t_{-10} \\ t_{-20} \\ t_{-30} \\ t_{-40} \\ t_{-50} \\ t_{-60} \end{bmatrix}. \quad (5.12)$$

Figure 5.7 shows the objective axis at a position relative to the sample normal of $\theta_S = -30^\circ$.

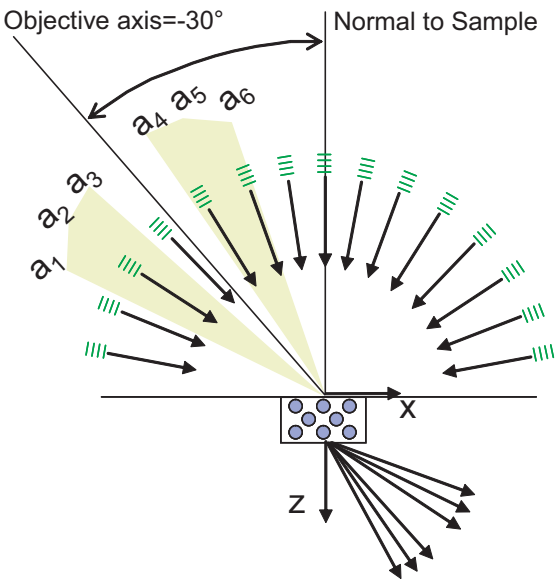

Figure 5.7: With the objective oriented at and angular orientation of $-30°$, plane waves with the θ_{ob} ranges of the objective are selected and weighted for the measurement.

This corresponds to the last row of the matrix in Eq. (5.12). At this axis position, incident plane waves in the angular range from $0°$ to $-20°$ and $-40°$ to $-60°$ are selected and weighted by the objective.

For a symmetric structure $t_{-j} = t_j$, the single-angle transmittance matrix can be compacted. Rewriting the matrix problem yields

$$\begin{bmatrix} T_{30} \\ T_{20} \\ T_{10} \\ T_0 \\ T_{-10} \\ T_{-20} \\ T_{-30} \end{bmatrix} = \begin{bmatrix} a_1 & a_2 & a_3 & 0 & a_4 & a_5 & a_6 \\ 0 & a_1 & a_2 & a_3 & 0 & a_4+a_6 & a_5 \\ 0 & 0 & a_1 & a_2 & a_3+a_6 & a_5 & a_4 \\ 0 & 0 & 0 & a_1+a_6 & a_2+a_5 & a_3+a_4 & 0 \\ 0 & 0 & a_6 & a_5 & a_1+a_4 & a_2 & a_3 \\ 0 & a_6 & a_5 & a_4 & 0 & a_1+a_3 & a_2 \\ a_6 & a_5 & a_4 & 0 & a_3 & a_2 & a_1 \end{bmatrix} \begin{bmatrix} t_{60} \\ t_{50} \\ t_{40} \\ t_{30} \\ t_{20} \\ t_{10} \\ t_0 \end{bmatrix}. \tag{5.13}$$

For this problem, the T_{θ_S}'s are measured with the apparatus and the weighting matrix is constructed from the measured beam profile and calculated weights. The t_j's are the unknown single-angle plane-wave transmittances. In a noise-free environment, the single-angle plane-wave transmittances t_j are computed by inverting the coefficient matrix and multiplying through by $[T]$. With added measurement noise and discretization error, the

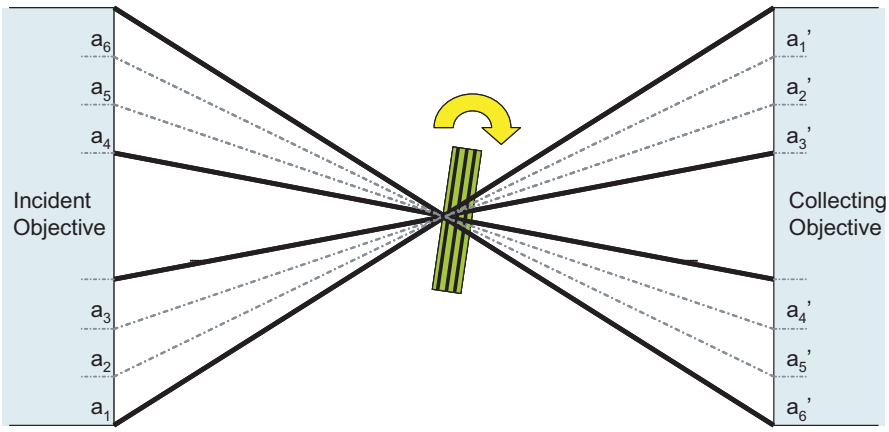

Figure 5.8: The addition of a collector objective in the transmission problem formulation requires an additional coefficient to be assigned to each ray. The second coefficient accounts for the imperfect collection of light by the collector objective. With the objective orientation shown above, for all positions of the sample, the two objectives align so that the incident light is always within the collection range of the collector. The additional coefficients a'_n are included in the matrix equation.

problem solution is more complicated. An approach for solving for the single-angle plane-wave transmittances in the case of non-negligible noise is discussed in the next section.

The above formulation is correct for direct transmittance measurements where light is detected immediately after being transmitted through the sample. In some experimental apparatus, a second objective is used as a collecting objective to collect the light.

The spatial arrangement of the two-objective measurement apparatus is shown in Fig. 5.8. Each incident ray passes through the sample and is collected by the collector objective. As the sample rotates in the beam, each incident angle is within the collection range of the collecting objective. In the matrix problem, this manifests itself as a second coefficient that must be included to account for the imperfect collection of light by the collecting objective. For the transmission problem when a collecting objective is used, the updated system matrix equivalent to Eq. (5.12) is shown in Eq. (5.14). The added coefficient follows through the problem formulation as the matrix is reduced by symmetry.

$$\begin{bmatrix} T_{30} \\ T_{20} \\ T_{10} \\ T_{0} \\ T_{-10} \\ T_{-20} \\ T_{-30} \end{bmatrix} = \begin{bmatrix} a_1a'_1 & a_2a'_2 & a_3a'_3 & 0 & a_4a'_4 & a_5a'_5 & a_6a'_6 & 0 & 0 & 0 & 0 & 0 & 0 \\ 0 & a_1a'_1 & a_2a'_2 & a_3a'_3 & 0 & a_4a'_4 & a_5a'_5 & a_6a'_6 & 0 & 0 & 0 & 0 & 0 \\ 0 & 0 & a_1a'_1 & a_2a'_2 & a_3a'_3 & 0 & a_4a'_4 & a_5a'_5 & a_6a'_6 & 0 & 0 & 0 & 0 \\ 0 & 0 & 0 & a_1a'_1 & a_2a'_2 & a_3a'_3 & 0 & a_4a'_4 & a_5a'_5 & a_6a'_6 & 0 & 0 & 0 \\ 0 & 0 & 0 & 0 & a_1a'_1 & a_2a'_2 & a_3a'_3 & 0 & a_4a'_4 & a_5a'_5 & a_6a'_6 & 0 & 0 \\ 0 & 0 & 0 & 0 & 0 & a_1a'_1 & a_2a'_2 & a_3a'_3 & 0 & a_4a'_4 & a_5a'_5 & a_6a'_6 & 0 \\ 0 & 0 & 0 & 0 & 0 & 0 & a_1a'_1 & a_2a'_2 & a_3a'_3 & 0 & a_4a'_4 & a_5a'_5 & a_6a'_6 \end{bmatrix} \begin{bmatrix} t_{60} \\ t_{50} \\ t_{40} \\ t_{30} \\ t_{20} \\ t_{10} \\ t_{0} \\ t_{-10} \\ t_{-20} \\ t_{-30} \\ t_{-40} \\ t_{-50} \\ t_{-60} \end{bmatrix} \tag{5.14}$$

The added coefficients differ from the focusing objective coefficients. The focusing objective coefficients account for both the nonuniform intensity of the incident beam and the imperfect focusing performance of the objective. The second objective coefficients, the collector objective coefficients, only need to account for the imperfect collection of light by the objective.

The collector coefficients are constant for each objective that is used as a collector. The coefficients must be measured along the plane that is used to collect light. This plane's orientation is determined by the objective slit orientation in the experimental apparatus. With the objective mounted in the experimental apparatus, the plane of the objective corresponding to the objective slit plane must be identified and noted relative to the collecting objective. Once this plane is identified, the collecting objective coefficient can be measured in a separate apparatus.

Figure 5.9 shows the method used to compute the collector coefficients for each objective. The incident beam profile is measured at a plane before the objective and at a plane in the focusing beam. The objective specification for the central obscuration O_c and the small mirror radius r_{mirror} can be used to determine the width of the central obscuration in the incident beam profile. The central obscuration specification is given as a percent of a full-field uniform beam that is reflected back through the central aperture. The radius of the central obscuration, r_{co}, equal to half of the central obscuration width in the incident beam profile, can be computed by

$$r_{co} = \sqrt{O_c r_{mirror}^2}. \tag{5.15}$$

With the central obscuration region of the beam intensity profile removed from the power profile, the coefficients for the incident beam can be computed by determining the area under the incident beam profile for each sector and dividing by the sum of the area under all sectors in the incident beam. The sum does not include the sector where light reflects out of the system due to the central obscuration. The coefficients in the focusing beam can be computed in the same manner as described in section 5.4 when discussing the computation of the weighting coefficients a_i. If the objective perfectly focuses light, the coefficients measured in the focusing beam will be equal to the coefficients computed in the incident

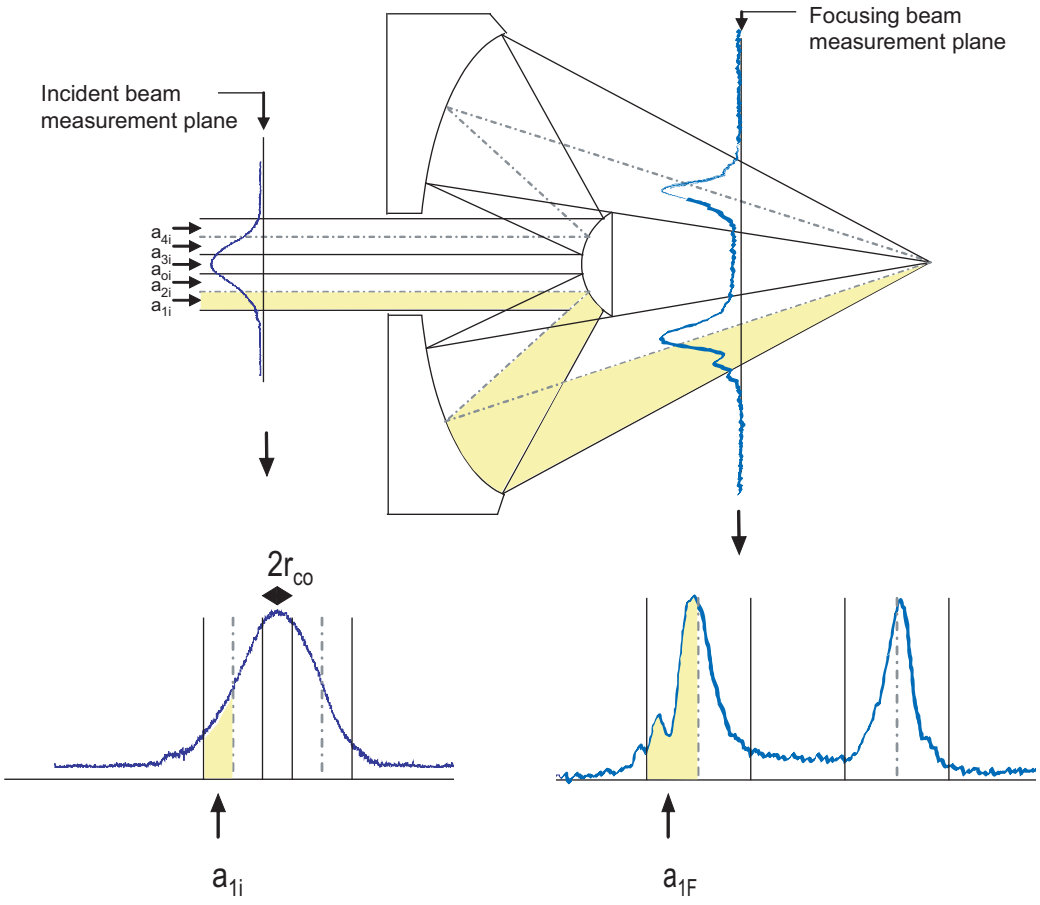

Figure 5.9: The coefficients for the collector objective are measured by comparing coefficients computed before the objective focuses the beam with the coefficients of the focused beam. If the objective perfectly focuses the light, the coefficients will remain constant. In the diagram, the incident beam is shown divided into 5 sectors. The center sector corresponds to the light that reflects from the small mirror out of the system through the aperture.

beam.

Once the coefficients are computed for the incident beam and for the focusing beam, the collecting objective coefficients can be computed by comparing the incident beam coefficients with the focusing beam coefficients. For each sector, the collecting objective coefficient is determined by dividing the focusing beam coefficient by the incident beam coefficient and normalizing with respect to the quotients for all sectors.

With the objectives oriented as shown in Fig. 5.8, for all positions of the sample in a transmittance measurement, the two objectives align so that all incident light is always within the collection range of the collector. The additional coefficients a'_n can be inserted into the matrix equation.

5.6.2 Reflection Problem Formulation

Although transmittance measurements that accurately measure actual power transmitted through a structure are preferred, in cases where source power is low or where the structure does not transmit sufficient detectable power, reflectance measurements that measure reflected power may need to suffice. For reflection-based characterization, the problem formulation changes to account for the reflection of light from the surface as the test device is rotated with respect to the objective axis. Additionally, the focusing objective also acts as the collecting objective.

In matrix notation, reflectance measurements are represented by

$$[R] = [A_R][r], \tag{5.16}$$

where $[R]$ is a matrix containing the composite reflectances at each objective axis angular orientation, $[A_R]$ is the coefficient matrix containing the sector weighting coefficients a_i that weight individual plane waves for the reflection case, and $[r]$ is a matrix containing the single-angle plane-wave reflectances of the structure. The formulation of the weighting coefficient matrix for the reflection problem differs from the transmission coefficient matrix formulation. This is the result of the change in the optical path.

The light is focused on the sample by the objective and reflects from the sample back through the objective to the detector. Reflected light is only collected over a limited range

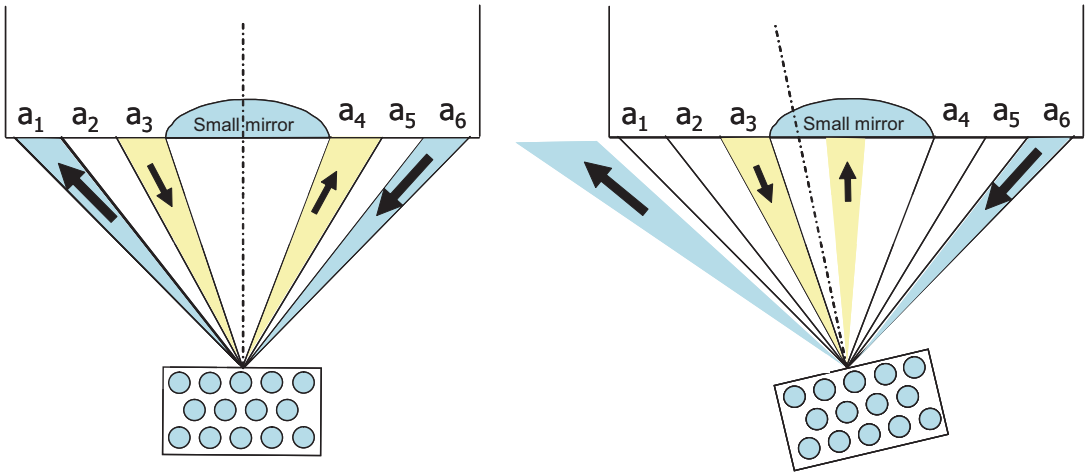

Figure 5.10: In the left diagram, $\theta_S = 0$ so all incident light is in the collection range of the objective. The light passes from the objective onto the sample and is reflected back through the objective on the other side of the small objective mirror. As the sample rotates, some light reflected from the sample escapes from the objective and is not be measured while other light reflects from the sample and is blocked by the small mirror.

of angles. Figure 5.10 shows several optical paths for light for a reflection measurement at normal incidence, $\theta_S = 0$, and for a second case where the sample has been rotated with respect to the objective. In the normal incidence case, light in one sector reflects from the surface and returns through a second sector on the other side of the small mirror. In the normal incidence situation, all incident light is collected. In the second case, where $\theta_s \neq 0$, some light reflects from the surface and escapes from the system and some light will reflect from the surface and be blocked by the small mirror. The maximum rotation angle for the sample in reflection measurements is $\theta_S = \theta_{ob,max}$. At objective axis positions greater than this angle, all incident light is reflected at angles outside of the angular collection range of the objective.

To illustrate this problem, the coefficients for the reflection formulation will first be formed as two separate matrices, one for the focusing beam and one for the collecting objective, and then combined using element-by-element multiplication. For the illustration, the objective values are $\theta_{ob,min} = 10°$, $\theta_{ob,max} = 30°$, $\Delta\theta_S = 10°$ and θ_S ranges from $-\theta_{ob,max}$ to $+\theta_{ob.max}$. The focusing objective coefficient matrix accounts for beam intensity irregularities and the imperfect focusing of the light. The collecting objective coefficient matrix accounts for the imperfect collection of light. The focusing and collecting objective

coefficients are measured with the same procedures as discussed for transmittance measurements.

The first matrix is the focusing objective matrix and represents the intensity of light focused by the Schwarzchild objective. This coefficient matrix is identical to the coefficient matrix formed for the transmission problem. The coefficients in the matrix shift at each measurement and coefficients will be constant along the diagonals of the matrix. This focusing objective coefficient matrix is

$$[A_{focusing}] = \begin{bmatrix} a_1 & a_2 & a_3 & 0 & a_4 & a_5 & a_6 & 0 & 0 & 0 & 0 & 0 & 0 \\ 0 & a_1 & a_2 & a_3 & 0 & a_4 & a_5 & a_6 & 0 & 0 & 0 & 0 & 0 \\ 0 & 0 & a_1 & a_2 & a_3 & 0 & a_4 & a_5 & a_6 & 0 & 0 & 0 & 0 \\ 0 & 0 & 0 & a_1 & a_2 & a_3 & 0 & a_4 & a_5 & a_6 & 0 & 0 & 0 \\ 0 & 0 & 0 & 0 & a_1 & a_2 & a_3 & 0 & a_4 & a_5 & a_6 & 0 & 0 \\ 0 & 0 & 0 & 0 & 0 & a_1 & a_2 & a_3 & 0 & a_4 & a_5 & a_6 & 0 \\ 0 & 0 & 0 & 0 & 0 & 0 & a_1 & a_2 & a_3 & 0 & a_4 & a_5 & a_6 \end{bmatrix}. \tag{5.17}$$

The collector coefficient matrix is constructed in a similar manner. The coefficient for each sector corresponds to the plane wave that is collected by that sector. The coefficients still shift in each row; however, the coefficients are constant along the anti-diagonal of the collecting objective matrix. The collecting objective coefficient matrix is

$$[A_{collector}] = \begin{bmatrix} 0 & 0 & 0 & 0 & 0 & 0 & a'_1 & a'_2 & a'_3 & 0 & a'_4 & a'_5 & a'_6 \\ 0 & 0 & 0 & 0 & 0 & a'_1 & a'_2 & a'_3 & 0 & a'_4 & a'_5 & a'_6 & 0 \\ 0 & 0 & 0 & 0 & a'_1 & a'_2 & a'_3 & 0 & a'_4 & a'_5 & a'_6 & 0 & 0 \\ 0 & 0 & 0 & a'_1 & a'_2 & a'_3 & 0 & a'_4 & a'_5 & a'_6 & 0 & 0 & 0 \\ 0 & 0 & a'_1 & a'_2 & a'_3 & 0 & a'_4 & a'_5 & a'_6 & 0 & 0 & 0 & 0 \\ 0 & a'_1 & a'_2 & a'_3 & 0 & a'_4 & a'_5 & a'_6 & 0 & 0 & 0 & 0 & 0 \\ a'_1 & a'_2 & a'_3 & 0 & a'_4 & a'_5 & a'_6 & 0 & 0 & 0 & 0 & 0 & 0 \end{bmatrix}. \tag{5.18}$$

The focusing and collector coefficient matrices are multiplied together element-by-element to produce the total coefficient matrix for reflectance calculations. Since the coefficients appear along opposite diagonals, many incident rays will reflect along a path that is not in the collection range of the objective. The combined coefficient matrix is

$$[A] = \begin{bmatrix} 0 & 0 & 0 & 0 & 0 & 0 & a_6a'_1 & 0 & 0 & 0 & 0 & 0 & 0 \\ 0 & 0 & 0 & 0 & 0 & a_4a'_1 & a_5a'_2 & a_6a'_3 & 0 & 0 & 0 & 0 & 0 \\ 0 & 0 & 0 & 0 & a_3a'_1 & 0 & a_4a'_3 & 0 & a_6a'_4 & 0 & 0 & 0 & 0 \\ 0 & 0 & 0 & a_1a'_1 & a_2a'_2 & a_3a'_3 & 0 & a_4a'_4 & a_5a'_5 & a_6a'_6 & 0 & 0 & 0 \\ 0 & 0 & 0 & 0 & a_1a'_3 & 0 & a_3a'_4 & 0 & a_4a'_6 & 0 & 0 & 0 & 0 \\ 0 & 0 & 0 & 0 & 0 & a_1a'_4 & a_2a'_5 & a_3a'_6 & 0 & 0 & 0 & 0 & 0 \\ 0 & 0 & 0 & 0 & 0 & 0 & a'_6 & 0 & 0 & 0 & 0 & 0 & 0 \end{bmatrix}. \tag{5.19}$$

The columns of the coefficient matrix that contain all zero-valued elements are the result of incident light escaping from the optical system upon reflection from the sample or reflecting into the back of the small mirror. These columns can be eliminated and the reflection problem formed as follows:

$$\begin{bmatrix} R_{30} \\ R_{20} \\ R_{10} \\ R_0 \\ R_{-10} \\ R_{-20} \\ R_{-30} \end{bmatrix} = \begin{bmatrix} 0 & 0 & 0 & a_6a'_1 & 0 & 0 & 0 \\ 0 & 0 & a_4a'_1 & a_5a'_2 & a_6a'_3 & 0 & 0 \\ 0 & a_3a'_1 & 0 & a_4a'_3 & 0 & a_6a'_4 & 0 \\ a_1a'_1 & a_2a'_2 & a_3a'_3 & 0 & a_4a'_4 & a_5a'_5 & a_6a'_6 \\ 0 & a_1a'_3 & 0 & a_3a'_4 & 0 & a_4a'_6 & 0 \\ 0 & 0 & a_1a'_4 & a_2a'_5 & a_3a'_6 & 0 & 0 \\ 0 & 0 & 0 & a'_6 & 0 & 0 & 0 \end{bmatrix} \begin{bmatrix} r_{30} \\ r_{20} \\ r_{10} \\ r_0 \\ r_{-10} \\ r_{-20} \\ r_{-30} \end{bmatrix}. \tag{5.20}$$

The pattern formed by the non-zero coefficients in Eq. (5.20) is shown by the diamonds in Fig. 5.11. This form, with four regions containing non-zero values, is apparent in all cases if measurements can be recorded for reflectances up to the objective axis angle maximum value of $\theta_S = \theta_{ob,max}$. The four diamond shaped regions show the non-zero coefficient values. If measurements are restricted to the center of the matrix and do not include the upper or lower diamond regions, plane-wave reflectances at normal and near normal incidence may not be possible to calculate. To be able to compute plane wave reflectances from $\theta_{Smax} + \theta_{ob,max}$ to normal incidence, the minimum rotation range is $2\theta_{ob,min}$. This ensures that incident angles less than $\theta_{ob,min}$ have been reflected at sufficient angles to clear the center mirror of the objective and be collected on the opposite side of the small mirror.

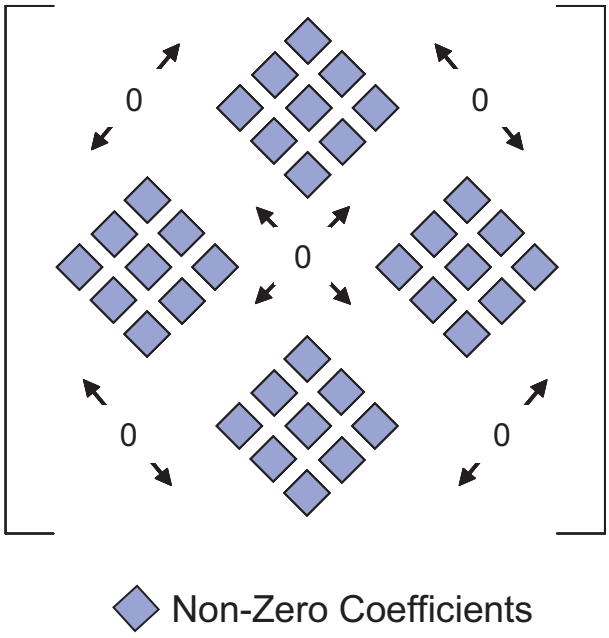

Figure 5.11: The reflection coefficient matrix contains four regions with non-zero coefficients. The four diamond-shaped sectors will be present if there are no restrictions on the rotation limits of the problem and objective axis θ_S is rotated to $\pm\theta_{ob,max}$. If the rotation range is limited to less than $\theta_{ob,max}$, all four full regions may not be present. If the rotation range is less than $\theta_{ob,min}$ the upper and lower diamond shaped regions will not be included and the data containing information on the reflectance of the structure to near-normal incident light will not be present in the measurements.

If sample symmetry is present, the matrix dimension is further reduced since the single-angle plane-wave reflectance $r_{-\theta} = r_{\theta}$,

$$\begin{bmatrix} R_{30} \\ R_{20} \\ R_{10} \\ R_{0} \\ R_{-10} \\ R_{-20} \\ R_{-30} \end{bmatrix} = \begin{bmatrix} 0 & 0 & 0 & a_6 a_1' \\ 0 & 0 & a_4 a_1' + a_6 a_3' & a_5 a_2' \\ 0 & a_3 a_1' + a_6 a_4' & 0 & a_4 a_3' \\ a_1 a_1' + a_6 a_6' & a_2 a_2 +' a_5 a_5' & a_3 a_3' + a_4 a_4' & 0 \\ 0 & a_1 a_3' + a_4 a_6' & 0 & a_3 a_4' \\ 0 & 0 & a_1 a_4' + a_3 a_6' & a_2 a_5' \\ 0 & 0 & 0 & a_1 a_6' \end{bmatrix} \begin{bmatrix} r_{30} \\ r_{20} \\ r_{10} \\ r_{0} \\ r_{-10} \\ r_{-20} \\ r_{-30} \end{bmatrix}. \tag{5.21}$$

For this problem, the R_{θ_S}'s are measured with the apparatus and the weighting matrix is constructed from the measured beam profile and calculated coefficients. The r_j's are the unknown single-angle plane-wave reflectances. In a noise-free environment, the single-angle plane-wave reflectances are computed by inverting the coefficient matrix and solving for r_j. With added noise and discretization error, the problem is more complicated and is discussed in the next section.

5.7 Single-Angle Plane-Wave Transmittance and Reflectance Calculations

If a sufficient number measurements are made and appropriate values for system variables are selected, the sets of linear equations represented by Eq.(5.13), Eq.(5.14) (when reduced by symmetry), and Eq.(5.21) are fully specified or overdetermined sets of equations. The system is fully specified if the number of measurements is equal to the number of plane-wave transmittances or reflectances and the system is overdetermined if more measurements are recorded than the number of plane-wave transmittances or reflectances. The number of measurements used to solve the problem can be adjusted by changing the angular spacing between objective axis measurements as the objective axis is incremented through its rotation angular range. The solution to a fully specified problem can often be solved using matrix inversion. For an overdetermined set of equations, a least-squares solution can often be calculated that minimizes the error in the solution for all equations using the Moore-Penrose pseudoinverse technique [85]. These methods are successful in cases when

the coefficient matrix is well-conditioned.

However, the coefficient matrix in the single-angle plane-wave computation discussed in this thesis is ill-conditioned. Even though more measurements (equations) can be recorded than the number of desired single-angle plane-wave transmittances or reflectances (unknown values), the ill-conditioned system is effectively underdetermined due to redundant information in the measurements. Inversion of the poorly conditioned coefficient matrix produces an unstable solution where small changes in the measurements can result in large changes in the computed solution. Errors caused by measurement noise or rounding errors in the discretization of data are amplified and dominate the solution. To compute a meaningful solution for the single-angle plane-wave transmittance or reflectance, the problem must be regularized. Regularization methods, where additional information is included to assist in solving the problem, can aid in obtaining stable solutions. Hansen describes some typical regularization methods including direct regularization, truncated regularization, iterative solutions, and statistical methods in [86]. Appropriate regularization methods for each problem depend on the class of ill-conditioning.

The amplification of noise in an ill-conditioned problem and methods of regularization can be understood by examining matrix inversion in terms of the singular value decomposition (SVD) of the coefficient matrix. The singular values are used to classify the type of ill-conditioning and the SVD-produced solution provides a test, the discrete Picard condition test, to determine whether a stabilized solution exists. Since the ill-conditioned problem is effectively underdetermined, regularization requires the addition of more information to solve the problem. The additional information and the filtered inverted solution are both used to obtain meaningful solutions for the single-angle plane-wave transmittances and reflectances.

5.7.1 Problem Regularization and Stabilization

For both the transmission and reflection problem formulations, the matrix systems of equations that must be solved were given in Eq. (5.11) and Eq. (5.16). In these equations, the coefficient matrices were given as $[A_T]$ for the transmission problem and $[A_R]$ for the

reflection problem. Although these matrices are different, both are ill-conditioned. The regularization and single-angle plane-wave computation for transmittance and reflectance measurements are similar and, in this thesis, are addressed in terms of the transmission case with the coefficient matrix represented by $[A]$.

The noise-free solutions to well-conditioned systems of equations are simple inverse problems. If the systems contain an equal number of measurements and unknowns values then $[A]$ is a square matrix with $[A] \in \Re^{n \times n}$. The problem, and ideal solution $[t]$, can be written

$$[T] = [A][t] \Rightarrow [t] = [A]^{-1}[T]. \tag{5.22}$$

In the case where $[A]$ is overspecified and the inverse of $[A]$ does not exist ($A \in \Re^{m \times n}$ where $m > n$) a similar problem is substituted for the original problem and solved by the least squares method [85]. The noise-free overspecified problem and its ideal solution can be written

$$[A^T T] = [A^T A][t] \Rightarrow [t] = [A^T A]^{-1}[A]^T[T], \tag{5.23}$$

Noise complicates the problem by introducing a residual amount of error into the equation. With added noise from the measurement, experimental discretization of continuous problems, or numerical rounding errors, the problem becomes

$$[T + e_{noise}] = [A][t], \tag{5.24}$$

where e_{noise} represents the total or residual error. In attempting to solve the problem, the inversion of $[A]$ or $[A^T A]$ amplifies the noise and stabilization methods are required to obtain a meaningful solution.

To generalize the presentation of this material, a notation change is necessary to prevent confusion with the T designation used for both the composite transmittance matrix and the transpose of a matrix. Standard linear algebra variable designations are used, replacing the composite measured transmittance matrix $[T]$ with $[b]$ and the single-angle plane-wave transmittance matrix $[t]$ with $[x]$. With this change, the problem is represented by

$$[b + e_{noise}] = [A][x]. \tag{5.25}$$

In the problem with the added noise term, the residual $[A][x]-[b] \neq 0$, must be minimized. The least squares solution, $[x^*]$, can be determined by setting e_{noise} equal to zero and recovering the solutions that require inversion of $[A]$ or $[A^TA]$. Rewriting these solutions and designating the least-squares solution as $[x^*]$ yields

$$[x^*] = [A]^{-1}[b], \tag{5.26}$$

for the fully-specified case and

$$[x^*] = [A^TA]^{-1}[A]^T[b], \tag{5.27}$$

for the over-specified case.

For the single-angle plane-wave computation, the coefficient matrix is ill-conditioned. Inversion of the $[A]$ or $[A^TA]$ matrix amplifies the noise. This amplification of noise and a method to filter the noise and regularize the problem can be better understood by examining the $[A]$ matrix through its SVD.

5.7.1.1 Singular Value Decomposition

The SVD of a matrix provides insight into the instability of the inversion problem and the filtering scheme necessary to stabilize the problem; this is accomplished by examining the least-squares solution solved using the SVD of a coefficient matrix $[A] \in \Re^{m \times n}$. The SVD is a decomposition of the matrix into three matrices represented by

$$[A] = [U][\Sigma][V]^T, \tag{5.28}$$

where $[U] \in \Re^{m \times m}$ is a matrix where the columns of $[U]$ are the eigenvectors of $[AA^T]$ and can be represented by

$$[U] = [u_1 u_2 \ldots u_m]. \tag{5.29}$$

The matrix $[\Sigma] \in \Re^{m \times n}$, containing the singular values, σ_r, in decreasing order in the first r rows of the main diagonal of the matrix where r is the numerical rank of $[A]$ is given by

$$[\Sigma] = \begin{bmatrix} \sigma_1 & 0 & \dots & 0 \\ 0 & \sigma_2 & & \vdots \\ \vdots & & \ddots & 0 \\ 0 & \dots & 0 & \sigma_r \\ & -\mathbf{0}- & & \end{bmatrix}. \tag{5.30}$$

Also, $[V] \in \Re^{n \times n}$ is a matrix where the columns of $[V]$ are the eigenvectors of $[A^T A]$ given by

$$[V] = [v_1 v_2 \dots v_n]. \tag{5.31}$$

Substituting this decomposition in for $[A]$ and $[A]^T$ in equation Eq. (5.27) results in

$$[x^*] = [(U\Sigma V^T)^T (U\Sigma V^T)]^{-1} [(U\Sigma V^T)^T][b]. \tag{5.32}$$

With matrix algebra, this can be reduced to

$$[x^*] = [V][\underbrace{(\Sigma^T \Sigma)^{-1}][\Sigma^T}_{\Sigma_\dagger}][U^T][b]. \tag{5.33}$$

Returning the $[U]$ and $[V]$ matrices to vector notation and combining the elements of the $\Sigma_\dagger$ term results in

$$[x^*] = [v_1 v_2 \dots v_n] \begin{bmatrix} \frac{1}{\sigma_1} & 0 & \dots & 0 \\ 0 & \frac{1}{\sigma_2} & \dots & 0 \\ \vdots & & \ddots & \vdots \\ 0 & 0 & & \frac{1}{\sigma_n} \\ & -\mathbf{0}- & & \end{bmatrix} [u_1 u_2 \dots u_n]^T [b]. \tag{5.34}$$

Rewriting this expression as a sum yields

$$[x^*] = \sum_{i=1}^{n} \frac{u_i^T b}{\sigma_i} v_i. \tag{5.35}$$

Equation (5.35) provides insight into the instability of an ill-conditioned problem: an ill-conditioned problem is characterized by a large condition number where the condition number is the ratio of the smallest singular value to the largest the singular value, σ_1/σ_n.

Since the singular value term is in the denominator of the solution, the parts of the solution associated with the smallest singular values are amplified by the inversion. On the other hand, if the problem is well-posed, the singular values are all relatively large and inversion produces a usable solution.

Two classes of ill-conditioned problems exist and can be identified by observing the singular values of the coefficient matrix. Rank deficient problems, where columns and rows are linearly dependent, have a cluster of small singular values with a well determined gap between the small and large singular values. Solution methods for this type of ill-conditioned problem use the linearly independent information in the coefficient matrix $[A]$ to form a problem with a well-conditioned matrix. The second class of ill-conditioned problems, discrete ill-posed problems, are characterized with singular values that gradually decay to zero. Solution methods for this class of problem add additional information to the problem and filter the solution to minimize the parts of the solution associated with the small singular values of the coefficient matrix [86].

To classify the type of ill-conditioning present in the coefficient matrix for the single-angle plane-wave computation, the coefficient matrix $[A]$ was constructed for the transmittance problem using an objective and incident beam with objective and focused beam parameters $\theta_{ob,min} = 10°$, $\theta_{ob,max} = 25°$, $\theta_{S,min} = -30°$, $\theta_{S,max} = 30°$, $\Delta\theta_S = 5°$, and weighting coefficients $[a_1\ a_2\ a_3\ a_4\ a_5\ a_6] = [0.125\ 0.250\ 0.125\ 0.125\ 0.250\ 0.125]$. The singular values were computed and are plotted in Fig. 5.12. The singular values gradually decay, thereby classifying the single-angle plane-wave computation as an ill-posed problem. Many additional beam weighting coefficient sets and objective parameters were tested for both transmittance and reflectance coefficient matrices. In all cases, the singular values decay towards zero. With the class of ill-conditioning identified, methods to stabilize the problem were investigated.

5.7.1.2 Discrete Picard Condition

To stabilize an ill-posed problem, it is often possible to filter the solution using filter factors that reduce the parts of the solution associated with the small singular values. A filter

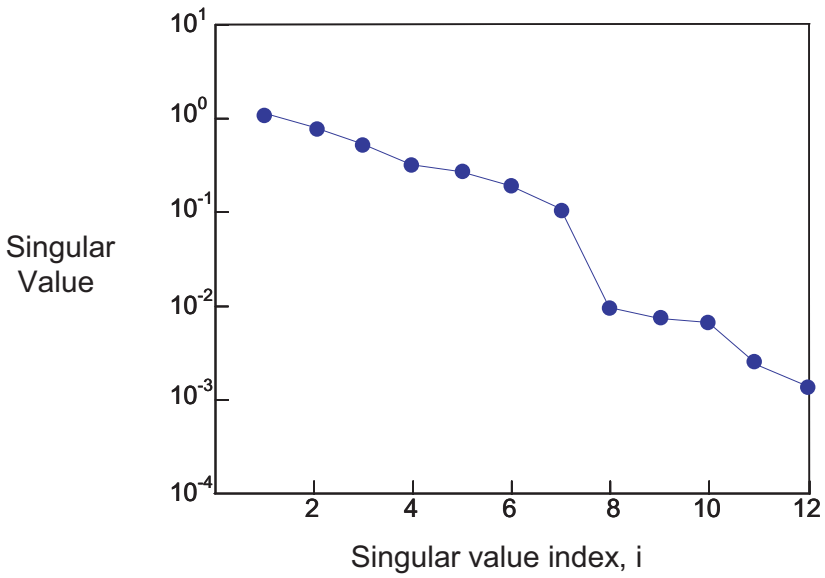

Figure 5.12: The class of ill-conditioning can be identified by examining the coefficient matrix singular values. Realistic beam weighting coefficients and objective parameters were used to construct a representative coefficient matrix. The singular values of the coefficient matrix are plotted showing a gradual decrease towards zero. This classifies the single-angle plane-wave computation as an ill-posed problem.

factor associated with each singular value can be incorporated into Eq. (5.35) to yield

$$[x^*_{reg}] = \sum_{i=1}^{n} f_i \frac{u_i^T b}{\sigma_i} v_i, \tag{5.36}$$

where f_i are the filter factors and $[x^*_{reg}]$ is the filtered solution. The discrete Picard condition [87] is a method to determine if filter factors exist that will stabilize the problem; in some ill-posed problems, filter factors capable of stabilizing the problem do not exist.

A Picard plot compares the rates of decay of the numerator and denominator of Eq. (5.35) graphically. As the singular values approach zero, the ratio of the numerator to the denominator approaches infinity unless the numerator coefficients approach zero as rapidly as the singular values. To meet the discrete Picard condition, in a noise-free problem, the numerator coefficients must decay as fast as the singular values. If this qualitative condition is met, it is likely that filter factors exist that will stabilize the solution.

To test if the single-angle plane-wave computation meets the Picard condition, the theoretical single-angle plane-wave normalized transmittances, matrix $[x]$, of a hypothetical structure were computed for plane waves over the range from $\theta_k = -55°$ to $\theta_k = 55°$ at 5°

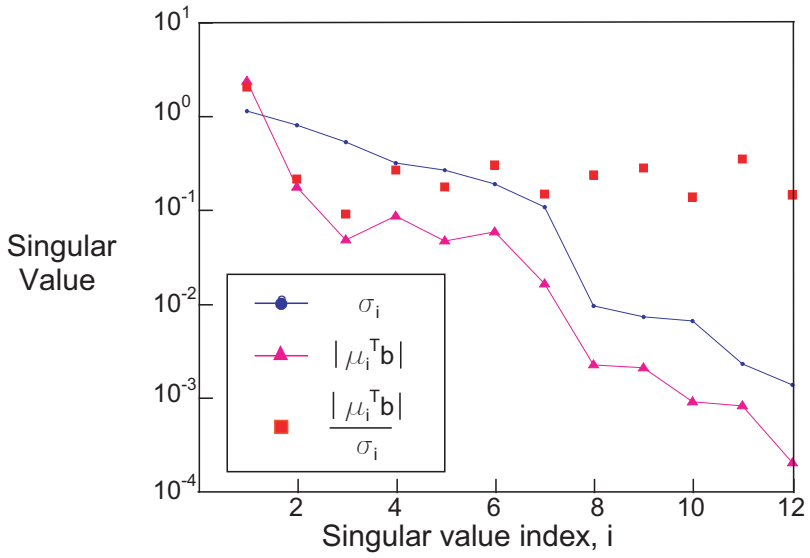

Figure 5.13: The Picard plot is used to determine if filter factors exist that will regularize a problem. The numerator of the noise-free problem solution must decay at least as fast as the singular values. In this case, the magnitude of the numerator, $|\mu_i^T b|$, decays as fast as the singular values, σ_i, so filter factors capable of stabilizing the problem exist.

increments using the MIP-SI program. The simulated structure consisted of 15 periods of alternating regions of silicon and air where $t_{Si} = 2.88\,\mu m$ and $t_{air} = 5.12\,\mu m$. The coefficient matrix, $[A]$, and the single-angle plane-wave matrix were multiplied to compute the ideal noise-free composite transmittances, matrix $[b]$, over the $\pm 30°$ range at increments of $5°$. Figure 5.13 shows the Picard plot for an ideal noise-free model of the transmission problem. The magnitude of the numerator coefficients, $|\mu_i^T b|$, the singular values (denominator), σ_i, and the quotient, $\frac{|\mu_i^T b|}{\sigma_i}$ are plotted for each singular value. Since the numerator coefficients decay as rapidly as the singular values, filter factors can be computed that stabilize the single-angle plane-wave computation. Simulations conducted on similar structures with various objective parameters and beam coefficients yielded similar Picard plots. In all cases, the Picard condition, the requirement that the magnitude of the numerator coefficients decay at least as fast as the singular values, was met.

5.7.1.3 Side Constraint Selection

Since the Picard condition is satisfied, the single-angle plane-wave computation can be solved with the appropriate selection of filter factors. Many regularization methods are

available to compute suitable filter factors to stabilize the problem. Hansen [86] provides a summary of several of these regularization methods and a discussion of the algorithms used to determine the filter factors. A standard method, and the method used in this thesis, is called Tikhonov regularization [88]. In Tikhonov regularization, filter factors are used to reduce the effects of the parts of the solution associated with the small singular values while balancing the solution with an added side constraint, $\Omega(x)$. The addition of a side constraint is necessary to account for the loss of information that results from the filtering. Without the additional information, the problem would be underdetermined.

Typical side constraints in this type of problem are based on a minimization of the norm of various derivatives of the solution. In this case, as the objective axis is rotated in small increments, the change in the solution between increments is also expected to be small. The side constraint used in this thesis is the minimization of the norm of the first derivative of the solution, $min \parallel \Omega(x) \parallel$. Minimization of the magnitude of the solution and minimization of the norm of the second derivative were also tested with the minimization of the first derivative norm producing the lowest solution errors.

5.7.1.4 Regularization Parameter Selection Via the L-Curve

The Tikhonov regularized solution is determined by finding a solution that balances the minimization of both the residual norm, $min \parallel [A][x] - [b] \parallel$, and the side constraint norm, $min \parallel \Omega(x) \parallel$. Since different solutions will minimize each individual function, the minimization is balanced using a regularization parameter, ξ. The regularized plane-wave solution $[x^*_\xi]$ is the solution that minimizes a weighted combination of the residual and side constraint norms,

$$[x^*_\xi] = min \parallel [A][x] - [b] \parallel^2 + \xi^2 \parallel [\Omega(x)] \parallel^2 . \tag{5.37}$$

Each value of ξ corresponds to a unique set of filter factors. In Tikhonov regularization, the filter factors and regularization parameter are related by the equation

$$f_i = \frac{\sigma_i^2}{\sigma_i^2 + \xi^2}. \tag{5.38}$$

In problems with significant amounts of measurement noise, the selection of ξ can be

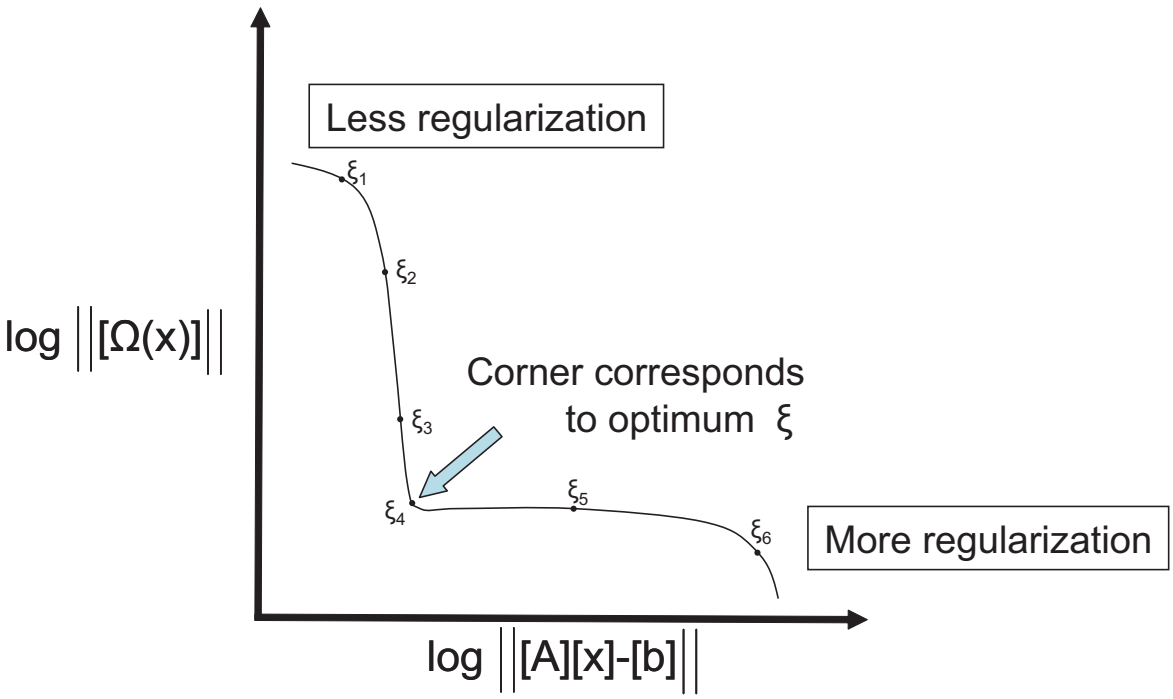

Figure 5.14: The regularization parameter ξ can be determined by computing the optimal value of ξ that balances the minimization of the residual norm and the minimization of the side constraint norm. The plot of the log of the residual norm versus the log of the side constraint norm has a characteristic L-shape with the optimal regularization parameter being the value that corresponds to the solution at the corner of the L-curve.

optimized by computing the solutions for all values of ξ and determining which value minimizes the function shown in Eq. (5.37). The L-curve [86] is a plot of the log of the side constraint norm versus the log of the residual norm for all values of ξ. Figure 5.14 shows a typical L-curve plot. The plot has a characteristic "L" shape and the point that minimizes Eq. (5.37) corresponds to the corner of the curve. Solutions where a relatively small regularization parameter is selected favor minimization of the residual norm and correspond to the solutions near the y-axis while solutions that favor minimization of the side constraint norm are near the x-axis. The arrow in Fig. 5.14 identifies the optimum value of the regularization parameter.

If the total measurement noise is very low, the regularization error caused by imposition of the side constraint will dominate the L-curve. In this case, the L-curve looses its characteristic shape and the selection of an optimal parameter is not assured. Similarly, in cases with extreme amounts of noise, the residual error dominates the L-curve and makes

the selection of an optimal regularization parameter difficult.

In this thesis, Hansen's algorithms [87] for the Tikhonov method are used to compute the optimum regularization parameter. The regularization parameter is then used as an input to a second algorithm that computes the regularized Tikhonov solution.

5.7.2 Regularization Simulations

For the single-angle plane-wave computation, the coefficient matrix has been identified as being ill-conditioned. The Picard plot (Fig. 5.13) verifies that suitable filter factors exist to stabilize the problem. A side constraint, minimization of the first derivative of the solution, is included to add additional information that will allow the computation of a useful solution. The Tikhonov regularization scheme is applied; the scheme balances the minimization of the residual norm and the side constraint norm to obtain a solution.

The Tikhonov regularization algorithms must be tested to verify that the method will regularize the present problem. The amount of measurement noise that can be tolerated by the algorithms must also be determined. For the test, the simulated composite noise-free transmittances used to verify that the problem satisfied the Picard condition are perturbed with a uniformly distributed, random variation and normalized to create noisy simulated composite transmittances that mimic actual measured data. To compute the simulated normalized transmittance, T_N, the coefficient matrix and the normalized noisy simulated transmittances are used as the inputs to select the regularization parameter. The Tikhonov regularized single-angle plane-wave transmittance solutions are computed and compared to the ideal normalized single-angle plane-wave transmittances.

The root mean square (RMS) error for each simulated (regularized) single-angle plane-wave transmittance solution, expressed as a decimal, quantifies the agreement between the simulated single-angle plane-wave transmittance solution and the normalized ideal single-angle plane-wave transmittance. The RMS error is computed using the equation

$$RMS\,error = \left(\frac{1}{N_w} \sum_{N_w} \mid x_{\xi}^{*} - x_{ideal} \mid \right)^{\frac{1}{2}}, \tag{5.39}$$

with N_w being the total number of discrete wavelengths in the computed spectra and x_{ideal} being the ideal plane-wave transmittance.

5.7.2.1 Noise Levels and Additional Filtering

For the simulations, uniformly distributed random variations of the ideal composite transmittance matrix are computed for added noise ranging from 0.01% to 20% of the ideal composite transmittance matrix values. In this thesis, the term *noise level* refers to the percent of random variation that exists in to the composite measurements before the regularized single-angle plane-wave solution is computed.

After processing, the computed single-angle plane-wave transmittances possessed some negative valued elements for some wavelengths. Since a negative-valued transmittance is not physically meaningful, the computed response at these wavelengths is set equal to zero. Additionally, the computed plane-wave transmittances are filtered to remove extreme positive outliers. A maximum element-to-element change of 0.4 on a normalized scale of 1.0 is allowed in the algorithm and any single computed solution for a single wavelength that deviates greater 0.4 between the preceding wavelength solution and the subsequent wavelength solution is set equal to the average of the preceding and subsequent wavelength solutions. The number of data points that require filtering varies depending on the noise level. At noise levels exceeding 10%, up to 15% of the computed solution data points are filtered. At noise levels from 3% to 10%, less than 5% of the data points are filtered. As the noise level decreased, below 3%, few data points were filtered.

5.7.2.2 Qualitative Single-Angle Plane-Wave Transmittance Solution Comparison

Figures 5.15 through 5.17 show the simulated (regularized) single-angle plane-wave transmittances and the ideal plane wave normalized transmittances at three different plane-wave angles for cases when the added noise level was 0.1%, 1%, and 5% and are compared to the ideal normalized transmittances.

At all three plane-wave angles, when the noise level was 0.1%, the regularization algorithm was the most successful at recovering the single-angle plane-wave transmittances showing almost all of the spectral features of the ideal transmittance. As expected, as the noise level increased, the recovered plane-wave solution quality decreased. At 1% and 5% noise levels, the general transmission structure showing bands of increased transmission and

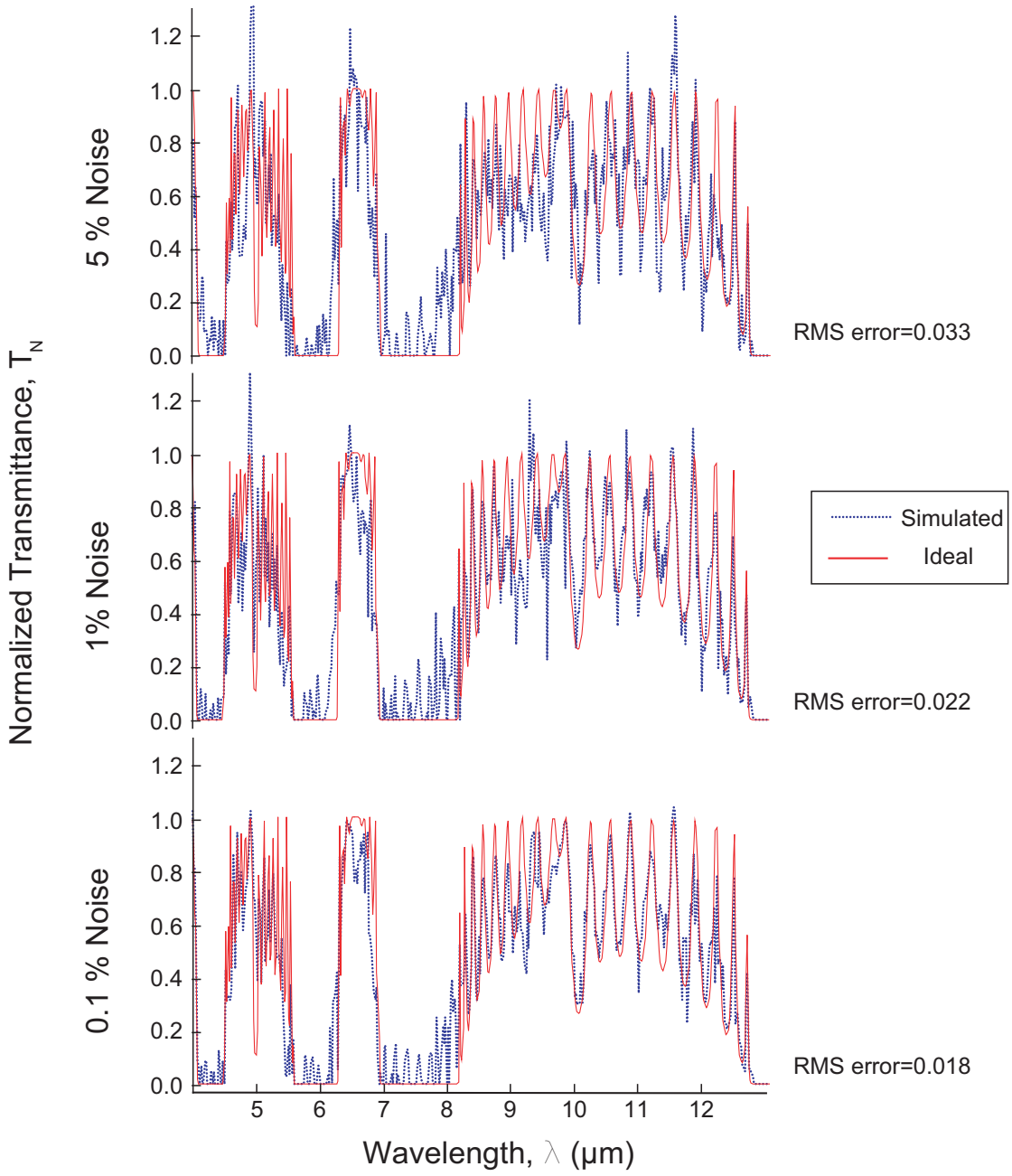

Figure 5.15: The single-angle plane-wave transmittances were computed with Tikhonov regularization for a $\theta_k = 10°$ plane wave with uniformly distributed random noise levels of 0.1%, 1%, and 5% and are compared to the ideal normalized transmittances.

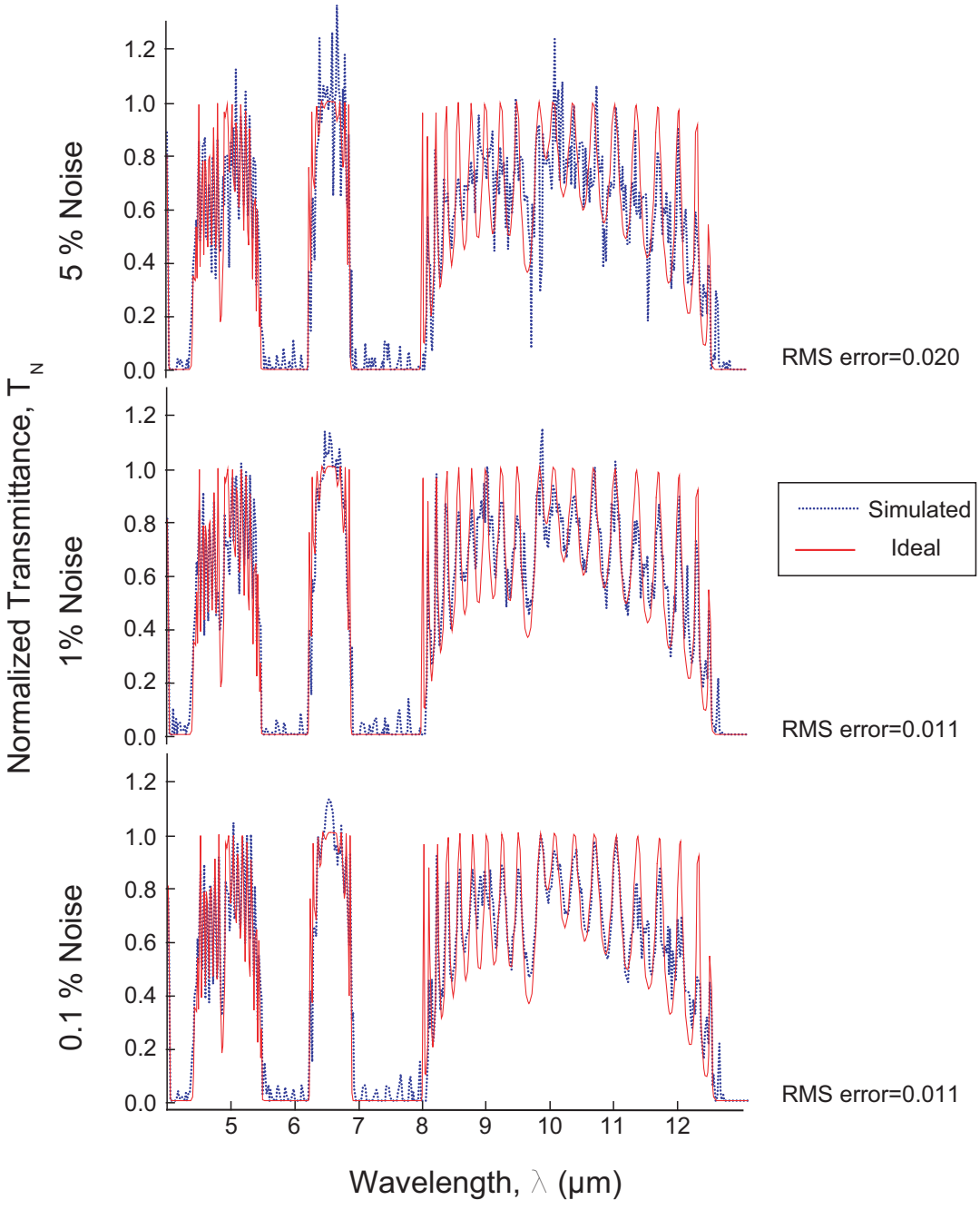

Figure 5.16: The single-angle plane-wave transmittances were computed with Tikhonov regularization for a $\theta_k = 20°$ plane wave with uniformly distributed random noise levels of 0.1%, 1%, and 5% and are compared to the ideal normalized transmittances.

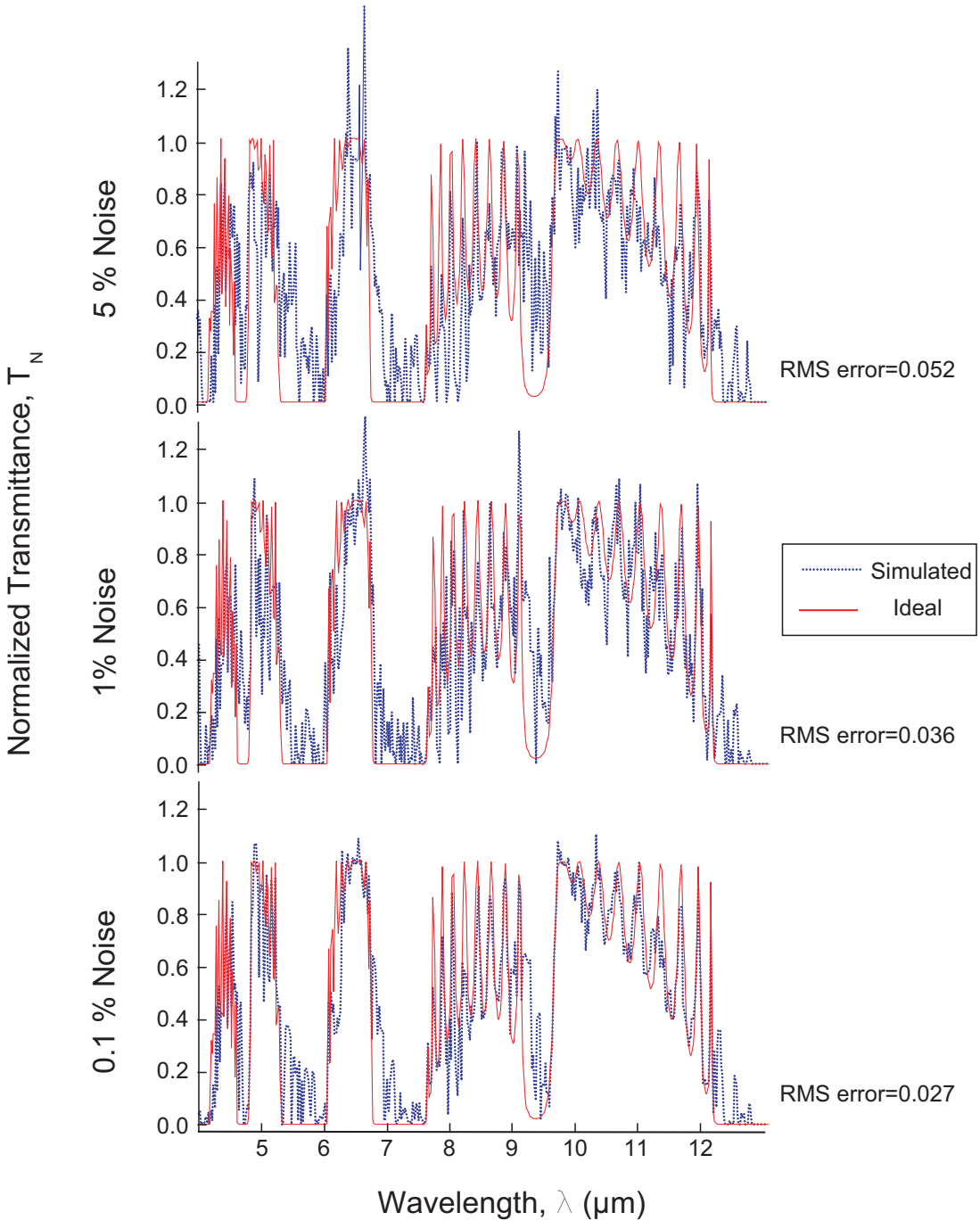

Figure 5.17: The single-angle plane-wave transmittances were computed with Tikhonov regularization for a $\theta_k = 30°$ plane wave with uniformly distributed random noise levels of 0.1%, 1%, and 5% and are compared to the ideal normalized transmittances.

regions with decreased transmission was recovered. Many of the interference peaks are still evident on these plots.

At significantly higher noise levels, the algorithm's success at recovering the single- angle plane-wave transmittances rapidly deteriorated. Figure 5.18 shows the computed $\theta_k = 10^\circ$ plane-wave transmittance and the ideal normalized transmittance for noise levels of 10%, 15%, and 20%. From these plots, it is apparent that as the noise level is increased over 10%, much of the transmission structure of the spectra is lost.

The recovery of the single-angle plane-wave transmittances shows large variation from angle to angle. The $\theta_k = 20^\circ$ plane-wave transmittance appears to be significantly better than the $\theta_k = 10^\circ$ plane-wave transmittance at all noise levels. The computed transmittance at angles where the transmission of the structure is decreased but does not drop to zero appears to have the most deviations from the ideal response. The reason for relatively large deviations from the ideal normalized transmittance for some plane-wave angles and significantly less deviation from ideal at other plane-wave angles remains unknown and is discussed further in Chapter 9.

5.7.2.3 Quantitative Single-Angle Plane-Wave Solution Comparison

Table 5.3 shows the RMS error between the ideal normalized transmittances and the simulated (regularized) plane-wave transmittances, for a large variation in the noise level percentage. The total error column in the table contains the sum of the RMS errors for all listed angles at each noise level. The RMS errors are used to compare the recovery of the single-angle plane-wave transmittances relative to the other angles and noise levels.

By comparing the computed plane-wave transmittances with the ideal normalized transmittance in Fig. 5.15 through Fig. 5.17, a maximum tolerable RMS error value for the single-angle plane-wave computations can be identified. Table 5.3 can then be used to identify the added noise level where the single-angle plane-wave solutions have RMS error values less than the identified maximum tolerable RMS error value. The selection of the maximum tolerable RMS error value is subjective and application dependent.

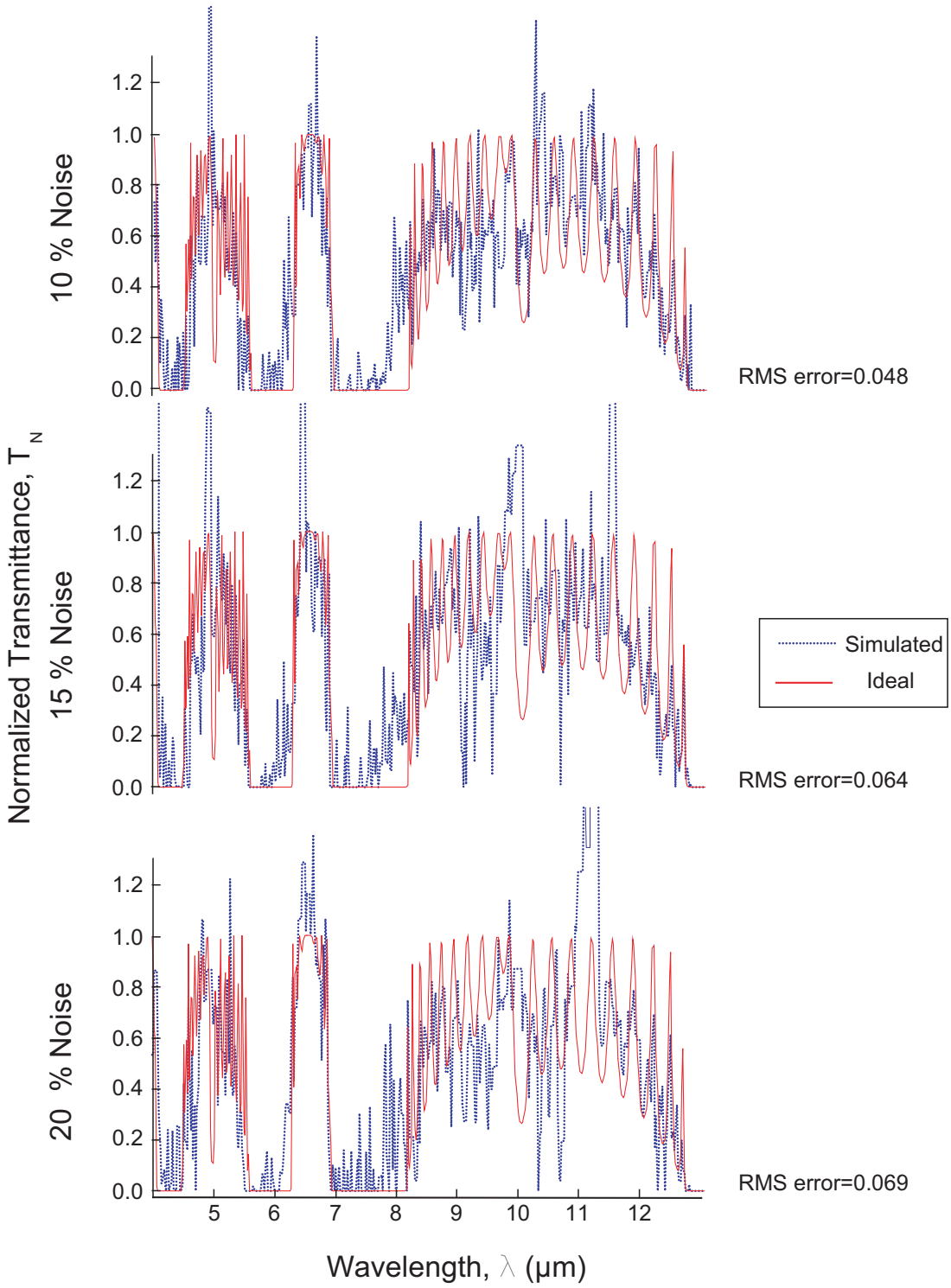

Figure 5.18: As noise levels increase, the regularized solution deteriorates. At noise levels above 10%, many spectral features are not reconstructed in the regularized solution. This plot shows the computed $\theta_k = 10°$ single-angle plane-wave transmittance for noise levels of 10%, 15%, and 20% compared to the ideal normalized transmittance.

Table 5.3: RMS error between the ideal normalized transmittances and the simulated (regularized) plane-wave transmittances, are shown for a large variation in the noise level percentage.

% Added	RMS Errors in Normalized Transmittance, T_N						Total
Noise	$\theta_k = 0°$	$\theta_k = 10°$	$\theta_k = 20°$	$\theta_k = 30°$	$\theta_k = 40°$	$\theta_k = 50°$	RMS Error
0.01	0.040	0.021	0.012	0.031	0.037	0.010	0.151
0.05	0.036	0.020	0.012	0.030	0.035	0.010	0.143
0.1	0.031	0.018	0.011	0.027	0.031	0.009	0.127
0.5	0.035	0.018	0.009	0.027	0.034	0.009	0.132
1.0	0.045	0.022	0.011	0.036	0.040	0.009	0.163
3.0	0.069	0.032	0.014	0.052	0.059	0.015	0.241
5.0	0.063	0.033	0.020	0.052	0.061	0.020	0.249
7.0	0.073	0.042	0.025	0.065	0.070	0.030	0.305
10.0	0.074	0.048	0.030	0.072	0.074	0.036	0.334
15.0	0.076	0.064	0.042	0.080	0.088	0.058	0.408
20.0	0.092	0.069	0.043	0.100	0.087	0.083	0.474

For application in the development of PC devices using the long-wavelength methodology, single-angle plane-wave transmittances with RMS error values below 0.070 exhibit many of the spectral features that will be useful in the development of PC structures. Spectra with RMS errors exceeding 0.070 lose many of the desired spectral details. In these simulations, RMS error values for plane-wave transmittance solutions at noise levels at or below 0.070 correspond to the condition of 5% or less added noise. The RMS error values for plane waves when the added noise level exceeded 5% are typically greater than 0.070.

The RMS error values between computed (regularized) plane-wave transmittances and ideal normalized transmittances in Table 5.3 also exhibit several trends that must be addressed. At very low noise levels, the RMS errors for solutions with the L-curve-selected regularization parameter increase as the noise decreases. This is caused by the algorithm's poor selection of regularization parameter. At low noise levels, the forced regularization of the problem results in the regularization error dominating the total system error. The L-curve looses its characteristic shape and the algorithm selects a regularization parameter that is higher than the optimum value. The solution is over-regularized resulting in the increased error. By decreasing the regularization parameter for extremely low noise levels, the simulated solutions improve. Figure 5.19 shows the regularized solution for noise levels

Table 5.4: RMS errors are shown comparing regularized plane-wave transmittances with ideal normalized plane-wave transmittances at low levels of added noise. For these computations, the L-curve selected regularization parameter was reduced by a factor of 10.

% Added	RMS Errors in Normalized Transmittance, T_N						Total
Noise	$\theta_k = 0°$	$\theta_k = 10°$	$\theta_k = 20°$	$\theta_k = 30°$	$\theta_k = 40°$	$\theta_k = 50°$	RMS Error
0.01	0.013	0.009	0.005	0.008	0.017	0.008	0.060
0.05	0.017	0.013	0.007	0.010	0.012	0.008	0.067
0.1	0.021	0.019	0.012	0.009	0.015	0.010	0.086
0.5	0.120	0.075	0.078	0.039	0.051	0.048	0.411

of 0.01%, 0.05% and 0.1% when the regularization parameter is decreased by a factor of 10 and the solution is recomputed. Corresponding RMS error values are displayed in Table 5.4.

Since a smaller regularization parameter improves the solution when the added noise is very low, a higher regularization parameter may be expected to improve the solution when the noise level is high. The L-curve-computed regularization parameter was multiplied by 3 and the single-angle plane-wave transmittance solutions were recomputed for data containing high levels of noise. Table 5.5 displays the resulting RMS error values and confirms that, at high noise levels, solutions computed with an increased regularization parameter resulted in lower RMS errors than the RMS errors computed using the L-curve-selected parameter.

At these significantly higher noise levels, the residual error dominates the total error and once again the L-curve looses its characteristic shape and makes optimal regularization parameter selection more difficult. Although the added regularization improves the solution, the RMS error values resulting from use of the increased regularization parameter do not fall below the maximum tolerable RMS value of 0.06 identified earlier in this section.

5.7.2.4 Noise Level Range for Optimal Parameter Selection

Since the successful selection of an optimal regularization parameter is dependent on the amount of noise present in a problem, the noise range over which the selected L-curve algorithm correctly selects an optimal regularization parameter must be identified. Regularized plane-wave transmittances were computed at $\theta_k = 20°$ incidence for the various noise levels

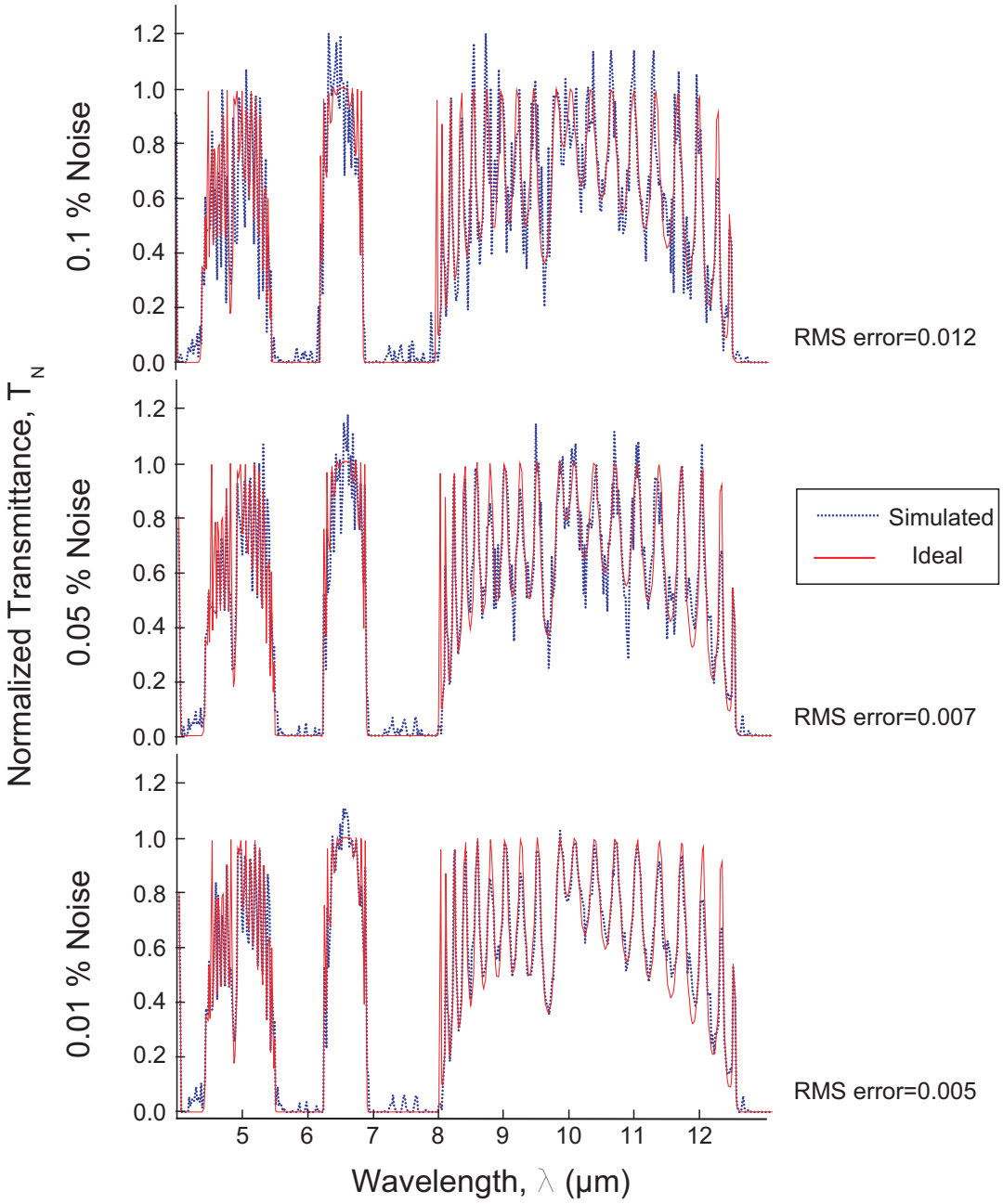

Figure 5.19: As noise levels decrease, the amount of regularization required decreases. At noise levels below 1%, the computed plane-wave transmittance solutions are improved by reducing the amount of regularization. The computed solutions show the single-angle plane-wave transmittances at $\theta_k = 20°$ incidence for low noise levels when the regularization parameter was divided by a factor of 10 for the computation.

Table 5.5: RMS errors comparing ideal normalized transmittances with regularized plane-wave transmittances. The regularized transmittances were computed from composite transmittances that contain high levels of noise. The computed solutions were improved by increasing the regularization parameter by a factor of 3.

% Added	RMS Errors in Normalized Transmittance, T_N						Total
Noise	$\theta_k = 0°$	$\theta_k = 10°$	$\theta_k = 20°$	$\theta_k = 30°$	$\theta_k = 40°$	$\theta_k = 50°$	RMS Error
5.0	0.058	0.032	0.018	0.053	0.060	0.019	0.240
7.0	0.060	0.033	0.023	0.058	0.064	0.023	0.261
10.0	0.060	0.039	0.024	0.067	0.065	0.030	0.285
15.0	0.062	0.037	0.031	0.073	0.075	0.050	0.328
20.0	0.080	0.044	0.032	0.078	0.072	0.056	0.362

using the L-curve-computed regularization parameter multiplied by a constant ranging from 0 to 6. A multiplier value less than 1 corresponds to a decreased amount of regularization compared to the amount selected by the algorithm. Likewise, a multiplier value greater than 1 corresponds to an increased amount of regularization compared to the algorithm-selected value. The RMS error values for these plane-wave calculations are displayed in Table 5.6. The computed RMS errors for the $\theta_k = 20°$ incident plane-wave transmittances are representative of the errors for all plane-wave angles. Positions without an RMS error value correspond to multiplier and noise level combinations that produce an RMS error greater than 1.

At $\theta_k = 20°$ incidence, the L-curve-selected regularization parameter produced the optimum plane-wave transmittances for noise levels from approximately 0.5% through 5%. At noise levels below 0.5%, the L-curve algorithm selected a parameter that over-regularized the problem. Similarly, at noise levels greater than 5%, the algorithm tended to under-regularize the problem. These results show that an estimate of the total measurement noise present in the characterization apparatus is important prior to computing the single-angle plane-wave solutions.

The algorithms are suitable for data collected using measurement apparatus that produce measurements with noise levels from 0.5% to 5%; the 0.5% noise minimum was identified as a limitation of the L-curve regularization parameter selection algorithm and the

Table 5.6: RMS errors in transmittances are shown for a $\theta_k = 20^\circ$ incident plane wave. Each plane-wave transmittance solution was computed using the L-curve selected parameter multiplied by a constant multiplier to force increased and decreased amounts of regularization compared to the algorithm-selected amount.

% Added	Regularization Parameter Multiplier						
Noise	0	0.01	0.1	0.5	1	3	6
0.01	0.004	0.005	0.005	0.009	0.012	0.015	0.017
0.05	0.009	0.009	0.007	0.009	0.012	0.014	0.016
0.1	0.018	0.017	0.012	0.008	0.011	0.013	0.015
0.5	0.213	0.199	0.078	0.009	0.009	0.011	0.013
1.0	0.455	0.380	0.064	0.012	0.011	0.012	0.015
3.0	-	-	0.077	0.014	0.014	0.015	0.019
5.0	-	-	0.082	0.022	0.020	0.018	0.021
7.0	-	-	0.092	0.030	0.025	0.023	0.023
10.0	-	-	0.136	0.034	0.030	0.024	0.026
15.0	-	-	0.144	0.056	0.042	0.031	0.027
20.0	-	-	0.166	0.068	0.043	0.032	0.030

5% maximum noise level was identified by comparing acceptable plane-wave transmittances with ideal normalized transmittances. If the apparatus produces measurement noise in excess of 5%, additional regularization may produce better plane-wave transmittances with a better match to ideal transmittances. When the measurement noise level falls below 0.05%, the problem may no longer need to be regularized; the least-squares solution, corresponding to a regularization parameter of 0, may compute a more accurate response.

5.7.2.5 Noise Reduction Through Repeated Measurements

If measurement noise does not fall in the 0.5% to 5% range, random noise can be reduced by repeating and averaging measurements on individual devices. Random noise in measurements decreases as the square root of the number of measurements,

$$Noise\ Reduction \propto \frac{1}{\sqrt{N_m}}, \tag{5.40}$$

where N_m is the number of measurements [89].

Noise reduction through multiple measurements was simulated by taking ten samples with 5% random error and computing the average noisy composite transmittance. The

single-angle plane-wave transmittances were computed and compared to the ideal single-angle normalized transmittances. Figure 5.20 shows the regularized transmittance and its corresponding plane-wave ideal normalized transmittance for a 5% uniform random variation in the upper plot. The RMS error for this solution was 0.019. The lower plot shows the computed and ideal plane-wave transmittances for the average of ten samples with 5% uniform random variation. The RMS error for this solution is 0.012. The computed random error for the averaged data is 1.6%. This is in agreement with relationship in Eq. (5.40).

In this section, the Tikhonov algorithms were tested to verify that the computation of the single-angle plane-wave transmittances or reflectances could be regularized. The algorithms were shown to select the regularization parameter and compute solutions for measurement noise levels from 0.5% to 5%. Finally, the technique of averaging multiple measurements was discussed as a method to decrease noise.

5.8 Summary

In this chapter, a characterization scheme suitable for use in the long-wavelength PC design and development methodology was presented. In this scheme, the single-angle plane-wave transmittance or reflectance of a fabricated structure is computed from the measured transmittance or reflectance of a composite beam. The focusing objective used in infrared characterization apparatus was analyzed and mathematically modeled. transmittance and reflectance measurements were analyzed and modeled resulting in matrix equations for the solution to the single-angle plane-wave transmittance or reflectance of the structure. The resulting coefficient matrix used in the modeled system is ill-conditioned. Tikhonov regularization was applied to the problem and regularized solutions were computed. The characterization method was simulated to demonstrate its effectiveness in computing the plane-wave transmittance of simulated structures. The regularization algorithm provides useful results for systems where the measurement error is less than approximately 5% but greater than 0.5%. The simulation identified the importance of noise analysis for the measurement systems. Finally the effect of averaging repeated measurements was shown as a

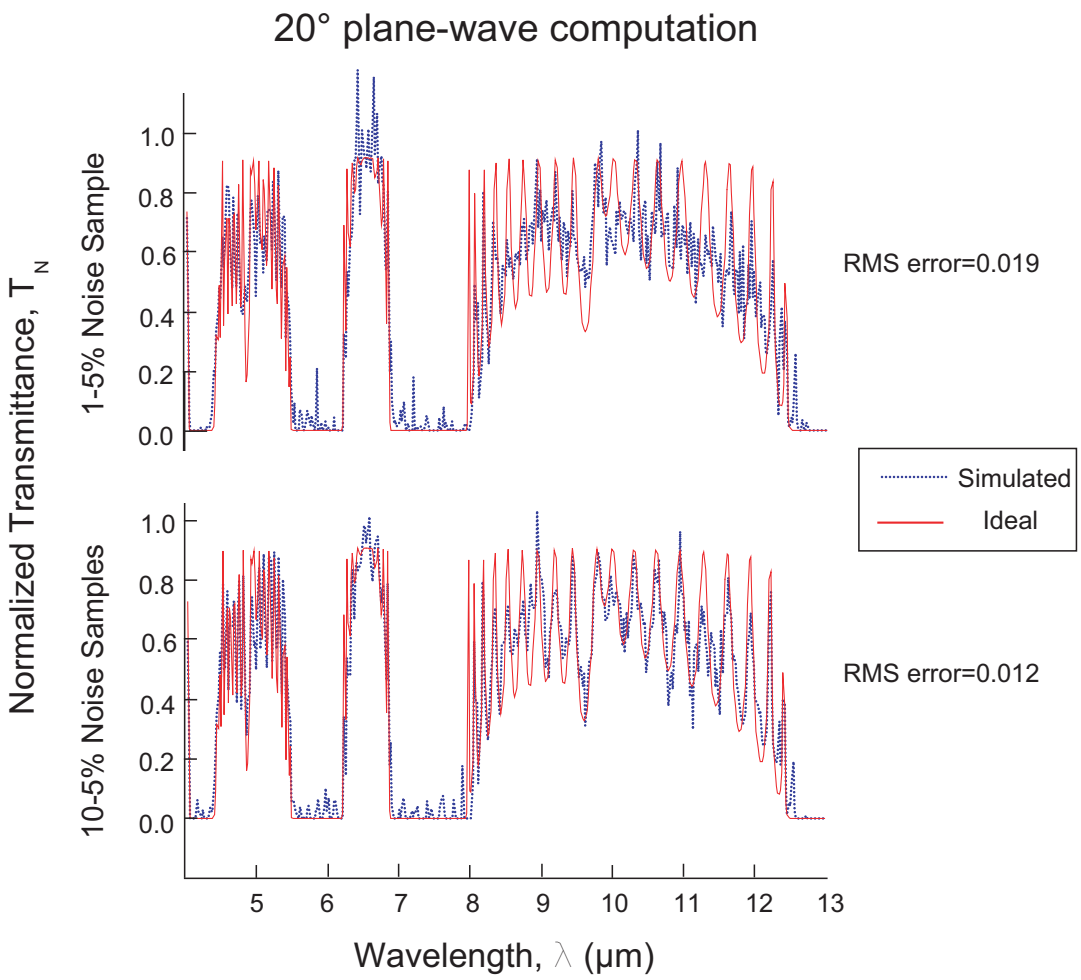

Figure 5.20: Random noise can be reduced through repeated measurements. The upper plot shows a regularized $\theta_k = 20°$ plane-wave transmittance when the composite transmittance measurements includes 5% noise. The lower plot shows the $\theta_k = 20°$ plane-wave transmittance computed for an average of 10 composite transmittance measurements that include 5% noise. The RMS error for the transmittance computed using the average measurements is 0.012. Using Table 5.3, this corresponds to a noise level between 1% and 3%. The actual noise level for the computed solution is 1.6%.

method to reduce the measurement error prior to the computation of the solution.

CHAPTER 6

MEASUREMENT CONFIGURATIONS

A discretely tunable CO_2-laser system and an FTIR microspectroscopy system are used to characterize the fabricated long-wavelength infrared PC structures by measuring their spectral response. With the CO_2-laser system, the transmittance of a sample is obtained by focusing a high-power, single-wavelength probe beam onto the sample and measuring the transmitted power. The CO_2-laser system is tuned to select additional laser wavelengths for further power measurements for each angular orientation of the objective axis. With the FTIR microspectroscopy system, the transmittance or reflectance of a sample is obtained by focusing a low-power, broad-spectrum beam onto the sample and measuring either the transmitted or reflected power. In this chapter, the characterization equipment, measurement apparatus, and measurement procedures used to obtain the transmittances and reflectances of PC structures are presented for both the CO_2-laser and FTIR microspectroscopy systems.

6.1 Discretely Tunable Carbon-Dioxide Laser System

The CO_2-laser system is used to measure the transmittance of the fabricated structures. Since the CO_2-laser system has a high-power probe beam, the laser and related measurement apparatus are suitable for investigating the varying spectral features of the designed structures such as band edges or defect modes.

6.1.1 Laser System

CO_2 lasers produce coherent light at wavelengths from 9.1 μm to 11.3 μm. The laser gain curve in Fig. 6.1 shows the expected gain for each lasing line across this wavelength range. Typical tunable CO_2-laser systems can provide sufficient output power over all or a portion of this wavelength range depending on the specific design of the laser.

The laser system used to conduct the measurements presented in this thesis is a Model

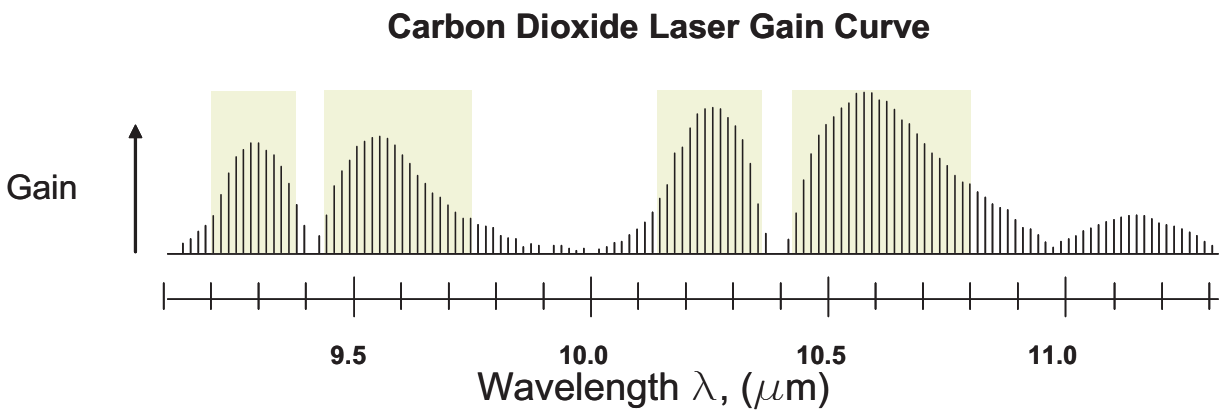

Figure 6.1: A discretely tunable CO_2-laser system can provide laser light across the wavelength range shown. Typical laser systems produce measurable output power levels over a subset of this wavelength range depending on the quality and design of the laser system. The available laser, Model GN-802 manufactured by MPB Technologies, produces measurable output at the wavelengths within the shaded regions.

GN-802 CO_2 laser produced by MPB Technologies [90]. The maximum output power for the laser is 12.5 W at a wavelength of 10.59 μm. Measurable output power is produced across the wavelength range from 9.18 μm to 10.78 μm with individual lasing lines selected through the adjustment of a grating at the rear of the laser chamber. For this model of laser, there are wavelength ranges in the spectrum where the output power is below the detection threshold. These wavelength ranges exist from 9.36 μm to 9.44 μm, 9.74 μm to 10.14 μm and 10.35 μm to 10.45 μm.

The CO_2-laser output power is stabilized by an MPB Technologies Electro-Mechanical Translator (EMT) and Model 901 Laser Stabilizer. The stabilizer monitors the output power of the laser and continuously adjusts the position of the output mirror using the EMT so as to maintain constant output power.

A photograph of the CO_2-laser system mounted on an optical table is shown in Fig. 6.2. The system components include the laser, cooling system, oscilloscope, stabilizer, and power supply.

6.1.2 Testing Apparatus

Figure 6.3 is a diagram of the optical components used to conduct transmittance measurements of long-wavelength PC structures using the CO_2-laser system. The beam from the

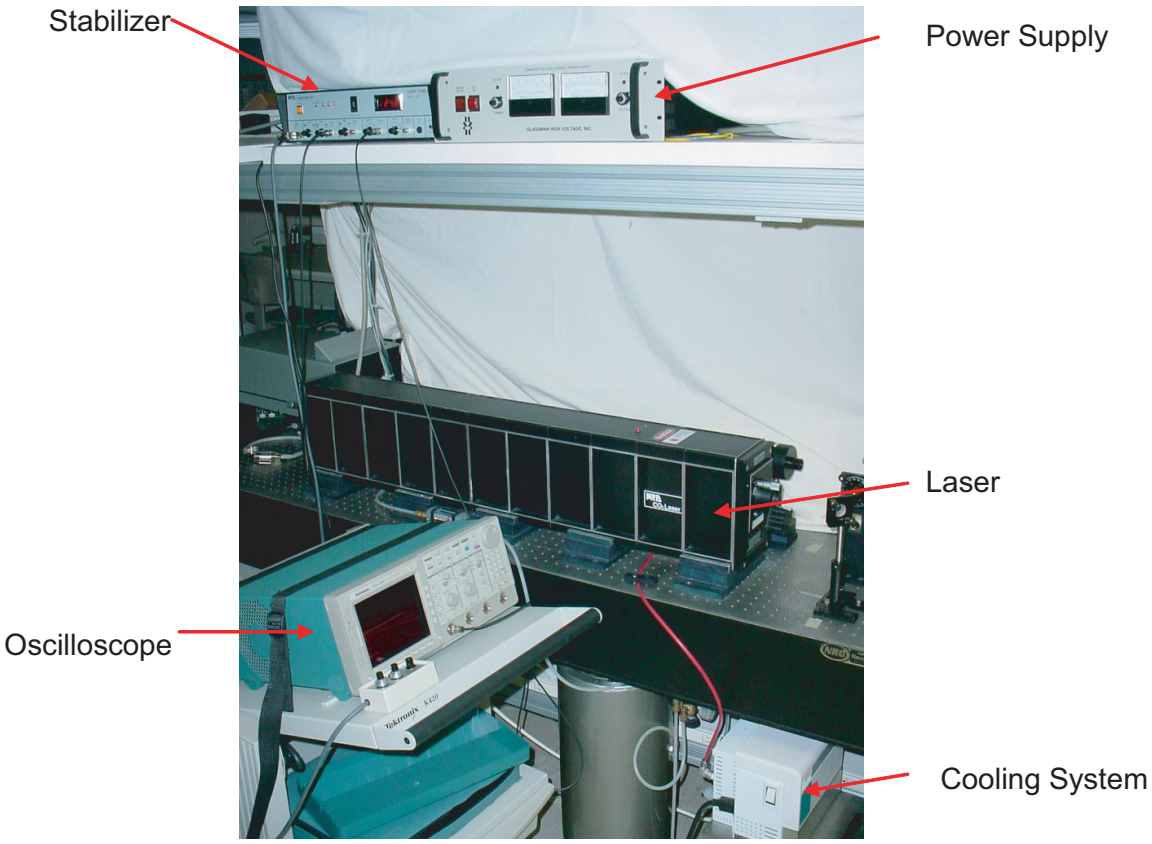

Figure 6.2: The MPB Technologies GN-802 CO_2-laser system.

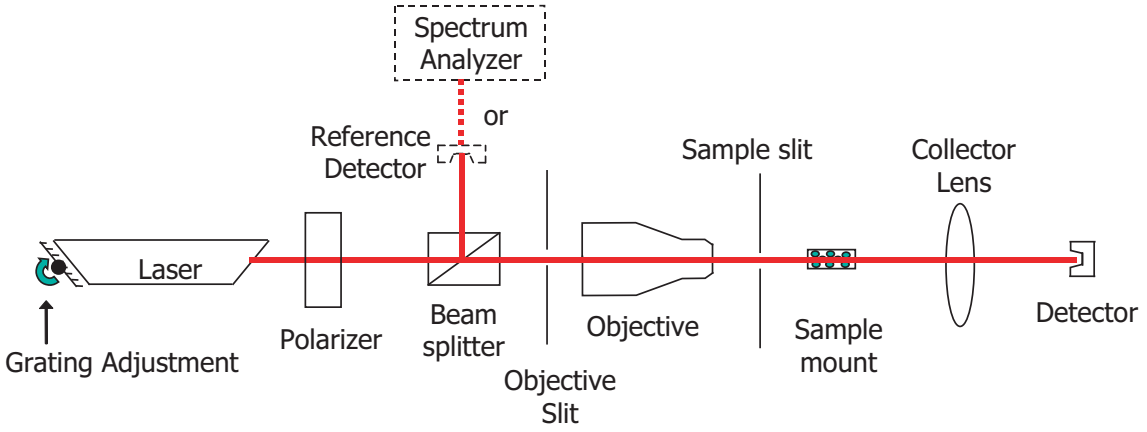

Figure 6.3: Apparatus for transmittance measurements with the CO_2-laser system.

laser is first incident on a thin film Brewster angle polarizer. The polarizer is used to select TE or TM polarization of the beam with respect to the plane of incidence at the sample. After the polarizer, the beam is split into a probe beam and a reference beam by using a beam splitter. The reference beam is used to monitor continuously the output power of the CO_2 laser. The probe beam continues through the apparatus towards the sample.

The reference beam power is measured using a Thermo-Oriel Model 71965 High-Powered Thermopile Optical Power Meter (OPM) detector; the reference beam power measurement is used to normalize measurements taken over a wide range of laser output power levels so the transmission spectra of the sample can be constructed. A spectrum analyzer is aligned directly behind the reference power detector and is used to select or monitor the CO_2-laser wavelength following removal of the reference power detector from the optical path. The lasing wavelength indicated by the spectrum analyzer is observed while the grating at the end of the CO_2 laser is tuned. Tuning of the grating continues until the correct lasing wavelength is selected and the detector is then re-inserted into the beam.

The probe beam propagates from the beam splitter to the objective slit. The objective slit is mounted within a manual rotation stage. The stage allows the objective slit to rotate freely about the optical axis of the laser beam, thus enabling the objective slit to be aligned with other system components. The beam passes through the objective slit into the aperture of the reflecting microscope objective.

The objective is mounted onto a micrometer-driven, 3-axis linear translation stage.

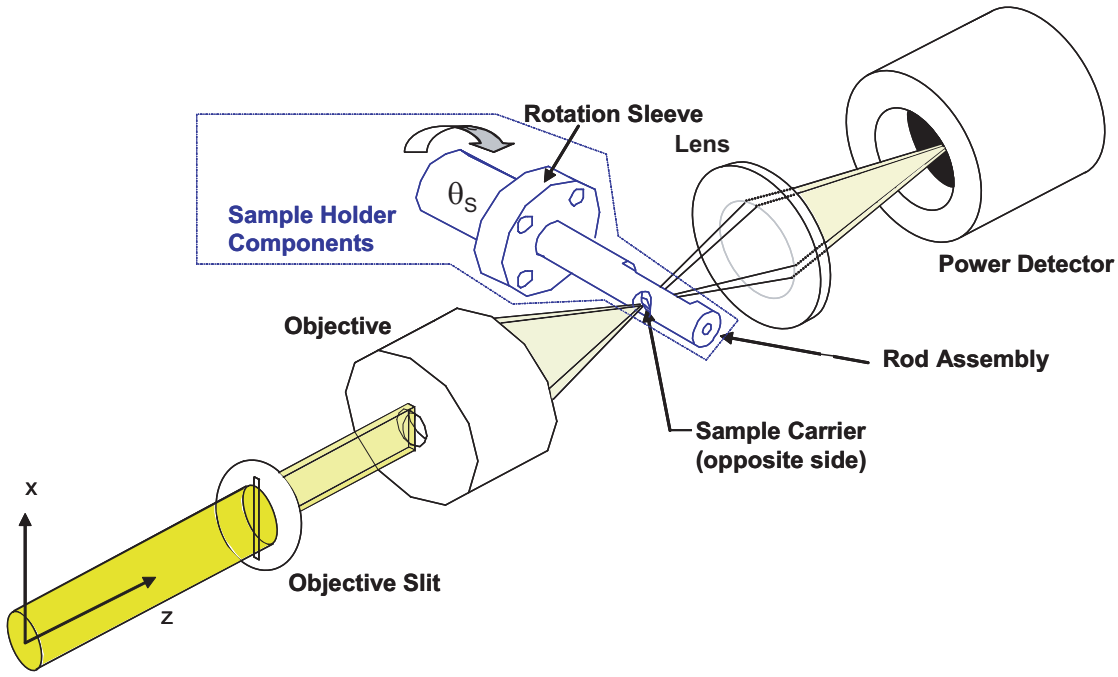

Figure 6.4: The PC sample and sample slit are mounted onto a sample holder that fits into a computer-controlled rotation stage. The sample holder consists of 3 components: the sample carrier (not visible in this diagram), the sample rod, and the rotation sleeve. The focused light passes through voids in the rod and through the sample before being collected by a lens and focused onto a power detector. The sample can be rotated through a range from $+50°$ to $-50°$.

The objective focuses the light through an additional slit (sample slit). The sample slit prevents light from propagating around the sample or propagating through the substrate of the sample. Typical sample slit dimensions are 600 μm long by 45 μm wide. The slit width, along the short axis, can vary depending upon the depth of the PC structure; the PC structure depth must exceed the sample slit's short-axis dimension. The focused probe beam passes through the sample slit and is incident on the PC sample.

To rotate the sample normal with respect to the objective axis, the sample slit and the PC sample are mounted onto a sample holder that is attached to a computer-controlled rotation stage. In turn, the rotation stage is attached to a 3-axis micrometer-driven linear positioning stage. The light transmitted through the PC structure is collected by a lens and focused onto a second Thermo-Oriel OPM thermopile power detector. A diagram showing the position of the sample holder components in reference to the incident laser beam is shown in Fig. 6.4.

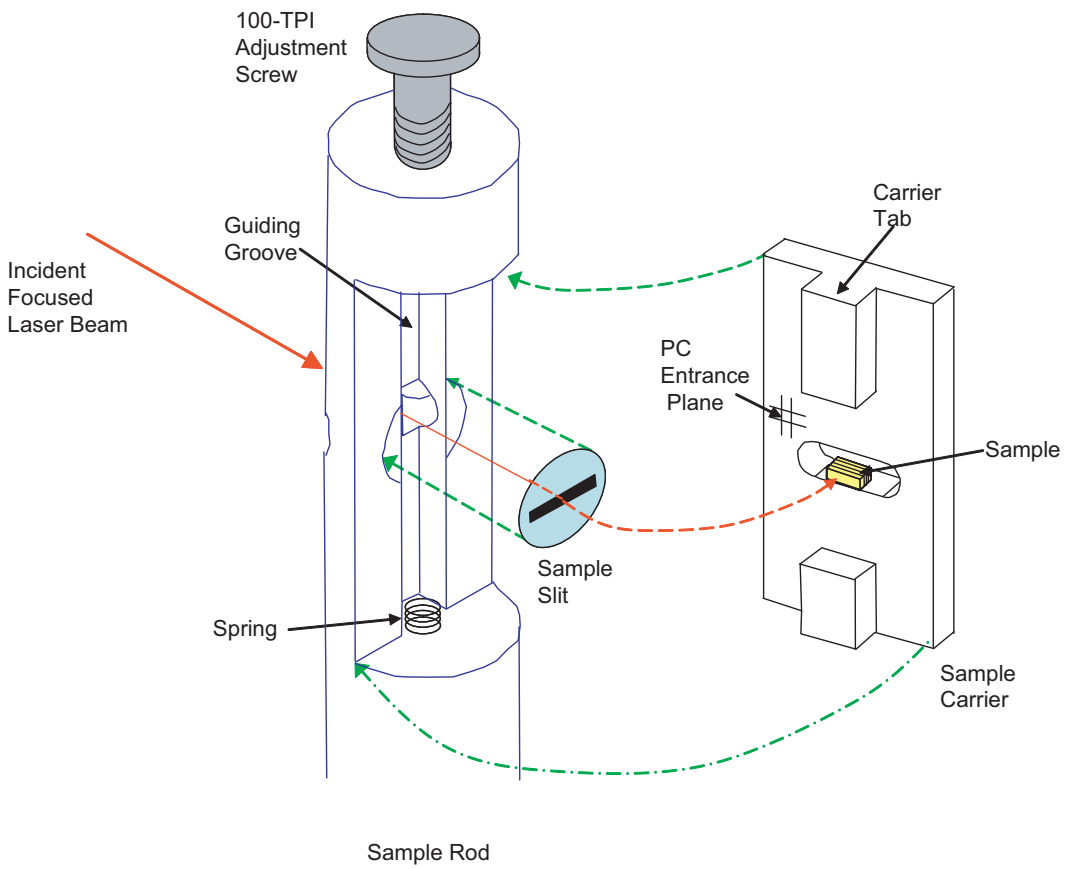

Figure 6.5: The PC sample is mounted onto a carrier which is mounted onto a rod. The rod is inserted into the rotation sleeve (not shown). The focused light passes through a hole in the rod, through the sample slit and finally to the PC crystal sample. The sample holder was designed to provide rotation of the sample from approximately $+50°$ to $-50°$ with respect to the optical axis of the system.

6.1.3 Sample Holder Components

The sample holder components are designed to hold the PC sample and permit the sample to rotate while maintaining a fixed position in the probe beam. By rotating the sample with respect to the objective axis, multiple measurements at various angular orientations can be recorded in order to produce the required number of equations to compute the single-angle plane-wave responses. The sample holder consists of the sample carrier, the sample rod, and the rotation sleeve. A diagram of the sample carrier and the sample rod is shown in Fig. 6.5.

The PC sample is mounted onto the sample carrier. The sample is positioned so that the input plane of the structure is aligned with the inside surface of the sample carrier.

The inside surface of the sample carrier is the surface that has the protruding tabs and is positioned against the slit on the inside of the sample rod when fully assembled. The sample slit is mounted in a fixed position on the sample rod. The tabs from the sample carrier straddle the sample slit and slide in a groove in the sample rod. When correctly assembled, the PC entrance plane, the inside surface of the carrier, the sample slit, and the center of the rotation rod are all aligned.

The sample carrier travels in the guiding groove and is held in a set position by a spring in one end of the groove and a 100-threads-per-inch (TPI) adjustment screw (threaded through the end of the rod) at the other end of the groove. As the 100-TPI adjustment screw is turned, the sample carrier, with the sample attached, slides against the slit. The spring applies compressive force to keep the carrier positioned against the adjustment screw.

Once the sample carrier is positioned within the sample rod, the rod is inserted into the rotation sleeve. The sleeve is mounted in the center of a computer-controlled rotation stage that provides rotation control of the sample. The rotation mount permits the sample to rotate from approximately -50° to $+50^\circ$ with respect to the optical axis of the system. Outside of this range, the incident light strikes the rod assembly instead of the sample. The sample rod permits rotation of the sample along an axis perpendicular to the optical axis of the system. Ideally, the sample is located at the center of the rod assembly on the rotation axis and, as the rod assembly rotates in the rotation mount, the sample rotates at a fixed position in the center of the CO_2-laser beam.

In practice, however, the sample may not be precisely located on the rotation axis of the rod and some positioning adjustment of the sample is required after each rotation of the rod. The rotation sleeve is mounted onto a 3-axis linear translation stage so the entire assembly can be repositioned into the center of the beam. A photograph of the experimental apparatus for the CO_2 laser is shown in Fig. 6.6.

6.1.4 Objective Slit and Sample Slit Alignment

Prior to mounting a PC sample onto the sample carrier, the objective slit is aligned with the sample slit. The rod assembly, holding the fixed sample slit, is placed into the rotation

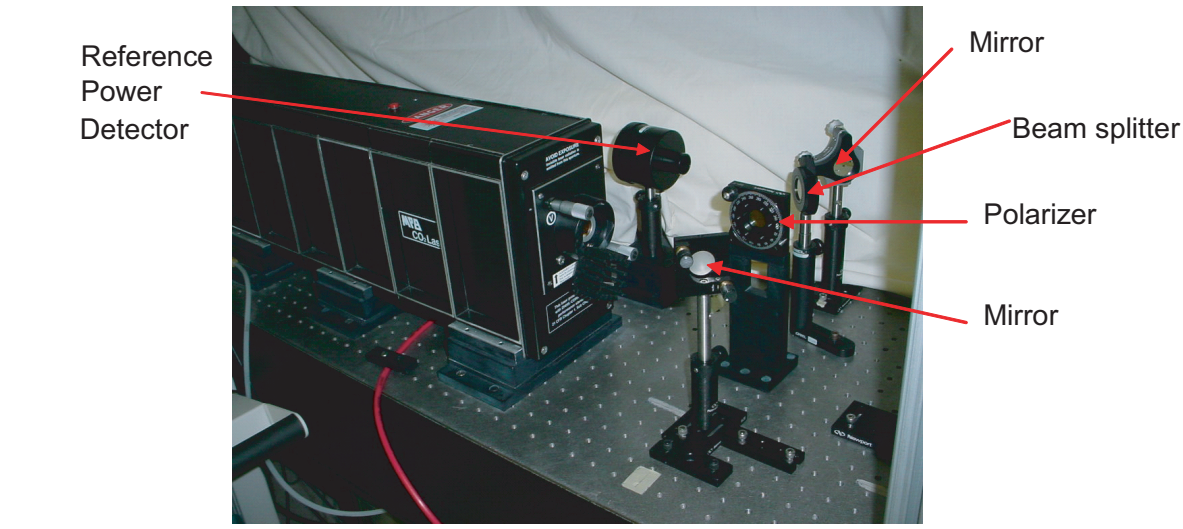

(a)

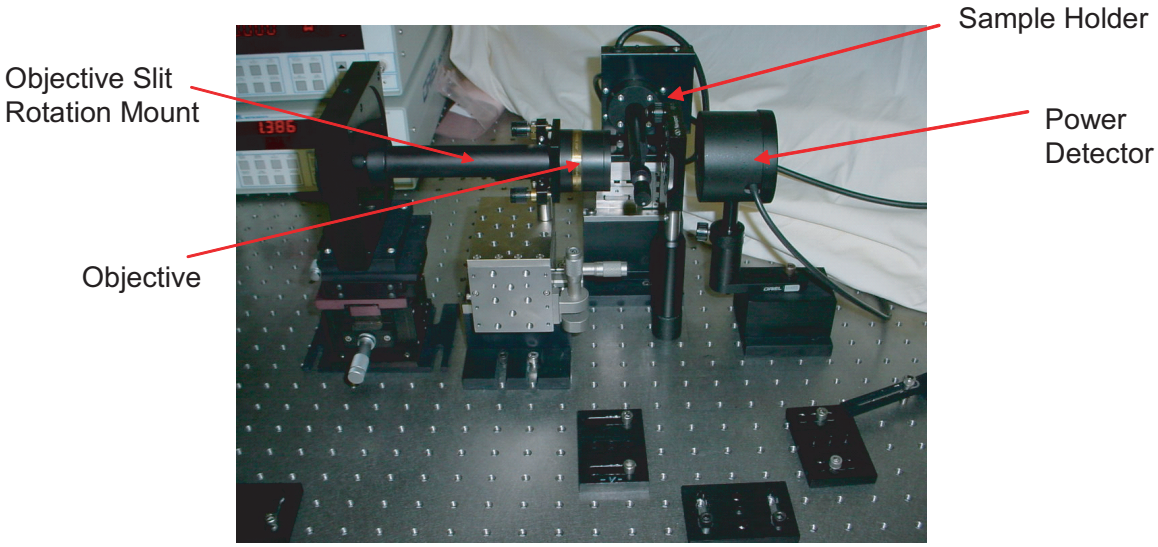

(b)

Figure 6.6: Components of the CO_2-laser measurement apparatus. (a) Polarizer, beam splitter, reference power detector, and beam steering mirrors. (b) Objective slit rotation mount, objective, sample holder, and power detector.

sleeve and aligned with the microscope objective. This is accomplished by maximizing the power transmitted through the sample slit. Then, the objective slit is inserted into the optical path and rotated around the optical axis until the power transmitted through both the sample slit and the objective slit is maximized. At this position, the long axis of the objective slit and the long axis of the sample slit are aligned. The rod assembly can be removed from the rotation sleeve and a PC sample can be mounted. When the rod is inserted back into the rotation mount, the fixed-position sample slit returns to the same orientation, thus ensuring that the objective and sample slit orientation remain aligned.

6.1.5 Photonic Crystal Sample Alignment

The entrance plane of the PC sample is in contact with the sample slit when the carrier is mounted onto the rotation rod. To align the slit and the sample, the rod assembly with the mounted sample carrier is placed in a temporary rod holder and the sample is viewed through the sample slit using a microscope. The 100-TPI adjustment screw is turned until the PC structure is aligned and fills the slit. The spring provides sufficient compressive force to keep the sample and slit aligned while the rod assembly is removed from the temporary microscope holder and inserted into the rotation sleeve.

6.1.6 CO_2-Laser Focusing Beam Coefficients

To determine the focusing coefficients for the CO_2-laser system, the CO_2-laser beam power profile is measured using a Photon Inc. [91] BeamScan system. The BeamScan system detector head is placed directly in the path of the laser beam. A 25 μm slit in the detector head scans across the beam and measures the beam power profile. The slit width is deconvolved from the measured profile to determine the actual beam power profile. The slit can be rotated around the optical axis to scan the beam at any angular orientation.

The coefficients for the focused beam are measured using the method described in Chapter 5. The beam power profile is recorded in the focusing beam along the direction of the major axis of the objective slit at a plane a known distance from the objective focal point. The width of the central obscuration and the location of the mirror edges of the objective are computed for this plane. The resulting beam profile is divided into sectors and

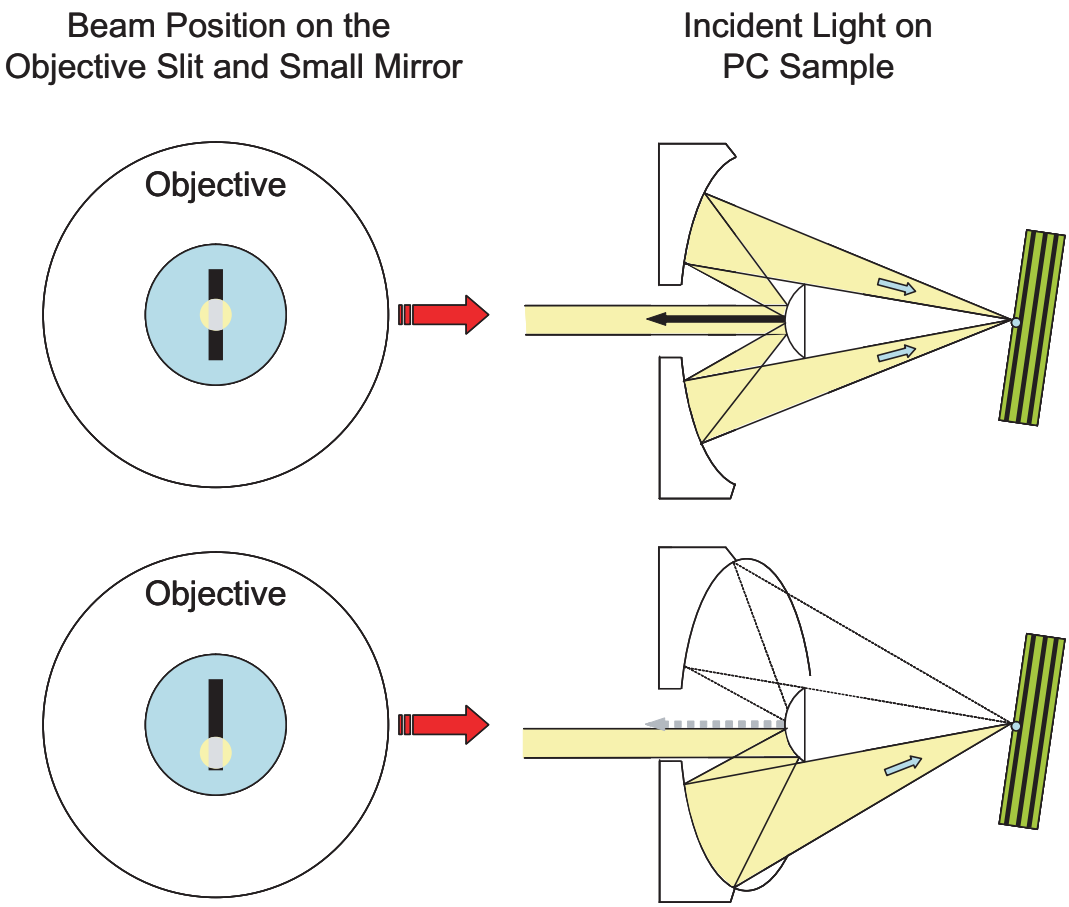

Figure 6.7: The CO_2-laser beam's position on the small mirror determines whether the PC sample is illuminated with one or two lobes of incident light. If the objective slit is centered on the objective aperture and the beam is centered on the slit, two lobes of light are incident on the sample (top diagram). By lowering the beam position on the small objective mirror, only the lower half of the mirror is illuminated resulting in one lobe being incident on the sample (bottom diagram). For the single-angle plane-wave computation, this improves the condition of the coefficient matrix.

the area of each sector under the profile is computed to determine the coefficients. Since the coefficients account for beam non-uniformities and imperfect focusing of light, only the coefficients in the focusing beam need to be computed.

To improve the stability of the coefficient matrix in the transmission configuration and increase the incident power with the CO_2-laser apparatus, the objective is positioned so that the laser beam is incident on the small mirror of the objective away from the mirror's center. Figure 6.7 shows the positioning of the beam in reference to the objective small mirror and the resulting beam that is incident on the PC structure. If the incident beam is

centered on the mirror, as shown in the top diagram, light is reflected from the small mirror to the large mirror on both sides of the small mirror and the converging beam focused on the sample consists of two lobes of light incident from each side of the small mirror. Light is also reflected from the small mirror out of the system back through the aperture. If the objective position is raised with respect to the incident beam, as shown in the lower portion of the figure, the light reflects from the small mirror to the large mirror and converges to the focal point in a single lobe from one side of the small mirror. Depending on the width of the laser beam, the entire beam may be reflected through the lower light path without reflecting light back through the aperture. In the single-lobe case, the beam weighting coefficients on the upper side of the small mirror are all equal to zero.

When objective coefficients are substituted into the coefficient matrix, the condition number of the coefficient matrix for the single incident lobe is decreased by an order of magnitude from the value of the condition number for two incident lobes. Consequently, for the single-angle plane-wave computation, the use of the single-lobe beam increases the stability of the computation.

Table 6.1 lists the coefficients for 2° sectors of the probe beam for several wavelengths of the CO_2 laser. The seven coefficients correspond to the single-lobe coefficients. Coefficients for the second lobe, a_8 through a_{14}, are zero. Since the beam power profile varies at each wavelength, the individual coefficients and the coefficient matrix vary with wavelength.

6.1.7 CO_2-Laser Transmittance Measurement Procedure

Initial measurements with the CO_2-laser system showed that despite attempts to place the sample in contact with the slit, light was able to bypass the structure enroute to the detector by passing over the top of the structure. To block this light, a small section of silicon wafer was mounted onto each sample prior to testing with the CO_2 laser. The small section of silicon was placed in contact with the top surface of the structure and bonded to the sample. A microscope was used to examine the bond between the sample and the small silicon section to ensure there was no light transmitted in between the bonded surfaces.

Table 6.1: Computed beam profile coefficient values for various CO_2-laser wavelengths. Since the profile of the beam varies for each wavelength, the coefficients and the coefficient matrix also vary for each wavelength.

Wavelength	Beam Profile Coefficients						
(μm)	a_1	a_2	a_3	a_4	a_5	a_6	a_7
10.81	0.0861	0.1849	0.2350	0.1582	0.1480	0.1146	0.0732
10.69	0.0843	0.1817	0.2350	0.1597	0.1488	0.1165	0.0741
10.59	0.0857	0.1825	0.2201	0.1584	0.1529	0.1268	0.0737
10.49	0.0900	0.1840	0.2072	0.1527	0.1513	0.1352	0.0796
10.27	0.0815	0.1804	0.2434	0.1641	0.1479	0.1100	0.0726
10.14	0.0868	0.1863	0.2273	0.1571	0.1493	0.1187	0.0745
9.66	0.0842	0.1852	0.2243	0.1579	0.1491	0.1233	0.0760
9.50	0.0875	0.1862	0.2099	0.1556	0.1483	0.1301	0.0824
9.31	0.0819	0.1853	0.2285	0.1593	0.1483	0.1196	0.0770
9.18	0.0636	0.1440	0.2663	0.2261	0.1371	0.0989	0.0640

A flowchart detailing the procedure for taking measurements with the CO_2-laser apparatus is shown in Fig. 6.8. The CO_2-laser system is started and the polarization and initial wavelength are selected. After the wavelength is selected, the reference power detector is placed in front of the spectrum analyzer and the beam profiling system is used to check the location of the beam center at several positions in front of the objective to determine the propagation direction of the beam. If necessary, the beam direction is adjusted. Once the beam is incident on the desired off-center location on the small mirror of the objective, the beam profile of the focused beam is recorded.

The sample is aligned in the sample carrier so that the device fills the sample slit and the rotation rod is placed into the rotation sleeve. The spatial position of the rotation rod is then adjusted to achieve maximum transmitted power through the sample. Proper alignment is confirmed by measuring the translation range over which power passes through the structure; this range should correspond with the 600 μm sample slit length. Once aligned and centered, transmitted power is recorded for the current angular position of the rotation rod. The sample is then rotated to a new angular orientation and the transmitted and reference power measurements are recorded. This is repeated for all specified objective axis angular orientations. After all measurements are recorded at a single wavelength, the

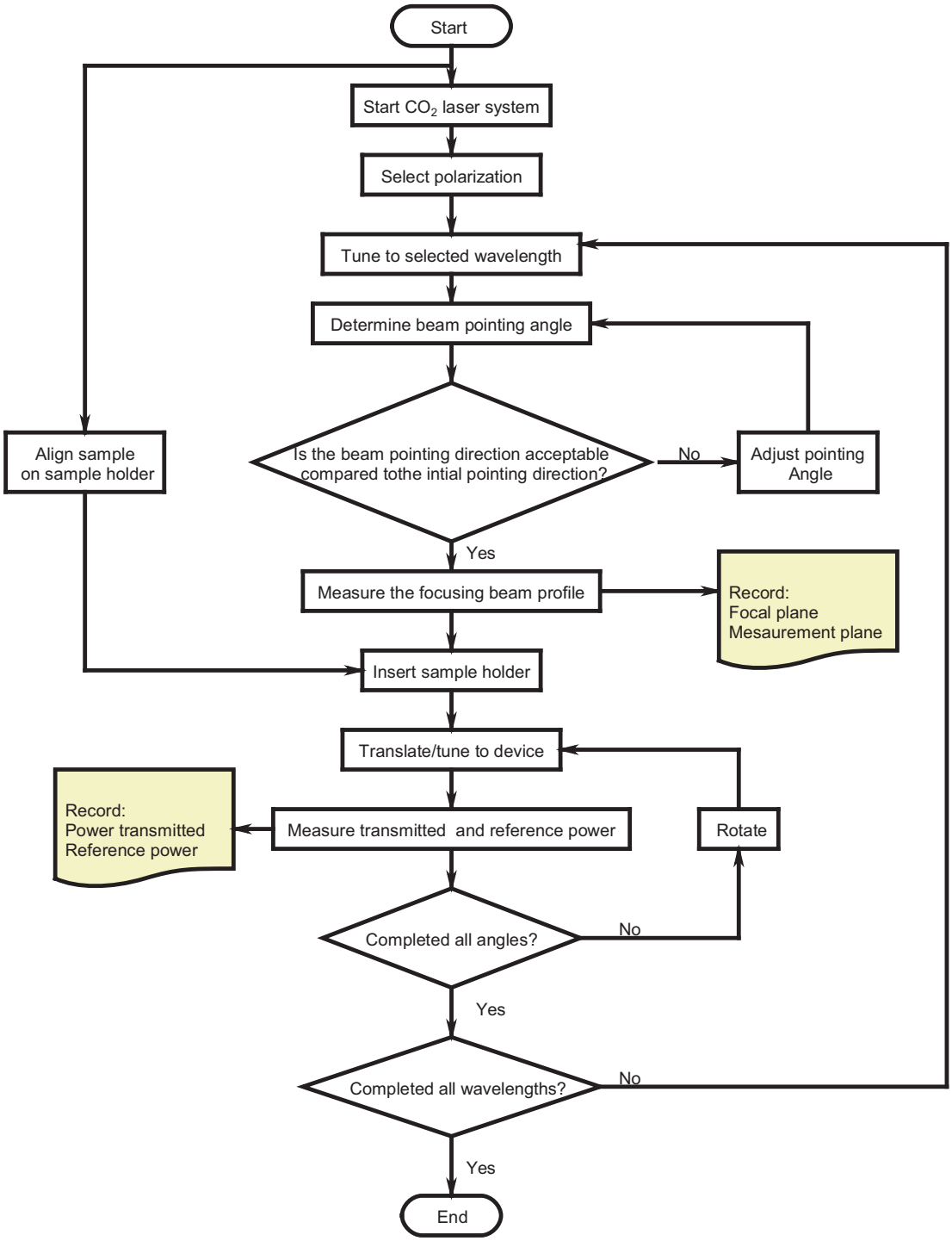

Figure 6.8: Flowchart for measurements with the CO_2 laser.

laser wavelength is adjusted and the cycle is repeated until all desired wavelengths have been measured. The profile of the focused beam must be recorded for each wavelength and the transmitted and reference power must be recorded for each angular position at each wavelength.

6.1.8 Apparatus and Model Validation

Prior to measuring the transmittances of PC structures, the CO_2-laser apparatus and objective model were tested by measuring the transmittance of TM polarized light through a single dielectric layer. A 10 mm $\times$ 20 mm, 230 μm thick, double-side-polished (DSP) silicon wafer section was used for the dielectric layer. The wafer section was mounted onto the sample rod so it could rotate in the focused beam. TM polarized CO_2-laser light at a wavelength of $\lambda = 10.59$ μm was focused onto the sample. The beam was positioned to strike the lower portion of the objective's small mirror, the beam profile of the focused beam was measured, and the coefficients were computed. The sample normal was rotated from -82° to $+50^\circ$ with respect to the optical axis and the transmitted power was measured. The composite transmittance measurements were compared to the theoretical transmittance calculations for a composite beam. The theoretical calculation was constructed by weighting the calculated single-angle plane-wave transmittances with the measured coefficients for all plane-wave components present in the beam. The measured results are shown in Fig. 6.9. Both the theoretical transmittance calculation and measured transmittance show the interference peaks of the single dielectric layer. The Brewster angle, theoretically calculated to be 73.7°, is evident in the measured data although not exactly at the calculated angle. The measurements are in overall good agreement with theory.

6.1.9 CO_2-Laser Apparatus Summary

The CO_2-laser system provides a method to record transmittance measurements of PC structures. The apparatus has been designed so the PC sample can rotate freely in the laser beam and multiple transmittance measurements can be recorded over a range of objective axis angular orientations. The laser is manually tuned across its spectral range and measurements recorded for each angular orientation of the objective axis relative to the

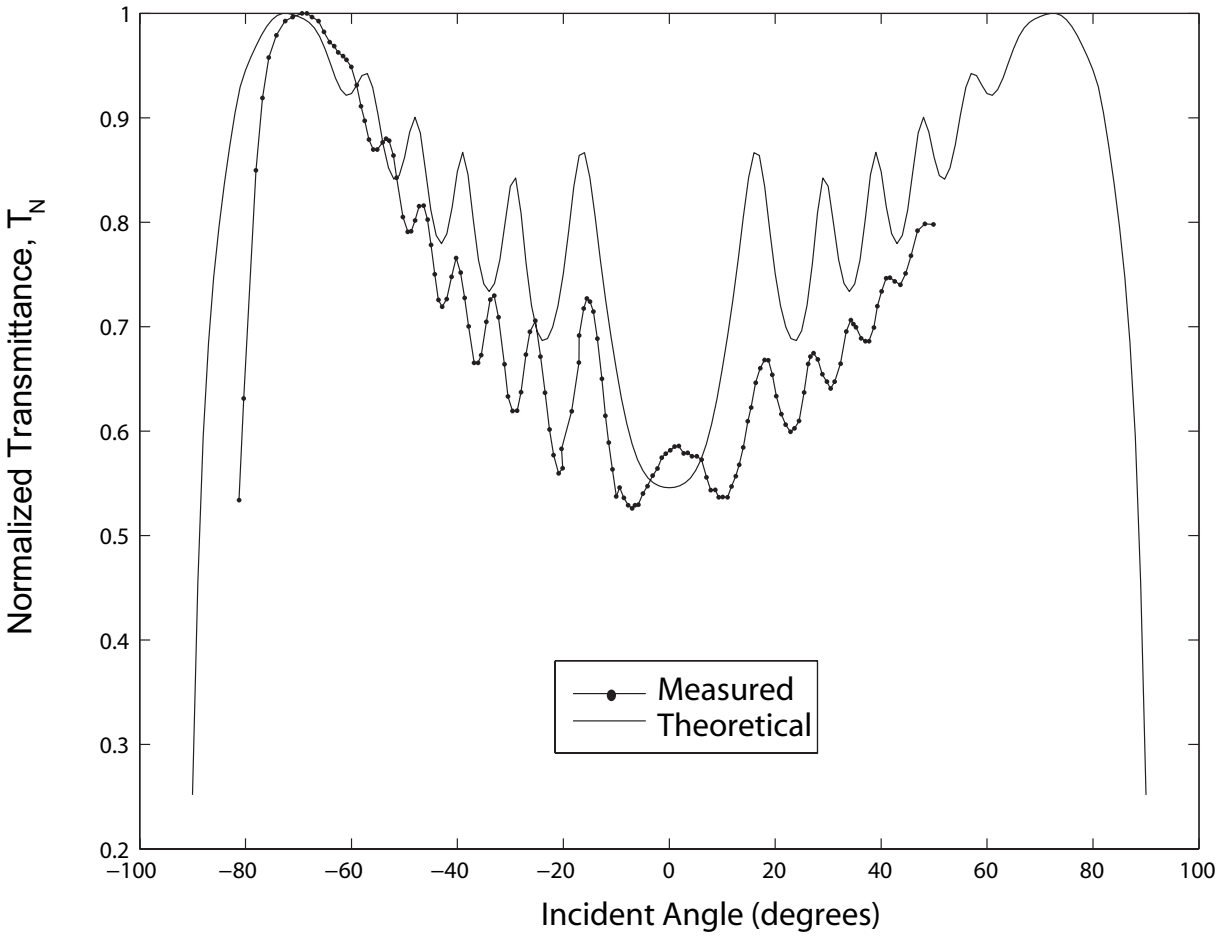

Figure 6.9: Measured and simulated TM polarized transmittance for a range of incident angles for a beam focused onto a double-side-polished silicon sample. The composite beam was modeled with a summation of plane-waves over the range of angles being focused by the objective.

sample normal at each wavelength. In an initial test of the apparatus and objective models, the results were in agreement with theoretical calculations.

6.2 Fourier Transform Infrared Spectrometer System

The FTIR microspectroscopy system is an alternative or additional system that can be used to characterize PC structures. In the CO_2-laser experiment, each wavelength in the 9 μm to 11 μm range is measured separately at each angular orientation of the objective axis with respect to the sample normal. Separate measurements for each wavelength are not necessary with the FTIR system; the FTIR system uses a broadband source to measure the entire spectrum over the wavelength range from $\lambda = 2$ μm to $\lambda = 30$ μm simultaneously at each specific objective axis angular orientation. This significantly reduces the amount of time required to characterize the PC structures. The sample holder components designed for the CO_2-laser apparatus are also used in the FTIR microspectroscopy apparatus. The equipment, apparatus, and measurement procedures for both transmittance and reflectance measurements are discussed in this section.

6.2.1 Spectrometer and Microscope System

A FTIR microspectrometer consists of an FTIR spectrometer coupled to an infrared microscope. The FTIR microspectrometer used in this thesis is a Bruker IFS 66/S research-grade FTIR spectrometer [92] coupled to a Bruker Hyperion 1000 infrared microscope [93]. The entire system is controlled by a personal computer and proprietary control software (Optical User Software (OPUS)) provided by Bruker. The added features and rapid characterization capability come at the expense of greatly reduced incident power compared to the CO_2-laser system.

6.2.2 Testing Apparatus

The spectrometer unit holds the broadband globar source, interferometer, and several detectors. When coupled to the microscope, the optical path of the spectrometer can be re-routed through the microscope by selecting the microscope's detector in the OPUS software. The microscope focuses light onto the sample and collects transmitted or reflected light using

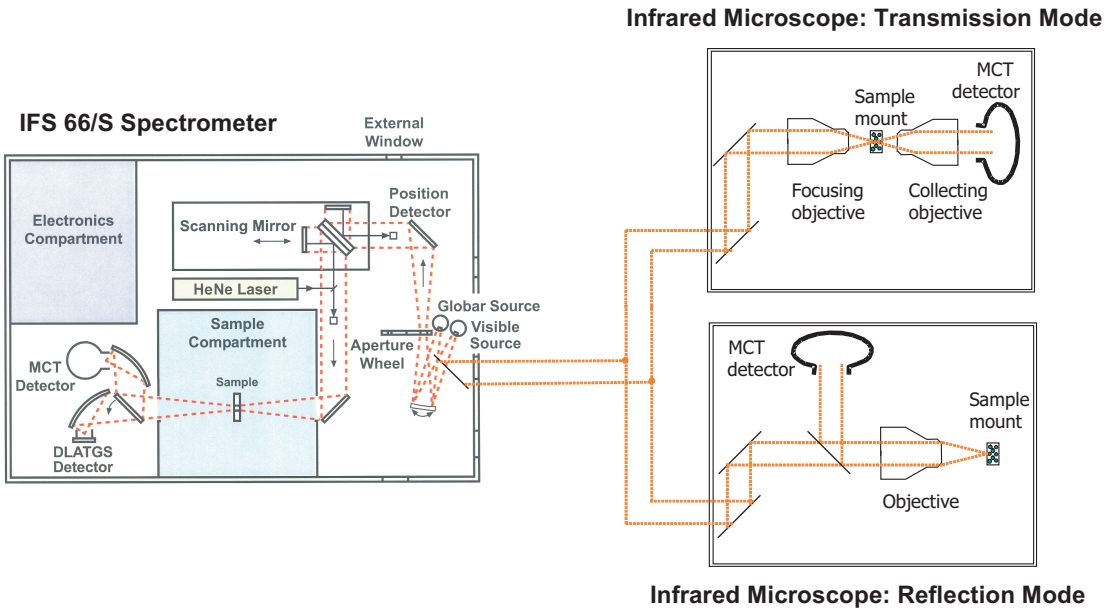

Figure 6.10: Components needed for transmittance and reflectance measurements with the FTIR system.

Schwarzchild reflecting microscope objectives and has an integrated detector used for microscope measurements. A diagram of the testing apparatus for FTIR microspectroscopy system is shown in Fig. 6.10.

The optical path in the microscope is dependent on the type of measurement, either reflection or transmission. For transmittance measurements, the beam is directed through the lower portion of the microscope up through the lower objective to the upper objective and finally to the detector. For reflectance measurements, the light is routed on a path through the microscope directly to the upper objective. The upper objective focuses the light onto the sample. Reflected light is collected and is incident on the detector. The detector is a liquid-nitrogen-cooled mercury-cadmium-telluride (MCT) detector.

The microscope system has an integrated double-knife-edge aperture that functions as the sample slit (as described in the previous section). The aperture is aligned to the structure by viewing the slit and sample as the slit is adjusted. The objective slit is positioned in the optical path by inserting the slit into a ring mount in a polarizer mounting stage. Automatic stop points on the polarizer mount ensures that the objective slit is centered in the optical path of the system.

The only component not directly integrated into the FTIR microspectroscopy system is the sample holder. The sample holder designed for the CO_2-laser system is also used in the FTIR microspectroscopy system. The stage supplied with the microscope is removed exposing the optical path between the upper and lower reflecting objectives. The working space between the two objectives is approximately 5 cm. The sample holder is mounted on a platform adjacent to the microscope. The sample slit and sample alignment steps used with the CO_2-laser system are not necessary in the FTIR microspectroscopy apparatus.

The sample rotates freely in the beam with the sides of the sample holder interfering after a rotation of approximately $\pm 50^\circ$. However, the low power levels associated with the FTIR source prevents rotation beyond $\pm 30^\circ$ as beyond this rotation limit, optical power is no longer detected. Images of the FTIR system are shown in Fig. 6.11.

6.2.3 FTIR Focusing Beam Coefficients

Similar to the CO_2-laser characterization apparatus, it is necessary to measure beam coefficients for both reflectance and transmittance measurements with the FTIR microspectroscopy system. The infrared source in the FTIR system is a globar element. The element is placed in a source port of the unit and is aligned with the optical axis by visually centering the glowing portion of the globar on the aperture wheel of the FTIR system. Once positioned in the desired location, clamps are tightened holding the globar in place. The intensity of the globar source is not uniform over its extent (approximately $9\ mm \times 7\ mm$). As a result, the focused beam is not uniform.

To measure the intensity of the focusing beam, a Model 71961 Thermo-Oriel Miniature Thermopile OPM power detector is physically scanned across the focusing beam. To compute the focusing beam coefficients for reflectance measurements, the detector is mounted on a 3-axis micrometer-driven stage and the microscope is focused on the detector with the microscope operating in the visible mode. The detector is translated from the focal point to the selected measurement plane and the power is measured at 25 μm increments as the detector is scanned across beam. The resulting measurements consist of the beam profile convolved with the detector response function. The detector response is deconvolved from

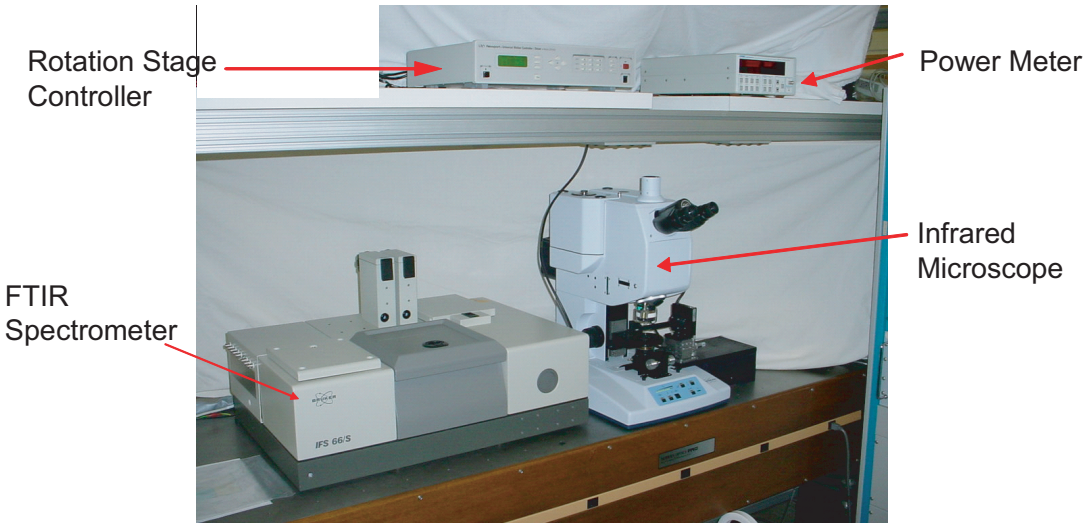

(a)

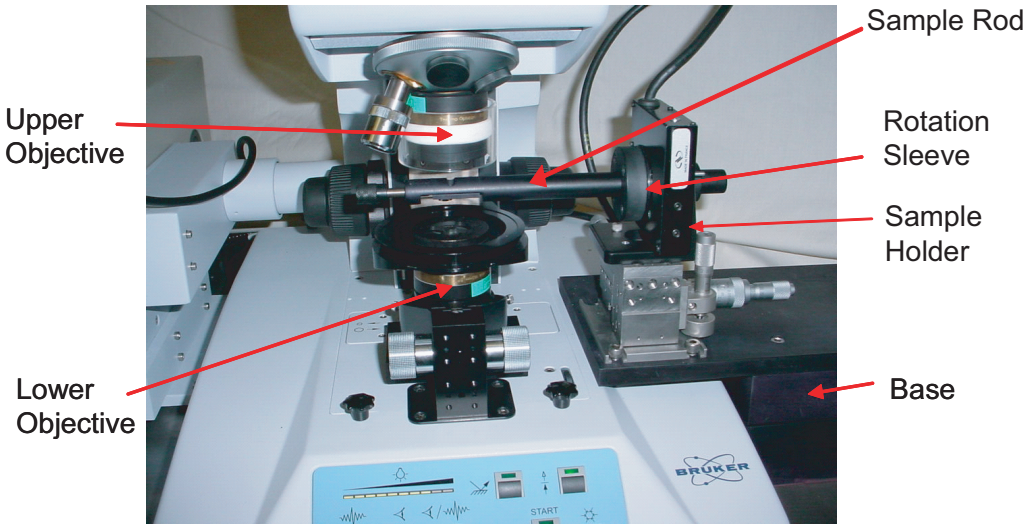

(b)

Figure 6.11: FTIR experimental apparatus: (a) The FTIR system consists of a Bruker IFS 66/S spectrometer coupled to a Bruker Hyperion 1000 infrared microscope. The system is controlled through a personal computer using Bruker's Optical User Software OPUS. (b) The microscope stage is removed and the sample holder is used to place the sample in the beam of the FTIR system.

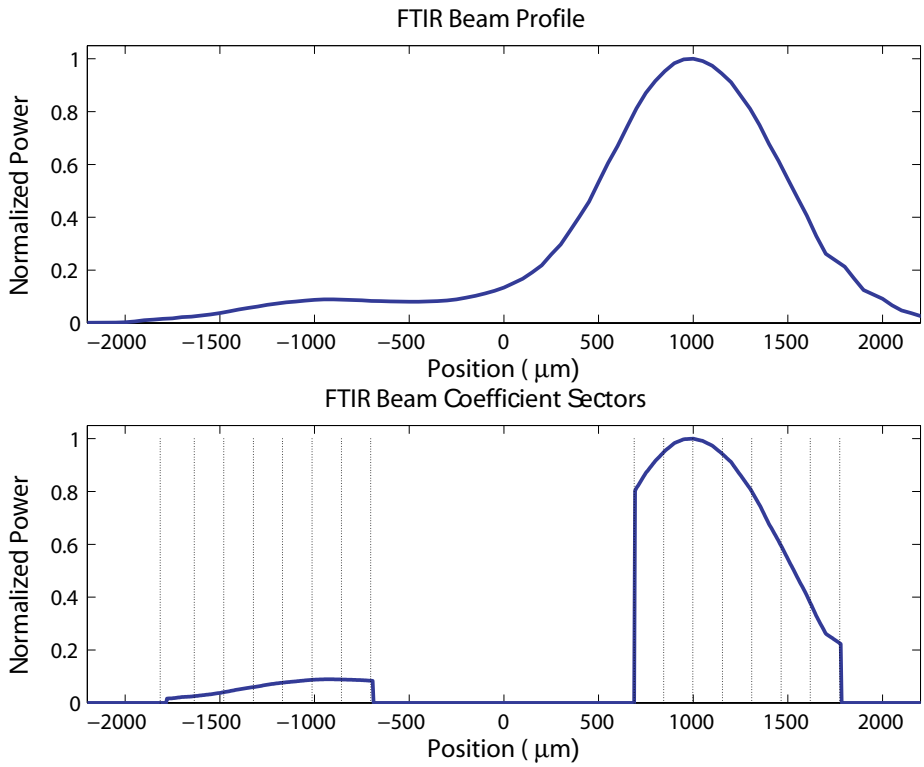

Figure 6.12: The globar source of the FTIR system produces a highly asymmetric probe beam. The measured profile for the reflectance measurement focusing objective is shown divided into approximately 2° sectors.

the measurement and the coefficients are calculated. The profile is shown in Fig. 6.12; as can be readily seen the FTIR beam is highly asymmetric.

The coefficients were also measured for the focusing beam of the infrared microscope in transmission mode. In transmission mode, the beam is focused by the lower objective and the detector cannot be observed by placing the microscope into the visible mode. The focal point must be determined by noting the focal point position for the reflectance measurements and positioning the detector in the same location. The detector is centered at the focal point by adjusting the position with the stage micrometers. From the focal point, the detector was moved to the measurement plane and the power was recorded. The profile was constructed and coefficients were computed. Coefficients for the focusing beam of the FTIR microspectroscopy system are listed in Table 6.2.

For the single-angle plane-wave computation, the asymmetric beam of the FTIR microspectroscopy system stabilizes the single-angle plane-wave computation. Just as the

Table 6.2: The coefficients were measured for the FTIR microspectroscopy focusing objectives and are shown in this table for 2° sectors for the objective used to focus light onto the sample.

	Beam Focusing Coefficients						
Measurement	a_1	a_2	a_3	a_4	a_5	a_6	a_7
Reflection	0.0035	0.0057	0.0090	0.0122	0.0146	0.0158	0.0155
Transmission	0.0062	0.0078	0.0140	0.0234	0.0243	0.0287	0.0201
	a_8	a_9	a_{10}	a_{11}	a_{12}	a_{13}	a_{14}
Reflection	0.1530	0.1760	0.1750	0.1570	0.1249	0.0871	0.0506
Transmission	0.1323	0.1634	0.1622	0.1602	0.1241	0.0911	0.0421

single lobe of incident light for the CO_2 experiment provided a more stable coefficient matrix for the CO_2-laser experiment, the condition number of the coefficient matrix for a one sided beam is more stable than a beam with energy equally distrubuted to both lobes.

6.2.4 FTIR Collector Coefficients

In the FTIR system, a collector objective is used in both transmittance and reflectance measurements. In transmittance measurements, the collector is the upper reflecting objective. In reflection mode, light is focused onto the sample by the upper objective and collected by the same objective after reflection. The collector coefficients are the same for both measurements. The upper objective was mounted into microscope and the plane used for the collection of light was noted. The objective was removed from the mount and the collecting objective coefficients were measured with the CO_2-laser system as described in Chapter 5. Table 6.3 lists the FTIR microspectroscopy system collector coefficients for 2° sectors of the objective.

6.2.5 FTIR Transmittance and Reflectance Measurement Procedures

A flow chart detailing the measurement procedures used for FTIR microspectroscopy of PC samples is shown in Fig. 6.13. The FTIR spectrometer and microscope are initialized and placed into operation using the OPUS software. The polarizer and objective slit are inserted into the system and a sample is mounted into the sample holder. A reference spectrum

Table 6.3: The coefficients were measured for the FTIR microspectroscopy collector objective and are shown in this table for 2° sectors.

Collector Coefficients						
a_1	a_2	a_3	a_4	a_5	a_6	a_7
0.0640	0.0687	0.0693	0.0700	0.0775	0.0818	0.0908
a_8	a_9	a_{10}	a_{11}	a_{12}	a_{13}	a_{14}
0.0951	0.0849	0.0784	0.0593	0.0570	0.0527	0.0505

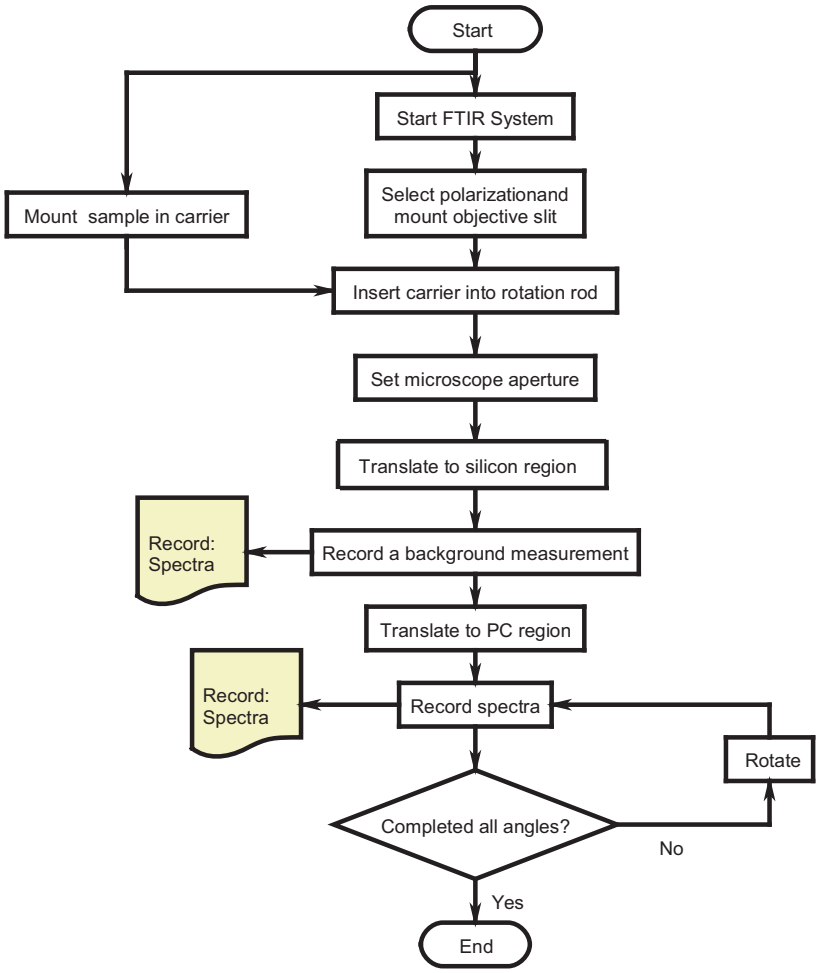

Figure 6.13: Flowchart detailing the procedures for conducting measurements with the FTIR microspectroscopy system.

must be recorded for the sample. The reference spectrum is obtained by measuring the spectrum of a silicon slab that is the same width as the PC sample. These regions were patterned and etched adjacent to each PC structure. Figure 4.9 shows an image of the cleaved device containing the silicon slab and adjacent PC region. The microscope aperture is aligned with the silicon region and the reference measurement is recorded. After the reference measurement, the sample holder is translated so that the PC region is aligned with the aperture and the transmittance or reflectance measurement of the PC sample is recorded. After the measurement at one angular orientation, the sample is rotated and the measurement is repeated at a new angle. For transmittance measurements, the detected power is relatively constant over a $\pm 30^\circ$ rotation range. For reflectance measurements, the detected power decreases rapidly as the sample is rotated and the maximum rotation range is reduced to approximately $\pm 15^\circ$. The FTIR software automatically computes the spectrum for each measurement using the recorded reference spectrum.

The FTIR microspectroscopy system is capable of rapidly recording multiple measurements at a single angular orientation. Prior to computing the spectrum, an average measurement is computed. As shown in Chapter 5, this can be expected to reduce the measurement noise by a factor proportional to the square root of the number of samples.

6.2.6 FTIR Characterization Apparatus Summary

The FTIR microspectroscopy system provides a rapid method to measure the transmittance or reflectance of the PC structures. The transmittance or reflectance for all wavelengths in the wavelength range of the source are measured simultaneously at a single angular orientation. The sample holder allows the sample to rotate freely in the beam of the system. The system is limited by the relatively low power of the globar source.

6.3 Summary

In this chapter, the apparatus and procedures used to collect data for the multiple-measurement scheme were presented. The apparatus for the CO_2-laser system was designed and each component was mounted onto an optical table. The measurement procedure for the CO_2-laser system was developed allowing the transmittance of PC structures to be measured over the

wavelength tuning range of the CO_2 laser. The sample apparatus was constructed to permit the sample to rotate freely in the CO_2-laser beam. The FTIR microspectroscopy system is an integrated system that enables the transmittance or reflectance of a PC sample to be rapidly measured over a broad wavelength range. Procedures and apparatus to conduct the measurements with the FTIR microspectroscopy system were presented.

CHAPTER 7

PHOTONIC CRYSTAL TRANSMITTANCE MEASUREMENTS USING THE CO_2-LASER APPARATUS

In this chapter, CO_2-laser transmittance measurements of 1-dimensional PC structures with spectral features in the 9 μm to 11 μm wavelength range are presented and analyzed. Sources of measurement error are identified to determine if the data recorded from the apparatus exceeds the identified maximum error threshold suitable for the single-angle plane-wave analysis scheme. The transmittance of the structure to a composite, multiple-incident-angle probe beam is compared to the theoretical composite beam transmittance. The single-angle plane-wave characterization scheme is applied to the measurements and the resulting measured single-angle plane-wave transmittances of the structure are compared to theoretical transmittances. The RMS error data for measured structures is analyzed to evaluate the effectiveness of the CO_2-laser characterization apparatus. Advantages and limitations of the apparatus are identified and discussed.

7.1 Sources of Measurement Error

In Chapter 5, the importance of computing an estimate of the measurement error expected in each characterization apparatus was presented. An approximate maximum tolerable measurement noise level of 5% was identified as the limit that would permit the recovery of representative single-angle plane-wave transmittances. The major sources of measurement error with the CO_2-laser characterization apparatus are the errors associated with obtaining of the objective weighting coefficients, the error introduced by the varying spectral response of the optical components, and the error introduced by the measurement of the transmitted power.

Errors in the measurement of the weighting coefficients directly affects the computed single-angle plane-wave transmittance of the PC structures. Coefficients are measured for the CO_2-laser apparatus using the scanning slit system as described in Chapter 6. The constructed profile is relatively constant at an individual wavelength. The results of many individual scans can be averaged to reduce further the measurement noise associated with the computation of the beam coefficients. The direct measurement of the profile and the ability to use multiple measurements to reduce random error decreases the estimated error associated with this source to levels less than the established 5% limit.

The optical components used in the CO_2-laser apparatus are constructed from zinc-selenide material and are anti-reflection coated for operation at a wavelength of $\lambda = 10.59\ \mu m$. Over the tuning range of the system, the optical transmission through the zinc-selenide components varies. Data can be corrected for this variation by characterizing the optical path through all coated components as a function of wavelength. The use of the power detector for this measurement introduces measurement error. However, for the optical path characterization, the power measured at each wavelength typically exceeds 3 W. At this relatively high power level, measurement noise associated with the detector is small. Consequently, the optical path characterization measurement noise is low. The optical path characterization noise is further reduced by averaging the results of multiple optical path characterization measurements.

The dominant measurement error source in the CO_2-laser apparatus is the noise associated with the transmitted power measurement. The Thermo-Oriel OPM thermopile power detector has a measurement range from 2 mW to 10 W. Over this power range, a single power measurement fluctuates by a percentage of the incident power. The fluctuation is the result of the detector measurement noise, the detector's relatively slow response time, and the small power fluctuations associated with the laser. The magnitude of the fluctuation ranges from less than 1% at power levels greater than 3 W to as high as 15% at power levels approaching the 2 mW detection threshold. In transmission bands of a PC structure, the measurement noise associated with the detector is typically in the 1% to 3% fluctuation

range. However, in photonic band gap regions of a PC structure spectrum, the low transmitted power associated with the photonic band gap moves the fluctuation into the range exceeding 10%. For transmittance measurements conducted near a photonic band gap, this noise level dominates the total characterization system error and exceeds the established thresholds for use of the single-angle plane-wave computation analysis scheme.

To summarize, the measurement noise for the CO_2-laser apparatus is dominated by the detector noise. A majority of measurements are conducted when the noise from this source ranges from 1% to 3%. However, at some wavelengths and angular orientations of the objective axis with respect to the sample normal, the detector measurement noise exceeds 10% and certainly impacts PC structure characterization. Improvements in the detection of transmitted power are required to reduce the measurement noise level of this apparatus to more acceptable levels.

At current noise levels, the computation of the single-angle plane-wave transmittance from data measured using the CO_2-laser apparatus can be expected to exceed the identified RMS error threshold of 0.700 as described in Chapter 5. Recommendations for reducing the noise present in CO_2-laser measurements are discussed in Chapter 9. Despite the relatively high-noise level associated with the data, the analysis of representative measurements from the CO_2-laser apparatus provides useful insight into the employment of this characterization apparatus and the single-angle plane-wave computation scheme for the long-wavelength PC infrared design and development methodology.

7.2 CO_2-Laser Composite Transmittance Measurements

A composite transmittance measurement obtained using the CO_2-laser apparatus consists of power transmittances at a single angular orientation of the objective axis with respect to the sample normal for all available wavelengths within the tuning range of the laser. The reference power measurement recorded at each wavelength is used to relate the varying power levels to each other (power normalization) at the various wavelengths. The normalized transmittance, T_N, for the CO_2-laser measurements is computed by normalizing the related power data for all wavelengths and all objective orientation angles. Since the data

used in the composite transmittance comparison are not processed other than for this normalization, the composite transmittance analysis can be used to evaluate the effectiveness of the apparatus at measuring the transmittance of the structure.

The composite transmittance analysis is illustrated using transmittance data recorded for a 28-period, 1-dimensional PC structure that consists of alternating layers of air and silicon with the thickness of the silicon regions equal to $t_{Si} = 4.40\ \mu m$ and the air regions thickness equal to $t_{air} = 6.20\ \mu m$. The optical axis of the CO_2 laser was positioned to strike the small mirror of the reflecting microscope objective off center, thus producing a single lobe of light that is incident on the structure. The objective axis angle was rotated with respect to the sample normal over the range from $\theta_S = 26^\circ$ to $\theta_S = -40^\circ$. The large rotation range in the negative direction compared to the positive direction is the result of the light being incident from only one side of the objective. The included plane-wave angles in a single measurement range from $\theta_S + 10^\circ$ to $\theta_S + 24^\circ$.

The theoretical transmittance calculation is computed by weighting theoretical single-angle plane-wave transmittances of the structure using the measured beam profile and computed beam coefficients. The MIP-GEN computation of the theoretical structure transmittance includes a 2% uniformly distributed, random deviation in the fill factor from one period to the next; the approximate 2% deviation in fill factor accounts for the variation in fill factor at different depths of the structure due to the sidewall taper. The 2% deviation value is based on SEM measurements of the variation. In a single structure, the variation ranges from approximately 1% to 3%. Figure 7.1 shows the effect of fill factor deviations from 0% to 2% on the theoretical transmittance. As shown, with a 0% deviation, the transmittance oscillates over a large range. As the random fill factor deviation increases, the oscillation range and overall transmittance decreases. Additionally, each computation, with a different set of random deviations, produces significantly different theoretical transmittance. Figure 7.2 shows 3 computations for the theoretical transmittance of the structure where each plot represents the average of 10 different computations with a 2% uniformly distributed, random deviation in the fill factor.

The large variation in the theoretical transmittance from trial to trial will effect the

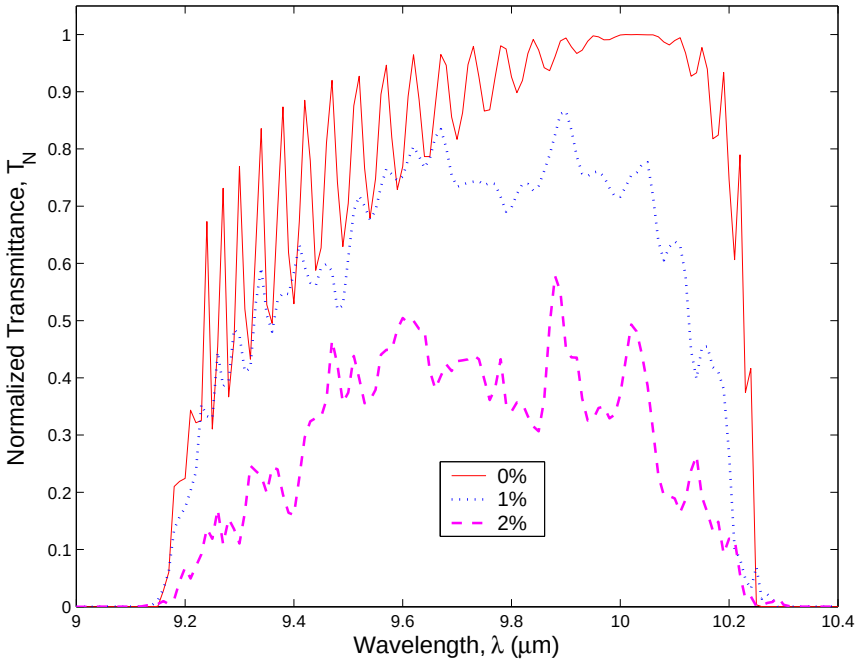

Figure 7.1: The theoretical composite transmittance for a PC structure with 0%, 1%, and 2% random deviation in fill factor. Each plot is an average transmittance of 10 simulated structures with the same fill factor random deviation.

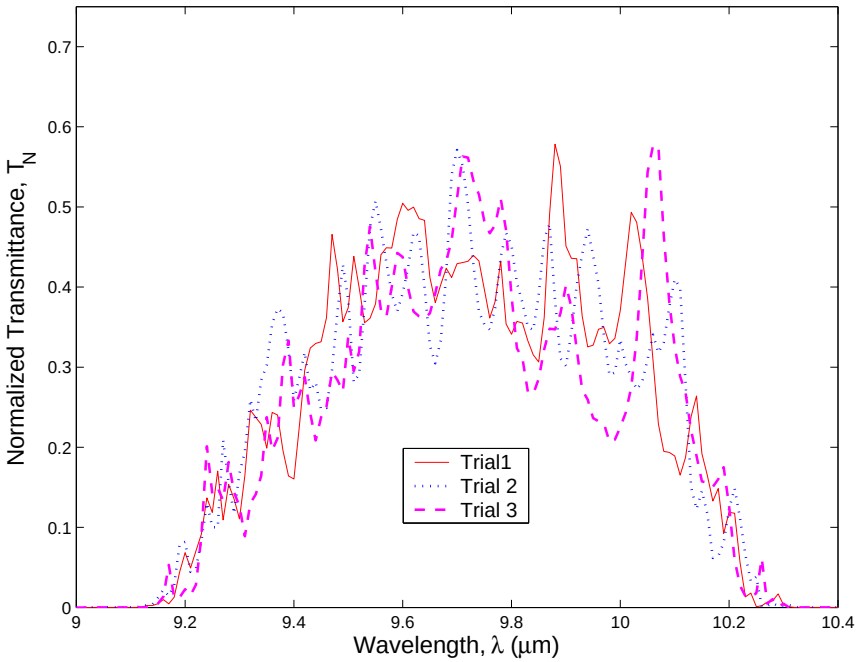

Figure 7.2: Three theoretical composite transmittance calculations for a PC structure with 2% random deviation in fill factor from period to period. Despite identical noise level parameter for each calculation, significant differences in the compute spectra are observed. Each plot is an average transmittance of 10 simulated structures .

RMS error calculation for each data set. Theoretical transmittances with identical noise level parameters may produce significant changes in the RMS error. Additionally, the erratic transmittance shown by a single computation can be expected in an single experimental measurement of a structure.

Figures 7.3 through 7.5 show the normalized measured composite transmittance of the structure compared to the theoretical normalized transmittance for various objective axis angles. The calculated RMS error comparing the measured transmittance with the theoretical transmittance for each angle is given along with each plot.

The plots in the figures show general agreement between the composite measured transmittance and the theoretical transmittance. The influence of the measurement noise, as discussed in the previous section, is also evident in the measurements. Because of noise effects, many spectral features of interest in the theoretical computations are not reproduced in the composite measured transmittance data.

In Fig. 7.3, the theoretical composite transmittances and measured composite transmittances for objective axis angular orientations of $\theta_S = 20^\circ$ and $\theta_S = 8^\circ$ are shown. At $\theta_S = 20^\circ$, the light is incident on the structure over the angular range from $\theta_k = 30^\circ$ to $\theta_k = 44^\circ$. The theoretical transmittance spectra shows constant, smooth, and relatively high transmittance across the wavelength range at this angular orientation. The corresponding measurements show large variation in the measured transmittance. Despite the variation, the overall transmittance at the larger incident angles is relatively high.

At $\theta_S = 8^\circ$, the light is incident at angles in the range from $\theta_k = 18^\circ$ to $\theta_k = 32^\circ$. The theoretical spectrum shows a transmission band centered at a wavelength of $\lambda = 9.5\ \mu m$ and a transmission null centered at a wavelength of $\lambda = 10.2\ \mu m$. The composite measurements show both the increased transmittance at transmission band wavelengths and the decreased transmittance at transmission null wavelengths. An approximate measurement floor of 0.1 is evident in the transmission null region of the spectrum. The composite measurement also shows increased transmittance at the edge of the tuning range near a wavelength of $\lambda = 10.8\ \mu m$. Despite the notable decrease in transmittance, accurate reproduction of the band edge between $\lambda = 9.8\ \mu m$ and $\lambda = 10.0\ \mu m$ cannot be assumed since the laser power

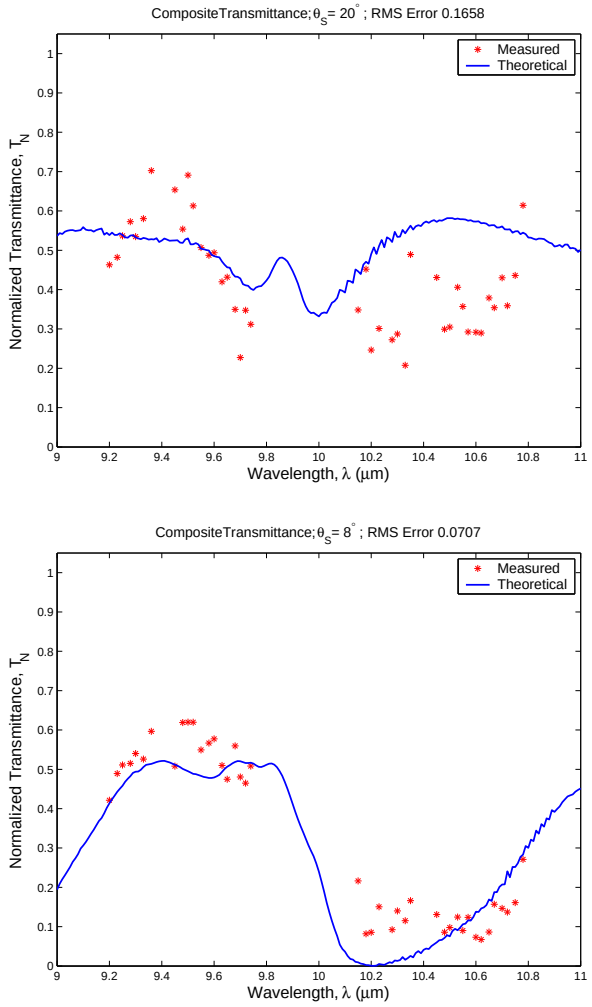

Figure 7.3: The measured composite transmittance of a scaled PC structure compared to the theoretical composite transmittance. The theoretical composite transmittance is calculated by weighting the objective-selected single-angle plane-wave transmittances of the structure for each included incident angle. The plots show the transmittance for an objective axis angular orientation of $\theta_S = 20°$ and $\theta_S = 8°$.

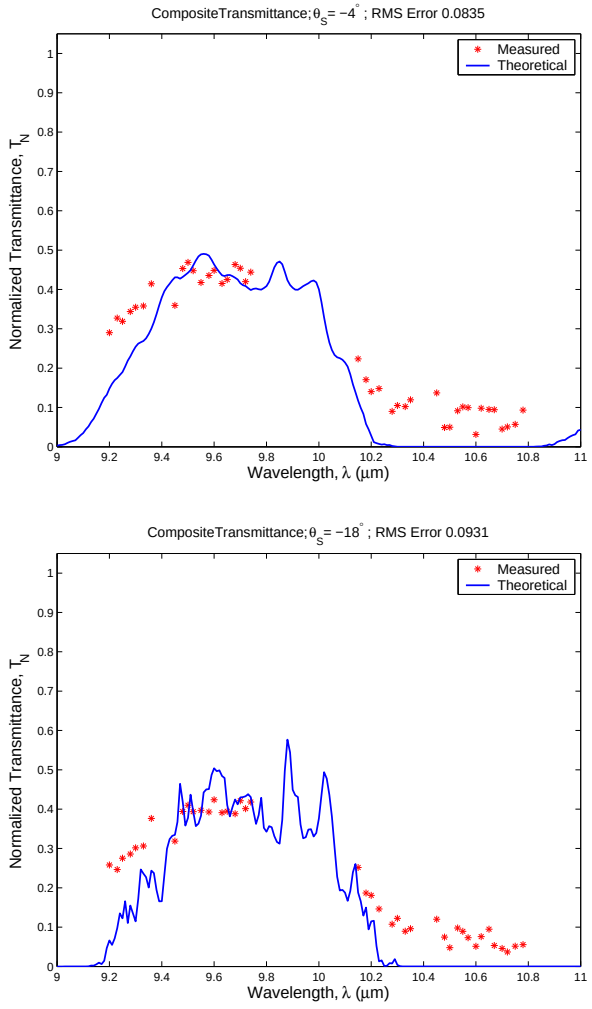

Figure 7.4: The measured composite transmittance of a scaled PC structure compared to the theoretical composite transmittance. The plots show the transmittance for an objective axis angular orientation of $\theta_S = -4°$ and $\theta_S = -18°$.

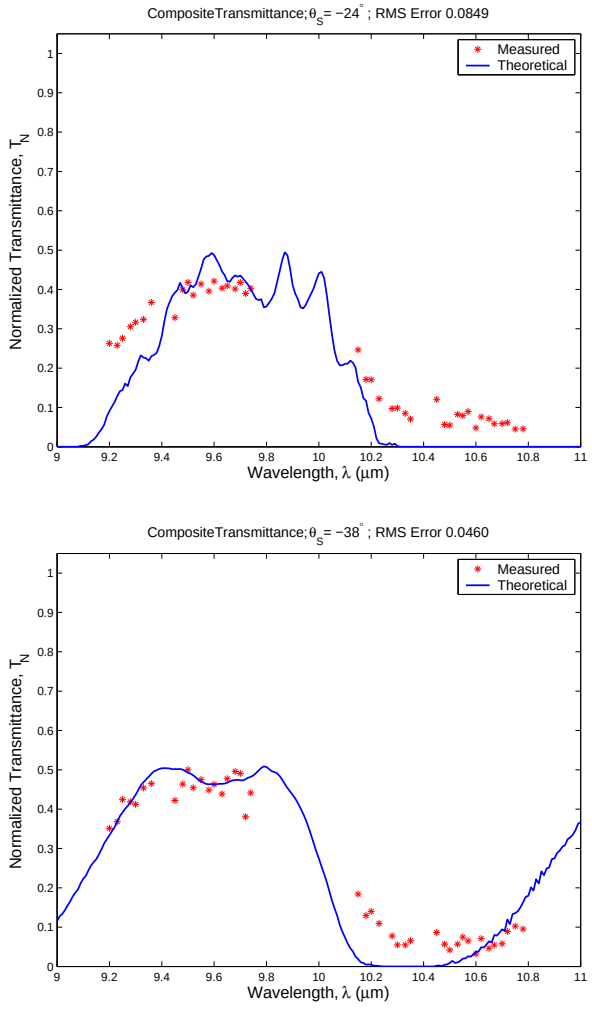

Figure 7.5: The measured composite transmittance of a scaled PC structure compared to the theoretical composite transmittance. The plots show the transmittance for an objective axis angular orientation of $\theta_S = -24°$ and $\theta_S = -38°$.

across this wavelength range is insufficient to record measurements.

Figure 7.4 shows the composite normalized transmittance measurements and theoretical transmittances for objective axis angular orientations of $\theta_S = -4°$ and $\theta_S = -18°$. Both plots of the measured data follow the theoretical trends over the transmission band. Additionally, since the band edge near $\lambda = 10.2\ \mu m$ has shifted toward wavelengths where the power level is sufficient to record measurements, the band edge is unquestionably reproduced.

As the included incident angles approach normal incidence, the theoretical plot shows increased variation in the transmittance from wavelength to adjacent wavelength. The relatively smooth curve in the plot at the top of the figure for $\theta_S = -4°$, corresponds to the situation where the included incident angles range from $\theta_k = 6°$ to $\theta_k = 20°$. In the lower plot, where $\theta_S = -18°$, the included incident angles are near normal incidence ranging from $\theta_k = -8°$ to $\theta_k = 6°$ and the erratic variation from wavelength to adjacent wavelength increases. The composite transmittance measurements do not show this trend. Finally, over the transmission null centered at $\lambda = 10.6\ \mu m$, the measurements continue to show significant transmission compared to the zero-valued transmittance shown in the theoretical calculation. The power level recorded at these data points falls near the detection threshold of the power detector.

Figure 7.5 shows the composite transmittances and theoretical transmittances for objective axis angular orientations of $\theta_S = -24°$ and $\theta_S = -38°$. Once again, as the objective axis is rotated to these extreme angles, the composite measurements show general agreement with theory but are unable to resolve rapid variations with wavelength to include local transmission minima or maxima.

Table 7.1 contains the RMS values for the composite normalized transmittances, T_N, calculated for all objective axis angular orientations at 2° increments of the objective axis. The RMS errors are relatively constant for most of the objective axis angular orientations. However, as the incidence angle of the included plane-waves increases, the RMS errors also increase. The error for composite transmittance measurements with included plane-wave angles in the range from $\theta_k = 32°$ to $\theta_k = -32°$ is constant. There is an increase in the

Table 7.1: RMS errors comparing the measured composite CO_2-laser transmittances with theoretical calculations.

θ_S (deg)	Included Plane-Wave Angles (deg)	RMS Error in T_N	θ_S (deg)	Included Plane-Wave Angles (deg)	RMS Error in T_N
26	36 to 50	0.2063	-8	2 to 16	0.0833
24	34 to 48	0.1717	-10	0 to 14	0.0854
22	32 to 46	0.1590	-12	-2 to 12	0.0890
20	30 to 44	0.1658	-14	-4 to 10	0.0924
18	28 to 42	0.1656	-16	-6 to 8	0.0939
16	26 to 40	0.1574	-18	-8 to 6	0.0931
14	24 to 38	0.1472	-20	-10 to 4	0.0908
12	22 to 36	0.1256	-22	-12 to 2	0.0886
10	20 to 34	0.0970	-24	-14 to 0	0.0849
8	18 to 32	0.0707	-26	-16 to -2	0.0823
6	16 to 30	0.0587	-28	-18 to -4	0.0794
4	14 to 28	0.0512	-30	-20 to -6	0.0730
2	12 to 26	0.0646	-32	-22 to -8	0.0728
0	10 to 24	0.0683	-34	-24 to -10	0.0634
-2	8 to 22	0.0756	-36	-26 to -12	0.0533
-4	6 to 20	0.0835	-38	-28 to -14	0.0460
-6	4 to 18	0.0776	-40	-30 to -16	0.0627

error at objective angular orientations where the included angles are near-normal incidence. This increase at near normal incidence is partly the result of the increased variation in the theoretical plot from wavelength to adjacent wavelength with light near normal incidence.

The composite transmittance measurements from the CO_2-laser apparatus show that the apparatus is capable of detecting the composite transmittance of PC structures. Currently, large transmission bands and band edges are detected. The apparatus is most effective over an angular range where the included incident angles range from $\theta_k = 32^\circ$ to $\theta_k = -32^\circ$. The measurement noise associated with the current apparatus must be reduced to enable detection of more detailed spectral features.

7.3 Single-Angle Plane-Wave Computations

Despite the large measurement noise associated with the CO_2-laser apparatus, the single-angle plane-wave characterization method was applied to the composite transmittance measurements. The single-angle plane-wave theoretical calculation is also significantly effected

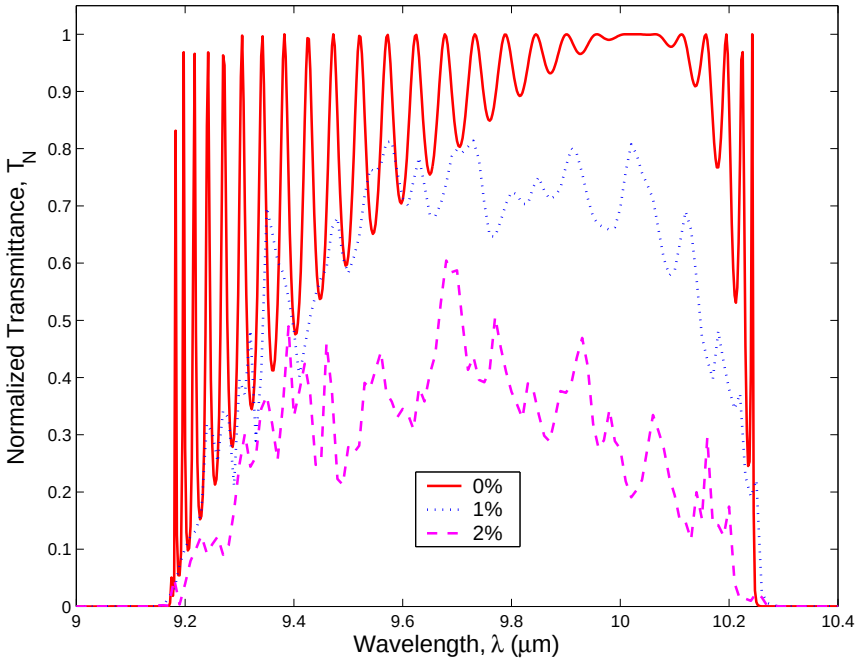

Figure 7.6: The single-angle plane-wave theoretical transmittance for period-to-period fill factor deviations of 0%, 1% and 2%. Each plot is an average single-angle plane-wave computation for 10 structures with the specified fill factor variation.

by the random fill factor variation as shown for the composite transmittance measurements. Figure 7.6 shows the effects of fill factor deviations over the range from 0% to 2% on the single-angle plane-wave theoretical transmittance calculations. Figure 7.7 shows the variation in the single-angle plane-wave transmittance from computation to computation under an equal 2% random deviation condition. These variations in the theoretical computations effect the RMS computation for a single angle plane-wave measured transmittance. Small deviations in the magnitude of the variation and can result in significant theoretical transmittance calculations.

Figures 7.8 through 7.10 show the measured single-angle plane-wave transmittances and the theoretical plane-wave transmittances for various angles. As expected, RMS errors are large.

Once again, the figures show general agreement between the measured single-angle plane-wave transmittances and the ideal transmittances. Rapidly varying spectral details are not evident in the measured single-angle plane-wave transmittances. Spectral regions where the theoretical transmission is equal to zero continue to show small, but still significant,

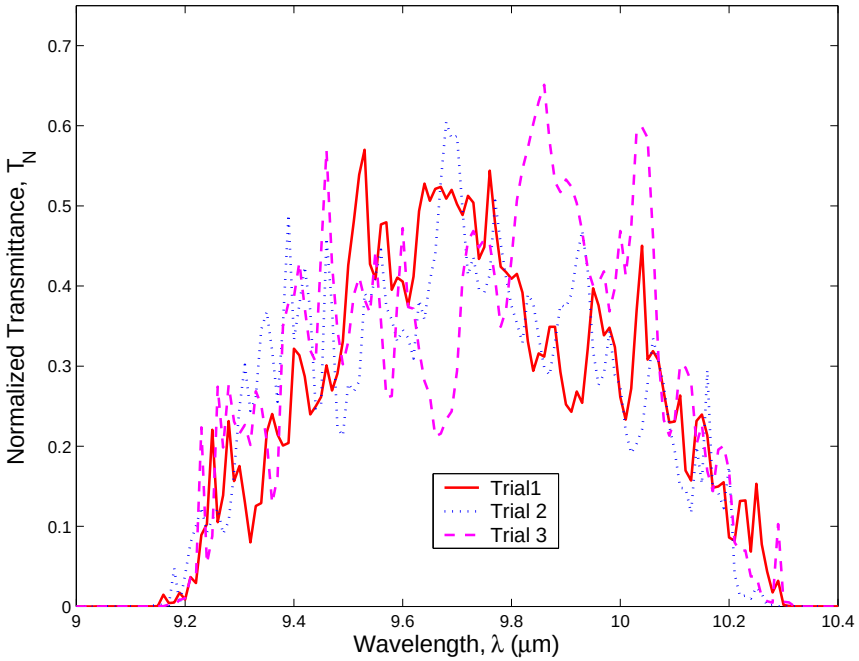

Figure 7.7: The theoretical single-angle plane-wave transmittances for 3 computations when the random fill factor variation is 2%. Each plot is an average single-angle plane-wave computation for 10 structures with the 2% fill factor variation.

transmittance; these regions correspond to the measurements where the detected power is near the 2 mW threshold of the detector. The single-angle plane-wave transmittance corresponding to an angle of $\theta_k = 19°$ possesses the smallest RMS error.

The RMS errors for measured single-angle plane-wave transmittances are listed in Table 7.2. The error is relatively constant for the plane-wave calculations over the angular range from $\theta_k = 1°$ to $\theta_k = 23°$. For angles exceeding $\theta_k = 23°$, the single-angle plane-wave solution deteriorates rapidly. This is consistent with the increased error present in the composite measurements when the included angles are incident at more oblique angles.

The large RMS error values also correspond to single-angle plane-wave computations where fewer measurements contribute to the computation of the solution. The plane-wave computations that utilize less measured data (at the extreme objective orientation angles at extreme objective axis angles) have greater deviations from the theoretical values. In the present data set, the objective axis was rotated from $\theta_S = 26°$ to $\theta_S = -40°$ with respect to the sample normal. At the extreme objective axis angular orientation of $\theta_S = 26°$, the included angles range from $\theta_k = 36°$ to $\theta_k = 50°$; this is the only measurement that

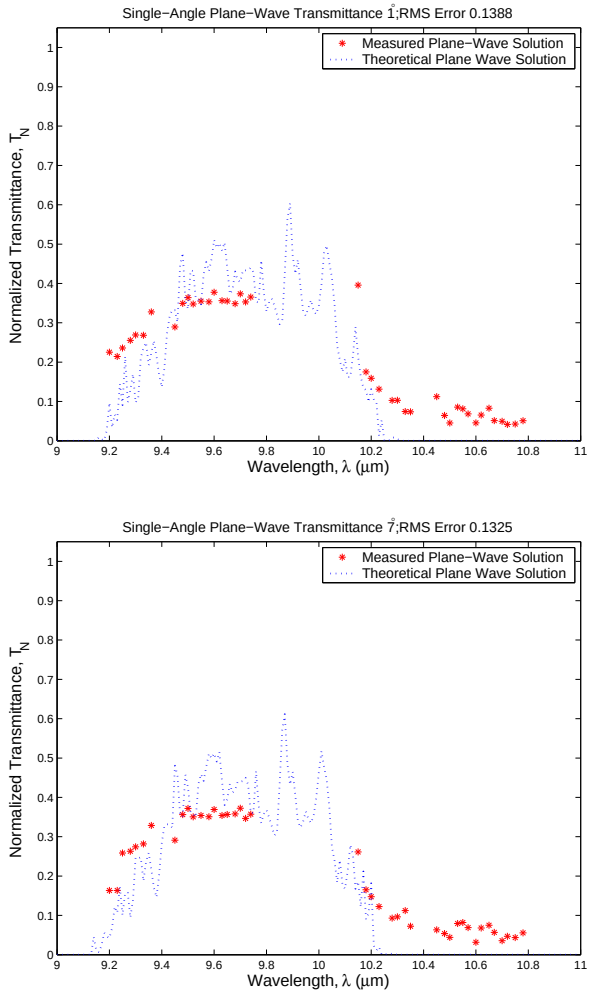

Figure 7.8: The measured single-angle plane-wave transmittance of a PC structure is compared to the theoretical single-angle plane-wave transmittance. The plots show the transmittances for incident plane-wave angles of $\theta_k = 1^\circ$ and $\theta_k = 7^\circ$.

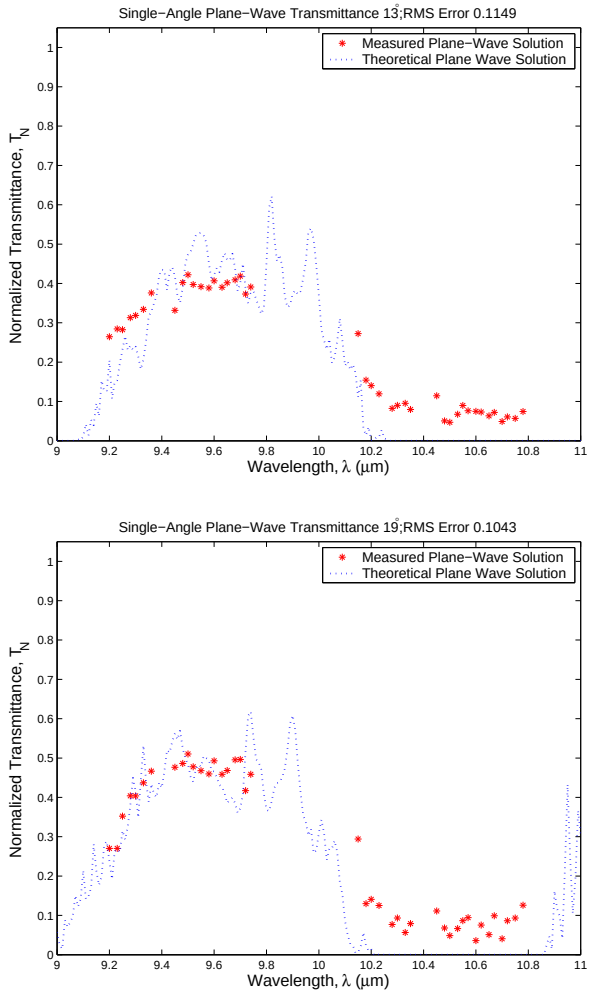

Figure 7.9: The measured single-angle plane-wave transmittance of a PC structure is compared to the theoretical single-angle plane-wave transmittance. The plots show the transmittances for incident plane-wave angles of $\theta_k = 13°$ and $\theta_k = 19°$.

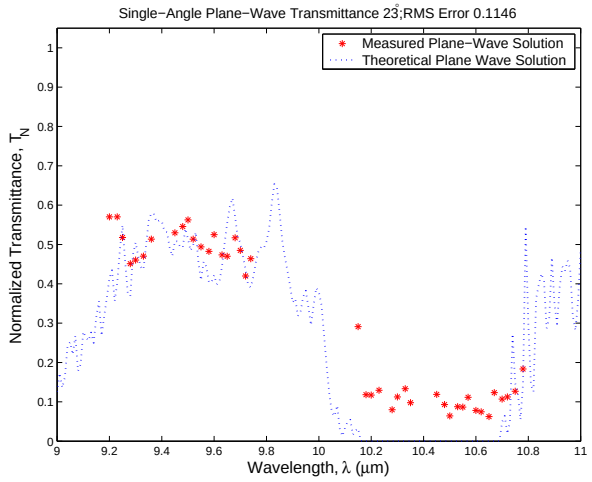

Figure 7.10: The measured single-angle plane-wave transmittance of a PC structure is compared to the theoretical single-angle plane-wave transmittance. The plots show the transmittances for incident plane-wave angles of $\theta_k = 23°$.

Table 7.2: RMS errors for the measured single-angle plane-wave CO_2-laser transmittances compared to theoretical calculations. The number of measurements utilized for each calculation is also listed.

Plane-Wave Angle (deg)	Number of Measurements	RMS Error in T_N	Plane-Wave Angle (deg)	Number of Measurements	RMS Error in T_N
49	1	0.2148	23	12	0.1146
47	2	0.2128	21	13	0.1166
45	3	0.2138	19	14	0.1043
43	4	0.2500	17	14	0.1188
41	5	0.2510	15	14	0.1256
39	6	0.2071	13	14	0.1149
37	7	0.2028	11	14	0.1337
35	7	0.2281	9	14	0.1247
33	7	0.2209	7	13	0.1325
31	8	0.2228	5	11	0.1321
29	9	0.2170	3	9	0.1254
27	10	0.2067	1	7	0.1388
25	11	0.1668			

includes light that is used to compute the single-angle plane-wave transmittance for an angle of incidence of $\theta_k = 49°$. As the single-angle plane-wave angle progresses towards $\theta_k = 0°$, the number of measurements used to compute each transmittance increases until it reaches a maximum of 14 measurements. As the incident angle decreases below $\theta_k = 9°$, the number of measurements again decreases. Table 7.2 lists the number of measurements that contribute to the computation of each single-angle plane-wave transmittance. The lowest RMS error occurs in the region from $\theta_k = 9°$ to $\theta_k = 23°$ where a large number of measurements contribute to the determination of the single-angle plane-wave solution.

The single-angle plane-wave transmittances derived from data collected using the CO_2-laser apparatus show trends similar to the composite transmittance comparison. General transmission spectra are recovered while rapidly varying details of the spectrum are less readily apparent. As expected, increased error in the composite transmittance results in large errors in the single-angle plane-wave transmittance calculation. Additionally, error appears to decrease as more measurements contribute to the computation of a single-angle plane-wave transmittance spectrum.

7.4 CO_2-Laser Apparatus Advantages and Limitations

The CO_2-laser apparatus measurements show that the spectral transmittances of PC structures can be measured with the CO_2 laser. The composite measurements of PC structures show agreement with the theoretical calculations. Measurements show the correct general trends in structure transmittance; however, many of the desired details of the structure transmittance characteristics are not evident in the composite transmittances or the measured single-angle plane-wave transmittances. Reduced measurement noise levels will produce better results.

7.4.1 Advantages

The CO_2-laser apparatus provides a low-cost method to measure the spectral transmittance of PC structures. The high-power available and corresponding large rotation range potentially enable the characterization of a PC structure over a large range of plane-wave angles. Theoretically, application of the single-angle plane-wave computation will provide

more detailed data than composite measurements. Current measurement noise levels must be reduced in order to demonstrate this claim through experiments.

7.4.2 Limitations

The noise level of measurements with the CO_2-laser apparatus is a major challenge to the use of the CO_2-laser apparatus in conducting spectral measurements of PCs. The power measurement error must be reduced in order to decrease the noise level. The use of a sensitive, high-dynamic-range power detector will reduce the noise level by enabling accurate measurement of extremely low transmitted power levels characteristic of a photonic band gap spectral range. The detector employed currently has a measurement floor that artificially skews the results.

The relatively short tuning range of the CO_2 laser and the wavelength ranges where the output power is below detection thresholds are significant limitations of this characterization tool. In particular, the spectral null in laser output over the wavelength range from $\lambda = 9.8\ \mu m$ to $\lambda = 10.15\ \mu m$ is large and approximately centered in the CO_2 laser's tuning range. Spectral features in this range cannot be observed. The laser output over this spectral range must be improved to employ the CO_2-laser apparatus in the characterization of PC structures.

Finally, data collection with the CO_2-laser apparatus is time consuming due to the need to measure the transmittance at each angle and at each wavelength individually. Recording a single data set for a single structure requires 15 to 20 hours over the limited spectral range of the CO_2-laser system. Repeated measurements to reduce measurement noise is not feasible with the existing system. To realize the full potential of this characterization system, automation of spectral measurements is required.

7.5 Summary

An analysis of the measurement error present in the CO_2-laser apparatus indicates that the noise associated with the measurements of the current apparatus should be reduced to utilize fully the single-angle plane-wave characterization method in the development of PC structures. The transmittance of PC structures was measured with the CO_2-laser apparatus.

In general, the theoretical and measured composite transmittances agree. The single-angle plane-wave characterization technique and algorithms were applied to the measured data. The measured single-angle plane-wave transmittance spectra match theoretical predictions though detailed spectral characteristics are not recovered in the single-angle plane-wave measured transmittances due to the measurement noise associated with this apparatus. Required improvements are discussed in Chapter 9.

CHAPTER 8

PHOTONIC CRYSTAL TRANSMITTANCE AND REFLECTANCE MEASUREMENTS USING THE FTIR MICROSPECTROSCOPY APPARATUS

In this chapter, FTIR measurements of 1-dimensional PC structures with spectral features in the 5 μm to 15 μm wavelength range are analyzed. Measurement noise present in the FTIR microspectroscopy system measurements is estimated to determine if the data recorded from the apparatus exceeds the identified maximum error threshold established for the single-angle plane-wave analysis scheme. The spectral transmittances or reflectances of PC structures are measured using the FTIR microspectroscopy system in both transmission and reflection modes. The transmittance or reflectance of the structure to a composite, multiple-incident-angle probe beam is compared to the theoretical composite beam transmittance or reflectance. The single-angle plane-wave characterization scheme is applied to the measurements and the measured single-angle plane-wave transmittances or reflectances of the structure are compared to theoretical single-angle plane-wave spectra. The RMS error data for measured structures is analyzed to evaluate the effectiveness of the FTIR microspectroscopy system as a characterization apparatus. Advantages and limitations of the apparatus for use in the spectral measurement of PC structures are identified and discussed.

8.1 Sources of Measurement Error

Current state-of-the-art FTIR microspectroscopy systems are designed to measure a variety of material transmission and reflection spectra. Optical components in the system are integrated and precisely controlled through a computer interface. The sophistication and advanced development state of the FTIR microspectroscopy system enables measurements to be recorded with relatively low noise. For this thesis, measurement noise for the FTIR

microspectroscopy system is estimated by comparing the amplitude of spectral oscillations over a small range of wavelengths ($\Delta\lambda = 0.3\ \mu m$) located in a reflection or transmission null of the spectrum to the maximum signal amplitude variation of the spectra over the entire 10 μm ($\lambda = 5\ \mu m$ to $\lambda = 15\ \mu m$) wavelength range. The amplitude variation of the spectra over the entire wavelength range is closely related to the strength of the detected signal.

In the transmission mode, the allowed sample rotation range where measurable signal levels are maintained, occurs from $\theta_S = 30°$ to $\theta_S = -30°$. The signal strength for spectral measurements remains relatively constant across the center of the rotation range from approximately $\theta_S = 20°$ to $\theta_S = -20°$ and then gradually decreases as the angular orientation is rotated to the extreme rotation limits. The peak-to-peak oscillation amplitude over the small $\Delta\lambda = 0.3\ \mu m$ wavelength range behaves similarly; it is relatively constant over the central $\theta_S = 20°$ to $\theta_S = -20°$ range and decreases as the rotation value approaches the extreme limits. However, the oscillation amplitude over the limited spectral wavelength range does not decrease as rapidly as the signal strength. The measurement noise over the central rotation range is from 0.5% to 3% while the measurement noise at the extreme measured angles ($\theta_S = 30°$ and $\theta_S = -30°$) approaches or exceeds 10%.

In the reflection mode, the allowed rotation range (theoretically from $\theta_S = \theta_{ob,max}$ to $\theta_S = -\theta_{ob,max}$) is restricted to approximately $\theta_S = 12°$ to $\theta_S = -12°$. For this measurement, the signal strength has a maximum value at $\theta_S = 0°$ and decreases as the sample is rotated to the extreme orientation angles. Although the oscillations over the restricted $\Delta\lambda = 0.3\ \mu m$ wavelength range also decrease, the oscillation amplitude over the restricted wavelength range relative to the signal amplitude increases, thus increasing the measurement noise level. Over the angular range from $\theta_S = 8°$ to $\theta_S = -8°$, the noise level ranges from 1% to 5%. At the extreme $\theta_S = \pm 12°$, the noise level falls within the 10% to 15% range.

To summarize, the measurement noise for the FTIR microspectroscopy apparatus is low and within the established 5% limit over a limited angular rotation range of the objective axis with respect to the sample normal. Transmittance measurements over a rotation range from $\theta_S = 20°$ to $\theta_S = -20°$ and reflectance measurements over a rotation range from $\theta_S = 8°$ to $\theta_S = -8°$ are within the 5% noise limit. As the angular orientation increases

beyond these limits, the noise level increases. Recommendations for reducing the noise level in an effort to increase the rotation range for the FTIR microspectroscopy measurements are presented in Chapter 9.

8.2 FTIR Microspectroscopy Composite Transmittance Measurements

A composite transmittance measurement using the FTIR microspectroscopy apparatus consists of a single spectral measurement for a single angular orientation of the objective axis with respect to the sample normal. The normalized transmittance, T_N, for the FTIR microspectroscopy measurements is computed by normalizing the measured spectra at each objective axis orientation angle. The measured composite normalized transmittance is then compared to the theoretical composite normalized transmittance.

The composite transmittance analysis is illustrated using measurements recorded for a 22-period, 1-dimensional PC structure that consists of alternating layers of air and silicon with the thickness of the silicon regions equal to $t_{Si} = 3.15\ \mu m$ and the air region thickness equal to $t_{air} = 4.55\ \mu m$. The objective axis angle was rotated with respect to the sample normal over the range from $\theta_S = 30°$ to $\theta_S = -30°$. Although the measured beam from the FTIR microscope has a majority of the optical power concentrated in one lobe as shown in Chapter 6 (Fig. 6.12), the light is incident from both sides of the objective. The included plane-wave angles in a single measurement range from $\theta_S + 10°$ to $\theta_S + 24°$ and from $\theta_S - 10°$ to $\theta_S - 24°$.

The theoretical transmittance calculation is computed by weighting theoretical single-angle plane-wave transmittances of the structure using the measured beam profile and computed beam coefficients. Similar to the theoretical computation for the CO_2-laser apparatus, the MIP-GEN computation of the theoretical structure transmittance includes a 2% uniformly distributed, random deviation in the fill factor; the 2% deviation accounts for the variation in fill factor at different depths of the structure due to the sidewall taper. The spectral variations caused by various values of the deviation percentage and the variations between individual theoretical computations using a constant deviation percentage

are similar to the variations shown in Chapter 7 (Fig. 7.1 and Fig. 7.2).

Figures 8.1 through 8.7 show the normalized composite measured transmittances compared to the theoretical normalized composite transmittances for all orientations of the objective axis over the angular rotation range from $\theta_S = 20^\circ$ to $\theta_S = -20^\circ$. This range corresponds to the rotation range when the measurement noise was below 5%. The RMS errors between the measured and theoretical normalized transmittances are listed.

The measured and theoretical composite transmittances show excellent agreement for the position of the transmission bands and photonic band gaps on the wavelength spectrum over the full $\theta_S = 20^\circ$ to $\theta_S = -20^\circ$ rotation range. Additionally, variations in spectral features across this rotation range are reproduced in the measurements as the objective axis rotates. For instance, the photonic bandgap centered at $\lambda = 7.6\ \mu m$ at an objective axis orientation of $\theta_S = 0^\circ$ (Fig. 8.4) shows a normalized transmittance near zero. As the objective axis is rotated to an angular position of $\theta_S = 20^\circ$ (Fig. 8.1), the transmittance at $\lambda = 7.6\ \mu m$ slowly increases showing the spectral variation theoretically calculated for an angular orientation of $\theta_S = 20^\circ$. At an angular orientation of approximately $\theta_S = 14^\circ$, the development of an additional variation in the spectrum at this wavelength can be observed. This spectral detail continues to correspond to the theoretical spectral variation through $\theta_S = 20^\circ$.

There is less agreement in the magnitude of the normalized transmittance throughout the objective rotation range. In the normalized plots, the theoretical transmittance maximum does not correspond to the measured maximum transmittance peak. In the theoretical computation, the transmittance maximum corresponds to the transmission band centered at a wavelength of $\lambda = 11.5\ \mu m$. In the measurements, the transmittance maximum is typically associated with the transmission band centered at $\lambda = 6.8\ \mu m$ at positive and near-normal objective axis orientations and at the transmission band centered at $\lambda = 8.5\ \mu m$ at the extreme negative objective axis orientations. Spectral variations resulting from scattering losses at the entrance plane of the PC may account for some of the differences in transmittance between the theoretical and measured spectra.

The RMS errors comparing the measured and theoretical normalized transmittances,

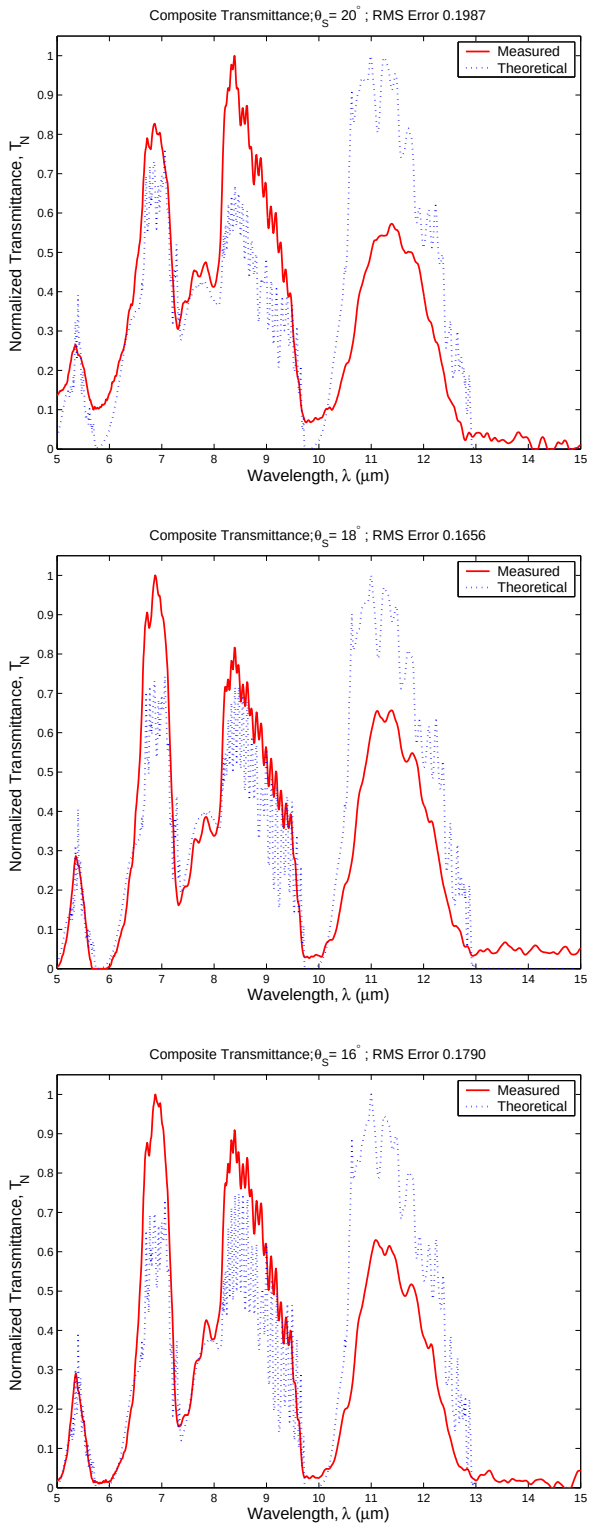

Figure 8.1: Composite normalized FTIR microspectroscopy transmittance measurements and normalized theoretical transmittance calculations of a PC structure. The measured and theoretical transmittances are shown for objective axis positions of $\theta_S = 20°$, $\theta_S = 18°$, and $\theta_S = 16°$ with respect to the sample normal.

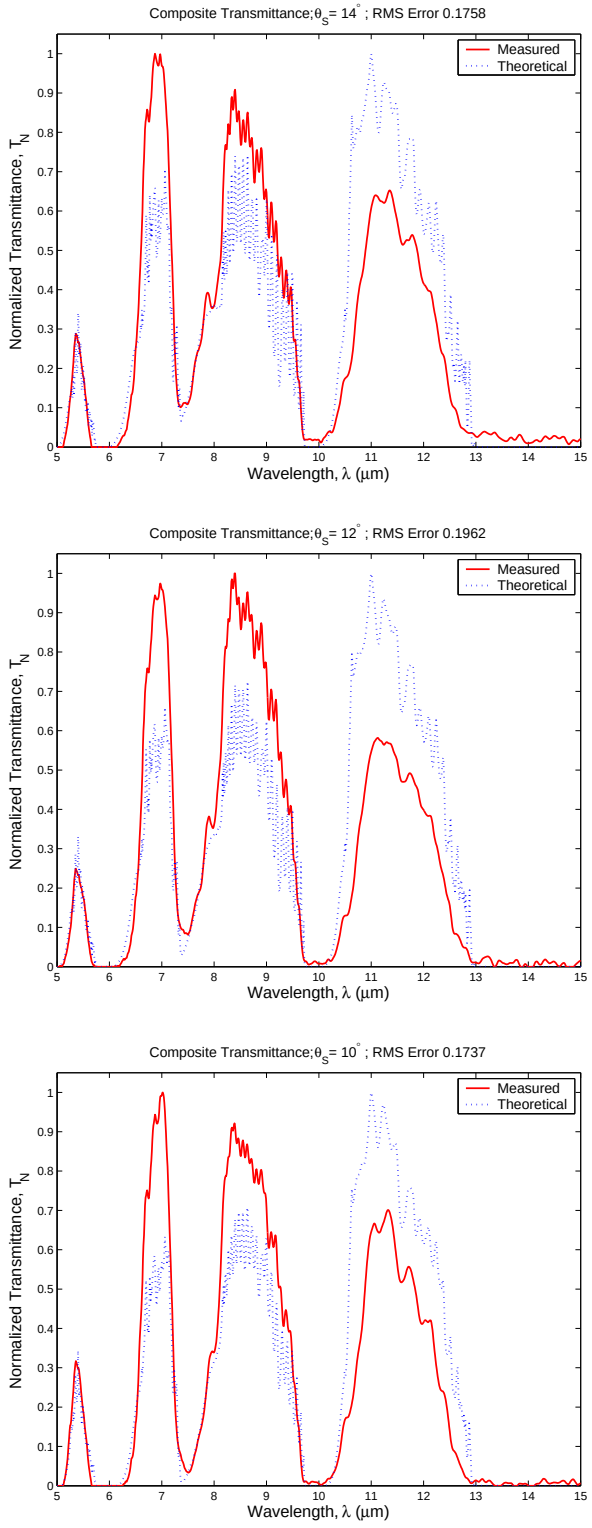

Figure 8.2: Composite normalized FTIR microspectroscopy transmittance measurements and normalized theoretical transmittance calculations of a PC structure. The measured and theoretical transmittances are shown for objective axis positions of $\theta_S = 14°$, $\theta_S = 12°$, and $\theta_S = 10°$ with respect to the sample normal.

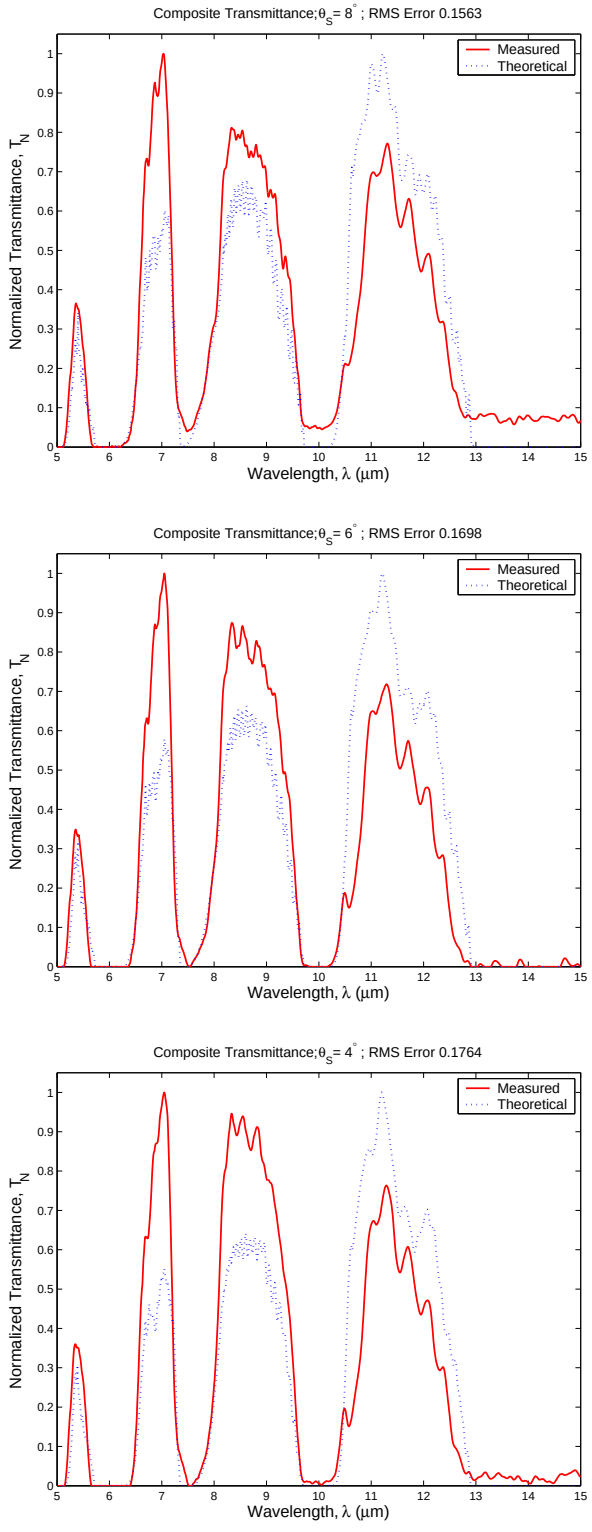

Figure 8.3: Composite normalized FTIR microspectroscopy transmittance measurements and normalized theoretical transmittance calculations of a PC structure. The measured and theoretical transmittances are shown for objective axis positions of $\theta_S = 8°$, $\theta_S = 6°$ and $\theta_S = 4°$ with respect to the sample normal.

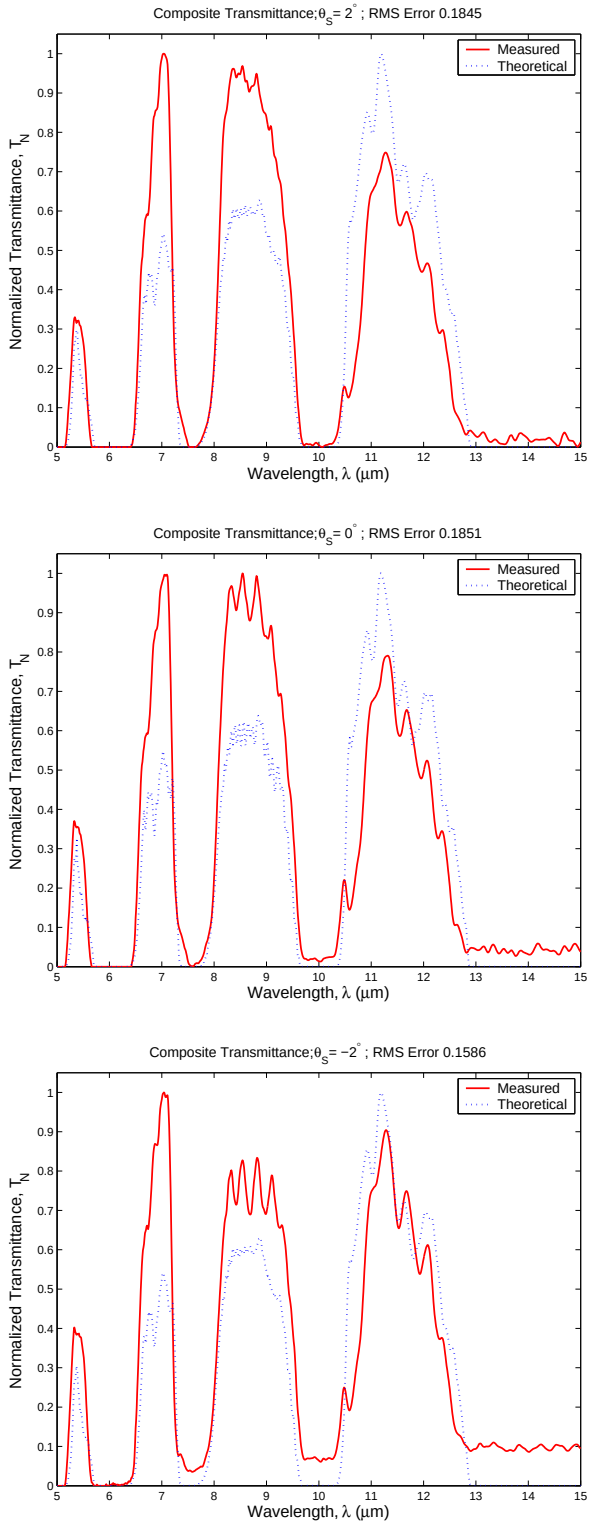

Figure 8.4: Composite normalized FTIR microspectroscopy transmittance measurements and normalized theoretical transmittance calculations of a PC structure. The measured and theoretical transmittances are shown for objective axis positions of $\theta_S = 2°$, $\theta_S = 0°$, and $\theta_S = -2°$ with respect to the sample normal.

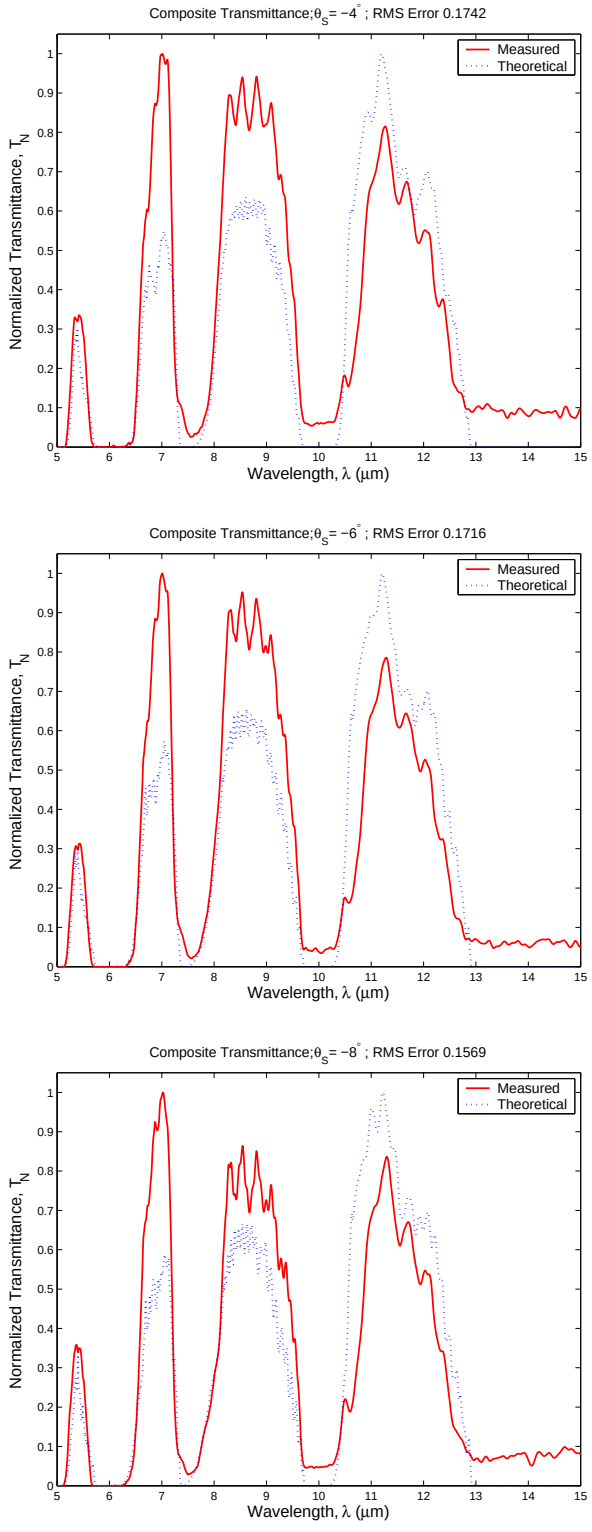

Figure 8.5: Composite normalized FTIR microspectroscopy transmittance measurements and normalized theoretical transmittance calculations of a PC structure. The measured and theoretical transmittances are shown for objective axis positions of $\theta_S = -4°$, $\theta_S = -6°$, and $\theta_S = -8°$ with respect to the sample normal.

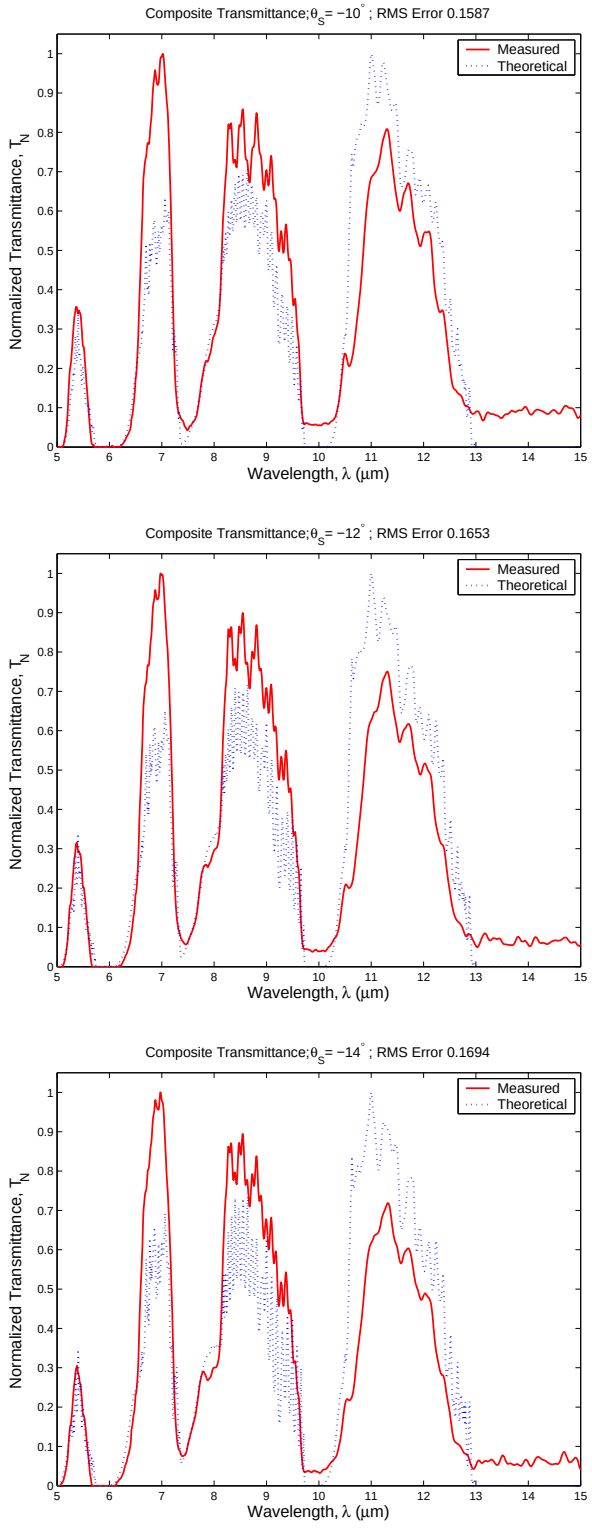

Figure 8.6: Composite normalized FTIR microspectroscopy transmittance measurements and normalized theoretical transmittance calculations of a PC structure. The measured and theoretical transmittances are shown for objective axis positions of $\theta_S = -10°$, $\theta_S = -12°$, and $\theta_S = -14°$ with respect to the sample normal.

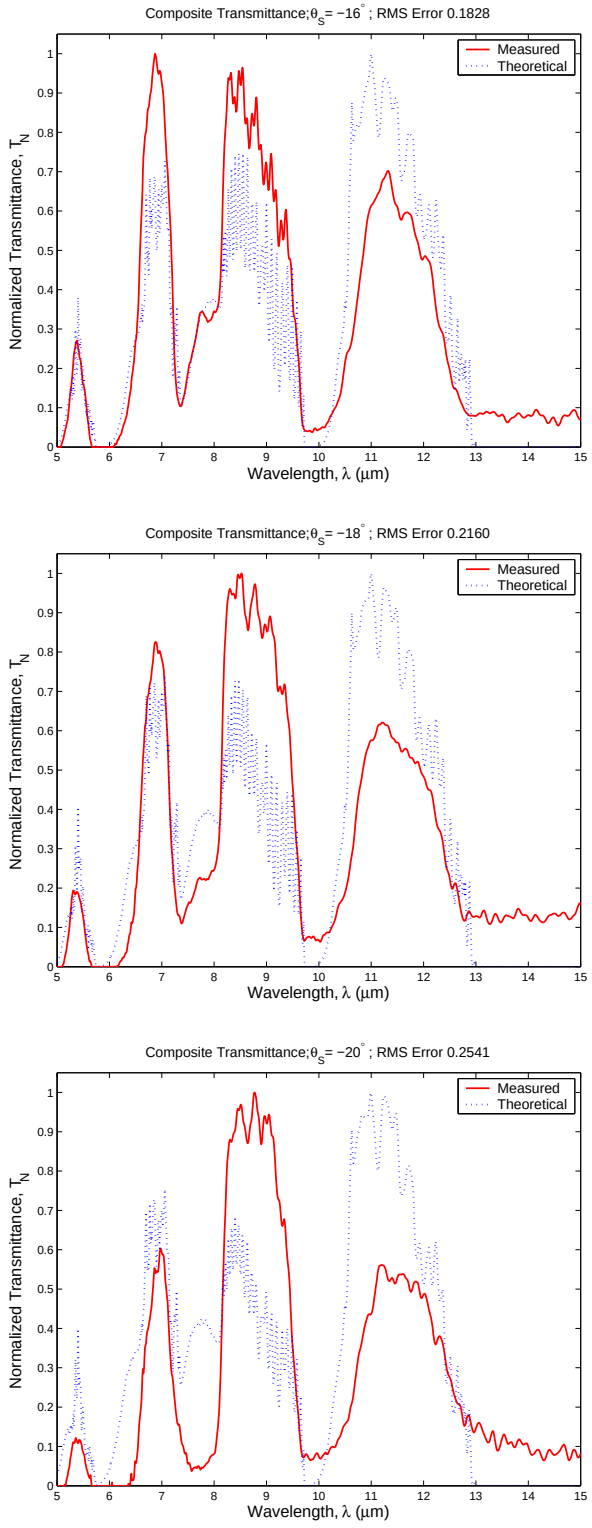

Figure 8.7: Composite normalized FTIR microspectroscopy transmittance measurements and normalized theoretical transmittance calculations of a PC structure. The measured and theoretical transmittances are shown for objective axis positions of $\theta_S = -16°$, $\theta_S = -18°$, and $\theta_S = -20°$ with respect to the sample normal.

Table 8.1: RMS errors comparing the FTIR system composite normalized transmittance measurements with theoretical calculations.

θ_S (deg)	Included Plane-Wave Angles (deg)	RMS Error in T_N	θ_S (deg)	Included Plane-Wave Angles (deg)	RMS Error in T_N
30	6 to 20 and 40 to 54	0.2536	-2	-26 to -12 and 8 to 22	0.1586
28	4 to 18 and 38 to 52	0.2495	-4	-28 to -14 and 6 to 20	0.1742
26	2 to 16 and 36 to 50	0.1813	-6	-30 to -16 and 4 to 18	0.1716
24	0 to 14 and 34 to 48	0.1848	-8	-32 to -18 and 2 to 16	0.1569
22	-2 to 12 and 32 to 46	0.2023	-10	-34 to -20 and 0 to 14	0.1587
20	-4 to 10 and 30 to 44	0.1987	-12	-36 to -22 and -2 to 12	0.1653
18	-6 to 8 and 28 to 42	0.1656	-14	-38 to -24 and -4 to 10	0.1694
16	-8 to 6 and 26 to 40	0.1790	-16	-40 to -26 and -6 to 8	0.1828
14	-10 to 4 and 24 to 38	0.1758	-18	-42 to -28 and -8 to 6	0.2160
12	-12 to 2 and 22 to 36	0.1962	-20	-44 to -30 and -10 to 4	0.2541
10	-14 to 0 and 20 to 34	0.1737	-22	-46 to -32 and -12 to 2	0.2497
8	-16 to -2 and 18 to 32	0.1563	-24	-48 to -34 and -14 to 0	0.2467
6	-18 to -4 and 16 to 30	0.1698	-26	-50 to -36 and -16 to -2	0.2669
4	-20 to -6 and 14 to 28	0.1764	-28	-52 to -38 and -18 to -4	0.3093
2	-22 to -8 and 12 to 26	0.1845	-30	-54 to -40 and -20 to -6	0.3913
0	-24 to -10 and 10 to 24	0.1851			

T_N, are shown in Table 8.1. The RMS error values for all measured spectra are high partially due to the significant differences in magnitude between the measured and theoretical values in the transmission band regions. Additionally, the theoretical computation shows significant variation from simulation to simulation as a result of the random fill factor deviation. Despite the large magnitude of the RMS error, the RMS calculation provides insight into the agreement between the theoretical and measured data at each angle with respect to the spectral transmittance at other angles.

Overall, the RMS errors are relatively constant over the rotation range from $\theta_S = 26^\circ$ to $\theta_S = -18^\circ$. The asymmetry in this range is caused in part by the asymmetry of the incident beam. At large negative angular orientations of the objective axis, the most intense lobe of incident light from the objective is at very oblique angles with respect to the sample normal. The large RMS errors for angles greater than $\theta_S = 26^\circ$ and for angles less than $\theta_S = -18^\circ$ also roughly corresponds to measurements when the measurement noise exceeds 5%. The very high errors near the angular orientation $\theta_S = -30$ correspond to measurements where

the most intense side of the incident beam is aligned with plane waves at incident angles in the range from $\theta_k = -54°$ to $\theta_k = -40°$.

The composite measurements from the FTIR microspectroscopy apparatus show that the apparatus accurately measures the composite transmittance of PC structures. Spectral variations from angular orientation to angular orientation are detected. The apparatus is most effective over an angular orientation range from $\theta_S = 26°$ to $\theta_S = -18°$ when the included incident plane-waves are incident at angles less than $\theta_k = 50°$. The measurement noise associated with the apparatus at these orientations is within the previously identified noise threshold.

8.3 FTIR Microspectroscopy Transmission-Based Single-Angle Plane-Wave Transmittance Computations

The single-angle plane-wave characterization method was applied to the composite transmittance measurements and the results then compared to the theoretical single-angle plane-wave transmittance calculation. The theoretical calculation for the single-angle plane-wave transmittances is significantly affected by the random fill factor deviation as shown for the composite measurements in Chapter 7.

Figures 8.8 through 8.10 show the normalized measured single-angle plane-wave transmittances and the theoretical normalized theoretical plane-wave transmittances for representative plane-wave angles along with the computed RMS errors. The measured transmittances show generally good agreement with theory. Since the large difference in transmittance magnitude was observed in the measured values, the large differences in magnitudes are expected in the measured single-angle plane-wave transmittance solutions. At large incident angles, the transmission bands in the theoretical calculation tend to shift to shorter wavelengths. This detail is not reproduced in the measured single-angle plane-wave transmittances. A possible cause is the increased number of large-error measurements that contribute to the solution at these plane-wave angles.

The RMS errors between the normalized measured and theoretical single-angle plane-wave transmittances are listed in Table 8.2. All RMS errors are high partially due to

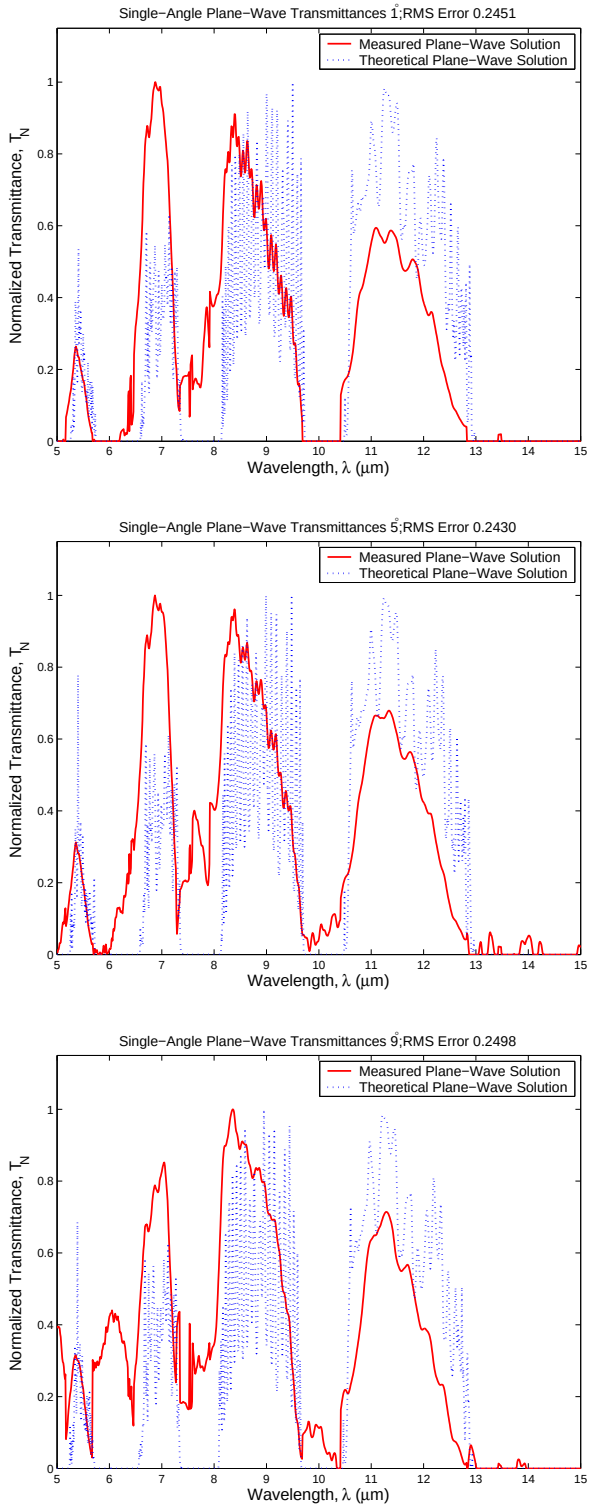

Figure 8.8: FTIR system transmission-based single-angle plane-wave normalized transmittance computations and theoretical single-angle plane-wave ideal normalized transmittances of a PC structure. The measured and theoretical transmittances are shown for objective axis positions of $\theta_k = 1°$, $\theta_k = 5°$, and $\theta_k = 9°$ with respect to the sample normal.

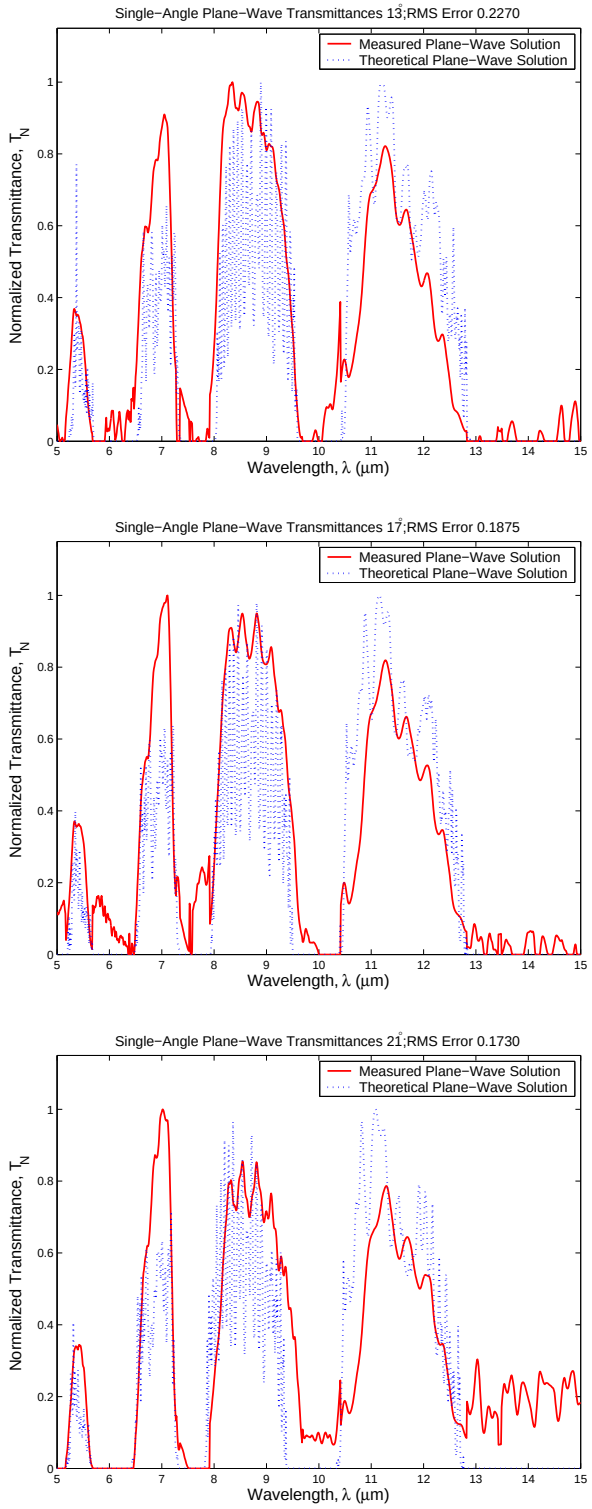

Figure 8.9: FTIR system transmission-based single-angle plane-wave normalized transmittance computations and theoretical single-angle plane-wave ideal normalized transmittances of a PC structure. The measured and theoretical transmittances are shown for objective axis positions of $\theta_k = 13°$, $\theta_k = 17°$, and $\theta_k = 21°$ with respect to the sample normal.

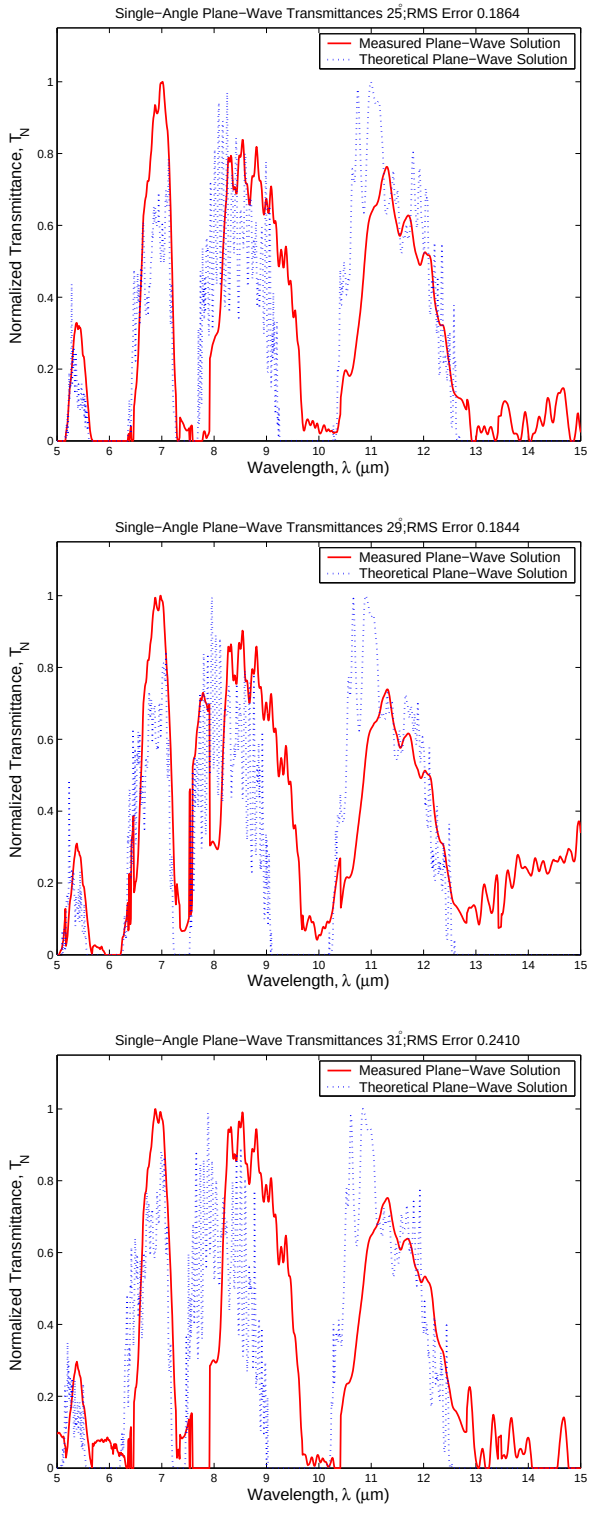

Figure 8.10: FTIR system transmission-based single-angle plane-wave normalized transmittance computations and theoretical single-angle plane-wave ideal normalized transmittances of a PC structure. The measured and theoretical transmittances are shown for objective axis positions of $\theta_k = 25°$, $\theta_k = 29°$, and $\theta_k = 31°$ with respect to the sample normal.

Table 8.2: RMS errors for measured single-angle plane-wave FTIR system normalized transmittances compared to theoretical normalized transmittances. The number of measurements used for each calculation is also listed.

Plane-Wave Angle (deg)	Number of Measurements	RMS Error in T_N	Plane-Wave Angle (deg)	Number of Measurements	RMS Error in T_N
53	2	-	25	14	0.1864
51	4	-	23	13	0.1770
49	6	-	21	13	0.1730
47	8	0.3841	19	13	0.1742
45	10	0.3807	17	14	0.1875
43	12	0.3986	15	17	0.2079
41	14	0.3996	13	21	0.2270
39	14	0.3766	11	25	0.2420
37	14	0.3284	9	28	0.2498
35	14	0.3072	7	26	0.2480
33	14	0.2769	5	22	0.2430
31	14	0.2410	3	18	0.2402
29	14	0.1844	1	14	0.2451
27	14	0.1820			

the large magnitude variation in the transmission band regions. At plane-wave angles that correspond to computations where few measurements contribute to the transmittance solution, agreement between the theoretical and measured transmittances decreases. The agreement is relatively constant over the range of plane-wave angles from $\theta_k = 1^\circ$ to $\theta_k = 29^\circ$.

Initially, the computation included plane-wave angles in the range from $\theta_k = 1^\circ$ to $\theta_k = 53^\circ$. The corresponding transmittance solutions for angles ranging from $\theta_k = 49^\circ$ to $\theta_k = 53^\circ$ consisted of spurious peaks in otherwise null spectra. Additionally, in the range from $\theta_k = 27^\circ$ to $\theta_k = 47^\circ$, although the spectra contained some expected features, the transmittances were in relatively poor agreement with theory. This resulted from the attempt to optimize the solution including the angles where insufficient information was available to reproduce accurately the single-angle plane-wave transmittances. The inclusion of these angles in the optimization skewed the results for other angles where sufficient information was available. The computation was truncated by removing the plane-wave computations for incidence angles in the range from $\theta_k = 49^\circ$ to $\theta_k = 53^\circ$. The removal of these angles from the

computation improved the agreement between measured and theoretical transmittances at all other plane-wave angles.

The single-angle plane-wave transmittance solutions derived from transmittance data collected using the FTIR microspectroscopy apparatus show trends similar to the composite transmittance comparison; namely, the spectral transmittance is recovered. As the number of measurements contributing to a single-angle plane-wave transmittance solution decreases, the error and agreement between theoretical transmittance and measured transmittance decreases.

8.4 FTIR Microspectroscopy Composite Reflectance Measurements

The composite reflectance analysis for reflection measurements is illustrated using measurements recorded for a 53-period, 1-dimensional PC structure that consists of alternating layers of air and silicon with the thickness of the silicon regions equal to $t_{Si} = 2.20\ \mu m$ and the air region thickness equal to $t_{air} = 2.20\ \mu m$. The objective axis orientation angle was rotated with respect to the sample normal over the range from $\theta_S = 10^\circ$ to $\theta_S = -12^\circ$. The arrangement of the objective in reference to the reflected light for the reflection problem limits the included plane-wave angles for this objective rotation range to the plane-wave angles from $\theta_k = 24^\circ$ to $\theta_k = 10^\circ$, from $\theta_k = 2^\circ$ to $\theta_k = -2^\circ$, and from $\theta_k = -10^\circ$ to $\theta_k = -24^\circ$, as described for the reflection problem formulation in Chapter 5. Similar to the theoretical transmittance calculations, the theoretical reflectance calculations include a 2% uniformly distributed, random deviation in the fill factor of the structure.

The normalized reflectance, R_N, is computed by normalizing the measured reflectance spectra at each objective axis orientation angle. The measured composite normalized reflectance is then compared to the theoretical composite normalized reflectance.

Figures 8.11 through 8.14 show the measured normalized composite reflectances compared to the theoretical normalized reflectances for all positions of the objective axis over the angular rotation range from $\theta_S = 10^\circ$ to $\theta_S = -12^\circ$. The RMS errors between the measured and theoretical normalized reflectances are listed in each figure. At objective axis

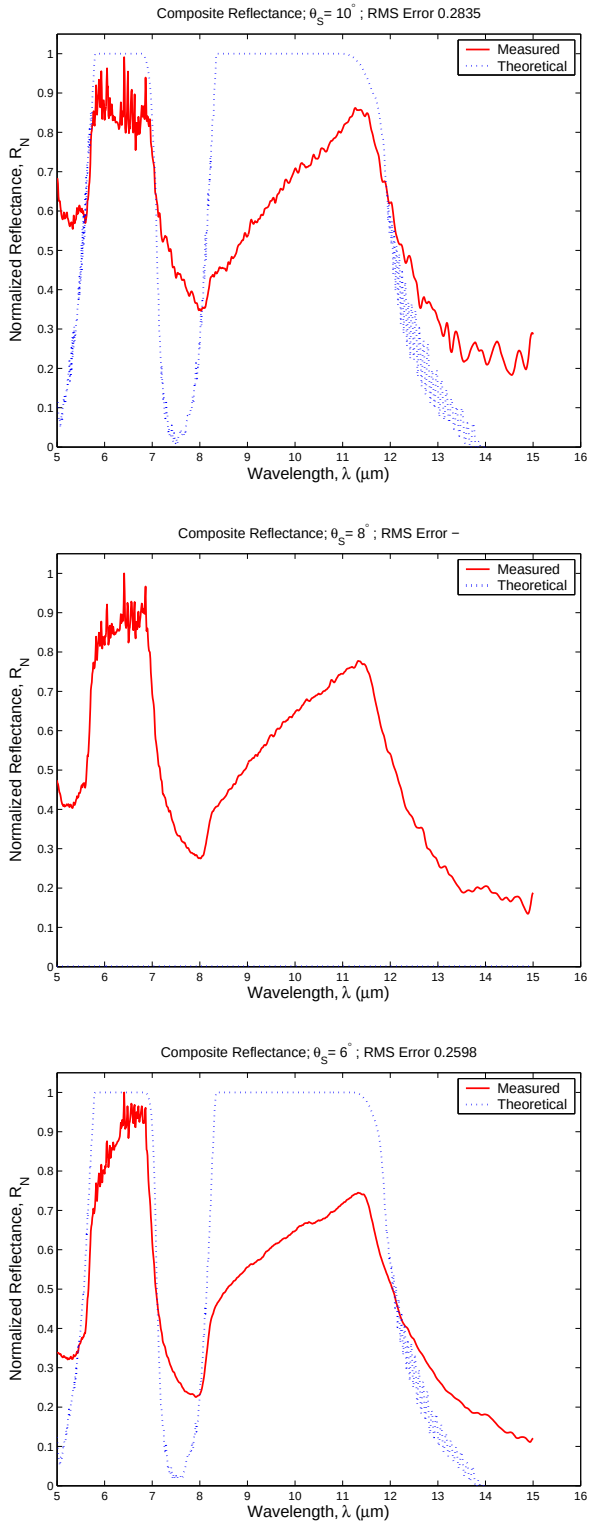

Figure 8.11: Measured composite FTIR microspectroscopy normalized reflectance measurements and theoretical composite normalized reflectance calculations of a PC structure. The measured and theoretical reflectances are shown for objective axis positions of $\theta_S = 10°$, $\theta_S = 8°$, and $\theta_S = 6°$ with respect to the sample normal.

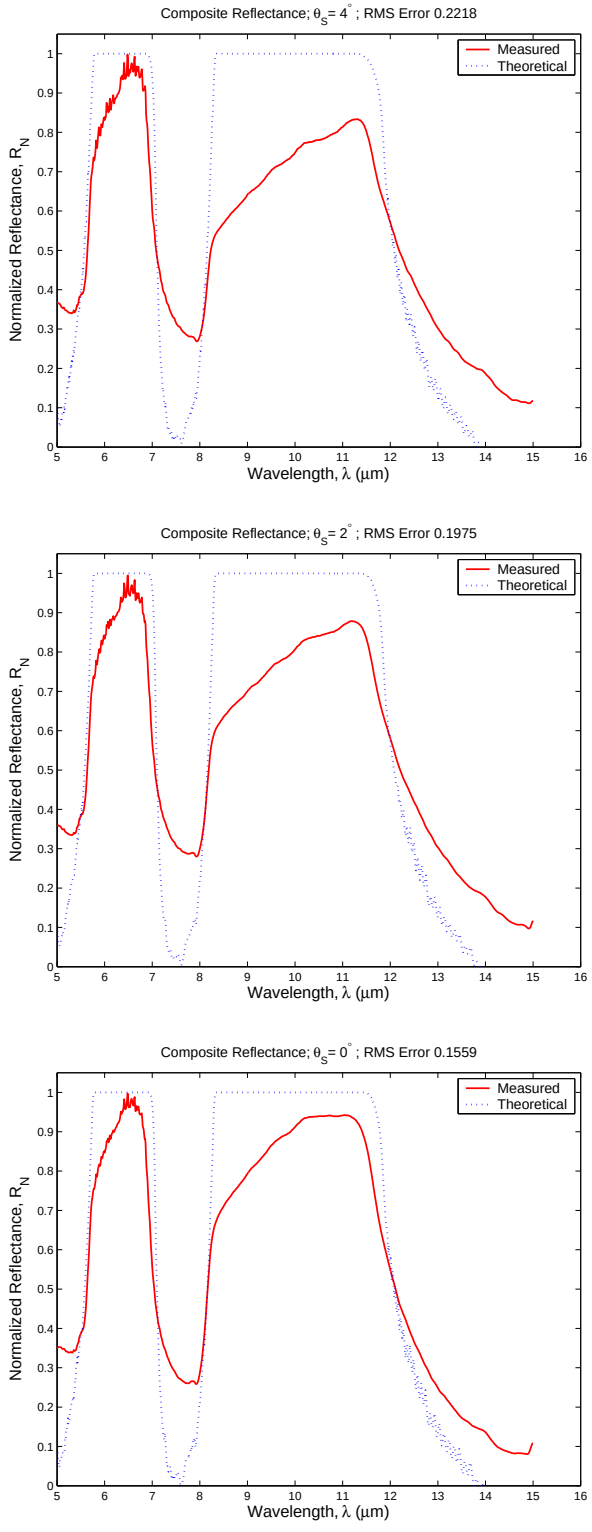

Figure 8.12: Measured composite FTIR microspectroscopy normalized reflectance measurements and theoretical composite normalized reflectance calculations of a PC structure. The measured and theoretical reflectances are shown for objective axis positions of $\theta_S = 4°$, $\theta_S = 2°$, and $\theta_S = 0°$ with respect to the sample normal.

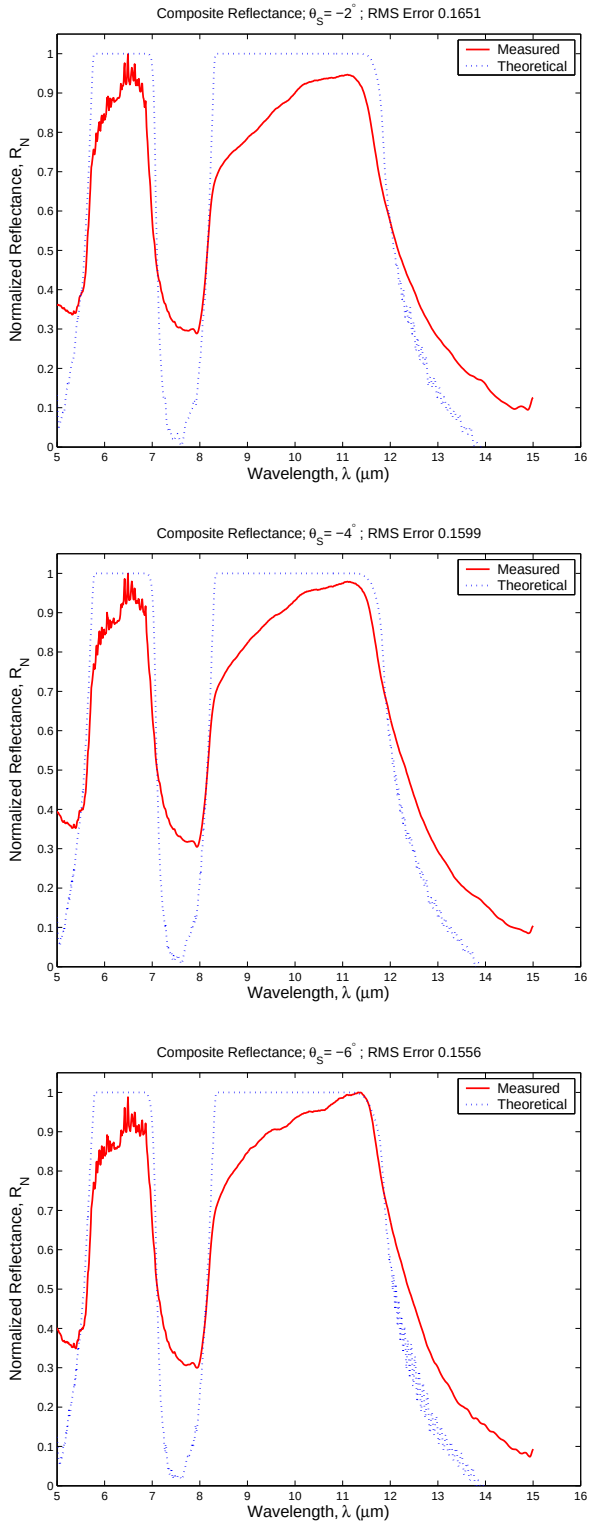

Figure 8.13: Measured composite FTIR microspectroscopy normalized reflectance measurements and theoretical composite normalized reflectance calculations of a PC structure. The measured and theoretical reflectances are shown for objective axis positions of $\theta_S = -2°$, $\theta_S = -4°$, and $\theta_S = -6°$ with respect to the sample normal.

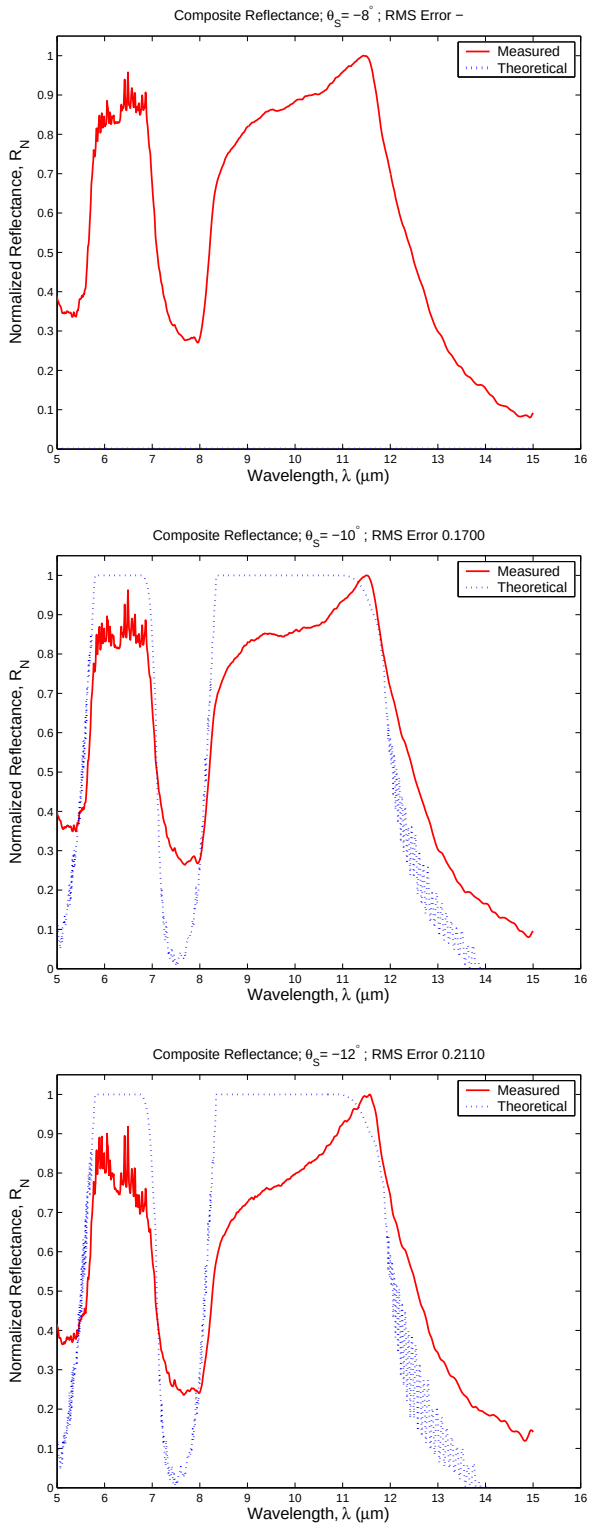

Figure 8.14: Measured composite FTIR microspectroscopy normalized reflectance measurements and theoretical composite normalized reflectance calculations of a PC structure. The measured and theoretical reflectances are shown for objective axis positions of $\theta_S = -8°$, $\theta_S = -10°$, and $\theta_S = -12°$ with respect to the sample normal.

orientations of $\theta_S = 8^\circ$ and $\theta_S = -8^\circ$, according to the theoretical formulation, all light is either reflected out of the system or reflected into the back of the small mirror on the objective. Consequently, at $\theta_S = 8^\circ$ and $\theta_S = -8^\circ$, the theoretical reflectance is zero across the entire wavelength range. As shown in the figures, this was not observed. Non-zero transmission was recorded. The non-zero measurements may be partially due to scattering of reflected light that is collected at these objective axis angular orientations.

Once again, there is excellent agreement in the position of transmission bands and photonic band gaps in the wavelength spectra between the theoretical and measured spectra over the rotation range. At the extreme objective axis angular orientations corresponding to measurements recorded when the signal strength was extremely low, the agreement between the theoretical reflectance and the measured reflectance decreases. Over the limited rotation range, there are few variations in the spectra from orientation angle to orientation angle.

Similar to the transmission case, there is less agreement in the magnitude of the reflectance throughout the objective rotation range. Again this is partially caused by spectral variations in the scattering of light at the interface of the PC structure. At extreme angles, as shown in Fig. 8.11 and Fig. 8.14, measurement noise (small oscillations in the reflectance curve) in the wavelength range from $\lambda = 8\ \mu m$ to $\lambda = 11\ \mu m$ is apparent in the measured spectrum.

The RMS errors comparing the normalized measured reflectance, R_N, and the theoretical normalized reflectance for all measurements and the included angles for the reflection geometry are listed in Table 8.3. The RMS errors are relatively constant over rotation range from $\theta_S = 2^\circ$ to $\theta_S = -10^\circ$. The increased errors starting at angular positions when $\theta_S > 2^\circ$ correspond to measurements when the more intense incident lobe is at a greater incident angle. In this situation, a significant quantity of light reflects from the surface of the sample directly out of the optical system. The large RMS error values at $\theta_S = 10^\circ$, and $\theta_S = -12^\circ$ corresponds to measurements where the estimated measurement noise exceeds 5%.

The composite measurements from the FTIR microspectroscopy apparatus in reflection mode show that the apparatus is capable of measuring the composite reflectances of PC

Table 8.3: RMS errors are shown comparing the FTIR system measured normalized composite reflectances with normalized theoretical reflectances.

θ_S (deg)	Included Plane-Wave Angles (deg)	RMS Error in R_N
10	2 to -2	0.2835
8	0	-
6	18 to 16 and -16 to -18	0.2598
4	20 to 14 and -14 to -20	0.2218
2	22 to 12 and -12 to 22	0.1975
0	24 to 10 and -10 to -24	0.1559
-2	22 to 12 and -12 to -22	0.1651
-4	20 to 14 and -14 to -20	0.1599
-6	18 to 16 and -16 to 18	0.1556
-8	0	-
-10	2 to -2	0.1700
-12	4 to -4	0.2110

structures. The few spectral variations in the spectra over the limited tuning range makes it difficult to conclude whether spectral details are recovered. The limited tuning range also restricts the included incident plane waves in the measurement range.

8.5 FTIR Microspectroscopy Reflection-Based Single-Angle Plane-Wave Reflectance Computations

The single-angle plane-wave characterization method was applied to the composite reflectance measurements and the results compared to the theoretical single-angle plane-wave reflectances. Figures 8.15 through 8.17 show the measured normalized single-angle plane-wave reflectances and the theoretical plane-wave reflectances for the structure along with the computed RMS errors.

The measured reflectances show good agreement with theory with respect to the location of photonic band gaps and transmission bands on the wavelength spectrum. The reflectance magnitude between the theoretical and the measured reflectance solutions show less agreement. Few additional spectral details are evident partially due to the limited variation present over the limited rotation range available for reflection measurements. The

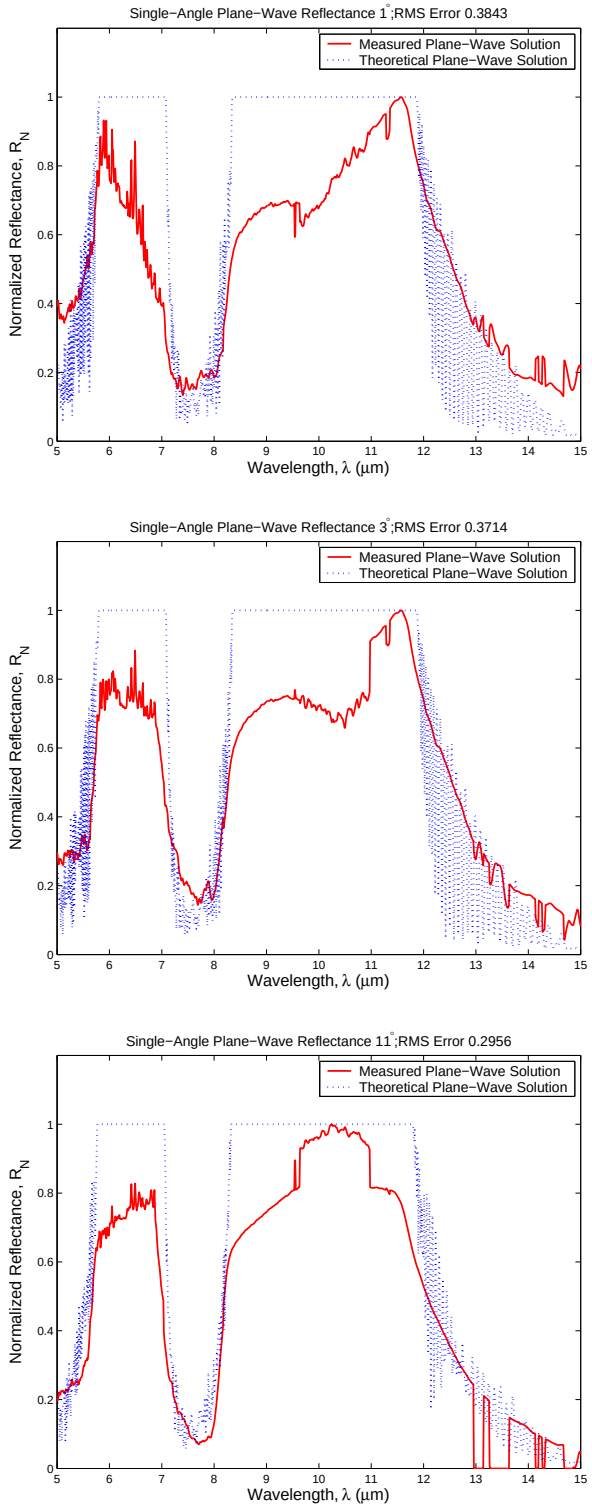

Figure 8.15: FTIR system reflection-based measured single-angle plane-wave normalized reflectances and theoretical single-angle plane-wave normalized reflectances of a PC structure. The measured and theoretical reflectances are shown for objective axis positions of $\theta_k = 1°$, $\theta_k = 3°$, and $\theta_k = 11°$ with respect to the sample normal.

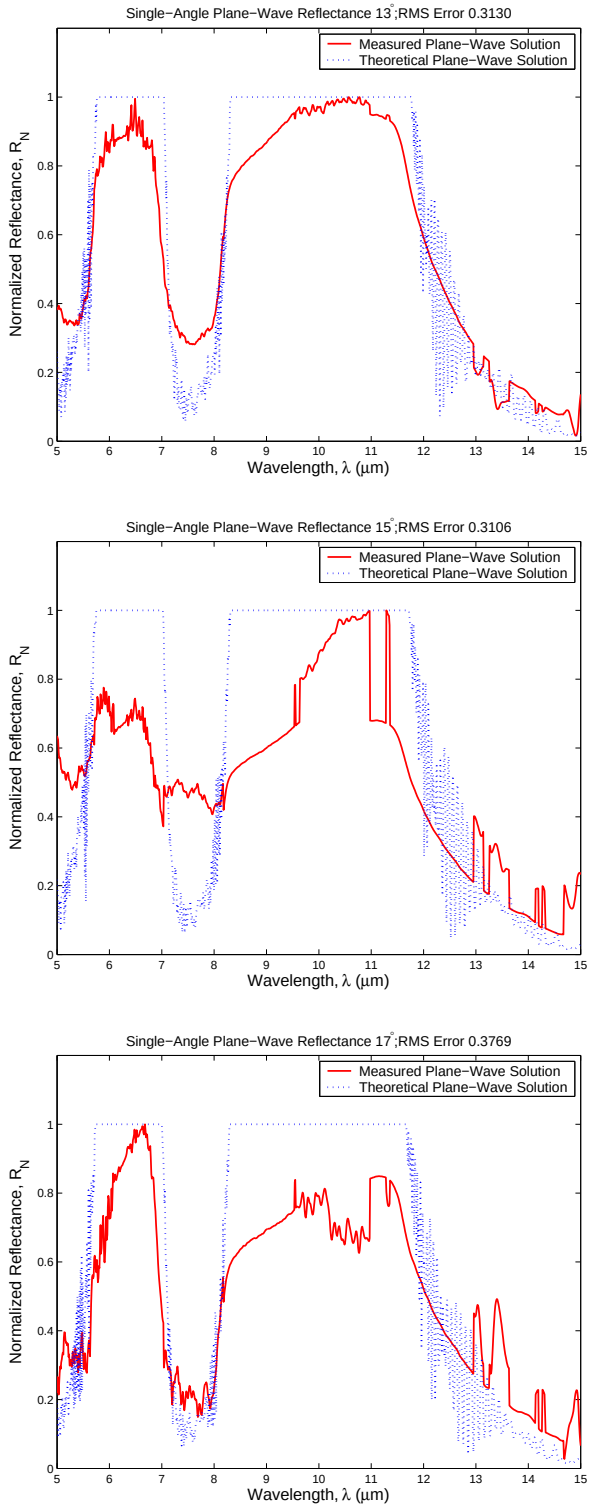

Figure 8.16: FTIR system reflection-based measured single-angle plane-wave normalized reflectances and theoretical single-angle plane-wave normalized reflectances of a PC structure. The measured and theoretical reflectances are shown for objective axis positions of $\theta_k = 13°$, $\theta_k = 15°$, and $\theta_k = 17°$ with respect to the sample normal.

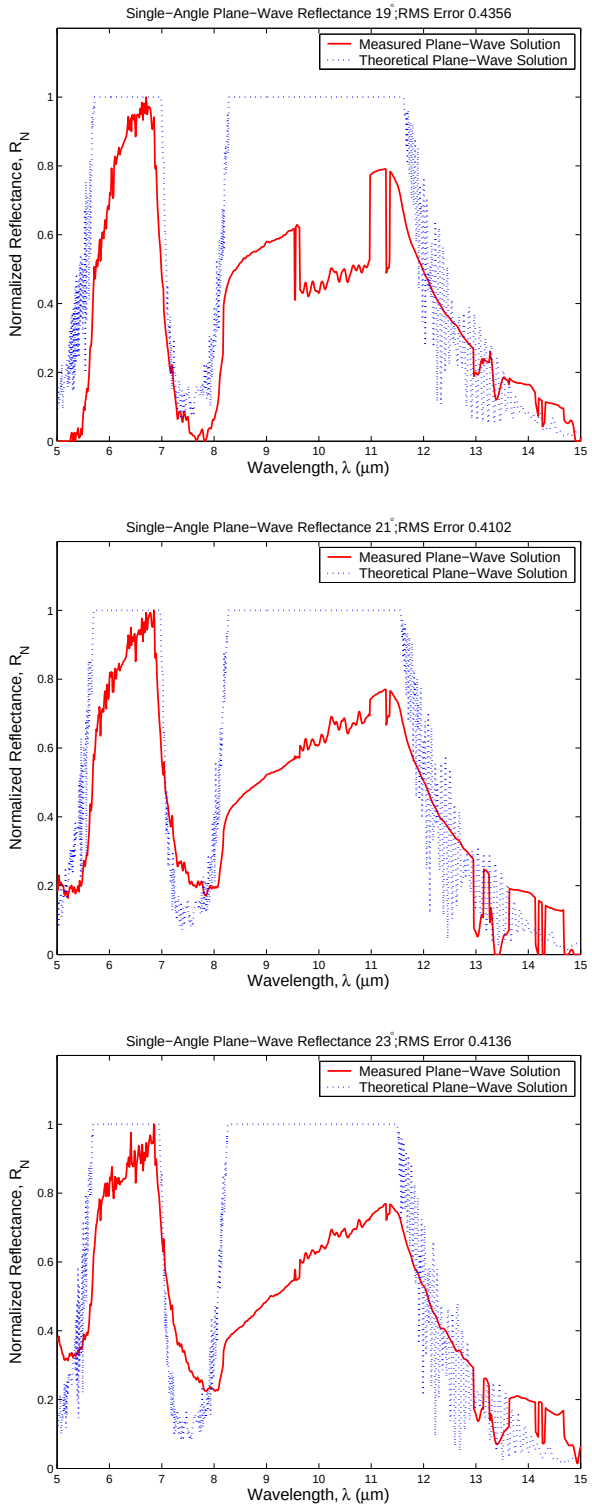

Figure 8.17: FTIR system reflection-based measured single-angle plane-wave normalized reflectances and theoretical single-angle plane-wave normalized reflectances of a PC structure. The measured and theoretical reflectances are shown for objective axis positions of $\theta_k = 19°$, $\theta_k = 21°$, and $\theta_k = 23°$ with respect to the sample normal.

Table 8.4: RMS errors for measured FTIR system single-angle plane-wave normalized reflectances compared to theoretical normalized reflectances. The number of composite spectral measurements used for each calculation is also listed.

Plane-Wave Angle (deg)	Number of Measurements	RMS Error in R_N
23	1	0.4136
21	3	0.4102
19	5	0.4356
17	7	0.3769
15	5	0.3106
13	3	0.3130
11	1	0.2956
3	1	0.3714
1	3	0.3843

RMS errors between the theoretical and measured single-angle plane-wave normalized reflectances are listed in Table 8.4 along with the number of measurements that contributed to each single-angle plane-wave computation.

The single-angle plane-wave reflectance solutions derived from reflection data collected using the FTIR microspectroscopy apparatus must be expanded to include additional measurements and additional plane waves. This requires an increase in the detected signal power in the measurement apparatus or a decrease in the system losses. Recommendations for improvement to the FTIR microspectroscopy reflection problem are suggested in Chapter 9.

8.6 FTIR Microspectroscopy Apparatus Advantages and Limitations

The FTIR microspectroscopy system measurements show that the transmittances and reflectances of PC structures can be accurately measured with the FTIR microspectroscopy system. In the transmission mode, spectral details in the transmittance of structures were accurately measured. The angular deconvolution using the single-angle plane-wave method produced additional spectral details. In reflection mode, the limited rotation capability of the system (with adequate signal levels maintained only between $\theta_S = 8^\circ$ and $\theta_S = -8^\circ$) is

a limiting factor in recovering useful spectral details.

8.6.1 Advantages

The FTIR microspectroscopy apparatus is an excellent tool for use in the characterization of PC structures at infrared wavelengths. In the transmission mode, the system is capable of accurately measuring the transmittance of a structure to include small variations in the transmission spectrum. The low-noise transmittance measurements enable the computation of the single-angle plane-wave transmittances of PC structures.

The turn-key system consists of fully integrated components and can be employed with consistent results. The integrated components and use of a broad-band source provide a method to characterize rapidly the PC structure. Though not demonstrated here, system capabilities permit automation of measurements.

8.6.2 Limitations

The FTIR microspectroscopy system suffers from low available optical power. The low optical power limits the angular range over which spectral measurements can be recorded. In turn, variations in the spectra are more difficult to detect and the number of plane-wave transmittances or reflectances that can be computed using the single-angle plane-wave characterization scheme decreases.

In the current configuration, as the sample is rotated from normal incidence in the beam, the detected signal amplitude decreases. The rotation range permitted to maintain acceptable detected signal levels is well below the theoretical maximum allowed by the characterization scheme. Although in transmission mode the rotation range is sufficient in the current apparatus, in the reflection mode, the angular rotation range must be increased for useful employment of the reflection formulation in the characterization of PC structures.

8.7 Summary

The transmittances and reflectances of PC structures were measured using the FTIR microspectroscopy system. For transmission measurements, the system provided excellent

results over an angular rotation range from $\theta_S = 20°$ to $\theta_S = -20°$. The single-angle plane-wave transmittance computation produced single-angle spectral transmittances in agreement with theory. To improve and fully test the single-angle plane-wave characterization technique, increased optical power is needed. For reflectance measurements, the rotation range where the detected signal strength was acceptable was restricted from $\theta_S = 8°$ to $\theta_s = -8°$. This limited rotation range restricts the number of composite reflectances that can be measured with the apparatus and the number of single-angle plane-wave reflectances that can be computed with the characterization scheme. For more accurate and precise PC structure characterization in the long-wavelength methodology, the available reflection rotation range must be increased. Required system improvements are described in Chapter 9.

CHAPTER 9

CONCLUSIONS

The main objective of this research has been to develop a long-wavelength infrared PC design methodology to assist in the development and application of PC technology. The methodology development, structure design, structure fabrication, characterization methods, and characterization tools have been presented in this thesis. In this chapter, the main contributions in each area are summarized and possible directions for future research are suggested.

9.1 Summary of Results

The long-wavelength infrared design and development methodology, the incident infrared focusing beam model, the single-angle plane-wave characterization method, the CO_2-laser measurement apparatus, and the application of the single-angle plane-wave technique to FTIR microspectroscopy transmittance and reflectance measurements represent the main contributions of this research. The use of these tools and the continued development of these components will contribute to the accelerated development of PC technology.

9.1.1 Long-Wavelength Methodology

PCs have been shown to be a promising technology for future optoelectronic systems. Theoretically, devices incorporating PC technology are capable of significantly out-performing their existing counterparts. Despite the potential advantages, large-scale introduction of PC technology into commercial products has been hampered by research and development challenges.

In this thesis, a framework for the application of well-developed infrared tools and techniques to PC research has been presented. The framework calls for the long-term, iterative, and repeated use of characterization tools at longer operating wavelengths to address challenges and development problems. Scaling the operating wavelength to the

infrared spectral region increases the structure dimensions, thereby significantly reduces the difficulty of fabricating PC structures. With fewer resources and less effort committed to fabrication, the pace of PC technology development can be increased.

The overall methodology incorporates infrared-scale research as a tool to be used in parallel with research at shorter wavelengths. Previous infrared PC research efforts using similar tools have viewed the long-wavelength work as an interim step in the development of structures that operate at shorter wavelengths. Once structures were fabricated at the shorter-wavelength scale, the long-wavelength research was discontinued. In the present developed methodology, frequent transitions between long- and short-wavelength research are envisioned.

The tools and techniques necessary for the methodology have been developed and demonstrated in this thesis. The modeling and simulation tools demonstrated are used to compare the performance of fabricated PC structures to corresponding realistic simulations of the fabricated structures. Previous efforts typically characterize the infrared performance of PC structures by comparing the fabricated finite-structure performance to infinite band diagram calculations. The increased fidelity of the models helps to identify the conditions for which the long-wavelength methodology tools, such as the single-angle plane-wave characterization method, can be used. A new characterization scheme and a new characterization apparatus have been developed and demonstrated through simulation and experimental measurements. Finally, existing characterization tools have been adapted and employed for use in the long-wavelength methodology.

9.1.2 Incident Focused Beam Characterization and Analysis

The incident beam from a Schwarzchild reflecting microscope objective has been analyzed and a mathematical model developed for the specification of the focused beam [94]. The model accounts for the physical geometry of the objective, the intensity profile of the incident beam, and the focusing performance of the objective. For the model, methods to measure the beam intensity weighting coefficients and the focusing performance of a specific reflecting objective have been developed and demonstrated.

The objective model was first verified by comparing the theoretical and measured optical transmittance through a slab of dielectric material. The theoretical transmittance, using the objective model, and the measured transmittance were shown to be in good agreement. Subsequently, the model was employed in the transmittance and reflectance measurements of PC structures. In the composite measurements, when the theoretical transmittances and reflectances were computed by superimposing single-angle plane-wave transmittances and reflectances using the model, there was excellent agreement between the theoretical and measured transmittances and reflectances.

The mathematical model representing the objective was also used in the single-angle plane-wave characterization method. The developed model for Schwarzchild-objective-focused light can be applied to other infrared problems that employ Schwarzchild and similar objectives.

9.1.3 Single-Angle Plane-Wave Characterization Method

A novel characterization method capable of computing the single-angle plane-wave transmittances and reflectances of a test structure has been presented in this thesis [84]. Multiple spectral measurements using a composite multiple-incident-angle probe beam are deconvolved to compute the single-angle transmittance or reflectance. Simulations demonstrate that the method effectively recovers the single-angle transmittances or reflectances in situations with relatively low measurement noise. A measurement noise threshold of approximately 5% was identified as a limit to the application of the characterization method. The method employs matrix regularization algorithms [87] to stabilize the computations.

The single-angle plane-wave characterization method was applied to CO_2-laser and FTIR microspectroscopy measurements. The agreement between theoretical transmittances and measured transmittance was dependent on the noise level of the measurement. When the computations included measurements that exceeded the identified noise threshold, the agreement suffered. Over the range of measurements when the measurement noise was within the established threshold, the spectral characteristics, to include rapid variations in the spectra from wavelength to adjacent wavelength, were recovered. The regularization

and deconvolution of the single-angle spectral transmittances and reflectances has potential application in other areas of research.

9.1.4 CO_2-Laser Transmittance Measurements

The first demonstration of the spectral characterization of a PC structure using a discretely tunable CO_2-laser system was presented in this thesis [95]. The measurement apparatus used to record measurements for application of the single-angle plane-wave characterization method was constructed.

The high incident power available for the apparatus permitted spectral measurements over a 66° angular rotation range. The measurements from the apparatus successfully characterized the location of transmission bands and photonic band gaps on the wavelength spectrum. Although the general spectral characterization of a structure was demonstrated, the apparatus was unable to measure minor spectral variations from one wavelength to an adjacent wavelength. Additionally, the current apparatus is unable to measure accurately the low power levels associated with photonic band gap regions of the spectrum. Improvements in the equipment and apparatus are required to realize fully the potential of this infrared characterization tool.

9.1.5 FTIR Microspectroscopy Reflectance Measurements

A new method to measure the reflectance of PC structures using FTIR microspectroscopy reflection measurements was developed in this thesis. The formulation of the reflection configuration and the employment of the objective models for reflectance measurements are significantly different than the employment of the models used in transmittance measurements.

The characterization of PC structures using the reflection formulation was demonstrated. The measured spectral location of band edges was in excellent agreement with theory over the $\theta_S = 8°$ to $\theta_S = -8°$ angular rotation range. The rotation range was limited by low detectable power at the extreme rotation angles; the power level outside of the $\theta_S = 8°$ to $\theta_S = -8°$ range could not accurately be measured. The single-angle plane-wave

characterization method was applied to the reflectance measurements. The resulting single-angle plane-wave reflectances were in good agreement with theory over this rotation range.

9.1.6 FTIR Microspectroscopy Transmittance Measurements

The single-angle plane-wave characterization method was successfully applied to FTIR transmittance measurements. Composite transmittance measurements over the rotation range from $\theta_S = 30^\circ$ to $\theta_S = -30^\circ$ showed excellent agreement with theoretical calculations. The single-angle plane-wave characterization method produced plane-wave transmittances in good agreement with theoretical calculations. The single-angle plane-wave transmittances corresponding to plane-wave angles that contain low measurement noise and are included in the most number of composite measurements produced the best agreement. As the number of measurements that contribute to a plane-wave transmittance decreased, the agreement between measured and theoretical transmittances decreased.

9.2 Future Research

To realize all of the potential advantages of the long-wavelength design and development methodology described in this thesis, continued development of the presented tools is needed. Refinement and further development of the tools will improve the performance of the characterization method and validate the employment of the long-wavelength infrared PC methodology. Future research plans, discussed in this section, are divided into near-term extensions of the current work and long-term research objectives.

9.2.1 Near-Term Extensions of the Current Work

In the current work, the long-wavelength methodology was demonstrated and tools, apparatus, and procedures were developed to characterize PC structures. Subsequently, the transmittances and reflectances of 1-dimensional PC structures were measured to illustrate the use of the long-wavelength methodology and characterization tools. The observed results highlighted several immediate, near-term extensions of this research.

9.2.1.1 CO_2-Laser Measurement Noise Reduction

The CO_2-laser characterization apparatus measurements presented in this thesis currently exceed the identified measurement noise threshold that permits use of the single-angle plane-wave characterization scheme. Although the approximate spectral transmittance of a structure can be measured, the noise must be significantly reduced in order to improve the agreement between theoretical and measured composite measurements and theoretical and measured single-angle plane-wave transmittances.

The major measurement error source in the present configuration is the power detector. The response of the thermopile detector and the variation of detected power during a single measurement, particularly at low power levels, must be improved. Camera-based detectors [96] or the use of another detector with a large dynamic range and low noise floor will decrease the measurement noise and, therefore, improve the agreement between theoretical computations and measurements. The ability to measure accurately the extremely low power levels associated with a photonic band gap is important to the employment of this characterization tool. A suitable replacement detector is needed to improve the measurements conducted using the CO_2-laser characterization apparatus.

9.2.1.2 Single-Angle Plane-Wave Experimental Noise Threshold Refinement

An approximate measurement noise threshold of 5% has been identified by simulation as the maximum measurement noise percentage that can be present in measurements before the spectral characteristics of a PC structure are distorted. In this research, the CO_2-laser measurements clearly exceed the identified threshold. The FTIR measurements, at certain orientation angles, also exceeded this noise limit. Despite the fact that, in the single-angle plane-wave computations for this thesis, some data were at or exceeded the identified threshold, the technique was shown to recover some of the desired spectral characteristics. Additional measurement noise analysis using fabricated structures is needed to refine the value of the allowed threshold. The threshold may not be constant for all measurements or structures.

9.2.1.3 Measurement Automation

Data collection with the CO_2-laser apparatus is currently time consuming due to the need to measure the transmittance at each angle and at each wavelength. Manual tuning of the apparatus for each measurement is required to position properly the sample in the focused beam of the CO_2 laser. To record a single data set at coarse resolution for a single structure requires from 15 to 20 hours over the limited spectral range of the CO_2-laser system. Repeated measurements to reduce random measurement noise are not feasible with the existing system. To realize the full potential of this characterization system, automation of spectral measurements is needed. Automation of the measurement requires a change to the apparatus so the structure can be mounted and will rotate at a fixed position in the CO_2-laser beam.

The broad-band source of the FTIR system and the existing ability to specify the number of individual scans used in a single measurement makes current measurement procedure for the FTIR microspectroscopy system feasible. However, apparatus improvements that permit automatic data collection with the CO_2-laser system would also improve the capabilities of the FTIR microspectroscopy characterization tool.

9.2.1.4 Two-Dimensional Photonic Crystal Structures

Transmission and reflection measurements of 1-dimensional PC structures have been used to illustrate the methodology and tools developed in this thesis. The developed tools need to be applied to more complex structures. A natural progression in the development of the long-wavelength PC infrared methodology is to apply the tools to 2-dimensional PC structures. Fabrication and measurement procedures for these structures are identical to the methods presented in this thesis.

9.2.2 Long-Term Research Objectives

In the long term, several methodology demonstrations are needed. Additionally, in this research, existing infrared characterization tools designed for other applications, were used.

The feasibility of significant apparatus alterations tailored for the long-wavelength methodology should be investigated.

9.2.2.1 Transitions Between Wavelength Scales

An integral component of the long-wavelength methodology is the ability to transition from the long-wavelength scale to the short-wavelength scale as research challenges are addressed. A demonstration of the successful transition between the long- and short-wavelength scales is needed. The feasibility of repeated transitions from one wavelength range to the other must be demonstrated before the PC research community will fully embrace the long-wavelength methodology.

9.2.2.2 Addressing Photonic Crystal Research Challenges

A demonstration of the long-wavelength methodology applied to present-day PC development issues is needed. Once demonstrated, the methodology can be applied to a variety of challenges in the development of PC technology. Challenges such as integration of PC technology with existing components or the identification of fabrication tolerances may be investigated.

9.2.2.3 Demonstration of Large-Scale, Multiple-Component Photonic Crystal Systems

A demonstration of the integration of multiple long-wavelength PC devices is needed to show how the methodology can reduce the risk associated with PC system development. A long-wavelength, functioning prototype system can be used, along with the methodology, to develop a functioning system at the short-wavelength scale. Such a demonstration will potentially encourage additional commercial development ventures in PC technology.

9.2.2.4 CO_2-Laser Improvements

The wavelength ranges for the CO_2-laser system where the output power is below detection thresholds significantly limit the use of the current apparatus. In particular, the spectral null in laser output over the wavelength range from 9.8 μm to 10.15 μm is large and approximately centered in the CO_2 laser's tuning range. Spectral features in this range cannot be measured by the current system. The theoretical CO_2-laser gain curve (Fig. 6.1)

indicates that output is possible over this range. An evaluation of other commercially available CO_2-laser systems or further refinements in the design of the current system are needed to obtain measurable laser output over the 9.8 μm to 10.15 μm spectral range.

9.2.2.5 CO_2-Laser Visual Optical Path

The addition of a visual optical path, similar to the visual optical path available in the FTIR microspectroscopy system, would significantly improve the CO_2-laser apparatus. Investigation into the feasibility of adding such an optical path is needed. This would essentially require the construction or adaptation of a microscope system to the CO_2-laser apparatus.

9.2.2.6 Increased FTIR Microspectroscopy Source Intensity

In the current configuration of the FTIR microspectroscopy apparatus, as the sample is rotated from normal incidence in the beam, the detected signal amplitude decreases. The restricted rotation range, established to maintain acceptable detected signal levels, is well below the theoretical maximum allowed by the single-angle plane-wave characterization scheme. Although in transmission mode the rotation range is sufficient in the current apparatus, in the reflection mode the angular rotation range must be increased for useful employment of the reflection formulation in the characterization of PC structures.

Investigation into the use of an alternate, higher-power source is needed. Such sources are not commercially available for systems; however, more intense infrared sources, with beam brightness levels reported as 3 orders of magnitudes higher than globar sources, are being investigated in the research community [97, 98].

9.2.3 Summary

The main objective of this research and the major results from this thesis were reviewed. Suggestions for future research efforts, in both the near- and long-term, were presented.

REFERENCES

[1] J. Hickmann, D. Solli, C. F. McCormick, R. Plambeck, and R. Y. Chiao, "Microwave measurements of the photonic band gap in a two-dimensional photonic crystal slab," *J. Appl. Phys.*, vol. 92, pp. 6918–6920, Dec. 1, 2002.

[2] S. Rowson, A. Chelnokov, and J. M. Lourtioz, "Two-dimensional photonic crystals in macroporous silicon: From mid-infrared (10 μm) to telecommunications wavelengths (1.3-1.5 μm)," *J. Lightwave Technol.*, vol. 17, pp. 1989–1995, Nov. 1999.

[3] E. Yablonovitch, "Inhibited spontaneous emission in solid-state physics and electronics," *Phys. Rev. Lett.*, vol. 58, pp. 2059–2062, May 18, 1987.

[4] S. John, "Strong localization of photons in certain disordered dielectric superlattices," *Phys. Rev. Lett.*, vol. 20, pp. 2486–2489, Jun. 8, 1987.

[5] G. Parker and M. Charlton, "Photonic crystals," *Phys. World*, vol. 13, pp. 193–200, Aug. 2000.

[6] M. Kafesaki, M. Agio, and C. M. Soukoulis, "Waveguides in finite-height two-dimensional photonic crystals," *J. Opt. Soc. Amer. B*, vol. 19, pp. 2232–2240, Sept. 2002.

[7] T. Sondergaard, A. Bjarklev, J. Arentoft, M. Kristensen, J. Erland, J. Broeng, and S. E. B. Libori, "Designing finite-height photonic crystal waveguides: Cconfinement of light and dispersion relations," *Opt. Comm.*, vol. 194, pp. 341–351, Jul. 15, 2001.

[8] S. G. Johnson, P. R. Villeneuve, S. Fan, and J. D. Joannopoulos, "Linear waveguides in photonic-crystal slabs," *Phys. Rev. B*, vol. 62, pp. 8212–8222, Sep. 15, 2000.

[9] M. Notomi, A. Shinya, K. Yamada, J. Takahashi, C. Takahashi, and I. Yokohama, "Structural tuning of guiding modes of line-defect waveguides of silicon-on-insulator photonic crystal slabs," *IEEE J. Quantum Electron.*, vol. 38, pp. 736–742, July 2002.

[10] A. Birner, A.-P. Li, F. Müller, U. Gösele, P. Kramper, V. Sandoghdar, J. Mlynek, K. Busch, and V. Lehmann, "Transmission of a microcavity structure in a two-dimensional photonic crystal based on macroporous silicon," *Mats. Sci. in Semiconductor Processing.*, vol. 3, no. 5, pp. 487–491, 2000.

[11] A. Mekis, J. Chen, I. Kurland, S. Fan, P. Villeneuve, and J. D. Joannopoulos, "High transmission through sharp bends in photonic crystal waveguides," *Phys. Rev. Lett.*, vol. 77, pp. 3787–3790, Oct. 28, 1996.

[12] S. Lin, E. Chow, V. Hietala, P. Villeneuve, and J. D. Joannopoulos, "Experimental demonstration of guiding and bending of elecromagnetic waves in a photonic crystal," *Science*, vol. 282, pp. 274–276, Oct. 9, 1998.

[13] M. Tokushima and H. Yamada, "Light propagation in a photonic-crystal-slab line-defect waveguide," *IEEE J. Quantum Electron.*, vol. 38, pp. 753–759, July 2002.

[14] T. Zijlstra, E. van der Drift, M. J. A. de Dood, E. Snoeks, and A. Polman, "Fabrication of two-dimensional photonic crystal waveguides for 1.5 μm in silicon by deep anisotropic dry etching," *J. Vac. Sci. Technol. B*, vol. 17, pp. 2734–2739, Nov. 1999.

[15] M. Lončar, T. Doll, J. Vučković, and A. Scherer, "Design and fabrication of silicon photonic crystal optical waveguides," *J. Lightwave Technol.*, vol. 18, pp. 1402–1411, Oct. 2000.

[16] N. Makkova and V. Gopalan, "Resonant light propagation through 90°-bend waveguide based on a strained two-dimensional photonic crystal," *J. Opt. Soc. Amer. B*, vol. 21, pp. 1679–1684, Sept. 2004.

[17] A. Chutinan and S. Noda, "Highly confined waveguides and waveguide bends in three-dimensional photonic crystal," *Appl. Phys. Lett.*, vol. 75, pp. 3739–3741, Dec. 13, 1999.

[18] A. Yariv, Y. Xu, R. K. Lee, , and A. Scherer, "Coupled-resonator optical waveguide: a proposal and analysis," *Opt. Lett.*, vol. 24, pp. 711–713, Jun. 1, 1999.

[19] S. Y. Lin, E. Chow, S. G. Johnson, and J. D. Joannopoulos, "Direct measurement of the quality factor in a two-dimensional photonic-crystal microcavity," *Opt. Lett.*, vol. 26, pp. 1903–1905, Dec. 1, 2001.

[20] P. Kramper, A. Birner, M. Agio, F. Müller, U. Gösele, J. Mlynek, and V. Sandoghdar, "Direct spectroscopy of a deep two-dimensional photonic crystal microresonator," *Phys. Rev. B.*, vol. 64, p. 233102, Dec. 15, 2001.

[21] S. Olivier, C. J. M. Smith, H. Benisty, C. Weisbuch, T. Krauss, R. Houdré, and U. Oesterle, "Cascaded photonic crystal guides and cavities: Spectral studies and their impact on integrated optics design," *IEEE J. Quantum Electron.*, vol. 38, pp. 816–824, July 2002.

[22] P. E. Barclay, K. Srinivasan, and O. Painter, "Design of photonic crystal waveguides for evanescent coupling to optical fiber tapers and intergration with high-Q cavities," *J. Opt. Soc. Amer. B*, vol. 20, pp. 2274–2284, Nov. 2003.

[23] E. Centano, B. Guizal, and D. Felbacq, "Multiplexing and demultiplexing with photonic crystals," *J. Opt. A: Pure Appl. Opt.*, vol. 1, pp. L10–L13, 1999.

[24] M. Koshiba, "Wavelength division multiplexing and demultiplexing with photonic crystal waveguide couplers," *J. Lightwave Technol.*, vol. 19, pp. 1970–1975, Dec. 2001.

[25] A. Sharkawy, S. Shi, and D. W. Prather, "Multichannel wavelength division multiplexing with photonic crystals," *Appl. Opt.*, vol. 40, pp. 2247–2252, May 10, 2001.

[26] S. Fan, P. Villeneuve, J. D. Joannopoulos, and H. Haus, "Channel drop tunneling through localized states," *Phys. Rev. Lett.*, vol. 80, pp. 960–963, Feb. 2, 1998.

[27] M. Imada, S. Noda, A. Chutinan, M. Mochizuki, and T. Tanaka, "Channel drop filter using a single defect in a 2-d photonic crystal slab waveguide," *J. Lightwave Technol.*, vol. 20, pp. 845–849, May 2002.

[28] S. Noda, M. Imada, M. Okano, S. Ogawa, M. Mochizuki, and A. Chutinan, "Semiconductor three-dimensional and two-dimensional photonic crystals and devices," *IEEE J. Quantum Electron.*, vol. 38, pp. 726–735, July 2002.

[29] B. Z. Steinberg, A. Boag, and R. Lisitsin, "Sensitivity analysis of narrowband photonic crystal filters and waveguides to structure variations and inaccuracy," *J. Opt. Soc. Amer. A*, vol. 20, pp. 138–146, Jan. 2003.

[30] C. Seassal, Y. Désières, X. Letartre, C. Grillet, P. Rojo-Romeo, P. Viktorovitch, and T. Benyattou, "Optical coupling between a two-dimensional photonic crystal-based microcavity and single-line defect waveguide on InP membranes," *IEEE J. Quantum Electron.*, vol. 38, pp. 811–815, July 2002.

[31] E. Miyai, M. Okano, M. Mochizuki, and S. Noda, "Analysis of coupling between two-dimensional photonic crystal waveguide and external waveguide," *Appl. Phys. Lett.*, vol. 81, pp. 3729–3731, Nov. 11, 2002.

[32] A. Martinez, A. Griol, P. Sanchis, and J. Marti, "Mach-Zehnder interferometer employing coupled-resonator optical waveguides," *Opt. Lett.*, vol. 28, pp. 405–407, Mar. 15, 2003.

[33] W. D. Zhou, J. Sabarinathan, P. Bhattacharya, B. Kochman, E. W. Berg, P.-C. Yu, and S. W. Pang, "Characteristics of a photonic bandgap single defect microcavity electroluminescent device," *IEEE J. Quantum Electron.*, vol. 37, pp. 1153–1160, Sept. 2001.

[34] M. Lončar, T. Yoshie, A. Scherer, P. Gogna, and Y. Qiu, "Low-threshold photonic crystal laser," *Appl. Phys. Lett.*, vol. 81, pp. 2680–2682, Oct. 7, 2002.

[35] B. L. Shoop, *Photonic Analog-to-Digital Conversion*. Berlin: Springer-Verlag, 2001.

[36] E. Yablonovitch, "Photonic crystals: Semiconductors of light," *Sci. Am.*, vol. 285, pp. 47–55, Dec. 2001.

[37] J. Mills, "Photonic crystals head toward the marketplace," *Opto and Laser Europe*, vol. 100, pp. 10–11, Nov. 2002.

[38] *Neophotonics*. 2911 Zanker Road, San Jose, CA 95134.

[39] *Galian Photonics*. 300 - 1727 W Broadway Vancouver, BC V6J 4W6 (closed).

[40] *Mesophotonics*. 2 Venture Road, Chilworth Science Park, Southampton, Hampshire, United Kingdom, SO16 7NP.

[41] *NanoOpto*. 1600 Cottontail Lane, Somerset, NJ 08873-5117.

[42] *Luxtera*. 1819 Aston Avenue, Suite 102, Carlsbad, CA 92008.

[43] *Clarendon Photonics*. 153 Needham St., Newton, MA 02464.

[44] *Crystal Fibre A.S.* Blokken 84, DK-3460 Birkerød, Denmark.

[45] *Photeon Technologies Gmbh.* Kirchstrasse 35, 6900 Bregenz, Austria.

[46] J. D. Joannopoulos, R. D. Meade, and J. N. Winn, *Photonic Crystals Molding the Flow of Light*. Princeton: Princeton University Press, 1995.

[47] E. Yablonovitch, "Photonic band-gap structures," *J. Opt. Soc. Amer. B*, vol. 10, pp. 283–295, Feb. 1993.

[48] W. M. Robertson, G. Arjavalingam, R. D. Meade, K. D. Brommer, A. M. Rappe, and J. D. Joannopoulos, "Measurement of photonic band structure in a two-dimensional periodic dielectric array," *Phys. Rev. Lett.*, vol. 68, pp. 2023–2026, Mar. 30, 1992.

[49] S. Rowson, A. Chelnokov, J. M. Lourtioz, and F. Carcenac, "Reflection and transmission characterization of a hexagonal photonic crystal in the mid infrared," *J. Appl. Phys.*, vol. 83, pp. 5061–5064, May 15, 1998.

[50] P. Parimi, W. T. Lu, P. Vodo, J. Sokoloff, J. Derov, and S. Sridhar, "Negative refraction and left-handed electromagnetism in microwave photonic crystals," *Phys. Rev. Lett.*, vol. 92, pp. 127401–1–127401–4, Mar. 26, 2004.

[51] V. Tolmachev, T. Perova, and K. Berwick, "Design criteria and optical characteristics of one-dimensional photonic crystals based on periodically grooved silicon," *Appl. Opt.*, vol. 42, pp. 5679–5683, Oct. 1, 2003.

[52] A. Xing, M. Davanco, D. J. Blumenthal, and E. L. Hu, "Fabrication of InP-based two-dimensional photonic crystal membrane," *J. Vac. Sci. Technol. B.*, vol. 22, pp. 70–73, Jan. 2004.

[53] E. Yablonovitch, T. J. Gmitter, and K. M. Leung, "Photonic band structure: The face-centered-cubic case employing nonspherical atoms," *Phys. Rev. Lett.*, vol. 67, pp. 2295–2298, Oct. 21, 1991.

[54] E. Özbay, E. Michel, G. Tuttle, R. Biswas, M. Sigalas, and K.-M. Ho, "Micromachined millimeter-wave photonic-bandgap crystals," *Appl. Phys. Lett.*, vol. 64, pp. 2059–2061, Apr. 18, 1994.

[55] M. Sigalas and C. A. Flory, "Microwave measurements of stub tuners in two-dimensional phtoonic crystal waveguides," *Phys. Rev. B*, vol. 65, pp. 125209–1–125209–5, Mar. 13, 2002.

[56] C.-Y. Chang and W.-C. Hsu, "Photonic bandgap dielectric waveguide filter," *IEEE Microwave and Wireless Components Lett.*, vol. 17, pp. 137–139, Apr. 2002.

[57] A. de Lustrac, F. Gadot, S. Cabaret, J.-M. Lourtioz, T. Brillat, A. Priou, and E. Akmansoy, "Experimental demonstration of electrically controllable photonic crystals at centimeter wavelengths," *Appl. Phys. Lett.*, vol. 75, pp. 1625–1627, Sep. 13, 1999.

[58] J.-M. Lourtioz, A. de Lustrac, F. Gadot, S. Rowson, A. Chelnokov, T. Brillat, A. Ammouche, J. Danglot, O. Vanbésien, and D. Lippens, "Toward controllable photonic crystals for centimeter- and millimeter-wave devices," *J. Lightwave Technol.*, vol. 17, pp. 2025–2031, Nov. 1999.

[59] F. Cuesta, A. Griol, A. Martínez, and J. Martí, "Experimental demonstration of photonic crystal direction coupler at microwave frequencies," *Electron. Lett.*, vol. 39, pp. 455–456, Mar. 6, 2003.

[60] S. Rowson, A. Chelnokov, C. Cuisin, and J.-M. Lourtioz, "Three-dimensional characterisation of a two-dimensional photonic bandgap reflector at mid-infrared wavelengths," *IEE Proc. - Optoelectron.*, vol. 145, pp. 403–408, Dec. 1998.

[61] S. Rowson, A. Chelnokov, C. Cuisin, and J.-M. Lourtioz, "Two-dimeanional photonic bandgap reflectors for free-propagating beams in the mid-infrared," *J. Opt. A: Pure Appl. Opt.*, vol. 1, pp. 483–489, July 1999.

[62] J. Schilling, A. Birner, F. Müller, R. B. Wehrspohn, R. Hillebrand, U. Gösele, K. Busch, S. John, S. W. Leonard, and H. M. van Driel, "Optical characterization of 2D macroporous silicon photonic crystals with bandgaps around 3.5 and 1.3 μm," *Opt. Mats.*, vol. 17, pp. 7–10, Feb. 2001.

[63] S. W. Leonard, H. M. van Driel, K. Busch, S. John, A. Birner, A.-P. Li, F. Müller, U. Gösele, and V. Lehmann, "Attenuation of optical trasnmission within the band gap of thin two-dimensional macroporous silicon photonic crystals," *Appl. Phys. Lett.*, vol. 75, pp. 3063–3065, Nov. 15, 1999.

[64] U. Grüning, V. Lehmann, and C. M. Engelhardt, "Two-dimensional infrared photonic bandgap structure based on porous silicon," *Appl. Phys. Lett.*, vol. 66, pp. 3254–3256, Jun. 12, 1995.

[65] Y. Xu, H. Sun, J.-Y. Ye, S. Matsuo, and H. Misawa, "Fabrication and direct transmission measurement of high-aspect-ratio two-dimensional silicon-based photonic crystal chips," *J. Opt. Soc. Amer. B*, vol. 18, pp. 1084–1091, Aug. 2001.

[66] *RSoft Design Group*, Ossining, New York, *BandSOLVE 1.0*, 2002.

[67] N. W. Ashcroft and N. D. Mermin, *Solid State Physics*. Philadelphia: Saunders College, 1976.

[68] B. Hiett, J. M. Generowicz, S. J. Cox, M. Molinari, D. H. Beckett, and K. S. Thomas, "Application of finite element methods to photonic crystal modelling," *IEE Proc - Sci. Meas. Technol.*, vol. 149, pp. 293–296, Sept. 2002.

[69] W. Nakagawa, R. C. Tyan, P.-C. Sun, and Y. Fainman, "Analysis of near-field effects in artificial dielectric structures using rigorous coupled-wave analysis," *1999 IEEE LEOS Annual Meeting Conf. Proc.*, vol. 2, pp. 495–496, 1999.

[70] E. Kosmidou and T. D. Tsiboukis, "An FDTD analysis of photonic crystal waveguides comprising third-order nonlinear materials," *Opt. Quant. Elect.*, vol. 35, pp. 931–946, 2003.

[71] K. S. Yee, "Numerical solution of initial boundary value problems involving Maxwell's equations in isotropic media," *IEEE Trans. Antennas Propagat.*, pp. 302–307, May 1966.

[72] *RSoft Design Group*, Ossining, New York, *FullWAVE 3.0*, 2002.

[73] F. L. Pedrotti and L. S. Pedrotti, *Introduction to Optics (Second Edition)*. New Jersey: Prentice Hall, 1993.

[74] *The Math Works*. 3 Apple Hill Drive, Natick, MA 01760.

[75] M. Born and E. Wolf, *Principles of Optics Electromagnetic Theory of Propagation, Interference and Diffraction of Light (Sixth Edition)*. New York: Pergamon Press, 1980.

[76] S. A. Campbell, *The Science and Engineering of Microelectronic Fabrication.* New York: Oxford University Press, 1996.

[77] C. Jamois, R. B. Wehrspohn, J. Schilling, F. Müller, R. Hillebrand, and W. Hergert, "Silicon-based photonic crystal slabs: Two concepts," *IEEE J. Quantum Electron.*, vol. 38, pp. 805–810, July 2002.

[78] *AutoDesk Inc.* 111 McInnis Parkway, San Rafael, CA 94903, 2002.

[79] J. Bhardwaj and H. Ashraf, "Advanced silicon etching using high density plasmas," in *Micromachining and Microfabrication Process Technology*, vol. 2639, pp. 224–233, SPIE-Int. Soc. Opt. Eng, 1995.

[80] J. Hopkins, H. Ashraf, J. Bhardwaj, A. M. Hynes, I. Johnston, and J. N. Shepard, "The benefits of process parameter ramping during the plasma etching of high aspect ratio silicon structures," in *Proceeding of the Materials Research Society Fall Meeting*, 1998.

[81] A. Chelnokov, S. David, K. Wang, F. Marty, and J.-M. Lourtioz, "Fabrication of 2-D and 3-D silicon photonic crystals by deep etching," *IEEE J. Selected Topics Quantum Electron.*, vol. 8, pp. 919–927, July 2002.

[82] *Ealing Catalog.* 3845 Atherton Road, Rocklin, CA 95765.

[83] *Thermo-Oriel.* 150 Long Beach Blvd., Stratford, CT 06497.

[84] T. K. Gaylord and G. R. Kilby, "Optical single-angle plane-wave transmittances/reflectances from Schwarzchild objective variable-angle measurements," *Rev. Sci. Inst.*, vol. 75, pp. 317–323, Feb. 2004.

[85] G. Strang, *Linear Algebra and its Applications Third Edition.* San Diego: Harcourt, Brace, Jovanovich, 1988.

[86] P. C. Hansen, *Rank-Deficient and Discreete Ill Posed Problems Numerical Aspects of Linear Inversion.* Philadelphia: Society for Industrial and Applied Mathematics, 1998.

[87] Department of Mathematical Modeling, Technical University of Denmark, Building 305, DK-2800 Lyngby, Denmark, *Regularization Tools A Matlab Package for Analysis and Solution of Discrete Ill-Posed Problems Version 3.1 for Matlab 6.0*, 2001.

[88] A. Tikhonov and V. Y. Arsenin, *Solutions of Ill-Posed Problems.* Washington D. C.: Winston and Sons, 1977.

[89] P. R. Brevington and D. K. Robinson, *Data Reduction and Error Analysis for the Physical Sciences (Second Edition).* New York: McGraw-Hill, Inc., 1992.

[90] *MPB Technoloiges Inc.* 147 Hymus Blvd., Montreal, Quebec, H9R 1E9.

[91] *Photon Inc.* 6860 Santa Teresa Blvd., San Jose CA 95119-1205.

[92] *Bruker Optics*, 19 Fortune Drive, Billerica, MA 01821, *IFS 66/S User's Manual*, 2000.

[93] *Bruker Optics*, 19 Fortune Drive, Billerica, MA 01821, *Hyperion User's Manual*, 2003.

[94] G. R. Kilby and T. K. Gaylord, "FTIR characterization of scaled-up photonic crystal structures," in *Frontiers in Optics: The 87th OSA Annual Meeting*, p. 70, Optical Society of America, 2003.

[95] G. R. Kilby and T. K. Gaylord, "Characterization of scaled-up photonic crystal structures using a diescretely tunable carbon-dioxide laser," in *Frontiers in Optics: The 88th OSA Annual Meeting*, p. 48, Optical Society of America, 2004.

[96] *Spiricon, Inc.*, 2600 North Main, Logan UT 84341, *Pyrocam III*.

[97] G. L. Carr, F. A. Reffner, and G. P. Williams, "Performance of an infrared microspectrometer at the nsls," *Rev. Sci. Inst.*, vol. 66, pp. 1490–1492, Feb. 1995.

[98] W. D. Duncan and G. P. Williams, "Infrared synchrotron radiation from electron storage rings," *Appl. Opt.*, vol. 22, pp. 2914–2923, Sep. 15, 1983.

VITA

Gregory R. Kilby was born on June 29, 1965 in Minneapolis, Minnesota. He received a Bachelor of Science Degree in Electrical Engineering from the United States Miliary Academy at West Point, New York in 1987. He received the Master of Science degree in Electrical Engineering from the University of Minnesota in 1996. During this time, he performed research on a dynamic-focus lens systems with diffractive optic correction. While serving as an instructor in the Department of Electrical Engineering and Computer Science at the United States Military Academy, he also conducted research on diffractive elements for application in digital half-tone imaging. He is a member of the Institute of Electrical and Electronics Engineers (IEEE), the Optical Society of America (OSA), the Society for Industrial and Applied Mathematics (SIAM), and Eta Kappa Nu.